

# **Combustion Synthesis of Nanomaterials for Photocatalytic and Photovoltaic Applications**

A. Daya Mani

A Dissertation Submitted to  
Indian Institute of Technology Hyderabad  
In Partial Fulfillment of the Requirements for  
The Degree of Doctor of Philosophy



भारतीय प्रौद्योगिकी संस्थान हैदराबाद  
Indian Institute of Technology Hyderabad

Department of Chemistry

August, 2014

## Declaration

I declare that this written submission represents my ideas in my own words, and where others' ideas or words have been included, I have adequately cited and referenced the original sources. I also declare that I have adhered to all principles of academic honesty and integrity and have not misrepresented or fabricated or falsified any idea/data/fact/source in my submission. I understand that any violation of the above will be a cause for disciplinary action by the Institute and can also evoke penal action from the sources that have thus not been properly cited, or from whom proper permission has not been taken when needed.

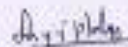
*A. D. Mani*

A. Daya Mani

(CY10P006)

## Approval Sheet

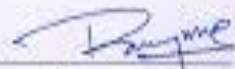
This thesis entitled "Combustion Synthesis of Nanomaterials for Photocatalytic and Photovoltaic Applications" by A. Dayu Mani is approved for the degree of Doctor of Philosophy from IIT Hyderabad.



L. H. PRASAD

-Name and affiliation-

Examiner



-Name and affiliation-

Examiner

B. V. Prasad



Dr. Ch. Subrahmanyam

-Name and affiliation-

Associate Professor  
Department of Chemistry  
Indian Institute of Technology, Hyderabad  
Yeddumalaram, 502 205, A. P., INDIA

-Name and affiliation-

Co-Adviser



-Name and affiliation-

Chairman

S. KEESHAV

## **Acknowledgements**

It is my great pleasure to express my deep sense of gratitude to my Ph.D. supervisor Dr. Ch. Subrahmanyam, Associate Professor, Department of Chemistry, IIT Hyderabad for his support, motivation, guidance, incessant encouragement and moral support. His indefatigable professional interests, ever willingness to help have had a profound influence on my thinking. I will ever remain grateful to him for his constant encouragement and sustained help throughout the progress of my research work.

I am highly beholden to Dr. M. Deepa for her valuable suggestions during the solar cell studies. I wish to express my sincere thanks to my Doctoral Committee members Dr. M. Deepa and Dr. G. Prabu Sankar for their valuable and critical comments and suggestions during my research work. I express my deep sense of thanks to the authorities of University Grants Commission, New Delhi for providing research fellowship and the authorities of IIT Hyderabad for providing necessary research facilities.

With great pleasure I acknowledge the vital role of my family. At this moment, I wish to thank my father Sri Rama Krishna (Late) for his great love and responsibility, encouragement and blessings which I can never forget. I am both lucky and thankful for the continual love, encouragement and support given by my mother and brother. I am very much thankful to my colleagues Ms. Sk. Mahammadunnisa, Mr. P. Manoj Kumar Reddy, Mr. K. Krushnamurthy, Mr. B. Rama Raju, Mr. J. Karupiah, Mr. E. Linga Reddy, Ms. Chandana, Mr. B. Lakshmi Narayana and Ms. Remya Narayanan for their invaluable support, help, friendliness and encouragement throughout my research life in IIT Hyderabad. Last but not least, research is collective work, I thank all those who have helped me directly or indirectly for my research work and to the Almighty for his grace and presence with me.

Dedicated to

My beloved Parents and Brother.

## Abstract

The major problems the world is facing today are related to energy production and environmental pollution. Increasing oil prices, environmental pollution and energy demand stimulated vigorous research on the development of alternative energy sources. Utilization of solar energy by photocatalytic route may facilitate the removal of pollutants, whereas photocatalytic/(photovoltaic) fuel/(energy) generation may meet the energy demand. The concerns due to the depletion of fossil fuels and environmental problems fostered the research on development of clean energy sources. In this context, hydrogen has the potential to surpass the fossil fuels. From long time, water has been advocated as the choice of compound for hydrogen production. Even though photocatalytic water splitting by either ultraviolet or solar irradiation has been extensively studied, still the efficiency of this process is not satisfactory. Another potential application of photocatalysis is the pollutant degradation, which was carried out both under homogeneous and heterogeneous conditions. Solid semiconductors offer additional advantages like less expensive, robust and can be easily recovered and reused. Even though various attempts have been reported to synthesize a series of semiconductors, there exists a need to revisit the synthetic strategies to design tailor made photocatalysts.

Photovoltaic way of converting solar radiation into electricity may offer a solution to the electricity demand. However for practical applications, the high cost of traditional silicon based PV technology has to transform to low cost alternatives like dye sensitized solar cells (DSSC), whose performance can still be increased with the advent of nanomaterials. Especially quantum dot sensitized solar cells (QDSSCs) offer unique advantage of tuning the absorption of visible light by simply changing the nanoparticle's diameter. Therefore a solution for the above mentioned challenges is the effective utilization of solar energy by designing materials that can harvest visible part of the solar spectrum.

The objectives of this thesis work are to use the energy and time efficient combustion syntheses technique for the preparation of different semiconductor

nanomaterials that are capable of harvesting solar energy. This thesis mainly focusses on

- Combustion synthesis of efficient visible light harvesting C,N doped TiO<sub>2</sub> nanomaterials by optimizing the titanium nitrate synthesis and its photocatalytic applications
- Synthesis of C,N-doped TiO<sub>2</sub> nanomaterials, optimization of fuel by correlating the number of moles of gases evolved during the combustion with the physico-chemical properties and study of their photocatalytic activity for the removal of aqueous organic pollutants
- Synthesis of C-doped TiO<sub>2</sub> nanomaterials, optimization studies for choosing a better fuel and their application towards simultaneous removal of aqueous organic pollutants.
- Synthesis of metal sulfides such as cadmium sulfide and zinc sulfide under atmospheric conditions and their photocatalytic activity for pollutant removal and H<sub>2</sub> production from water.
- Single step syntheses of CdS/TiO<sub>2</sub> composite materials by using combustion synthesis and their applications towards photocatalytic H<sub>2</sub> production.
- Stoichiometry selective synthesis of transition metal sulfides such as nickel sulfide, cobalt sulfide and copper sulfide by using combustion and their application as substitutes for Pt electrode in QDSSCs.

## **Nomenclature**

**XRD:** X-ray diffraction

**TEM:** Transmission Electron Microscopy

**SEM:** Scanning Electron Microscopy

**UV-Vis Spectroscopy:** Ultra violet and visible spectroscopy

**TGA-** Thermo gravimetric analysis

**CV:** Cyclic Voltammetry

**EIS:** Electrochemical Impedance Spectroscopy

**XPS:** X-ray photoelectron spectroscopy

**GC:** Gas chromatograph

**TCD:** Thermal conductivity detector

**MB:** Methylene blue

**ppm:** parts per million



# Contents

Declaration	ii
Approval Sheet	iii
Acknowledgements	iv
Abstract	vi
<b>Nomenclature</b>	viii
<b>List of Tables</b>	xiv
<b>List of Figures</b>	xv
<b>Chapter 1 Introduction</b>	
1.1 Preface	1
1.2. Renewable energies	1
1.2.1. Wind Energy	1
1.2.2. Geothermal Energy	2
1.2.3. Solar Energy	2
1.3. Photovoltaics	2
1.3.1. The physical processes in a solar device	4
1.3.2. Quantum dot sensitized solar cells	5
1.4. Photocatalysis	5
1.4.1. Mechanism of semiconductor photocatalysis	7
1.4.2. Recombination of excitons	8
1.4.3. Photocatalytic H <sub>2</sub> production	9
1.4.4. Photocatalytic degradation of pollutants	10
1.5. Materials for solar energy harvesting	11
1.6. How to overcome the limitations of harvesting solar energy	13
1.6.1. Doping TiO <sub>2</sub> with cations	14
1.6.2. Doping TiO <sub>2</sub> with anions	14
1.6.3. Coupling with small band gap semiconductors	15
1.6.4. Sensitizing with dyes	16
1.7. Available methods for the synthesis of nanomaterials	17

1.7.1.	Hydrothermal method	17
1.7.2.	Gas phase methods	18
1.7.3.	Sol-gel method	19
1.8.	Combustion synthesis	19
1.9	Why combustion synthesis...?	20
References.....		24

## **2 Materials, Methods and Characterization**

2.1.	Chemicals	36
2.2.	Experimental procedures	36
2.3.	Characterization techniques	38
2.3.1.	Powder X-ray diffraction	38
2.3.2.	X-ray photoelectron spectroscopy	41
2.3.3.	UV-Vis absorption spectroscopy	43
2.3.4.	UV-Vis Diffuse Reflectance Spectroscopy	44
2.3.5.	N <sub>2</sub> sorption analysis	46
2.3.6.	Transmission electron microscopy	48
2.3.7.	Photoluminescence spectroscopy	51
2.3.8.	Gas chromatography	52
2.3.9.	Raman spectroscopy	53
2.3.10.	Electrochemical Impedance Spectroscopy	53
2.3.11.	Solar simulator	55
References.....		57

## **Chapter 3 Section I: Optimization of titanyl nitrate synthesis and photocatalytic activity under natural sunlight**

3.1.1.	Introduction	59
3.1.2.	Experimental Section	60
3.1.3.	Results and discussion	62
3.1.3.1	XRD	62
3.1.3.2	TEM	63
3.1.3.3	UV- Visible spectroscopy	63
3.1.3.4	N <sub>2</sub> adsorption	64
3.1.3.5	XPS	64
3.1.3.6	Photocatalytic activity studies under direct sunlight	67
3.1.3.7.	Conclusion	68

References.....	70
-----------------	----

**Chapter 3 Section II: Opimization of fuel for the combustion synthesis of C, N doped TiO<sub>2</sub>**

3.2.1.	Introduction	73
3.2.2.	Experimental section	74
3.2.3.	Results and Discussion	75
3.2.3.1.	XRD	75
3.2.3.2.	TEM	75
3.2.3.3.	UV- Visible spectroscopy	77
3.2.3.4.	N <sub>2</sub> adsorption	78
3.2.3.5.	XPS	78
3.2.3.6.	TGA studies	81
3.2.3.7.	CHNS studies	82
3.2.3.8.	Photocatalytic studies	83
3.2.4.	Conclusion	88
References.....		89

**Chapter 3 Section III: Optimization of fuel for combustion synthesis of C doped TiO<sub>2</sub>**

3.3.1.	Introduction	93
3.3.2.	Experimental Section	94
3.3.3.	Results and discussion	96
3.3.3.1.	XRD	96
3.3.3.2.	TEM	96
3.3.3.3.	UV- Visible spectroscopy	97
3.3.3.4.	N <sub>2</sub> adsorption	98
3.3.3.5.	XPS	99
3.3.3.6.	TGA studies	100
3.3.3.7.	Photocatalytic studies	101
3.3.4.	Conclusion	107
References.....		108

**Chapter 4 Section I: Combustion synthesis of cadmium sulfide nanomaterials for efficient hydrogen production from water**

4.1.1.	Introduction	112
4.1.2.	Experimental details	113

4.1.3.	Results and discussion	114
4.1.3.1.	XRD	114
4.1.3.2.	TEM	115
4.1.3.3.	UV- Visible spectroscopy	116
4.1.3.4.	XPS	116
4.1.3.5.	Raman Spectra	117
4.1.3.6.	Photocatalytic studies	118
4.1.4.	Conclusion	120
References.....		121
<b>Chapter 4 section II: Highly efficient C, N doped ZnS microstructures with rice grain morphology for visible light photocatalytic activity</b>		
4.2.1.	Introduction	124
4.2.2.	Experimental Details	125
4.2.3.	Results and discussion	126
4.2.3.1.	XRD	127
4.2.3.2.	TEM	127
4.2.3.3.	UV- Visible spectroscopy	128
4.2.3.4.	XPS	129
4.2.3.5.	CHNS analysis	130
4.2.3.6.	Photocatalytic studies	130
4.2.4.	Conclusion	136
References.....		137
<b>Chapter 5 One pot synthesis of CdS/ TiO<sub>2</sub> nanomaterials for enhanced H<sub>2</sub> Production from water and removal of pollutants</b>		
5.1.	Introduction	141
5.2.	Experimental details	142
5.3.	Results and discussion	143
5.3.1.	XRD	143
5.3.2.	TEM	144
5.3.3.	UV- Visible spectroscopy	147
5.3.4.	XPS	148
5.3.5.	Raman spectra	150
5.3.6.	N <sub>2</sub> adsorption studies	151
5.3.7.	Fluorescence quenching	151

5.3.8.	Photocatalytic studies	152
5.4.	Conclusion	155
References.....		156
<b>Chapter 6 Section I: Novel one pot stoichiometric synthesis of nickel sulfide nanomaterials as counter electrode materials in QDSSC</b>		
6.1.1.	Introduction	161
6.1.2.	Experimental Details	162
6.1.3.	Results and discussion	164
6.1.3.1.	Photoluminescence Spectral Studies	164
6.1.3.2.	Diffuse reflectance UV-Vis spectral analyses	165
6.1.3.3.	X-ray diffraction (XRD)	165
6.1.3.4.	Transmission Electron Microscopy (TEM)	166
6.1.3.5.	X-ray photoelectron spectroscopy (XPS)	167
6.1.3.6.	Photoelectrochemical Measurements	168
6.1.3.7.	Electrochemical Impedance Spectroscopy	170
6.1.4.	Conclusion	172
References.....		173
<b>Chapter 6 Section II: Single pot synthesis of metal (Pb, Cu, Co) sulfide nanomaterials as efficient counter electrodes in QDSSCs</b>		
6.2.1.	Introduction	177
6.2.2.	Experimental details	178
6.2.3.	Results and discussion	180
6.2.3.1.	XRD	180
6.2.3.2.	TEM	182
6.2.3.3.	Photoelectrochemical measurements	183
6.2.3.4.	Electro Chemical Impedance Spectroscopy	188
6.2.4.	Conclusion	189
References.....		190
<b>Chapter 7 Summary and Conclusions</b>		<b>195</b>

## List of Tables

<b>Table No.</b>	<b>Title</b>	<b>Page No.</b>
3.1.1.	Physico-chemical characteristics of combustion synthesized TiO <sub>2</sub> samples	65
3.2.1.	Physico-chemical characteristics of combustion synthesized TiO <sub>2</sub> samples	75
6.1.1.	Solar cell parameters for various QDSSCs fabricated by using different CE	160
6.1.2.	Solar cell parameters for various QDSSCs fabricated by using different working electrodes used in this study with CE 2 (Ni <sub>3</sub> S <sub>2</sub> ) and Pt as counter electrodes and the various impedance parameters	171
6.2.1.	Solar cell parameters for various QDSSCs fabricated by using different counter electrodes used in this study and the various impedance parameters obtained by fitting in an equivalent circuit.	174
6.2.2.	Solar cell parameters for various QDSSCs fabricated by using different metal sulfide counter electrodes	

## List of Figures

Figure No.	Title	Page No.
1.1.	Solar irradiation is the ultimate source of energy that is converted by green plants into chemical energy and, through their evolution, into fossil fuels (open arrow). Over the millennia, mankind has learned to exploit the renewable supply afforded by plants for obtaining food, materials and energy (green arrows). In the last two centuries man has learned to exploit a convenient, but non-renewable, source such as fossil fuels (red arrows). Will it be able to use solar irradiation directly for both energy and materials (blue arrows)?	6
1.2.	Diagrammatic representation of photocatalytic mechanism	7
1.3.	Diagrammatic representation of different recombination processes taking place in photocatalysis	8
1.4.	Schematic representation of photocatalytic mechanism in metal doped TiO <sub>2</sub>	13
1.5.	Photocatalytic mechanism in coupled semiconductor systems	15
1.6.	Diagrammatic representation of photocatalytic mechanism in dye sensitized TiO <sub>2</sub> system	16
2.1.	Bragg's law for X-ray diffraction. The diffracted X-rays exhibit constructive interference when the distance between paths ABC and A'B'C' differs by an integer number of wavelengths ( $\lambda$ ).	38
2.2.	Schematic diagram of a X-ray diffractometer	38
2.3.	Photoelectron( $e_p$ ) and Auger electron ( $e_A$ ) emission processes induced by X-rays	40
2.4.	Basic scheme of XPS instrumentation	41
2.5.	Schematic representation of the radiation interaction with the sample: $R_s$ stands for the specular reflected beam, $R_d$ for the diffuse reflected beam	43

2.6.	Signals generated when a high-energy beam of electrons interacts with a thin specimen. Most of these signals can be detected in different types of electron microscopes. The directions shown for each signal do not always represent the physical direction of the signal but indicate, in a relative manner, where the signal is stronger or where it is detected	47
2.7.	General scheme of a) SEM and b) TEM instrumentations.	48
2.8.	Generalized description of the three main imaging modes in TEM	49
3.1.1.	Powder X-ray diffraction patterns of combustion synthesized TiO <sub>2</sub> samples.	60
3.1.2.	(a) Transmission electron micrograph of G-TiO <sub>2</sub> -III with selected area diffraction pattern shown in the inset (b) HRTEM image of G-TiO <sub>2</sub> -III	61
3.1.3.	Diffused reflectance UV-vis spectra of combustion synthesized TiO <sub>2</sub> samples.	62
3.1.4.	XPS spectra of Ti 2p core levels of G-TiO <sub>2</sub> -I, G-TiO <sub>2</sub> -II, G-TiO <sub>2</sub> -III and G-TiO <sub>2</sub> -IV.	63
3.1.5.	XPS spectra of O 1s core levels of G-TiO <sub>2</sub> -I, G-TiO <sub>2</sub> -II, G-TiO <sub>2</sub> -III and G-TiO <sub>2</sub> -IV.	63
3.1.6.	XPS spectra of C 1s core levels of (a) G-TiO <sub>2</sub> -I (b) G-TiO <sub>2</sub> -II (c) G-TiO <sub>2</sub> -III and (d) G-TiO <sub>2</sub> -IV.	64
3.1.7.	XPS spectra of N 1s core levels of (a) G-TiO <sub>2</sub> -I (b) G-TiO <sub>2</sub> -II (c) G-TiO <sub>2</sub> -III and (d) G-TiO <sub>2</sub> -IV.	65
3.1.8.	Photocatalytic degradation of methylene blue concentration with time for all the combustion synthesized catalysts along with Evonik P-25. (inset shows the variation of initial rates with type of the catalyst) (C <sub>0</sub> = 10 mg/l and catalyst amount = 1 gm /l)	66
3.2.1.	Powder X-Ray Diffraction patterns of combustion synthesized TiO <sub>2</sub> samples	70



3.2.2.	(a) TEM image of combustion synthesized G -TiO <sub>2</sub> catalyst (b) HRTEM image of G-TiO <sub>2</sub> showing planes of G-TiO <sub>2</sub> (c) Selected area electron diffraction pattern of G-TiO <sub>2</sub>	71
3.2.3.	Diffused Reflectance UV-Vis spectra of combustion synthesized TiO <sub>2</sub>	71
3.2.4.	XPS spectra of Ti 2p core levels of G-TiO <sub>2</sub> , H-TiO <sub>2</sub> , TEA-TiO <sub>2</sub> , GH-TiO <sub>2</sub> and TEAG TiO <sub>2</sub> .	72
3.2.5.	(a) XPS spectra of N 1s core levels of G-TiO <sub>2</sub> , TEA-TiO <sub>2</sub> , GH-TiO <sub>2</sub> and TEAG TiO <sub>2</sub> . (b) XPS spectra of N 1s core levels of H-TiO <sub>2</sub> showing additional peak at 407.5 eV which is indicative of M-N bonding	73
3.2.6.	XPS spectra of C 1s core levels of (a) G-TiO <sub>2</sub> (b) H-TiO <sub>2</sub> (c) TEA-TiO <sub>2</sub> (d) GH-TiO <sub>2</sub> and TEAG-TiO <sub>2</sub> .	74
3.2.7.	TGA spectra of combustion synthesized samples under air atmosphere.	75
3.2.8.	First order kinetic plots for the photocatalytic degradation of MB in presence of different combustion synthesized photocatalysts (C <sub>0</sub> = 20 ppm, Catalyst amount =0.25gm/l).	76
3.2.9.	(a) First order kinetic plots showing the effect of catalytic amount on degradation of MB in presence of G-TiO <sub>2</sub> (C <sub>0</sub> = 20 ppm). (b) First order kinetic plots representing the effect of initial concentration of MB on its degradation in presence of G-TiO <sub>2</sub> (Catalytic amount- 1 gm/L).	77
3.2.10.	(a) Photocatalytic reduction of Cr(VI) in presence of various catalytic dosages of G-TiO <sub>2</sub> (C <sub>0</sub> = 20 ppm). (b) First order kinetic plots representing the effect of pH on photocatalytic reduction of Cr(VI) with G-TiO <sub>2</sub> photocatalyst (Catalytic amount- 1 gm/L).	80
3.3.1.	Powder X-ray diffraction patterns of the C-doped TiO <sub>2</sub> samples	85
3.3.2.	(a) TEM image of Asc -TiO <sub>2</sub> (inset shows the SAED pattern) (b) HRTEM image of Asc-TiO <sub>2</sub> showing lattice	87

	fringes characteristic of anatase phase TiO <sub>2</sub> (c) TEM image of Cit -TiO <sub>2</sub> (inset shows the SAED pattern) (d) HRTEM image of Asc-TiO <sub>2</sub> showing lattice fringes characteristic of anatase phase TiO <sub>2</sub>	
3.3.3.	Diffused reflectance UV-Vis spectra of C-doped TiO <sub>2</sub> samples along with commercial TiO <sub>2</sub> sample	88
3.3.4.	N <sub>2</sub> adsorption isotherms of (a) Asc-TiO <sub>2</sub> (b) Cit-TiO <sub>2</sub>	88
3.3.5.	(a) XPS spectra of Ti 2p core levels of Asc-TiO <sub>2</sub> and Cit-TiO <sub>2</sub> . (b) XPS spectra of O 1s core levels of Asc-TiO <sub>2</sub> and Cit- TiO <sub>2</sub> . (c) XPS spectra of C 1s core levels of Asc-TiO <sub>2</sub> (d) XPS spectra of C 1s core levels of Cit- TiO <sub>2</sub> .	89
3.3.6.	TGA spectra of C-doped TiO <sub>2</sub> samples under air atmosphere	90
3.3.7.	Comparison of photocatalytic activities of C-doped TiO <sub>2</sub> samples and commercial TiO <sub>2</sub> sample for the reduction of Cr(VI) under simulated solar light. (Catalyst amount = 1gm/l, C <sub>Cr(VI)</sub> = 100 ppm)	91
3.3.8.	(a). First order kinetic plots for the photocatalytic reduction of Cr(VI) in presence of Cit- TiO <sub>2</sub> photocatalyst at different initial concentrations of Cr(VI) (Catalyst amount = 1gm/l). (b) First order kinetic plots for the photocatalytic oxidation of phenol in presence of Cit-TiO <sub>2</sub> photocatalyst at different initial concentrations of phenol (Catalyst amount = 1gm/l)	92
3.3.9.	Comparison of first order kinetics of the individual and simultaneous oxidation of phenol and reduction of Cr(VI) in presence of Cit-TiO <sub>2</sub> photocatalyst (C <sub>Cr(VI)</sub> = 50 ppm, C <sub>phenol</sub> = 30 ppm, Catalyst amount = 1gm/l)	93
4.1.1.	Powder X-ray diffraction patterns of the cadmium sulfide samples	107
4.1.2.	(a) TEM images of the best active CdS(2) sample (b) Selected area electron diffraction pattern of CdS(2) sample.	108
4.1.3.	Diffuse reflectance UV-Vis spectra of CdS samples	108

4.1.4.	XPS spectra of (a) Cd 3d core levels (b) S 2p core levels (c) C 1s core levels (d) N 1s core levels of CdS (2) sample	109
4.1.5.	(a) Raman spectra of CdS samples (b) Enlarged view of A11LO phonon mode of CdS samples (c) Enlarged view of A1 2LO phonon mode of CdS samples	110
4.1.6.	Rate of photocatalytic H <sub>2</sub> evolution from splitting of water containing Na <sub>2</sub> S and Na <sub>2</sub> SO <sub>3</sub> sacrificial reagents under visible light in the presence of different CdS samples	111
4.1.7.	Rate of H <sub>2</sub> evolution profiles from water containing Na <sub>2</sub> S and Na <sub>2</sub> SO <sub>3</sub> sacrificial agents in the presence of CdS (2) (five runs in a continuous reaction were shown)	112
4.2.1.	Powder X-ray diffraction patterns of zinc sulfide samples	116
4.2.2.	TEM image of ZnS rice grain microstructures (b) Enlarged view of the selected portion from figure 2(a). (c) Enlarged portion of rice grain shaped ZnS showing several nanoparticles (d) Further magnified view of the selected portion in figure 2(c) showing distinct nanoparticles of ZnS (inset shows selected area diffraction pattern of ZnS)	117
4.2.3.	Diffused reflectance UV-Vis spectra of ZnS samples	117
4.2.4.	XPS spectra of (a) Zn 2p (b) S 2p (c) N 1s and (d) C 1s core levels	119
4.2.5.	(a) First order kinetic plots for the oxidation of MB by ZnS samples and commercial TiO <sub>2</sub> sample (C <sub>0</sub> (MB) = 20 ppm, catalytic amount=100 mg) (b) First order rate plots for oxidation of MB at different pH values (C <sub>0</sub> (MB) = 20 ppm, catalyst amount=100 mg, pH (2,4,7,9,11))	121
4.2.6.	(a) First order kinetic plots for the reduction of Cr(VI) by ZnS samples (C <sub>0</sub> (Cr(VI)) = 10 ppm, catalytic amount=100 mg) (b) Effect of pH on photocatalytic reduction of Cr(VI) (C <sub>0</sub> (Cr(VI)) = 10 ppm, catalytic amount=100 mg, pH (2,4,7,9,11))	122

4.2.7.	First order kinetic plots for the simultaneous removal of MB and Cr(VI) ( $C_0$ (Cr(VI)) = 10 ppm, $C_0$ (MB) = 20 ppm catalytic amount=100 mg)	123
4.2.8.	(a) Rate of $H_2$ evolution profiles from water containing 1M $Na_2S$ and 1 M $Na_2SO_3$ sacrificial agents in the presence of all combustion synthesized ZnS samples for a period of 5 hr. (b) Rate of $H_2$ evolution profiles from water containing 1M $Na_2S$ and 1 M $Na_2SO_3$ sacrificial agents in the presence of ZnS (1:5) (five runs in a continuous reaction were shown)	124
5.1.	X-ray diffraction patterns of CdS/ $TiO_2$ hetero nanostructures along with pure $TiO_2$ and pure CdS	135
5.2.	(a) Low magnification HRTEM image of CdS/ $TiO_2$ (0.5:1) (b) Enlarged view of the marked portion in figure 5.2(a). (c) High magnification HRTEM image of CdS/ $TiO_2$ (0.5:1)	136
5.3.	(a) Low magnification HRTEM image of CdS/ $TiO_2$ (1:1) (b) Enlarged view of the marked portion in figure 5.3(a). (c) High magnification HRTEM image of CdS/ $TiO_2$ (1:1)	137
5.4.	(a) HRTEM image of CdS/ $TiO_2$ (1:0.5) (b) High magnification HRTEM image of CdS/ $TiO_2$ (1:0.5)	138
5.5.	Diffuse reflectance UV-Vis spectra of CdS/ $TiO_2$ hetero nanostructures along with pure $TiO_2$ and pure CdS	139
5.6.	XPS spectra of CdS/ $TiO_2$ hetero nanostructures (a) Cd 3d spectra (b) S 2p spectra (c) Ti 2p core level spectra (d) O 1s spectra (e) C 1s spectra (f) N 1s spectra.	140
5.7.	Raman spectra of CdS/ $TiO_2$ hetero nanostructures along with pure $TiO_2$ and pure CdS	141
5.8.	PL spectra of CdS and CdS/ $TiO_2$ hetero nanostructures	142
5.9.	First order kinetic profiles of oxidation of MB over CdS/ $TiO_2$ hetero nanostructures ( $C_{MB}$ = 20 ppm)	143
5.10.	First order kinetic profiles of reduction of Cr(VI) over	144

	CdS/TiO <sub>2</sub> hetero nanostructures ( $C_{Cr(VI)} = 30$ ppm)	
5.11.	H <sub>2</sub> evolution with respect to time from water containing 1M Na <sub>2</sub> S and 1 M Na <sub>2</sub> SO <sub>3</sub> sacrificial agents in the presence of CdS and CdS/TiO <sub>2</sub> composites for a period of 5 hr	145
5.12.	Five successive cycles of H <sub>2</sub> production from water containing 1M Na <sub>2</sub> S and 1 M Na <sub>2</sub> SO <sub>3</sub> sacrificial agents to assess the stability of the photocatalyst CdS/TiO <sub>2</sub> (1:1)	145
	(a) Combustion synthesized CdS powder mixed with PVDF binder	
	(b) CdS paint after 30 min of sonication in ethanol	
	(c) Application of CdS paint on FTO glass plate, pretreated with TiCl <sub>4</sub>	
6.1.1.	(d) CdS working electrode after annealing at 673 K	154
	(e) Combustion synthesized nickel sulfide powder mixed with PVDF binder	
	(f) Nickel sulfide paint after 30 min of sonication in ethanol	
	(g) Nickel sulfide paint on FTO glass plate (h) Nickel sulfide counter electrode after annealing at 673 K	
6.1.2.	Photoluminescence spectra of combustion synthesized CdS and physically grounded CdS/TiO <sub>2</sub> samples	155
6.1.3.	Absorbance spectra of the combustion synthesized CdS and physically grounded CdS/TiO <sub>2</sub> samples	156
6.1.4.	X-ray diffraction patterns of combustion synthesized nickel sulfide samples (a) XRD pattern of CE 1 sample which was found to consist of NiO. (b) XRD patterns of CE 2, CE 3, CE 4 and CE 5 samples which were found to consists of Ni <sub>3</sub> S <sub>2</sub> , NiS, NiS <sub>2</sub> and NiS <sub>2</sub> stoichiometries respectively.	157
6.1.5.	(a) TEM image of CE 2 sample (inset shows the selected	158

	area diffraction pattern) (b) HRTEM image of the CE 2 sample.	
6.1.6.	X-ray photoelectron spectra of CE 2 sample (a) Cd 3d electrons (b) S 2p electrons (c) C 1s electrons (d) N 1s electrons	159
6.1.7.	(a) J-V characteristics of photoelectrochemical cells based on bare CdS photoanode and different nickel sulfide samples as counter electrodes (b) Comparison of J-V characteristics of photoelectrochemical cells based on bare CdS and different physically grounded CdS/TiO <sub>2</sub> samples versus combustion synthesized CE 2 as counter electrode.	160
6.1.8.	Comparison of J-V characteristics of photoelectrochemical solar cells constructed by using CdS/TiO <sub>2</sub> (1:1) as photoanode versus Pt and CE 2 as counter electrodes	161
6.1.9.	(a) Comparison of electro chemical impedance spectra of different combustion synthesized nickel sulfides and Pt/FTO counter electrode (b) Equivalent circuit used for fitting the EIS data of the symmetric cells. R <sub>s</sub> is the series resistance, CPE is the constant phase element, R <sub>ct</sub> is the charge transfer resistance.	162
6.2.1.	(a) Combustion synthesized CdS powder mixed with PVDF binder (b) CdS paint after 30 min of sonication in ethanol (c) Application of CdS paint on FTO glass plate, pretreated with TiCl <sub>4</sub> (d) CdS working electrode after annealing at 673 K (e) Combustion synthesized metal (Pb, Cu, Co) sulfide powders mixed with PVDF binder (f) Metal sulfide paint after 30 min of sonication in ethanol (g) Application of metal sulfide paint on FTO glass plate	165

	(h) Metal sulfide counter electrode after annealing at 673 K	
6.2.2.	(a) PXRD spectra of PbS(1) sample showing the presence of Pb <sub>3</sub> O <sub>4</sub> (b) PXRD spectra of PbS(2), PbS(3), PbS(4) and PbS(10) samples showing the presence of PbS stoichiometry in all the samples.	166
6.2.3.	(a) PXRD spectra of CuS(1) sample showing the presence of CuO (b) PXRD spectra of CuS(2) sample showing the presence of Cu <sub>2</sub> O stoichiometry (c) PXRD spectra of CuS(3) sample showing the presence of Cu <sub>2</sub> S stoichiometry (d) PXRD spectra of CuS(4) and CuS(10) samples showing the presence of CuS stoichiometry.	167
6.2.4.	(a) PXRD spectra of CoS (1) and CoS (2) samples showing the presence of Co <sub>3</sub> O <sub>4</sub> and Co <sub>9</sub> S <sub>8</sub> stoichiometry respectively (b) PXRD spectra of CoS (3), CoS (4) and CoS (10) samples showing the presence of CoS <sub>2</sub> stoichiometry.	168
6.2.5.	(a) TEM image of CuS(3) sample (inset shows the selected area diffraction pattern) (b) HRTEM image of the CuS(3) sample confirming the Cu <sub>2</sub> S stoichiometry (c) TEM image of CoS(2) sample (d) Selected area diffraction pattern of CoS(2) sample showing the planes corresponding to the Co <sub>9</sub> S <sub>8</sub> stoichiometry.	169
6.2.6.	(a) J-V characteristics of photoelectrochemical cells based on bare CdS as working electrode and different combustion synthesized lead sulfide samples as counter electrodes.	170
6.2.7.	(a) J-V characteristics of photoelectrochemical cells based on bare CdS as working electrode and different combustion synthesized copper sulfide samples as counter electrodes.	170
6.2.8.	(a) J-V characteristics of photoelectrochemical cells based on bare CdS as working electrode and different combustion synthesized cobalt sulfide samples as counter electrodes.	172

6.2.9.	Comparison of J-V characteristics of photoelectrochemical solar cells constructed by using CdS/TiO <sub>2</sub> (1:1) as working electrode versus CuS(3), CoS(2), PbS(2) and Pt as counter electrodes.	173
6.2.10.	(a) Electro chemical impedance (EIS) spectra of different lead sulfide counter electrodes (b) EIS spectra of different copper sulfide counter electrodes (c) EIS spectra of different cobalt sulfide counter electrodes (d) EIS spectra of Pt counter electrode (e) Equivalent circuit used for fitting the EIS data of the symmetric cells. R <sub>s</sub> is the series resistance, CPE is the constant phase element, R <sub>ct</sub> is the charge transfer resistance.	175



# Chapter 1

## Introduction

---

### 1.1. Preface

In the present day scenario, there are three major challenges to the scientific community. The first challenge is related to oil crisis, which stimulated tremendous research on the development of alternative energy sources. Moreover the release of greenhouse gases from the combustion of fossil fuels appears to be a thorn for the mitigation of global warming. During the search for alternative energy sources, it has been anticipated that man could imitate nature by using solar energy for the generation of clean fuel such as H<sub>2</sub> by photocatalytic water splitting [1,2]. The second challenge is the increased environmental pollution by industrial and domestic activities and it was predicted that photocatalysis is a wise solution to clean up waste water and air by avoiding the addition of further chemicals [3]. Since 1970's photocatalysis has been finding diverse applications in the hydrogen production from water, remediation of environmental pollutants and organic synthesis [1]

The third major challenge is the generation of electricity for the increasing industrial and domestic needs. Harvesting solar energy through photovoltaic (PV) technology has the potential to provide virtually unlimited supply of usable energy that is sustainable and environmentally benign [4–6]. However, economical implementation of PV technology on a massive scale requires critical advances in both materials and devices to decrease the cost and increase the power conversion efficiency [7,8]. Nano-chemistry and nanomaterials open up new opportunities to achieve higher solar energy conversion efficiencies at lower fabrication costs, as they allow the use of inexpensive materials and inexpensive processing technologies to harvest sunlight by efficiently capturing photon energy over a broad spectral range, and then quickly separating and collecting photo-generated charge carriers [9–12].

### 1.2. Renewable energies

Renewable energy is the energy that comes from resources which are continually replenished on a human time scale such as sunlight, wind and geothermal heat etc. from which electricity can be generated.

#### 1.2.1. Wind energy

Wind turbines convert the kinetic energy of the wind into electricity. Generally, a gearbox turns the slow-turning turbine rotor into faster-rotating gears, which convert mechanical energy to electricity in a generator. The efficiency of wind power generation increases with the turbine height as the wind speed increases with the height. Therefore, larger turbines capture faster winds. Large turbines are generally sited in flat open areas of land, within mountain passes, on ridges, or offshore. Although less efficient, small turbines (e.g., 1–10 kW) are convenient for use in homes or city street canyons. Although it is an effective renewable energy source, due to the several disadvantages like breakdown in the plants and extensive maintenance makes it less advantageous. Severe variations in weather conditions such as no wind or storm also become problem for the generation of wind energy. Off shore farms may also face problems like excessive corrosion from salt water.

### **1.2.2. Geothermal energy**

Geothermal energy is the energy extracted from hot water and steam present below the Earth's surface. Steam or hot water from the Earth has been used historically to provide heat for buildings, industrial processes, and domestic water. Hot water and/or steam have also been used to generate electricity in geothermal power plants. Three major types of geothermal plants are dry steam, flash steam, and binary plants [13, 14]. Dry and flash steam plants operate where geothermal reservoir temperatures are 180–370° C or higher. A binary system is used when the reservoir temperature is 120–180°C. Because the water from the reservoir stays in an enclosed pipe when it passes through the power plant and is reinjected to the reservoir, binary systems produce virtually no emissions of CO<sub>2</sub>, NO, SO<sub>2</sub> or H<sub>2</sub>S. About 15% of geothermal plants today are binary plants.

### **1.2.3. Solar energy**

Among the several energies for producing clean energy (H<sub>2</sub>) only solar energy is found to be an efficient renewable source without any carbon emissions [15, 16]. Solar energy is primary renewable source of energy, which is clean and abundant. It supports the life on earth and forms the basis for all forms of energy we are currently using. This abundant energy reaches the earth in the form of electromagnetic radiation [17]. The solar energy reaching the earth in one minute is approximately five times more than the amount of energy required worldwide per day.

## **1.3. Photovoltaics**

Photovoltaics or solar cells are devices that convert the energy from the sun into electric power. The power conversion efficiency  $\eta$  of these devices can be given by [18]

$$\eta = (V_{oc}J_{sc} FF) / P_{inc} \quad (1.1)$$

Where  $P_{\text{inc}}$  is the incident solar power on the device,  $V_{\text{oc}}$  is the open circuit voltage,  $J_{\text{sc}}$  is the short-circuit current density, and FF is the fill factor. The short-circuit current density  $J_{\text{sc}}$  is the current density derived at zero bias voltage, while the open circuit voltage  $V_{\text{oc}}$  is the maximum voltage that a solar cell can generate.

Photovoltaic technologies are categorized into three types based on their efficiency and cost [19]. Single-crystalline Si solar cells with p–n homo junctions are considered as the first generation photovoltaics, and they suffer from low efficiency and high manufacturing and installation costs [20]. Due to its indirect band gap single-crystalline Si is not a good light absorber. Although the use of thicker Si films (up to 100 microns) can increase light absorption, the distance that charge carriers must diffuse without recombining or becoming trapped before reaching the current collector may also increase. This necessitates the requirement of Si with extremely high purity and crystalline quality. Therefore the performance of these single-crystalline Si solar cells must be weighed against their high manufacturing and processing costs [21,22]. Second-generation PV technologies involve the use of polycrystalline semiconductor thin films, such as polycrystalline and amorphous Si, CdTe, CuInSe<sub>2</sub> (CIS), and CuIn<sub>x</sub>Ga<sub>1-x</sub>Se<sub>2</sub> (CIGS) [20]. Second generation solar cells are significantly less expensive than single-crystalline PV cells due to the reduced material processing costs, and increased manufacturing throughput. However, the quality of these materials is generally lower than that of the first-generation PV cells, resulting in an increased non-radiative recombination and less overall PV efficiency [23,24]. All of these single band gap absorber PV cells are subject to the so-called Shockley–Queisser detailed balance limit of efficiency, which thermodynamically limits the solar energy conversion efficiency to 33% under 1 Sun (AM 1.5) solar illumination [25].

Third generation solar cells incorporate contemporary technologies that aim to lower costs while maintaining high efficiencies, with the potential to exceed the intrinsic efficiency limits of the first and second generation solar cells, namely, the Shockley–Queisser theoretical limit. One proposed pathway to overcome the Shockley–Queisser theoretical limit is to use materials capable of producing multiple excited electrons per absorbed photon. In multiple exciton generation (MEG), photon energy in excess of the absorbing material's band gap could be used to generate additional excitons rather than being lost as heat [26–28]. Other proposed designs involve tandem cells, intermediate-band cells, hot-carrier cells, and upconversion [29]. Chemically synthesized nanomaterials and nanoscale heterostructures provide potential avenues towards achieving the goals of these third-generation solar cells.

### **1.3.1. The physical processes in a solar device**

#### **1.3.1.1. Light absorption**

The light absorbing material in the solar device undergoes excitation upon irradiation with suitable light source to produce excitons [30,31]. Although a variety of materials can satisfy the requirements for solar energy conversion, in practice, nearly all PV energy conversion devices use semiconductor materials (inorganic or organic). To make full use of the solar spectrum and to maximize  $J_{sc}$ , light-absorbing substances with a high extinction coefficient, low band gap, and an appropriate fermi level are preferred.

#### **1.3.1.2. Electron–hole separation**

The excitons produced in the first step are separated at an energetically favorable charge separating junction into long lived charge carriers through a diffusion driven process or by a built-in internal field. For example, c-silicon (crystalline) solar devices utilize a built-in electric field to drift the electron into the n-type silicon layer and the hole into the p-type silicon layer. A proper alignment of electronic energy band structures or Fermi levels at the charge-separation junction is of particular importance in dissociating the electron–hole pair to lead them into opposite directions. In addition, an efficient charge-separation also requires low electron–hole recombination rates (e.g., radiative recombination, Shockley–Read–Hall recombination), which are generally determined by interfaces of light-absorbing materials.

#### **1.3.1.3. Transport of photo-generated charge carriers to electrodes**

To ensure an efficient collection of charge carriers, carrier-transporting layers should have high mobility as well as long diffusion lengths for electrons and holes [32,33]. An obvious, but general principle is that electrons or holes move as majorities in carrier-transporting layers that have high mobility. Moreover, the collecting junctions between metallic electrodes and charge-transporting materials also need optimization to allow a flow of electrons or holes.

#### **1.3.1.4. Energy dissipation in the circuit**

The collected electrons then dissipate their energy in the external circuit, returning to the solar cell, and annihilating with holes. The open-circuit voltage is important for the performance of a solar cell device as it strongly affects the power conversion efficiency. It is determined by Fermi levels or work functions involved in a solar device. In addition, the fill factor FF is related to series resistance,  $R_s$  (the sum of film resistance, electrode resistance and the contact resistance between the film and the electrode), and shunt resistance,  $R_{sh}$  [18]. The series resistance and shunt resistance are associated with carrier mobility and carrier

recombination loss, respectively. High carrier mobility and low carrier recombination loss lead to a device with good FF.

### **1.3.2. Quantum dot sensitized solar cells (QDSSCs)**

The introduction of porous nanocrystalline TiO<sub>2</sub> substrates and the introduction of the Gratzel cell have significantly improved the efficiencies [34]. Because of the introduction of porous TiO<sub>2</sub>, due to high surface area that facilitates dye uptake and enables the absorption of photons to a considerable extent. This allows the dyes having high extinction coefficient, to absorb majority of the incident photons when compared to 1-2% absorption attained with non-porous supports.

Recently quantum dot sensitized solar cells (QDSSCs) have emerged as a successful alternative to the conventional dye sensitized solar cells (DSSCs) [35-37]. The intrinsic attractive properties of quantum dots (QDs) such as tunable band gap [38], high extinction coefficients [39] and large intrinsic dipole moment [40] offer certain advantages over metallorganic dyes. Moreover, the demonstration of multiple exciton generation by impact ionization in colloidal QDs [41] could push the thermodynamic efficiency limit of these devices up to 44% [42] from the current 31% of the Shockley-Queisser detailed balance limit.

### **1.4. Photocatalysis**

Photocatalysis can be regarded as a combination of photochemistry and catalysis. This implies that the light and a catalyst are essential to enhance the rates of thermodynamically favorable ( $\Delta G < 0$ ) but kinetically slow photophysical and photochemical transformations. Photocatalysis involves the simultaneous oxidation and reduction as a unique property compared to the other reactions where either oxidation or reduction may take place. The term catalysis can be thought of as a chemical reaction that results from the action of a catalyst. A catalyst is a substance that increases the rate of reaction without being consumed during the reaction. Over the years, the exact definition of photocatalysis has grown and evolved along with this area of research. One of the early definitions of what is now known today as photocatalysis was “a catalytic reaction involving light absorption by a catalyst or a substrate” [43]. Another definition for photocatalysis, which was termed as a complimentary definition was a “catalytic reaction involving the production of products by absorption of light”. This was commonly referred to as photo-assisted catalysis [43]. Today, catalysis is defined by Serpone et al. as “a process in which a substance (the catalyst) accelerates, through intimate interaction(s) with the reactant(s) and concomitantly providing a lower energy pathway, an otherwise thermodynamically favored

but kinetically slow reaction with the catalyst fully regenerated quantitatively at the conclusion of the catalytic cycle” [43].

Photocatalysis is considered to occupy the central place in ecological equilibria. Solar energy is the main source of energy on Earth (to all practical purposes). It can be considered as a perennial source that can overcome all the energy needs of mankind in the future (25000–75000 kWh per day and hectare). However at present human beings are using only a small fraction of such energy for getting warm, for generating vitamin D in the skin, in the vision process etc. On the other hand, green plants use solar energy in the photosynthesis which is regarded as a best photocatalytic process, a veritable chemical factory based on water splitting. The natural photosynthesis involves the release of oxygen with concomitant formation of reduced coenzymes. These reduced coenzymes are responsible for the formation of carbohydrates from CO<sub>2</sub>. The resulted carbohydrates are utilized in building the plant structure and for the supply of energy (starch). Therefore photosynthesis is the renewable source of food, energy and materials for mankind all along its history (Fig. 1, green arrows). It is well known that oil, coal and natural gas are resulting from the chemical transformations of the dead organisms over million years. Mankind has exploited the (relatively) large supply of such fossil fuels by means of a new science, chemistry, to act as the main source of energy, materials and chemicals (red arrows). Agriculture is made more efficient by the use of fertilizers and therefore indirectly depending on fossil fuels. Therefore presently mankind depends upon ‘fossil’ solar energy, a finite and non-renewable source that result from the irradiation of past eons. Obviously, learning to exploit directly solar energy (blue arrow in Fig. 1.1) would be a wise solution for future energy needs.

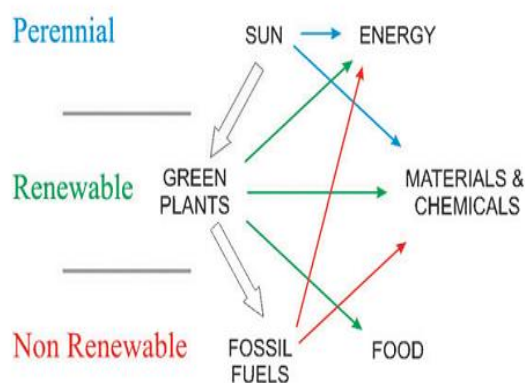


**Figure 1.1. Solar irradiation is the ultimate source of energy that is converted by green plants into chemical energy and, through their evolution, into fossil fuels (open arrow)<sup>44</sup>**

### 1.4.1. Mechanism of semiconductor photocatalysis

The basic physical and photochemical principles of photocatalysis are well discussed in the literature [45-47]. As illustrated in the schematic diagram (Fig. 1.2), when the semiconductor is irradiated by photons with energy equal to or exceeding the band gap ( $E_g$ ), excitonic transition occurs to promote a VB electron to CB. The electron vacancy at the VB results in a positive hole, forming electron( $e^-$ ) and hole ( $h^+$ ) pairs. The electron hole pairs can migrate to the semiconductor surface to induce the redox reactions with the surrounding medium if the conditions such as the potentials of the charges and the reactants are satisfied. On the other hand, reductive reactions can be initiated by the photogenerated CB electrons if its redox potential is sufficiently negative to allow the reduction of the adsorbed species. The adsorbed oxygen is the most common electron acceptor and can be reduced by the photogenerated electrons into  $\cdot O_2^-$ . The  $\cdot O_2^-$  is extremely unstable and part of them can be transferred into  $H_2O_2$ . Portions of resulting  $H_2O_2$  may also undergo the reactions to generate the  $\cdot OH$ . On the other hand, if the redox potential of the VB is more positive than that of  $H_2O/OH^-$  the photogenerated hole in the VB will oxidize the adsorbed  $H_2O$  or hydroxyl ion to generate  $\cdot OH$ . Of course photogenerated holes in VB can also degrade the adsorbed organic pollutants if its oxidative ability is powerful enough. Based on highly oxidative activities of the photogenerated holes in VB and ROSs, the various contaminants including the organic pollutant and microorganism can be destructed during the photocatalytic process.

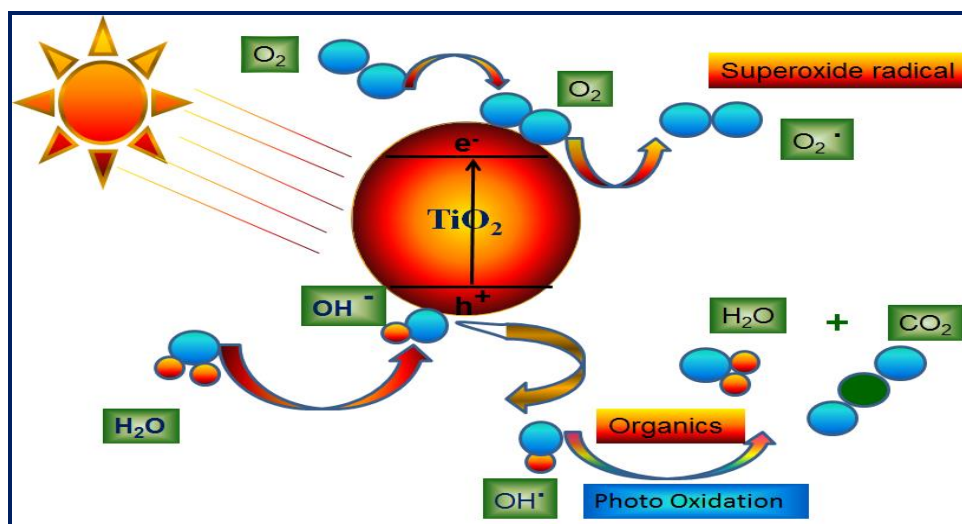
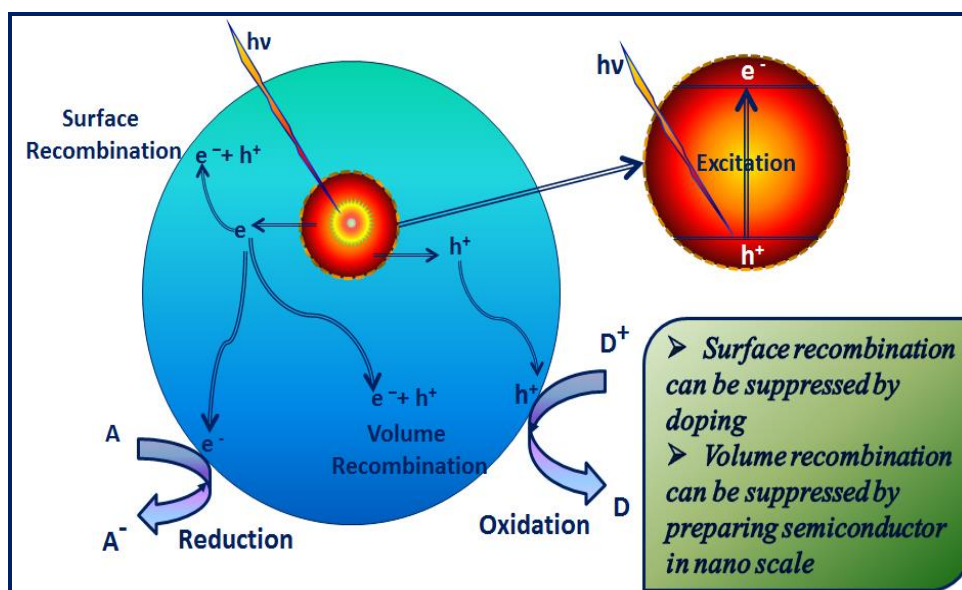


Figure 1.2. Diagrammatic representation of photocatalytic mechanism

### 1.4.2. Recombination of excitons

However, during the photocatalytic process, the electron-hole pairs readily recombine to inhibit the generation and dissipate the stored energy as heat or luminescence. This recombination process is the most significant competing reaction to inhibit the generation of ROSs. Recombination of excitons takes place mainly in two ways such as surface recombination and volume recombination. If the electron and hole recombines before reaching the surface it is termed as surface recombination, whereas the recombination taking place within the bulk of the material is called as volume recombination. Volume recombination can be minimized by preparing the material in nano size, so that the time taken for the electron to reach the surface might be less. Surface recombination can be reduced by doping with suitable materials that can trap the electron thereby preventing the exciton recombination. Figure 1.3 clearly depicts the different types of recombination that are taking place in a photocatalytic process.



**Figure 1.3. Diagrammatic representation of different recombination processes taking place in photocatalysis.**

### 1.4.3. Photocatalytic $H_2$ Production

Depletion of fossil fuels at a faster rate and the environmental problems associated with the usage of fossil fuels such as global warming have triggered a vigorous research for clean and renewable energy sources. Obviously hydrogen can be a clean and renewable energy source as this is the fuel with the highest energy capacity per unit mass as well as a clean energy carrier, because it produces neither  $CO_2$  nor pollutants. The obvious source of hydrogen is water, but splitting of this molecule requires temperatures in excess of  $2000^\circ C$ ,



thus making its implementation difficult [48]. Photocatalytic water splitting by solar irradiation is appealing and has been intensively studied in the last few decades [49]. Water splitting on an illuminated TiO<sub>2</sub> semiconductor surface has been first demonstrated by Fujishima and Honda in 1972 [49].

Water reduction to H<sub>2</sub> and oxidation to O<sub>2</sub> require that the bottom of the conduction band lies at a more negative potential than E<sub>red</sub>(H<sup>+</sup>/H<sub>2</sub>), 0 V vs. NHE at pH 0, and the top of the valence band at a more positive value than E<sub>ox</sub>(H<sub>2</sub>O/O<sub>2</sub>), 1.23 V vs. NHE at pH 0; Thus, the minimum energy required to drive reduction of water corresponds to 1.23 eV. However, electron transfer involves an activation barrier, and photon energy greater than the above value is required for driving water splitting at a reasonable rate.

#### **1.4.4. Photocatalytic degradation of pollutants**

##### **1.4.4.1. Waste water treatment**

Water pollutants can be divided into two types such as point sources and non-point sources [50]. Point sources of pollution occur when harmful substances are emitted directly into water stream. Non-point sources of pollutants enter the water streams indirectly through environmental changes. Point sources of pollution can be monitored and regulated by the existing technology whereas non-point sources are much more difficult to control. The pollution which is arising from the non-point sources accounts for a majority of the contaminants in streams and lakes [51]. This contamination modifies the water quality, producing large quantities of water that are unsuitable for various uses, including human consumption. Common water pollutants include textile dyes, herbicides, pesticides, alkanes, halo alkanes, aliphatic compounds, alcohols, carboxylic acids, aromatic compounds, detergents, surfactants, inorganic compounds like heavy metals, such as mercury, cadmium, silver, nickel, lead, noxious gases, and pathogens like bacteria fungi and viruses [52,53]. Both organic and inorganic pollutants can be found in ground water wells and surface waters; these residues can cause adverse effects to the environment and to human health. Many of the pollutants are so toxic that they can cause health problems in humans even at trace levels. Water pollution also reduces the available amount of freshwater resources for both human beings and ecosystems. Freshwater scarcity is already a reality in many developing countries. Thus one of the most pressing environmental issues of the present and most probably the future is the effective protection and utilization of the precious fresh water resources of the world. To alleviate the problem, contaminated water needs to be treated and re-used.

#### **1.4.4.2. Water treatment techniques**

The treatment of tainted water is based on various mechanical, biological, physical and chemical processes. After filtration and abolition of particles in suspension (primary treatments), biological treatment is ideal (secondary treatments) [54-56]. Unfortunately, there are certain products, called bio-recalcitrant (non-biodegradable), for which much more effective non-reactive systems, such as air stripping, adsorption on granulated activated carbon, incineration, ozone and oxidation (tertiary treatments), are desirable. These processes aim to treat wastewaters, and therefore improve water quality, but some of these technologies (such as adsorption and filtration) merely concentrate the pollutants by transferring them to other phases. The next problem, then, becomes how to properly dispose the new pollutant rich streams. These, organic pollutants are not completely removable by traditional water treatment technologies like distillation, reverse osmosis, ion-exchange, carbon adsorption, micro porous membrane filtration. Distillation and reverse osmosis remove a wide range of water contaminants. However, one of their major disadvantages is that they also remove the good stuff i.e. the trace mineral elements (heavy metals e.g. copper, zinc, iron) that are also present in water and vital to human health [57]. Therefore, management of toxic chemicals with strict environmental legislation drives the development of clean and green processes, to eliminate the pollutants before they are disposed into the environment. Furthermore, for these processes to be effective, complete mineralization and degradation of all organic and inorganic contaminants from water and wastewater, are required.

#### **1.4.4.3. Advanced Oxidation Processes (AOPs)**

The strong potential of tertiary treatments called Advanced Oxidation Processes (AOPs) for bio-recalcitrant wastewater treatment is universally recognized, and many researchers around the world are devoting their efforts to the development of these processes [58-60]. Although they make use of different reaction systems, AOPs are all characterized by the same chemical feature: the production of hydroxyl radicals ( $\text{OH}^\bullet$ ). These radicals can virtually oxidize any organic toxin present in water. They can even destroy pollutants that are not amenable to biological treatments, which are all characterized by high chemical stability and difficulty to be completely mineralized. In order to apply a decontamination technique to these cases, it is necessary to adopt reactive systems much more effective than those adopted in conventional purification processes. Among AOPs, heterogeneous photocatalysis is efficient in degrading a wide range of organic contaminants into  $\text{CO}_2$  and water.

Research on heterogeneous photocatalysis has emerged since 1972, when Fujishima and Honda observed the photocatalytic decomposition of water on  $\text{TiO}_2$  electrodes [61]. Heterogeneous photocatalysis is a technology, which involves the irradiation of a catalyst, generally a semiconductor, to form excitons providing great scope as redox reagents. It is a promising technique for the degradation of various hazardous chemicals that are present in the waste waters. Moreover the unique advantage of this technique is it can degrade (detoxify) various complex organic compounds which cannot be degraded by several other methods of purification. The main aim of the destructive oxidation processes is to mineralize organic contaminants, i.e., to convert them to carbon dioxide, water and the oxidized inorganic anions of heteroatoms present. Hydroxyl radicals are the active species which are found to be a very good oxidizing agent next to fluorine. In addition to this, photocatalysis does not require the consumption of expensive oxidizing chemicals, catalyst is non-toxic, and the only requirement is the suitable light source to activate the catalyst.

One of the widely practiced applications of photocatalysis is the recovery of water of industrial, agricultural or civil origin, as well as the decontamination of atmosphere and soil [62]. Photo catalysis is considered as a green approach for the removal of pollutants as it involves only the irradiation of solar energy and no further addition of chemicals [63]. Degradation is carried out both under homogeneous and heterogeneous [62] conditions, but solid semiconductors are more extensively used, because they are cheaper, more robust and easily recovered and reused than soluble photocatalysts.

### **1.5. Materials for solar energy harvesting**

Metal oxide semiconductors are eminently attractive candidates for the different applications such as solar cells [63] solar water splitting [64] and photocatalytic remediation of pollutants [65]. Especially among the metal oxide semiconductors titanium dioxide ( $\text{TiO}_2$ ) and zinc oxide ( $\text{ZnO}$ ) have sparked worldwide interest for the above mentioned applications. The prerequisite combination of materials properties for the above mentioned applications, however, is both stringent and daunting. For example, for solar photovoltaic applications, the semiconductor material has to have an optimal combination of optical (suitable band gap) and electronic (low surface-state density, large minority carrier lifetime and long diffusion length) properties [63].

On the other hand, for solar water splitting applications, in addition to the aforementioned combination of optical and electronic characteristics, the semiconductor has to have the appropriately juxtaposed conduction and valence band edges in the aqueous medium relative to the redox levels for water reduction and water oxidation respectively [64]. Moreover the semiconductor should be chemically inert and photo-chemically stable

over a wide pH range. Finally, for environmental remediation applications the semiconductor photocatalyst requires both highly reducing and highly oxidizing active species that are generated at the semiconductor/medium interface [65]. In order to satisfy the above requirements, the conduction band edge of semiconductor has to lie at a reasonably negative potential while the valence band edge of semiconductor should be at very positive potentials. Only then the photo generated electrons and holes can have the sufficient energy for either directly converting the toxic pollutants to environmentally benign products or for generating active mediator species (usually free radicals such as OH<sup>•</sup>) capable of oxidizing or reducing the toxins.

No one oxide semiconductor is likely to occur with the optimal combination of these properties for all the three targeted applications. However, TiO<sub>2</sub> has been proven to be able to split water [64], capable of oxidatively decomposing toxic organic compounds, inactivating microorganisms and it can reductively immobilize toxic metal ions from contaminated water streams [66,67].

Nevertheless, the major drawback of TiO<sub>2</sub> is its rather large band gap of 3.2 eV which allows only a small fraction (wavelength less than 380 nm) of the solar spectrum to be harvested. Because of this fact and its rather poor electronic properties, photocatalytic process efficiencies have been disappointingly low and TiO<sub>2</sub> is not suitable for solar photovoltaic applications, at least as an active light absorbing material. On the other hand, this oxide has indeed found extensive use as an electron sink in dye sensitized as well as quantum dot sensitized solar cells [68,69].

In case of other oxide semiconductors zinc oxide is widely deployed in solid state photovoltaic solar cells as a window material. However, its applicability for solar water splitting and photocatalytic environmental remediation systems is hampered by its poor chemical and photochemical stability in aqueous media. On the other hand even though Si has emerged as an important candidate in the microelectronics industry and in the solid-state solar photovoltaics industry its use in solar water splitting and environmental remediation applications is precluding since Si is very unstable in contact with aqueous media. More over its energy band gap and band edge positions are also not suitable for these applications.

## **1.6. How to overcome the limitations of harvesting solar energy**

### **1.6.1. Doping TiO<sub>2</sub> with cations**

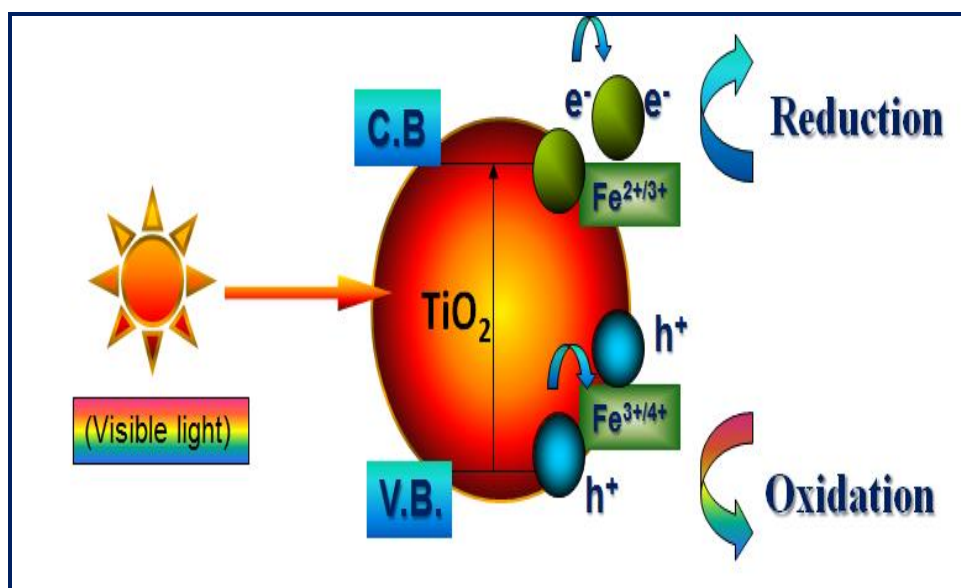


**Figure 1.4.** Schematic representation of photocatalytic mechanism in metal doped TiO<sub>2</sub>

During the past few decades, metal doped TiO<sub>2</sub> has been extensively studied for shifting the absorption of TiO<sub>2</sub> into the visible region. Transition metals and rare earth metal ions, including V, Cr, Fe, Co, Mo, and In and lanthanide metals such as La, Ce, Sm are studied as the important metal ions that are doped in to the TiO<sub>2</sub> matrix [70-76]. There are several reports showing that the band gap of TiO<sub>2</sub> can be effectively shifted to the visible region by doping with the metal ions such as Cr, Fe, Ni and V. The photocatalytic activity of metal doped TiO<sub>2</sub> is not fully understood and appears to be a complex function which is dependent on the type of metal ion, dopant concentration, distribution and their d-electron configuration [76]. The mechanism of decrease in band gap can be attributed to the replacement of Ti in the crystal lattice of TiO<sub>2</sub> with the metal ions which can create impurity energy levels within the band gap of TiO<sub>2</sub> [73]. Although band gap has been decreased with the metal doping it did not improve the photocatalytic activity consequently since the doped metal ion not only create the mid energy states but also can act as recombination centers for the photo-generated charge carriers. In literature it has been reported that Cu, Mn, and Fe ions can trap both e<sup>-</sup> and h<sup>+</sup>, thus doping TiO<sub>2</sub> with these metal ions found to increase the photocatalytic activity whereas Cr, Co, and Ni metals can only trap e<sup>-</sup> and thereby reduces the photocatalytic activity [83]. Figure 1.4 depicts the schematic representation of photocatalytic mechanism in metal doped TiO<sub>2</sub>.

### 1.6.2. Doping TiO<sub>2</sub> with anions

In recent years, anion doping such as N, C, S, F, and B doping in place of oxygen in the lattice structure of TiO<sub>2</sub> has proved as an effective way to enhance the visible light

response of  $\text{TiO}_2$  [77]. The mechanism involved in the decrease of band gap in anion doped  $\text{TiO}_2$  may be due to the new VB which is formed as a result of overlap of O 2p and the p states of the doped anions [77]. As a result of this overlap of O 2p states with the metal p states the VB has shifted up and consequently the band gap may decrease while the CB remains unchanged [78]. Thus during the photocatalytic water splitting, for anion doped  $\text{TiO}_2$ , oxidation ability decreases whereas the reduction ability may remain unchanged, since CB of  $\text{TiO}_2$  is just slightly higher than the reduction potential for water. Moreover compared to the cation doping, anion doping generally forms lesser recombination centers and there is significant defect state formation within the band gap [79] which is more effective for enhancing the photocatalytic activity.

### **1.6.3. Coupling with small band gap semiconductors**

Coupling of  $\text{TiO}_2$  with small band gap semiconductors has become an alternative strategy for harvesting solar energy with simultaneous prevention of recombination of excitons. As shown in Fig. 1.5 when  $\text{TiO}_2$  coupled small band gap semiconductor is irradiated with visible light the photo-generated  $e^-$  will be injected from the CB of small band gap semiconductor to the CB of  $\text{TiO}_2$  provided that the CB of semiconductor is more negative than the  $\text{TiO}_2$ . Thus the  $e^-$  accumulated in the CB of  $\text{TiO}_2$  is free enough to reduce water to  $\text{H}_2$  since the hole and electron are separated effectively. More is the CB difference of  $\text{TiO}_2$  and SC more favorable is the transfer of  $e^-$ . Strictly speaking, the visible light activity of such coupled photocatalyst does not originate from  $\text{TiO}_2$ , but from the SC. The role of  $\text{TiO}_2$  is mainly to separate the photo generated  $e^-$ , similar to a Pt co-catalyst. Among the small band gap semiconductors used for coupling with  $\text{TiO}_2$ , cadmium sulfide (CdS) is the most extensively studied semiconductor. Most of these small band gap semiconductors are chalcogenides. They will be oxidized by the remaining  $h^+$  during the hydrogen evolution reaction. In order to prevent the photocorrosion  $\text{S}^{2-}$  is commonly used as the sacrificial reagent.

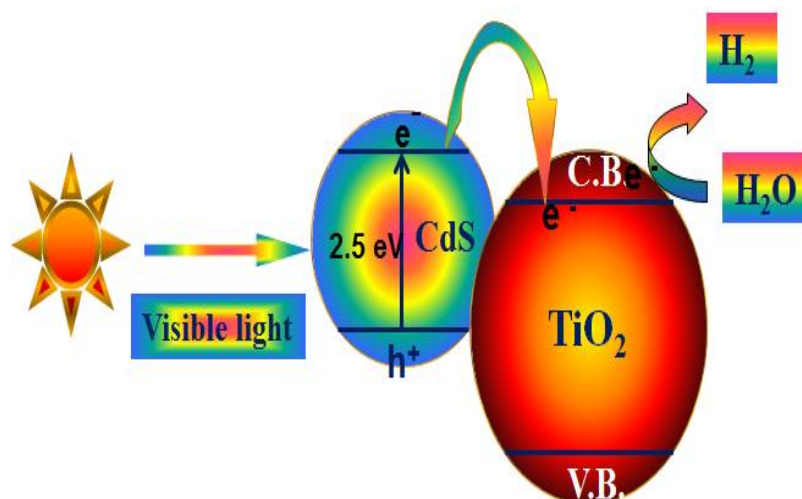


**Figure 1.5. Photocatalytic mechanism in coupled semiconductor systems**

Coupling  $\text{TiO}_2$  with other semiconductors (SCs) that have different redox energy levels is an attractive approach to prevent exciton recombination and thereby increasing photocatalytic activity. When this type of coupled systems are exposed to light both  $\text{TiO}_2$  and the SC can undergo activation simultaneously (or only one of them) and the photo-induced  $e^-$  would be injected from the semiconductor with a more negative CB level to the positive one, while  $h^+$  would be transferred from the semiconductor with a more positive VB level to the negative one. In this manner in case of coupled semiconductors efficient separation of photo-induced charges is achieved, and consequently interfacial charge transfer to water is also enhanced. In literature there are several reports on  $\text{TiO}_2$  coupled with other semiconductors, such as CdS [80]  $\text{Cu}_2\text{O}$  [81]  $\text{WO}_3$  [82,83]  $\text{V}_2\text{O}_5$  [84]  $\text{Bi}_2\text{O}_3$  [85]  $\text{Fe}_2\text{O}_3$  [86] and others. Based on the CB and VB, these composite photocatalysts can be classified into three groups.

(a)  $\text{CB}_{\text{SC}} < \text{CB}_{\text{TiO}_2}$  and  $\text{VB}_{\text{SC}} < \text{VB}_{\text{TiO}_2}$ . In this case,  $e^-$  travels from SC to  $\text{TiO}_2$  and  $h^+$  from  $\text{TiO}_2$  to SC.

(b)  $\text{CB}_{\text{SC}} > \text{CB}_{\text{TiO}_2}$  and  $\text{VB}_{\text{SC}} > \text{VB}_{\text{TiO}_2}$ . SC:  $\text{SnO}_2$ ,  $\text{WO}_3$ ,  $\text{V}_2\text{O}_5$ ,  $\text{Bi}_2\text{O}_3$  and  $\text{Ta}_2\text{O}_5$ . In this case,  $e^-$  travels from  $\text{TiO}_2$  to SC and  $h^+$  from SC to  $\text{TiO}_2$ .

(c)  $\text{CB}_{\text{SC}} > \text{CB}_{\text{TiO}_2}$  and  $\text{VB}_{\text{SC}} < \text{VB}_{\text{TiO}_2}$ . In this case,  $e^-$  and  $h^+$  both travel from  $\text{TiO}_2$  to SC.

Among these composites, only  $\text{TiO}_2$  coupled with  $\text{Cu}_2\text{O}$ , SiC, CdS, ZnO, CuO, and  $\text{Ta}_2\text{O}_5$  have the potential to evolve hydrogen from water because the  $e^-$  occupied CB level is more negative than  $E_{\text{H}_2/\text{H}_2\text{O}} = 0 \text{ V}$  (vs. NHE, pH 0). On the other hand other composite photocatalysts are commonly used to degrade toxic pollutants. The reason for the enhanced activity of composite photocatalysts may not be only due to the efficient separation of excitons, but also because of the some other factors such as the enhanced surface acidity

[87] or alkalinity [88]. This surface modification may promote the absorption of alkaline or acidic substrates to  $\text{TiO}_2$  and then result in improved photocatalytic activity.

#### 1.6.4. Sensitizing with dyes

Organic dyes, which can perform the same function as the small band gap semiconductors, have also been extensively used as sensitizers for  $\text{TiO}_2$  in order to utilize the visible part of the solar spectrum [89,90]. Dyes are natural light absorbers and electron transfer agents. Dye sensitization is a process occurring when a light excited dye molecule adsorbed at the semiconductor surface injects electrons into the conduction band of the semiconductor substrate. Titania based dye sensitization has potentially low cost, low environmental impact, and good power conversion efficiency. Figure 1.6 clearly shows the electron transfer processes taking place in case of dye sensitized  $\text{TiO}_2$  photocatalyst. However, its more general use is limited by low quantum efficiency, high carrier recombination, low adsorption of the dye to the surface of the semiconductor material, dye desorption from the  $\text{TiO}_2$  due to solvent effects, lack of long term stability of the dye under light and heat, etc [90].

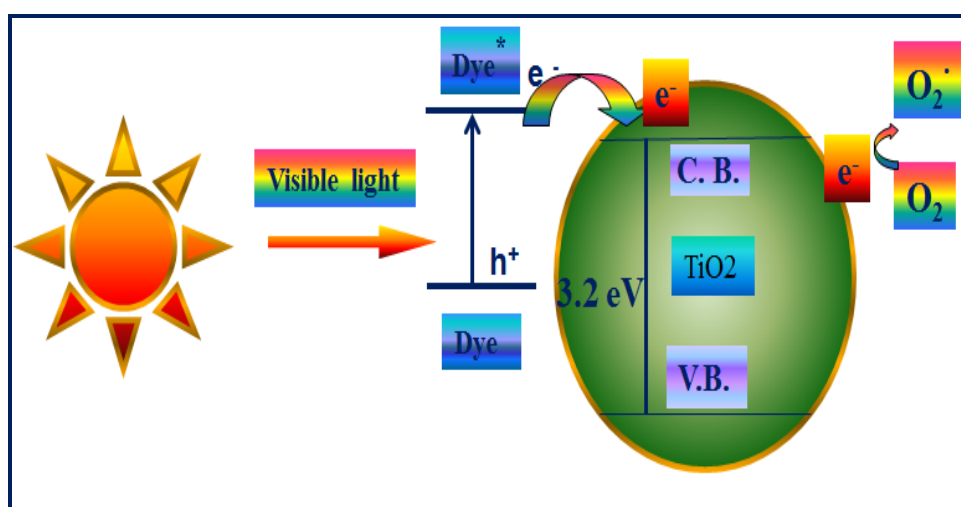


**Figure 1.6.** Diagrammatic representation of photocatalytic mechanism in dye sensitized  $\text{TiO}_2$  system

#### 1.7. Available methods for the synthesis of nanomaterials

In order to explore the novel physical properties and phenomena and also to understand the potential applications of nanostructures and nanomaterials, the ability to synthesize and process nanomaterials and nanostructures is the first corner stone in nanotechnology. The methods available for the synthesis of nanomaterials can be divided into two categories such as “top down and bottom up” approaches. Broadly, solid state



method and ball milling methods can be regarded as top down approaches whereas wet chemical methods like sol-gel, co-precipitation, etc. come into the category of bottom up approach. Top down approach involves the division of a massive solid into smaller and smaller portions which successively leads to nanometer size. On the other hand bottom-up approach method of nanoparticle fabrication involves the condensation of atoms or molecular entities in a gas phase or in solution to form the material in the nanometer range. Bottom-up approach is a familiar technique for the synthesis of nanoparticles due to several advantages associated with it. The main bottom up methods of synthesizing nanomaterials are hydrothermal, [91, 92] combustion synthesis [93], gas-phase methods [94, 95], microwave synthesis and sol-gel processing [96]. Combustion synthesis will be discussed in detail in this chapter because the materials reported in this thesis were fabricated by using modified combustion synthesis.

#### **1.7.1. Hydrothermal method**

Hydrothermal synthesis is generally carried out in a pressurized vessel called an autoclave with the reactants in aqueous media [97]. The temperature in the autoclave can be elevated above the boiling point of water, reaching the pressure of vapor saturation. Generally hydrothermal synthesis can be mostly used for the synthesis of kinetically controlled products like metal oxides [98]. Hydrothermal method can be useful to control grain size, particle morphology, crystalline phase and surface chemistry through regulation of the solution composition, reaction temperature, pressure, solvent properties, additives and aging time [99]. Although hydrothermal approach can be considered as an attractive method, there are some disadvantages such as longer reaction times which varies between 1-6 hours and the requirement of post preparation annealing of samples (temperatures higher than 450° C).

#### **1.7.2. Gas phase methods**

Generally gas phase methods are ideal for the production of thin films. Gas phase methods can be carried out chemically or physically. Chemical vapor deposition (CVD) is a familiar technique widely used in industries which can be used to coat large areas in a short span of time [100]. The procedure involves the synthesis of metal oxide thin films either from a chemical reaction or decomposition of a precursor in the gas phase [101, 102]. Physical vapor deposition (PVD) is another kind of thin film deposition technique. It is also similar to chemical vapor deposition (CVD) except that the raw materials/precursors, i.e. the material that is going to be deposited starts out in solid form, whereas in CVD, the precursors are introduced to the reaction chamber in the gaseous state. PVD process proceeds atomistically and mostly does not involve any chemical reaction. There are several

methods developed for the removal of growth species from the source or target. The thickness of the thin films deposited by either PVD or CVD can vary from angstroms to millimeters. The methods available for the removal of growth species can be divided into two groups such as evaporation and sputtering. During evaporation, the growth species are removed from the source by thermal means whereas during sputtering atoms or molecules are removed from solid target through impact of gaseous ions (plasma) [103]. Although these methods leads to pure product with no multiple steps the high temperatures required for the processes leads to aggregation of particles.

### **1.7.3. Sol-gel method**

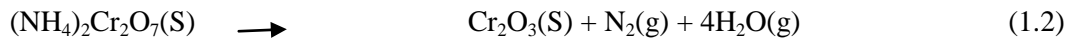
The sol-gel process is a wet chemical process widely used for the synthesis of ceramic and glass materials. The synthesis involves the conversion of a system from a colloidal liquid, named sol, into a semi-solid gel phase [104,105]. Sol-gel process can be used to synthesize ceramic as well as glass materials in a wide variety of forms such as ultra-fine or spherical shaped powders, thin film coatings, ceramic fibers, microporous inorganic membranes, monolithics, or extremely porous aerogels. The starting materials for the preparation of sol are usually inorganic metal salts or metal organic compounds, which by hydrolysis and polycondensation reactions form the sol [104]. Further processing of the sol enables the synthesis of materials in different forms. By using these sols thin films can also be produced either by spin-coating or dip-coating. The sol can be cast into a mould to get a wet gel which on drying and heat-treatment leads to dense ceramic or glass materials. A highly porous and extremely low density aerogel material can be obtained from the wet gel if the liquid in the wet gel is removed under supercritical conditions. By adjusting the viscosity of a sol into a suitable viscosity range, ceramic fibers can be obtained from the sol. sol-gel process is also a low temperature method, but it involves a series of successive steps and costly chemicals and it is very difficult to control the composition. Moreover the sample must be annealed in order to improve the photocatalytic activity. When compared to these methods, combustion synthesis exhibits advantages for the preparation of nanomaterials.

### **1.8. Combustion synthesis**

Combustion synthesis involves a highly exothermic redox chemical reaction between metals and nonmetals, and is widely used for the synthesis of oxide and non-oxide materials [105]. This method has several advantages like low energy requirement, generation of high reaction temperature, short duration of reaction, high yields, highly crystalline products, simplicity and low cost [106]. The synthesis has gained much importance owing to its exothermic, rapid, self-sustaining and self-propagating reaction properties. It is the large amount of heat released by the reaction which makes the technique

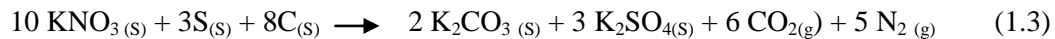
special and attractive [107]. As the name indicates combustion synthesis requires the presence of an oxidizer (oxygen or any other electronegative element) and a fuel (source of reducing elements to the reaction).

Combustion synthesis involves mainly redox reactions, which are carried out in two different approaches either by the use of redox compounds or redox mixtures [108]. The first approach involves the use of fuel-metal complexes, which after ignition undergo self-sustained combustion to yield the final product. The main requirement for this reaction is the presence of both the oxidizing and reducing groups together in the same compound. For example combustion of ammonium dichromate ((NH<sub>4</sub>)<sub>2</sub>Cr<sub>2</sub>O<sub>7</sub>) comes under this category because it contains oxidizing (Cr<sub>2</sub>O<sub>7</sub><sup>2-</sup>) and reducing (NH<sup>+4</sup>) groups. During this combustion reaction first ignition will take place followed by a self-propagating and self-sustained reaction to produce the final product (Cr<sub>2</sub>O<sub>3</sub>) in a glowing type of reaction known as artificial volcano:



In similar manner metal complexes containing hydrazine, carboxylate, formate and acetate ions can also undergo self-sustained combustion reactions. Although interesting the combustion reactions involving the use of redox compound have several disadvantages such as large preparation time (requires several days), low yield (20%) and because not all metals form complexes with the hydrazine carboxylate ligand it is not possible to use this method to prepare some metal oxides (i.e., chromites, alumina) [109].

Another approach of combustion synthesis which avoids the preparation of complex mixtures makes use of the combustion of redox mixtures [110,111]. In this approach metal nitrates can be used as oxidizing elements and one or more energetic fuels like urea, glycine or hydrazides can be used as redox elements [111]. For example the familiar gunpowder reaction can be used for better understanding of this exothermic and self-propagating reaction.



The large amount of gases evolved during this reaction act as the propellant power for a projectile.

While taking the redox mixture for combustion synthesis, the ratio of the oxidizer and fuel can be calculated using the equivalence ratio ( $\phi_e$ ), defined as [112]:

$$\phi_e = O/F \quad (1.4)$$

where (O) is the total oxidizing valence and (F) is the total reducing valence of the elements present in the mixture [113]. In general maximum energy can be released from a given mixture when the  $\phi_c$  value is equal to unity, and values higher or lower are referred as fuel rich or fuel lean mixture respectively [112]. According to propellant theory, the species  $M^{2+}$ ,  $M^{3+}$ ,  $M^{4+}$ , C and H are considered to be reducing with valencies of +2, +3,+4,+4 and +1 respectively. Oxygen is considered to be an oxidizing species with valence -2 and nitrogen is considered to be valence neutral with a value of zero [111, 112].

The latter approach i.e., combustion of redox mixtures, makes use of metal nitrates and different fuels, with ignition by gradual heating of the redox mixture in aqueous phase. Since this method involves the reaction in aqueous phase it offers all the advantages of the wet chemistry approach plus the capability of doping with different metal ions. Such capability has been proven in the literature for metal oxides and inorganic materials [110].

### **1.9. Why combustion synthesis....?**

Generally oxide semiconductors are synthesized by high temperature routes which become a handicap for the application of these materials in the energy (especially, renewable energy) sector. A key parameter in life cycle analyses of solar energy materials and devices is the energy payback time i.e., the time it takes for the energy needed for material synthesis to be recovered back. The energy payback time can be effectively minimized by deploying low-temperature synthesis routes such as electro deposition [113,114] chemical bath deposition (CBD) [115] and sol-gel chemistry [116]. Another way of reducing the energy payback time is to make the synthesis efficient, both in terms of energy requirement and time duration. In this respect, all the above mentioned synthesis methodologies demand rather long reaction times ranging from several minutes to hours.

Self-propagating high temperature synthesis (SHS) or simply combustion synthesis [117] is considered as both energy and time efficient method. In a typical combustion synthesis a solution mixture of metal precursor and an organic fuel is first dehydrated, then ignited and finally brought to combustion. The exothermic nature of the combustion reaction offers the high temperatures required for the synthesis and surprisingly in some cases, temperatures in excess of 3000° C can also be attained instantaneously.

In addition to the reduction in external energy requirement there are several other beneficial features for this synthesis: (a) reaction times are very short for this synthesis (typically only a few seconds) (b) The high reaction temperatures, coupled with copious gas evolution during the combustion process, result in a finely dispersed and porous morphology for the synthesized product (c) Simple and cost effective equipment (d) Environmentally benign chemical precursors can be used unlike the precursors used in chemical vapor

deposition or molecular beam epitaxy methods. From a chemical reaction viewpoint, another attractive feature of combustion synthesis is its intrinsic ability to tune the solid state chemical composition of the product by simply varying the precursor (metal salt + fuel) mixture chemistry.

**The objectives of this thesis are:**

Combustion synthesis is an established art in the ceramic oxides synthesis. However, this versatile technique has not been explored fully for energy applications such as solar cells and photocatalysis, where a single step synthesis of doped semiconductors plays an important role. This thesis furnish a small window into the many opportunities that exist for more wide spread use of this technique for developing and designing oxide, sulfide and composite semiconductors for harvesting solar energy for a wide variety of applications such as photocatalytic pollutant removal, H<sub>2</sub> production and solar cell applications.

Although combustion synthesis of TiO<sub>2</sub> has been done by several research groups, optimization of oxidant and fuel has not been carried out systematically. Therefore in the first part of the thesis optimization of oxidant (titanyl nitrate) has been carried out by preparing it in four different ways. The resulted titanyl nitrate samples have been used for the synthesis of TiO<sub>2</sub> with glycine as the common fuel and their photocatalytic activity was tested for the removal of water pollutant.

The second part of the thesis focuses on the optimization of fuels used for the synthesis of TiO<sub>2</sub>. Several fuels such as urea, glycine, ascorbic acid, citric acid, hexamine, triethylamine have been studied. The synthesized photocatalysts have been characterized by several techniques in order to understand the effect of fuel on the combustion synthesis of TiO<sub>2</sub>. It is observed that fuel also has significant effect on the physico-chemical properties of TiO<sub>2</sub> which can be correlated in terms of number of moles of gases evolved during the combustion.

In the third part of the thesis, for the first time, synthesis of metal sulfide nanomaterials such as cadmium sulfide and zinc sulfide nanomaterials have been attempted by using combustion synthesis at normal atmospheric conditions and without using any surfactants and capping agents. Since the sulfides are known for best absorption of visible portion of solar spectrum these materials have been well characterized and tested for photocatalytic H<sub>2</sub> production from water.

Thereafter in the next chapter this approach has been extended for the synthesis of composite materials in a single step. Efficient photocatalytic composite materials such as CdS/TiO<sub>2</sub> has been prepared and studied their efficient activity for the photocatalytic H<sub>2</sub> production from water.

In the last chapter we have further extended the combustion technique for the synthesis of various metal sulfides with variable stoichiometry such as nickel sulfides, lead sulfide, copper sulfide and cobalt sulfide nanomaterials. Since these materials are well known as the counter electrode materials for QDSSC applications where Pt counter electrode may undergo corrosion, solar applications of these materials have been studied and observed excellent electrocatalytic activity than the Pt counter electrode. Electrochemical impedance spectroscopy reveals the low charge transfer resistance for the metal sulfides compared to the Pt.

## References

- [1] A. Fujishima and K. Honda. Electrochemical photolysis of water at a semiconductor electrode. *Nature* 238, (1972) 37-38.
- [2] J. A. Turner. Sustainable hydrogen production. *Science* 305, (2004) 972-974.
- [3] N. Serpone and A. V. Emeline. Suggested terms and definitions in photocatalysis and radiocatalysis, *Int. J. Photoenergy* 4, (2002) 91-131.
- [4] W. Y. Wong and C. L. Ho. Organometallic Photovoltaics: A new and versatile approach for harvesting solar energy using conjugated polymetallaynes. *Acc. Chem. Res.* 43, (2010) 1246–1256.
- [5] N. S. Lewis. Toward cost-effective solar energy use. *Science* 315, (2007) 798–801.
- [6] A. Hagfeldt, G. Boschloo, L. C. Sun, L. Kloo and H. Pettersson. Dye-Sensitized Solar Cells. *Chem. Rev.* 110, (2010) 6595–6663.
- [7] A. Yella, H. W. Lee, H. N. Tsao, C. Y. Yi and A. K. Chandiran. Porphyrin-sensitized solar cells with cobalt (II/III)-based redox electrolyte exceed 12 percent efficiency. *Science* 334, (2011) 1203–1203.
- [8] P. K. Nayak, G. Garcia-Belmonte, A. Kahn, J. Bisquert and D. Cahen. Photovoltaic efficiency limits and material disorder. *Energy Environ. Sci.* 5, (2012) 6022–6039.
- [9] J. W. Schwede, I. Bargatin, D. C. Riley, B. E. Hardin, S. J. Rosenthal, Y. Sun, F. Schmitt, P. Pianetta, R. T. Howe, Z. X. Shen and N. A. Melosh. Photon-enhanced thermionic emission for solar concentrator systems. *Nat. Mater.* 9, (2010) 762–767.
- [10] H. A. Atwater and A. Polman. Plasmonics for improved photovoltaic devices. *Nat. Mater.* 9, (2010) 865–865.
- [11] J. A. Schuller, E. S. Barnard, W. Cai, Y. C. Jun, J. S. White and M. L. Brongersm. Plasmonics for extreme light concentration and manipulation. *Nat. Mater.* 9, (2010) 193-204.

- [12] H.K. Jun, M.A. Careem and A.K. Arof. Quantum dot-sensitized solar cells-perspective and recent developments: A review of Cd chalcogenide quantum dots as sensitizers. *Renew. Sust. Energ. Rev.* 22, (2013) 148–167.
- [13] J. W. Lund, D. H. Freeston and T. L. Boyd. Direct utilization of geothermal energy 2010 worldwide review. *Geothermics* 40, (2011) 159–180.
- [14] I. B. Fridleifsson. Status of geothermal energy amongst the world's energy sources. *Geothermics* 32, (2003) 379–388.
- [15] N. S. Lewis, G. Crabtree, A. J. Nozik, M. R. Wasielewski and P. Alivisatos. Basic Research Needs for Solar Energy Utilization. DOE, 2006, [www.sc.doe.gov](http://www.sc.doe.gov).
- [16] Photovoltaic Energy Program Contract Summary. DOE, 2000, [www.nrel.gov](http://www.nrel.gov)
- [17] S. Dag, S. Wang, and L.W. Wang. Large Surface Dipole Moments in ZnO Nanorods. *Nano Lett.* 11, (2011) 2348-2352.
- [18] J. A. Tang and E. H. Sargent. Infrared colloidal quantum dots for photovoltaics: fundamentals and recent progress. *Adv. Mater.* 23, (2011) 12–29.
- [19] M. A. Green. *Third Generation Photovoltaics: Advanced Solar Energy Conversion*. Springer-Verlag, Berlin, 2003.
- [20] C. A. Wolden, J. Kurtin, J. B. Baxter, I. Repins, S. E. Shaheen, J. T. Torvik, A. A. Rockett, V. M. Fthenakis and E. S. Aydil. Photovoltaic manufacturing: Present status, future prospects, and research needs. *J. Vac. Sci. Technol. A* 29, (2011) 030801-16.
- [21] P. V. Kamat. Meeting the clean energy demand: nanostructure architectures for solar energy conversion. *J. Phys. Chem. C* 111, (2007) 2834–2860.
- [22] G.W. Crabtree and N. S. Lewis. Solar energy conversion. *Phys. Today* 60, (2007) 37–42.
- [23] G. F. Brown and J. Wu. Third generation photovoltaics. *Laser Photonics Rev.* 3, (2009) 394–405.



- [24] W. Shockley and H. J. Queisser. Detailed Balance Limit of Efficiency of p-n Junction Solar Cells. *J. Appl. Phys.* 32, (1961) 510–519.
- [25] O. E. Semonin, J. M. Luther, S. Choi, H.-Y. Chen, J. Gao, A. J. Nozik and M. C. Beard. Peak external photocurrent quantum efficiency exceeding 100% via MEG in a quantum dot solar cell. *Science* 334, (2011) 1530–1533.
- [26] J. B. Sambur, T. Novet and B. A. Parkinson. Multiple exciton collection in a sensitized photovoltaic system. *Science* 330, (2010) 63–66.
- [27] J. A. McGuire, J. Joo, J. M. Pietryga, R. D. Schaller and V. I. Klimov. New Aspects of Carrier Multiplication in Semiconductor Nanocrystals. *Acc. Chem. Res.* 41, (2008) 1810–1819.
- [28] W. A. Tisdale, K. J. Williams, B. A. Timp, D. J. Norris, E. S. Aydil and X. Y. Zhu. Hot-electron transfer from semiconductor nanocrystals. *Science* 328, (2010) 1543–1547.
- [29] A. J. Nozik, Quantum dot solar cells. *Physica E* 14, (2002) 115–120.
- [30] A. Hagfeldt, G. Boschloo, L. C. Sun, L. Kloo and H. Pettersson. Solar Energy Conversion: Dynamics of Interfacial Electron and Excitation Transfer. *Chem. Rev.* 110, (2010) 6595–6663.
- [31] A.I. Hochbaum and P.D. Yang, Semiconductor Nanowires for Energy Conversion. *Chem. Rev.* 110, (2010) 527–546.
- [32] M. Graetzel, R. A. J. Janssen, D. B. Mitzi and E. H. Sargent. Materials interface engineering for solution-processed photovoltaics. *Nature* 488, (2012) 304–312.
- [33] G. Conibeer. Third-generation photovoltaics. *Mater. Today* 10, (2007) 42–50.
- [34] W. D. K. Clark and N. Sutin. Spectral sensitization of n-type titanium dioxide electrodes by polypyridineruthenium(II) complexes. *J. Am. Chem. Soc.* 99 (1977) 4676–4682.
- [35] A. J. Nozik. Quantum Dot Solar Cells. *Phys. E* 14, (2002) 115–200.

- [36] V. I. Klimov. Mechanisms for Photogeneration and Recombination of Multiexcitons in Semiconductor Nanocrystals: Implications for Lasing and Solar Energy Conversion. *J. Phys. Chem. B* 110, (2006) 16827–16845.
- [37] P. V. Kamat. Quantum Dot Solar Cells. *J. Phys. Chem. C* 112, (2008) 18737–18753.
- [38] P. Wang, S. M. Zakeeruddin, J. E. Moser, R. Humphry-Baker, P. Comte, V. Aranyos, A. Hagfeldt, M. K. Nazeeruddin and M. Gratzel. Stable New Sensitizer with Improved Light Harvesting for Nanocrystalline Dye-Sensitized Solar Cells. *Adv. Mater.* 16, (2004) 1806–1811.
- [39] R. Vogel, K. Pohl, H. Weller. Sensitization of Highly Porous, Polycrystalline  $\text{TiO}_2$  Electrodes by Quantum Sized CdS. *Chem. Phys. Lett.* 174, (1990) 241–246.
- [40] R. Vogel, P. Hoyer, H. Weller. Quantum-Sized PdS, CdS,  $\text{Ag}_2\text{S}$ ,  $\text{Sb}_2\text{S}_3$  and  $\text{Bi}_2\text{S}_3$  Particles as Sensitizers for Various Nanoporous Wide-Bandgap Semiconductors. *J. Phys. Chem.* 98, (1994) 3183–3188.
- [41] R. D. Schaller, M. Sykora, J. M. Pietryga, V. I. Klimov. Seven Excitons at Cost of One: Redefining the Limits for Conversion Efficiency of Photons into Charge Carriers. *Nano Lett.* 6, (2006) 424–429.
- [42] M. T. Trinh, A. J. Houtepen, J. M. Schins, T. Hanrath, J. Pirus, W. Knulst, A. P. L. M. Goossens and L. D. A. Siebbeles. In Spite of Recent Doubts Carrier Multiplication Does Occur in PbSe Nanocrystals. *Nano Lett.* 8, (2008) 1713–1718.
- [43] N. A. Serpone and A. V. Emeline. Suggested terms and definitions in photocatalysis and radiocatalysis. *Int. J. Photoenerg.* 4, (2002) 91-131.
- [44] D. Ravelli, D. Dondi, M. Fagnoni and A. Albini. Photocatalysis. A multi-faceted concept for green chemistry. *Chem.Soc.Rev.* 38, (2009) 1999–2011.
- [45] M. R. Hoffmann, S. T. Martin, W. Choi and D. W. Bahnemann. Environmental Applications of Semiconductor Photo catalysis. *Chem. Rev.* 95, (1995) 69-96.

- [46] D.S. Bhatkhande, V.G. Pangarkar, and A.C.M. Beenackers. Photocatalytic degradation for environmental applications — a review. *J. Chem. Technol. Biotechnol.* 77, (2001) 102–116,
- [47] A. Fujishima and K. Honda. Photolysis-decomposition of water at the surface of an irradiated semiconductor. *Nature*, 238, (1972) 37-38.
- [48] J. A. Turner. Sustainable hydrogen production. *Science* 305, (2004) 972-974.
- [49] A. J. Esswein and D. G. Nocera. Hydrogen production by molecular photocatalysis. *Chem. Rev.* 107, (2007) 4022-4047.
- [50] G. Umar Ibrahim and A. Abdul Halim. Heterogeneous photocatalytic degradation of organic contaminants over titanium dioxide: a review of fundamentals, progress and .problems, *J. Photochem. Photobiol. C* 9, (2008) 1-12.
- [51] A. Alm. Regulatory Focus: Nonpoint sources of water pollution. *Environ. Sci. Technol.* 24, (1990) 967–967.
- [52] R. Vinu and Giridhar Madras. Kinetics of Sono photocatalytic Degradation of Anionic Dyes with Nano-TiO<sub>2</sub>. *Environ. Sci. Technol.* 43, (2009) 473–479.
- [53] T. A. Ternes , M. M. Heimer , Derek Mcdowell , Frank Sacher , Heinz - Jurgen Brauch, Brigitte Haist - Gulde, Gudrun Preuss, Uwe Wilme and Ninette Zulei – Seibert. Removal of Pharmaceuticals during Drinking Water Treatment. *Environ. Sci. Technol.* 36, (2002) 3855-3863.
- [54] O. Legrini, E. Oliveros, and A. M. Braun. Photochemical Processes for Water Treatment. *Chem. Rev.* 93, (1993) 671-698
- [55] A. Hambidge. Reviewing efficacy of alternative water treatment techniques. *Health Estate.* 55, (2001) 23-25.
- [56] T. A. Kurniawan, G.Y.S. Chana, W.-H. Lo, S. Babel. Physico–chemical treatment techniques for wastewater laden with heavy metals. *Chem. Eng. J.* 118, (2006) 83–98.

- [57] P.P. Zolotarev, V.V. Ugrozov, I.B. Volkina and V.M. Nikulin. Treatment of waste water for removing heavy metals by membrane distillation. *J Haz. Mater.* 37, (1994) 77-82
- [58] I. Hua and M. R. Hoffmann. Optimization of Ultrasonic Irradiation as an Advanced Oxidation Technology. *Environ. Sci. Technol.* 31, (1997) 2237–2243.
- [59] E. J. Rosenfeldt and K. G. Linden. Degradation of Endocrine Disrupting Chemicals Bisphenol A, Ethinyl Estradiol, and Estradiol during UV Photolysis and Advanced Oxidation Processes. *Environ. Sci. Technol.* 38, (2004) 5476–5483.
- [60] M. Zaw and M. T. Emett. Arsenic removal from water using advanced oxidation processes. *Toxicol. Lett.* 133, (2002) 113-118.
- [61] M. M. Huber , S. Canonica , G.-Y. Park and U. von Gunten. Oxidation of Pharmaceuticals during Ozonation and Advanced Oxidation Processes. *Environ. Sci. Technol.* 37, (2003) 1016–1024.
- [62] K. Rajeshwar. Hydrogen generation at irradiated oxide semiconductor–solution interfaces. *J. Appl. Electrochem.*, 37, (2007) 765-787.
- [63] K. Rajeshwar, editor, special issue of *J. Appl. Electrochem.* On Heterogeneous Photocatalysis, 2005, 35.
- [64] K. Rajeshwar, C. R. Chenthamarakshan, S. Goeringer and M. Djukic. Titania-based heterogeneous photocatalysis. Materials, mechanistic issues, and implications for environmental remediation. *Pure Appl. Chem.* 73, (2001) 1849-1860.
- [65] K. Rajeshwar, C. R. Chenthamarakshan, Y. Ming and W. Sun. Cathodic photoprocesses on titania films and in aqueous suspensions. *J. Electroanal. Chem.* 538, (2002) 173-182
- [66] B. O'Regan and M. Gratzel. Low cost and highly efficient solar cells based on the sensitization of colloidal titanium dioxide. *Nature*, 335, (1991) 737-740.

- [67] E. Wang, W. Yang and Y. Cao. Unique surface chemical species on indium doped TiO<sub>2</sub> and their effect on the visible light photocatalytic activity. *J. Phys. Chem. C* 113, (2009) 20912 – 20917.
- [68] Y. Xie and C. Yuan. Visible-light responsive cerium ion modified titania sol and nanocrystallites for X-3B dye photodegradation. *Appl. Catal. B* 46, (2003) 251 –259.
- [69] (a) T. Umebayashi, T. Yamaki, H. Itoh and K. Asai. Analysis of electronic structures of 3d transition metal-doped TiO<sub>2</sub> based on band calculations. *J. Phys. Chem. Solids* 63, (2002) 1909–1920 ; b) S. Klosek and D. Raftery. Visible light driven V-doped TiO<sub>2</sub> photocatalyst and its photooxidation of ethanol. *J. Phys. Chem. B* 105, (2001) 2815 – 2819.
- [70] N. Serpone, D. Lawless, J. Disdier and J. M. Herrmann. Spectroscopic, Photoconductivity and Photocatalytic Studies of TiO<sub>2</sub> Colloids: Naked and with the Lattice Doped with Cr<sup>3+</sup>, Fe<sup>3+</sup>, and V<sup>5+</sup> Cations. *Langmuir* 10, (1994) 643 –652.
- [71] a) J. Zhu, Z. Deng, F. Chen, J. Zhang, H. Chen, M. Anpo, J. Huang and L. Zhang. Hydrothermal doping method for preparation of Cr<sup>3+</sup>-TiO<sub>2</sub> photocatalysts with concentration gradient distribution of Cr<sup>3+</sup>, *Appl. Catal. B* 62, (2006) 329 –335; b) C. C. Tsai and H. Teng. Chromium-doped titanium dioxide thin-film photoanodes in visible-light-induced water cleavage. *Appl. Surf. Sci.* 254, (2008) 4912 – 4918.
- [72] R. Dholam, N. Patel, M. Adami and A. Miotello. Hydrogen production by photocatalytic water-splitting using Cr-or Fe-doped TiO<sub>2</sub> composite thin films photocatalyst. *Int. J. Hydrogen Energ.* 34, (2009) 5337 –5346.
- [73] a) Y. Zhang, S. G. Ebbinghaus, A. Weidenkaff, T. Kurz, H. A. K. VonNidda, P. J. Klar, M. Gngerich and A. Rellert. Controlled iron-doping of macrot textured nanocrystalline titania. *Chem. Mater.* 15, (2003) 4028–4033; b) C. Y. Wang, D. W. Bahnemann and J. K.

Dohrmann. A novel preparation of iron-doped TiO<sub>2</sub> nanoparticles with enhanced photocatalytic activity. Chem. Commun. 2000, 1539–1540

[74] (a) M. Iwasaki, M. Hara, H. Kawada, H. Tada and S. Ito, Cobalt Ion-Doped TiO<sub>2</sub> Photocatalyst Response to Visible Light. J. Colloid Interface Sci. 224, (2000) 202–204; b)

H. Weng, X. Yang, J. Dong, H. Mizuseki, M. Kawasaki and Y. Kawazoe. Electronic structure and optical properties of the Co-doped anatase TiO<sub>2</sub> studied from first principles. Phys. Rev. B 69, (2004) 125219.

[75] (a) A. D. Paola, E. Garca-Lpez, S. Ikeda, G. Marc, B. Ohtani and L. Palmisano. Photocatalytic degradation of organic compounds in aqueous systems by transition metal doped polycrystalline TiO<sub>2</sub>. Catal. Today 75, (2002) 87–93; b)

Y. Yang, X. J. Li, J. T. Chen and L. Y. Wang. Effect of doping mode on the photocatalytic activities of Mo/TiO<sub>2</sub>. J. Photochem. Photobiol. , A 163, (2004) 517–522.

[76] W. Choi, A. Termin and M. R. Hoffmann. The role of metal ion dopants in quantum-sized TiO<sub>2</sub>: correlation between photoreactivity and charge carrier recombination dynamics. J. Phys. Chem. 98, (1994) 13669–13679.

[77] R. Asahi, T. Morikawa, T. Ohwaki, K. Aoki and Y. Taga. Visible-Light Photocatalysis in Nitrogen-Doped Titanium Oxides. Science 293, (2001) 269–271.

[78] M. Mrowetz, W. Balcerski, A. J. Colussi and M. R. Hoffmann. Oxidative power of nitrogen-doped TiO<sub>2</sub> photocatalysts under visible illumination. J. Phys. Chem. B 108, (2004) 17269–17273.

[79] Y. Gai, J. Li, S. S. Li, J. B. Xia and S. H. Wei. Design of Narrow-Gap TiO<sub>2</sub>: A Passivated Codoping Approach for Enhanced Photoelectrochemical Activity. Phys. Rev. Lett. 102, (2009) 036402–036402(04).

[80] J. S. Jang, S. M. Ji, S. W. Bae, H. C. Son and J. S. Lee. J. Photochem. Photo-biol. A 188, (2007) 112–119.

- [81] Y. Z. Yang, C. H. Chang and H. Idriss. Photocatalytic production of hydrogen from ethanol over M/TiO<sub>2</sub> catalysts (M = Pd, Pt or Rh), *Appl. Catal. B: Environ.* 67, (2006) 217 – 222.
- [82] J. S. Jang, S. H. Choi, H. G. Kim and J. S. Lee. Location and state of Pt in platinized CdS/TiO<sub>2</sub> photocatalysts for hydrogen production from water under visible light. *J. Phys. Chem. C* 112, (2008) 17200– 17205.
- [83] Y. Q. Wu, G. X. Lu and S. B. Li. The Role of Cu (I) Species for Photocatalytic Hydrogen Generation Over CuO x/TiO<sub>2</sub>, *Catal. Lett.* 133, (2009) 97–105.
- [84] J. Papp, S. Soled, K. Dwight and A. Wold. *Chem. Mater.* 14, (2002) 496 –500.
- [85] K. K. Kasem. Selective photolysis of aqueous colloidal nano-particles of some metal-oxide semiconductors for hydrogen generation. *Orient. J. Chem.* 25, (2009) 1–7.
- [86] Z. Bian, J. Zhu, S. Wang, Y. Cao, X. Qian and H. Li. Self-assembly of active Bi<sub>2</sub>O<sub>3</sub>/TiO<sub>2</sub> visible photocatalyst with ordered mesoporous structure and highly crystallized anatase. *J. Phys. Chem. C* 112, (2008) 6258 – 6262.
- [87] B. Pal, M. Sharon and G. Nogami. Preparation and characterization of TiO<sub>2</sub>/Fe<sub>2</sub>O<sub>3</sub> binary mixed oxides and its photocatalytic properties. *Mater. Chem. Phys.* 59, (1999) 254–261
- [88] X. Fu, L. Clark, Q. Yang and M. Anderson. The Enhanced Photocatalytic Performance of Titania-Based Binary Metal Oxides: TiO<sub>2</sub>/SiO<sub>2</sub>, TiO<sub>2</sub>/ZrO<sub>2</sub>. *Environ. Sci. Technol.* 30, (1996) 647 –653.
- [89] J. Zhang, P. Du, J. Schneider, P. Jarosz and R. Eisenberg. Photogeneration of hydrogen from water using an integrated system based on TiO<sub>2</sub> and Platinum (II) diimine dithiolate sensitizers. *J. Am. Chem. Soc.* 129, (2007) 7726 –7727.
- [90] M. Gratzel. Dye-sensitized solar cells. *J. Photochem. Photobiol. C* 4, (2003) 145 –153.
- [91] H. Cheng, J. Ma, Z. Zhao and L. Qi. Hydrothermal preparation of uniform nanosize rutile and anatase particles. *Chem. Mater.* 7 (1995) 663-671.

- [92] S. Ge, X. Shi, K. Sun, C. Li, C. Uher, J.R. Baker, J.M.M.B. Holl and B.G. Orr. Facile hydrothermal synthesis of iron oxide nanoparticles with tunable magnetic properties. *J. Phys. Chem. C* 113, (2009) 13593-13599.
- [93] Y. Kitamura, N. Okinaka, T. Shibayama, O.O.P. Mahaney, D. Kusano, B. Ohtani and T. Akiyama. Combustion synthesis of  $\text{TiO}_2$  nanoparticles as photocatalyst. *Powder Technol.* 176, (2007) 93-98.
- [94] A. C. Jones and P. R. Chalker. Some recent developments in the chemical vapour deposition of electroceramic oxides. *J. Phys. D: Appl. Phys.* 36, (2003) R80-R95.
- [95] W. Wang, I. W. Lenggoro, Y. Terashi, T. O. Kim and K. Okuyama. One-step synthesis of titanium oxide nanoparticles by spray pyrolysis of organic precursors. *Mat. Sci. Eng. B* 123, (2005) 194-202.
- [96] S. Watson, D. Beydoun, J. Scott and R. Amal. Preparation of nanosized crystalline  $\text{TiO}_2$  particles at low temperature for photocatalysis. *J. Nanopart. Res.* 6, (2004) 193-207.
- [97] X. Chen and S. S. Mao. Titanium dioxide nanomaterials: synthesis, properties, modifications and applications. *Chem. Rev.* 107, (2007) 2891-2959.
- [98] J. Yang, S. Mei and J. M. F. Ferreira. Hydrothermal synthesis of  $\text{TiO}_2$  nanopowders from tetraalkylammonium hydroxide peptized sols. *Mater. Sci. Eng. C* 15, (2001) 183-185.
- [99] O. Carp, C. L. Huisman and A. Reller. Photoinduced reactivity of titanium dioxide. *Progress in Solid State Chem.* 32, (2004) 33-177.
- [100] W. An, E. Thimsen and P. Biswas. Aerosol-chemical vapor deposition method for synthesis of nanostructured metal oxide thin films with controlled morphology. *J. Phys. Chem. Lett.* 1, (2009) 249-253.
- [101] K. L. Choy. Chemical vapour deposition of coatings, *Prog. Mater. Sci.* 48, (2003) 57-170.



- [102] O. Azzaroni, M. Fonticelli, P.L. Schilardi, G. Benitez, I. Caretti, J.M. Albella, R. Gago, L. Vazquez and R.C. Salvarezza. Surface nanopatterning of metal thin films by physical vapour deposition onto surface-modified silicon nanodots. *Nanotechnol.* 15, (2004) S197-S200.
- [103] C.J. Brinker and S.W. Scherer. *Sol–Gel science: the physics and chemistry of sol–gel processing*. Academic Press. New York, 1990.
- [104] C.J. Brinker, B.C. Bunker, D.R. Tallant, K.J. Ward and R.J. Kirkpatrick. Structure of Sol-Gel Derived Inorganic Polymers: Silicates and Borates. ACS Symposium series, Chapter 26, 360, (1988) 314-332.
- [105] C. N. R. Rao. Chemical synthesis of solid inorganic materials. *Mater. Sci. Eng. B* 18, (1993) 1-21.
- [106] K. C. Patil and S. T. Aruna. *Redox Methods in SHS Practice*. New York: Taylor and Francis, 2002.
- [107] K. Nagaveni, M. S. Hegde, N. Ravishankar, G. N. Subbanna and G. Madras. Synthesis and structure of nanocrystalline TiO<sub>2</sub> with lower band gap showing high photocatalytic activity. *Langmuir*. 20, (2004) 2900-2907.
- [108] K. C. Patil, S. T. Aruna, and S. Ekambaram. Combustion synthesis. *Curr. Opinion in solid state and Mater. Sci.* 2, (1997) 158-165.
- [109] K. C. Patil. Advanced ceramics: combustion synthesis and properties. *Bull. Mater. Sci.*, 16, (1993) 533-541.
- [110] S. R. Jain, K. C. Adiga, and V. R. P. Verneker. A new approach to thermochemical calculations of condensed fuel-oxidizer mixtures. *Combust. Flame*, 40, (1981) 71-79.
- [111] S. T. Aruna and K. C. Patil. Synthesis and properties of nanosize titania. *J. Mater. Synth. Process.* 4, (1996) 175-179.
- [112] K. Rajeshwar. Electrosynthesized thin films of group II–VI compound semiconductors, alloys and superstructures. *Adv. Mater.* 4, (1992) 23-29.

- [113] G. Hodes. *Physical Electrochemistry*. New York, 1995. chapter 11, 515–554.
- [114] D. Lincot, M. Froment and H. Cachet. *Advances in Electro-chemical Science and Engineering*. Wiley-VCH, Weinheim. 6, (1999) 165–235.
- [115] C. J. Brinker and G. W. Scherer. *Sol–Gel Science: The Physics and Chemistry of Sol–Gel Processing*. Academic Press, New York, 1990.
- [116] A. G. Merzhanov, *Int. J. Self-Propag. High-Temp Synth.*, 1993, 2, 113.
- [117] J. I. Moore and H. Feng. *Combustion synthesis of advanced materials: Part I. Reaction parameters*. *J. Prog. Mater. Sci.* 39, (1995) 243-273.

# Chapter 2

## 2. Materials, Methods and Characterization

In this chapter a brief description of materials and methods used for the synthesis of various catalysts and detailed description on characterization techniques was provided.

### 2.1. Chemicals

The chemicals used for the synthesis of various metal oxide and sulfide nanomaterials in the present thesis work are as follows: Titanium (IV) iso propoxide (Sigma Aldrich), and nitric acid (Merck) were used during the synthesis of titanyl nitrate, cadmium nitrate, copper nitrate, cobalt nitrate, lead nitrate and nickel nitrate obtained from Merck were used as oxidants for the synthesis of respective metal sulfides. Glycine, hexamethylene tetraamine, triethylamine, citric acid, ascorbic acid were obtained from Merck. Thiourea (Merck) was used as the fuel for the synthesis of metal sulfides. The benchmark TiO<sub>2</sub> (Evonik P-25) was predominantly anatase and has a specific surface area of 60 m<sup>2</sup>/g. Potassium dichromate (Merck), methylene blue and phenol were used model pollutants for assessing the photocatalytic activity. Sodium sulfide and sodium sulfite were used as sacrificial reagents during the water splitting experiments, whereas ethanol and polyvinylidene difluoride (sigma aldrich) were used during the preparation of solar paint. All solutions in this study were prepared from double-distilled (millipore) water.

### 2.2 Experimental procedures

The synthesis of TiO<sub>2</sub> and different metal sulfides used in this work was carried out by following the combustion synthesis using redox mixtures as discussed in section 1.7. In a typical synthesis metal nitrates were used as the oxidants whereas glycine, hexamine, triethylamine, citric acid, ascorbic acid and thiourea were used as fuels (reducing agents).

#### 2.2.1. Calculation of amounts of oxidant and fuel:

In general while taking the redox mixture for combustion synthesis the ratio of the oxidizer to fuel can be calculated using the equivalence ratio ( $\phi_e$ ), defined as [1]:

$$\phi_e = O/F \quad (2.1)$$

where (O) is the total oxidizing valence and (F) is the total reducing valence of the elements present in the mixture [2]. According to propellant theory, the species M<sup>2+</sup>, M<sup>3+</sup>, M<sup>4+</sup>, C and H are considered to be reducing with valencies of +2, +3, +4, +4 and +1 respectively.

Oxygen is considered to be an oxidizing species with valence -2 and nitrogen is considered to be neutral with a value of zero [3].

However in the present thesis work, for the synthesis of  $\text{TiO}_2$  the amounts of oxidant and fuel were calculated according to the balanced equations, which correspond to the fuel/oxidant ratio of 1.

The balanced equations are as follows:



### 2.2.2. Calculation of F/O ratio:

For example, in the case of  $\text{TiO}_2$  prepared by using glycine as fuel, the oxidant is titanyl nitrate  $\text{TiO}(\text{NO}_3)_2$  and fuel is glycine ( $\text{NH}_2\text{CH}_2\text{COOH}$ ).

#### (a) Calculation of oxidizing valence:

As mentioned above the valencies of elements present in titanyl nitrate are as follows: Ti(+4), O (-2) and N (0). So the total oxidizing valency is  $+4 + (-2) + 0 + 6(-2) = -10$ . Here the negative sign indicates the oxidizing valency.

#### (b) Calculation of reducing valence:

As mentioned above according to propellant theory the valencies of elements present in glycine are as follows: N (0), H (+1), C(+4) and O (-2). So the total reducing valency is  $0 + 5(+1) + 2(+4) + 2(-2) = +9$

Here the positive sign indicates the reducing valency.

$$\text{Hence F/O ratio} = \text{Total reducing valence} / \text{Total oxidizing valence} = 9/10$$

In this study we have taken this ratio as 1 i.e.  $9/10=1$ . This implies nine moles of oxidant and 10 moles of reductant or in other words for one mole of oxidant 1.1 moles of reductant can be taken so as to form the redox mixture for combustion synthesis. These mole ratios are in accordance with the stoichiometric equations as well.

### 2.2.3. Schematic of general combustion synthesis:

In a typical synthesis the calculated amounts of fuel and the oxidant were mixed in a quartz crucible by adding small volume of water. Thereafter the mixture was placed on a preheated hot plate (150°C), in order to ensure homogeneous mixing and dehydration of the aqueous mixture. Once the mixture acquired a viscous appearance, it was transferred to a preheated furnace (350°C), where the reaction was accompanied by release of a large amount of gases producing a dry final product.

### 2.3. Characterization techniques

#### 2.3.1. Powder X-ray diffraction (PXRD)

Powder X-ray diffraction (PXRD) is an extensively used characterization technique, from which one can reveal the valuable information about the crystalline nature of a material, nature of the phase present, lattice parameter and grain size [4-8]. It is possible to ascertain unknown materials, by matching the diffraction data with those in the standard data base. The technique can also be used for the characterization of heterogeneous solid mixtures, determination of relative abundance of crystalline compounds and if coupled with one of the refinement techniques (e.g. the Rietveld refinement) it can also provide quantitative structural information.

The principle involved in powder X-ray diffraction is as follows: When a monochromatic source of X-rays passes through a material which consists of regularly arranged atoms with the interatomic distances in the order of wavelength of X-rays, it can undergo diffraction by the atoms of the material. If the angle between incident and diffracted rays with a fixed crystal plane is assumed to be  $\theta$  then the diffraction phenomenon can be explained as shown in Fig. 2.1. If a constructive interference occurs among the scattered waves they may remain in phase as the path length of each wave is equal to an integral multiple of the wavelength (figure 2.1). The path difference between the constructive interference waves can be given by  $2d\sin\theta$ , where  $\theta$  is the scattering angle according to the Bragg's law [9].

$$\text{i.e. } n\lambda = 2d\sin\theta \quad (2.7)$$

where:

$\lambda$  = wavelength of incident X-rays.

$n$  = order of diffraction (0,1,2,3, etc.).

$d$  = interplanar spacing.

$\theta$  = angle between the incident radiation and the planes (h k l).

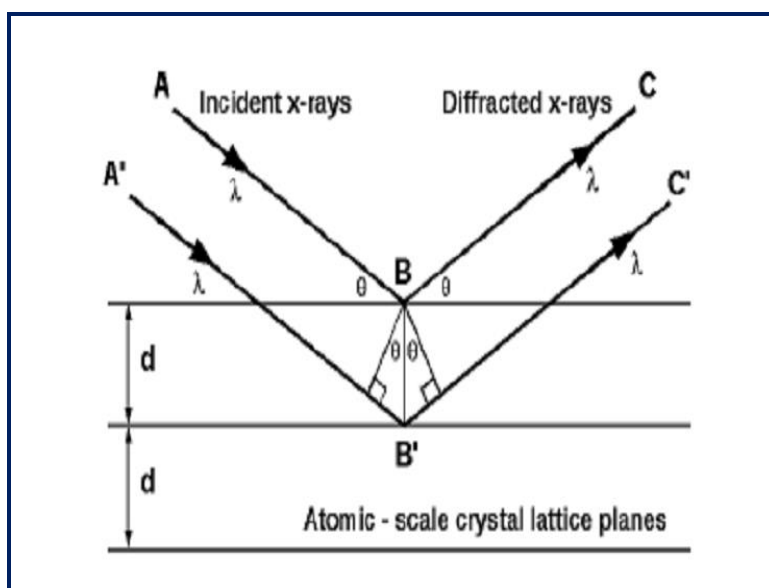


**Figure 2.1. Bragg's law for X-ray diffraction. The diffracted X-rays exhibit constructive interference when the distance between paths ABC and A'B'C' differs by an integer number of wavelengths ( $\lambda$ ).<sup>9</sup>**

For powder diffraction it is important to have the samples with smooth plane surface and randomly distributed crystallites. The monochromatic X-ray source has to be placed on a rotating arm, in order to light the sample with a variable angle  $\theta$ . The reflected radiation is collected by the detector, even fixed on a rotating arm, placed at twice this angle. As  $2\theta$  is the angle measured between the detector and the incident beam, as shown in Fig. 2.2, the diffracted radiation is collected by the detector at the very same incident angle  $\theta$ .

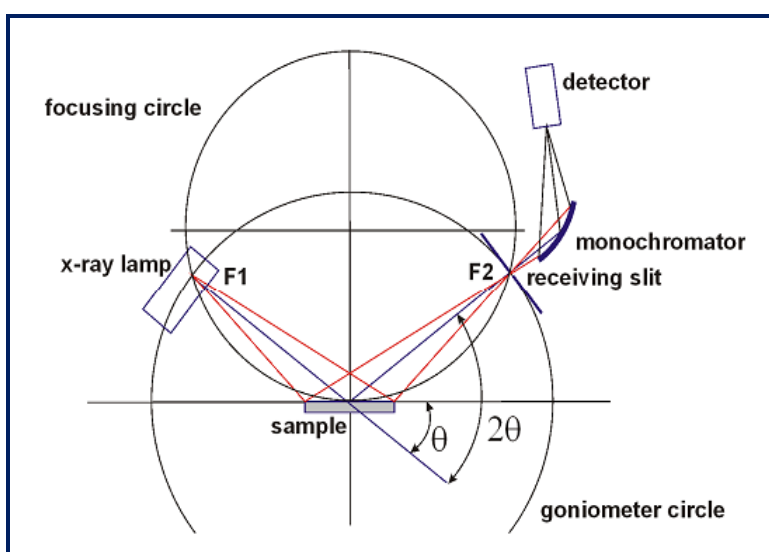


**Figure 2.2. Schematic diagram of a X-ray diffractometer**

In this thesis work, powder X-ray diffraction (PXRD) patterns of the samples were recorded on a PANalytical X'pert Pro powder X-ray diffractometer with a step size of 0.02 and at a scan rate of 0.50 min<sup>-1</sup> using Cu-K $\alpha$  (1.54 Å) radiation and Ni filter. The particle size was calculated by using the FWHM (full width at half maximum) of the most intense line and by applying the Scherrer formula:

$$d_{hkl} = (0.9 \lambda) / \beta \cos\theta \quad (2.8)$$

where:

$d(hkl)$  = particle size (nm) of the crystallites

$\lambda$  = incident wavelength of X-rays.

$\beta$  = line broadening at full width half maximum (FWHM) expressed in rad.

$\theta$  = incident angle of X-rays.

### 2.3.2 X-ray photoelectron spectroscopy (XPS)

X-ray photoelectron spectroscopy is a technique for surface chemical analysis which relies on monitoring the electron energy emitted by a system under stimulation of X-rays. Traditionally, when the technique has been used for surface studies it has been subdivided according to the source of exciting radiation into two categories such as:

- X-ray photoelectron spectroscopy (XPS) using soft X-ray (200-2000 eV) radiation to examine core levels;
- Ultraviolet photoelectron spectroscopy (UPS) using vacuum UV (10-45 eV) radiation to examine valence levels

Photoelectron spectroscopy is based upon a single photon in/electron out process. The energy of a photon is given by the Einstein relation:

$$E = h\nu \quad (2.9)$$

where  $h$  is the Planck's constant ( $6.62 \cdot 10^{-34}$  J/s), and  $\nu$  is the frequency (Hz) of the radiation. A monochromatic source of radiation is used in photoelectron. In XPS the absorption of photon by an atom in a molecule or solid, leads to the ionization and the emission of a core (inner shell) electron. On the other hand, in UPS the photon interacts with valence levels of the molecule or solid, leading to ionisation by removal of one of these valence electrons.

The kinetic energy distribution of the emitted photoelectrons (i.e. the number of emitted photoelectrons as a function of their kinetic energy) can be measured using any appropriate electron energy analyser and therefore photoelectron spectrum can be obtained. From the kinetic energy of the emitted electrons (KE), the electron binding energy (BE) of

each of the emitted electrons can be determined as a difference between the energy of the primary photon ( $h\nu$ ) and the kinetic energy of the photoelectron:

$$KE = h\nu - BE \quad (2.10)$$

Generally, XPS spectrum is a plot between emission intensity Vs. the electron binding energy from which one can obtain the information about the atomic composition of the sample surface. Moreover from the intensity of the peaks, concentration of the element within the sampled region can be calculated. As the technique provides a quantitative analysis of the surface composition it is also known as ESCA (Electron Spectroscopy for Chemical Analysis). The most commonly used X-ray sources are those giving rise to:

Mg  $K\alpha$  radiation:  $h\nu = 1253.6 \text{ eV}$

Al  $K\alpha$  radiation:  $h\nu = 1486.6 \text{ eV}$

The emitted photoelectrons will therefore have kinetic energies in the range of 0-1250 eV or 0-1480 eV .

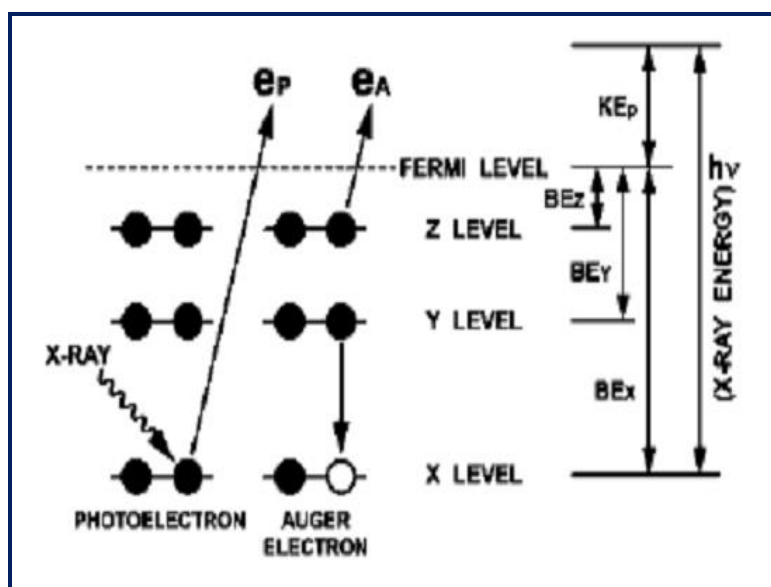


**Figure 2.3. Photoelectron ( $e_p$ ) and Auger electron ( $e_A$ ) emission processes induced by X-rays.** <sup>11</sup>

As shown in Fig. 2.3, the binding energies (BE) of energy levels in solids are usually measured with respect to the Fermi level of the solid, rather than the vacuum level. This indicates a necessary correction to the equation given above in order to account for the work function ( $\Phi$ ) of the solid, as described by the following relation:



$$KE = h\nu - BE - \phi \quad (2.11)$$

Moreover the exact binding energy of an electron depends not only upon the level from which photoemission is occurring, but also upon the formal oxidation state of the atom and the local chemical and physical environment. Changes in either of these two factors give rise to small shifts in the peak positions in the spectrum, so-called chemical shifts. Such shifts can also be readily observable and interpretable in XPS spectra because the advantages of technique such as its high intrinsic resolution (as core levels are discrete and generally of a well-defined energy) and it is a one electron process (thus simplifying the interpretation).

It is observed that atoms of a higher positive oxidation state exhibit a higher binding energy due to the extra coulombic interaction between the photo-emitted electron and the ion core. This ability to discriminate between different oxidation states and chemical environments is one of the major strengths of XPS technique.

Figure 2.4. shows the schematic representation of XPS instrumentation. Although there are many different designs of electron energy analyser but the preferred option for photoemission experiments is a concentric hemispherical analyser (CHA), which uses an electric field between two hemispherical surfaces to disperse the electrons according to their kinetic energy.

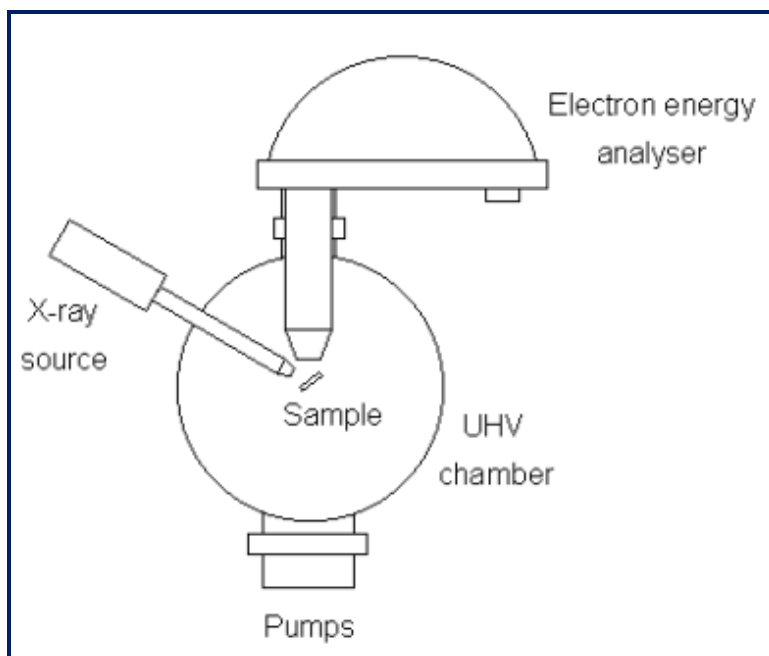


**Figure 2.4. Basic scheme of XPS instrumentation<sup>11</sup>**

In the present thesis work X-ray photoelectron spectroscopy (XPS) data were collected by an Axis Ultra instrument (Kratos analytical, Manchester, UK) under ultra-high vacuum condition ( $<10^{-8}$  Torr) and using a monochromatic Al K $\alpha$  X-ray source (1486.6 eV). The source power was maintained at 150 W and the emitted photoelectrons were sampled from a  $750 \mu\text{m} \times 300 \mu\text{m}$  area. The analyzer pass energy was 80 eV for survey spectra and 40 eV for high resolution spectra. The adventitious carbon 1s peak at 285 eV was used as an internal standard to compensate for any charging effects. Both curve fitting of the spectra and quantification were performed with the CasaXPS software, using relative sensitivity factors given by Kratos.

### **2.3.3. UV-Visible absorption spectroscopy:**

Ultraviolet-Visible (UV-Vis) absorption spectroscopy can be utilized for quantitative determination of both organic as well as inorganic nano sized molecules. The principle involved in this technique is mainly the irradiation of the sample with ultraviolet and visible light and thereby absorbed light can be analyzed by the resulting absorption spectra [12,13]. UV-Vis spectroscopy is useful in identifying the constituents of the test sample, concentrations of the sample and the functional groups in molecules. The technique can be utilized for different sized particles of wide variety of materials such as transition metal ions, small molecular weight organic molecules, polymers, supramolecular assemblies, nanoparticles and bulk materials. Moreover by using UV-Vis absorption spectra the size dependant properties of materials in nano and atomic scale ranges can be obtained from the peak broadening and shifts in the absorption wavelength of UV-Vis spectra. In case of nanomaterials the absorption peak's width gives valuable information about the chemical composition and their particle size which makes it easy to distinguish from their bulk counterparts. For example, in case of semiconductor nanocrystals due to the quantum confinement effects there will be broadening in the absorption spectrum [14,15] and as their size decreases further one can observe a band instead of a distinct peak. In addition to this it is generally observed that the absorption peak of semiconductor nanoparticles shows a shift in wavelengths as their crystal size varies [16-19]. Therefore one can determine the band gap of the materials by using UV-Vis spectroscopy.

During the UV-Vis spectroscopic measurement a beam of monochromatic light produced from the light source can be made into two beams to pass one through the sample, and the other through the reference [20]. The transmitted light from the sample and reference were collected by the detector where they can be detected and compared. The difference between the two transmitted beams is the basis of the measurement. Generally for liquid samples a cell called a cuvette which is made up of quartz with flat faces is used to

place the sample. Since quartz is well known as a transparent material to both UV and visible lights it is widely used in making cuvettes for spectroscopic techniques. Thus UV-Vis spectroscopy can be considered as a straight forward and effective way of quantitative determination of both organic and inorganic nanomaterials.

#### 2.3.4. UV-Vis diffuse reflectance spectroscopy

The principle of diffuse reflectance UV-Vis spectroscopy is based on the reflection of incident UV or visible beam of light in all directions by the powdered sample. However the fraction of light that is scattered within a sample and returned to the surface is said to be diffuse reflection. Thereafter the reflected radiation was collected by an integrating sphere, to enhance the signal-to noise ratio. The interior of the integrating sphere was usually covered with barium sulphate, a compound which has a reflectivity greater than 0.98 in the UV-Vis region. Moreover the reflectance spectrum of a reference standard ( $\text{BaSO}_4$ ) should be carried out prior to the unknown sample.

Diffuse reflectance spectrum differs from the absorption spectrum in the multiple surface reflections of the powder sample. In photocatalysis absorption spectra plays a key role according to the first law of photochemistry which states that light must be absorbed by a chemical substance in order to promote a photochemical reaction [20]. However, for solid photocatalysts it is very difficult to get precise expressions of photoabsorption spectra. Therefore in the literature for solid photocatalysts the absorption spectrum is usually expressed in terms of absorbance units or Kubelka–Munk function.

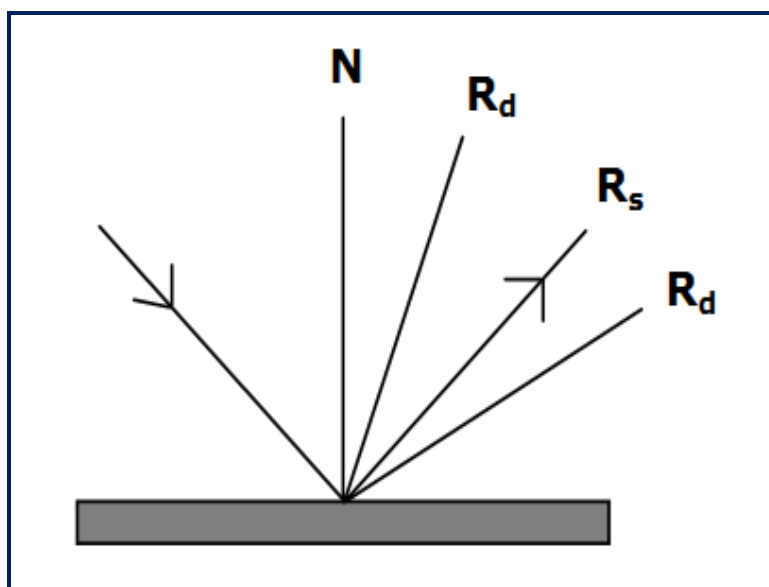


**Figure 2.5.** Schematic representation of the radiation interaction with the sample:  $R_s$  stands for the specular reflected beam,  $R_d$  for the diffuse reflected beam

The former, i.e. absorbance, is traditionally defined as  $\log(I_0/I)$ , where  $I_0$  and  $I$  are the intensities of incident and transmitted light, respectively. Otherwise when photoabsorption is measured in a reflection mode,  $I$  can be considered the reflection intensity, while  $I_0$  represents the reflection of a 'standard material', such as  $\text{BaSO}_4$ , which can reflect all the incident light, i.e. 100% reflection. In this regard the Kubelka-Munk (KM) function, usually employed for samples diluted with a medium of less photoabsorption, is otherwise defined as follows:

$$F(R_\infty) = (1 - R_\infty)^2 / 2 R_\infty = \alpha/s \quad (2.12)$$

where  $R_\infty$ ,  $\alpha$  and  $s$  are the diffuse reflectance ( $I/I_0$ ), the absorption coefficient in  $\text{cm}^{-1}$  units and the scattering factor, respectively.

Absorbance and K-M units are mainly proportional to the concentration of a given material dispersed in a homogeneous medium (liquid or solid matrix), but not to the number of photons absorbed by a solid sample. This is easily understood by the fact that absorbance values equal to 1 and 2 correspond to 90 and 99% absorption of incident light. In order to calculate the extent of photoabsorption of a solid sample, it's thus strongly recommended to measure absorption which can be calculated as  $(1-R)$ , where  $R$  represents the diffuse reflectance value.

### 2.3.5. $\text{N}_2$ sorption analysis

Surface area and porosity plays an important roles in the characterization of powder materials. The familiar techniques used for the estimation of surface area involves the measurement of physical adsorption of gas molecules on a solid surface.

The important characteristics of physical adsorption are:

- It is accompanied by low heats of adsorption with no significant or disruptive structural changes occurring on the surface during the adsorption measurements.
- It leads to surface coverage by more than one layer of adsorbate so pores can be filled by the adsorbate and thereby facilitates the pore volume measurements.
- At elevated temperatures physical adsorption does not occur or is sufficiently low. Thus at elevated temperatures relatively clean surfaces can be prepared and accurate surface area measurements can be carried out.
- During the physical adsorption equilibrium can be attained rapidly since there is no requirement of activation energy
- Physical adsorption is a reversible process which enables the study of both adsorption and desorption processes.

- During the physical adsorption molecules are not restrained to adsorb only on some places but are free to cover the entire sample surface. Therefore surface areas, rather than the number of sites can be calculated by using physical adsorption phenomenon.

In order to understand the kinetics and thermodynamics it is essential to establish the meaning of an adsorption (desorption) isotherm during the surface area and pore structure measurements. Adsorption isotherm can be used to calculate the molar quantity of gas ( $V_\alpha$ ) taken up, or released, at a fixed temperature of  $T$  by a clean solid surface with respect to the gas pressure  $P$ . Generally physisorption experiments were conducted at a cryogenic temperature, (usually liquid nitrogen temperature).

Generally the quantity of gas adsorbed can be expressed in terms of its volume at STP conditions (standard temperature and pressure conditions  $0^\circ\text{C}$  and  $760$  torr), whereas the pressure can be expressed in terms of relative pressure i.e. the actual gas pressure  $P$  divided by the vapor pressure  $P_0$  of the adsorbing gas at the temperature of the test.

The physical adsorption isotherm can be expressed as a plot between  $V_\alpha$  (ordinate) against  $P/P_0$  (abscissa) which can give much information about the structure of the adsorbing material (called the adsorbent) simply from their shape. The main theory utilized in order to get the essential information such as surface area and pore distribution from the obtained adsorption isotherm is BET theory (Brunauer, Emmett and Teller Theory) [21]. BET theory can be considered as an extension to multilayer adsorption of the Langmuir model (related to monolayer molecular adsorption). The principle involved is  $\text{N}_2$  molecules can be physisorbed at liquid nitrogen temperature ( $77\text{K}$ ) to form a monolayer covering the total area of the material provided that the saturated pressure ( $p/p_0$ ) is  $< 0.33$ . The amount of adsorbate (nitrogen) required to form a monolayer of molecules over the surface of a material can be obtained from the BET equation.

$$V_\alpha = (V_m CP) / (P_0 - P) [1 + (C-1) (P/P_0)] \quad (2.13)$$

where:

$V_\alpha$  = volume of adsorbed gas at pressure  $P$ .

$V_m$  = monolayer volume.

$P$  = gas pressure.

$P_0$  = saturation gas pressure.

The value of parameter  $C$  is fairly constant for a given class of materials (oxides and metals)

In simplest terms  $C$  can be obtained as follows:

$$C \propto \exp [(q_1 - q_L) / RT] \quad (2.14)$$

where:

$q_1$  = heat of adsorption of the first layer.

$q_L$  = heat of liquefaction of the adsorptive.

R = gas constant.

T = absolute temperature.

Small values of the C parameter signifies the higher affinity between molecules than between the molecules and the adsorbing species which results in lower wettability. On the contrary, high C values symbolizes a typical isotherm, characterized, firstly, by a monolayer adsorption and then by the multilayer one, layer by layer. The amount of adsorbate corresponding to the first monolayer,  $V_m$ , and the C parameter can be calculated from the slope and intercept values of the BET linear plot.

The surface occupied by a  $N_2$  molecule is  $16.2 \times 10^{-20} \text{ m}^2$ , and once  $V_m$  is calculated, it's easy to calculate the specific surface area (SSA) of the adsorbing material, by the following equation:

$$\text{SSA} = (V_m N_A S_{N_2}) / 22.414 \text{ g} \quad (2.15)$$

where:

$N_A$  = Avogadro number ( $6.023 \times 10^{23}$  molecules  $\text{mol}^{-1}$ ).

$S_{N_2}$  = surface occupied by a  $N_2$  molecule adsorbed on the monolayer.

22, 414 = volume ( $\text{dm}^3$ ) occupied by 1 mole of gas under standard conditions.

g = sample quantity (g).

### **2.3.6. Transmission Electron Microscopy (TEM):**

Since its invention, the electron microscope has been a valuable tool in the development of scientific theory and it contributed greatly to biology, medicine and material sciences. This wide spread use of electron microscope is based on the fact that they permit the observation and characterization of materials on a nanometer (nm) to micrometer ( $\mu\text{m}$ ) scale. This examination can yield information about the topography (surface features of an object), morphology (shape and size of the particles making up the object), composition (the elements and compounds that the object is composed of and the relative amounts of them) and crystallographic information (how the atoms are arranged in the object).

The Transmission Electron Microscope (TEM) was the first type of Electron Microscope to be developed and is patterned exactly on the Light Transmission Microscope except that a focused beam of electrons is used instead of light to "see through" the specimen. It was developed by Max Knoll and Ernst Ruska in Germany in 1931. The first Scanning Electron Microscope (SEM) debuted in 1942, with the first commercial instruments around 1965. Its late development was due to the electronics involved in "scanning" the beam of electrons across the sample. Electron Microscopes (EMs) function

exactly as their optical counterparts except that they use a focused beam of electrons instead of light to "image" the specimen and gain information as to its structure and composition.

### **2.3.6.1. Electron-matter interactions**

When an electron beam interacts with the atoms in a sample, individual incident electrons undergo two types of scattering - elastic and inelastic. In the former, only the trajectory changes and the kinetic energy and velocity remain constant. In the case of inelastic scattering, some incident electrons will actually collide with and displace different kind of electrons from the specimen, thus losing their kinetic energy. Figure 2.6 summarizes the main secondary signals (with different relative intensity) that can be produced due to electron-matter interactions [22].

By considering the large amount of information obtained by this kind of interaction it's essential try to amplify each single signal by using different kinds of instrumentation. In this regard the first main difference between SEM and TEM, mainly concerning the sample location in the microscope, can be outlined. In particular SEM studies the information related to secondary and backscattered electrons, detected on the same side with respect to the incident electrons beam. In this case the sample holder is located at the end of microscope's column (Fig. 2.7 a). On the contrary TEM deals with transmitted, elastically or inelastically scattered electrons, detected on the opposite side with respect to the incident electrons beam. In this case the sample holder is located in the middle of the microscope's column (Fig. 2.7 b).

Both SEM and TEM instruments must work under ultra high vacuum conditions ( $10^{-7}$ - $10^{-8}$  Pa) in order to avoid any kind of collision between the electrons beam and atoms, which are not those contained in the investigated sample. Moreover there are essential instrumental components which are common to SEM and TEM systems: electron guns, which can be divided into thermoionic and field-emission types, and metal apertures and magnetic lenses necessary to confine and focus the electron beam toward the specimen.

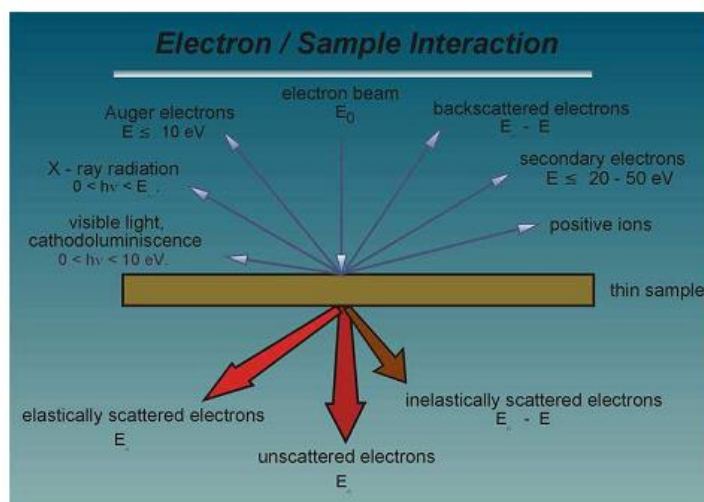


**Figure 2.6.** Signals generated when a high-energy beam of electrons interacts with a thin specimen. Most of these signals can be detected in different types of electron microscopes. The directions shown for each signal do not always represent the physical direction of the signal but indicate, in a relative manner, where the signal is stronger or where it is detected.

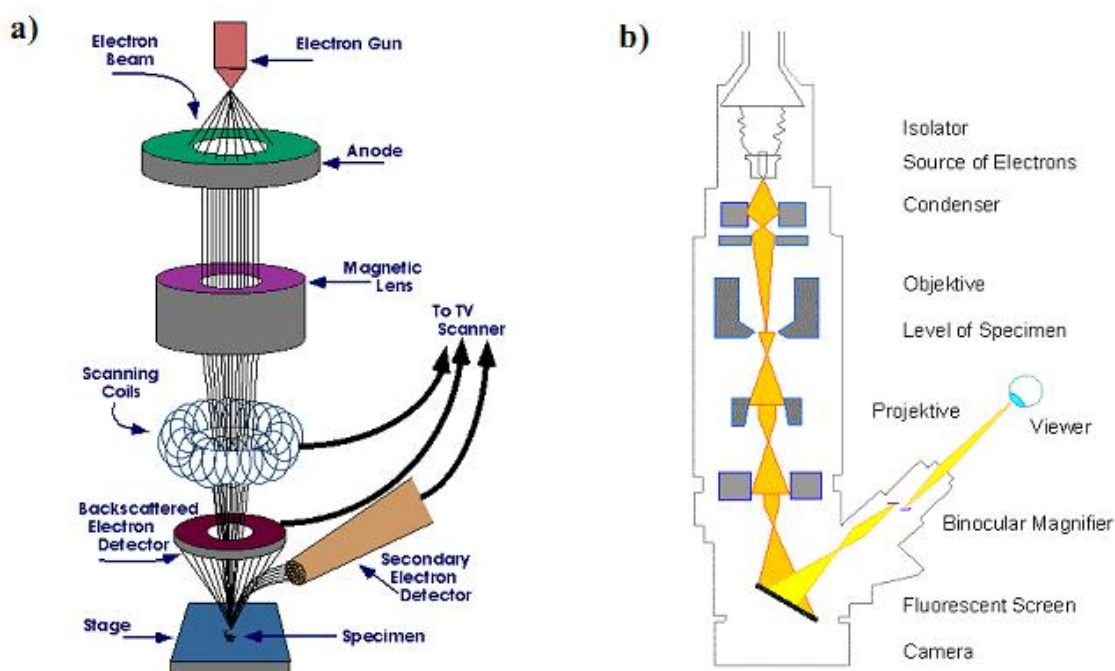


**Figure 2.7.** General scheme of a) SEM and b) TEM instrumentations. <sup>22</sup>

### 2.3.6.2. Electrons exploited in transmission electron microscopy

TEM exploits three different interactions of electron beam-specimen: unscattered electrons (transmitted beam), elastically scattered electrons (diffracted beam) and inelastically scattered electrons. When incident electrons are transmitted through the thin



specimen without any interaction occurring inside the specimen, then the beam of these electrons is called transmitted. The transmission of unscattered electrons is inversely proportional to the specimen thickness. Areas of the specimen that are thicker will have fewer transmitted unscattered electrons and so will appear darker; conversely the thinner areas will have more transmitted and thus will appear lighter. Another part of the incident electrons, are scattered (deflected from their original path) by atoms in the specimen in an elastic fashion (without loss of energy). These diffracted electrons according to Bragg's law are then transmitted through the remaining portions of the specimen. In this case a diffraction pattern and the related information about orientation, atomic arrangements and phases present in the examined area can be obtained.

There are essentially three different imaging modes in TEM, which can be selected by changing proper apertures of the back focal plane (after the objective lens) (Fig. 2.8):

1. **Bright field mode:** the aperture selects only transmitted electrons. In this case, factors such as mass and thickness of the sample influence the formation of the image.
2. **Dark field mode:** In this case only diffracted electrons, which gave strong interaction with the sample, are selected. The image obtained can give information about the presence of defects or different phases of the specimen.
3. **High resolution (HR-TEM):** In this case both transmitted and diffracted electrons are selected. Using proper corrections for spherical aberration, special high resolution TEMs can generate images with a resolution below 0.1 nm; it's thus possible observe reticular planes and get crystallographic information of the examined sample. By considering that for TEM analysis the analyzed electrons have to pass through the sample, the specimens have to be rather thin, less than 100 nm.

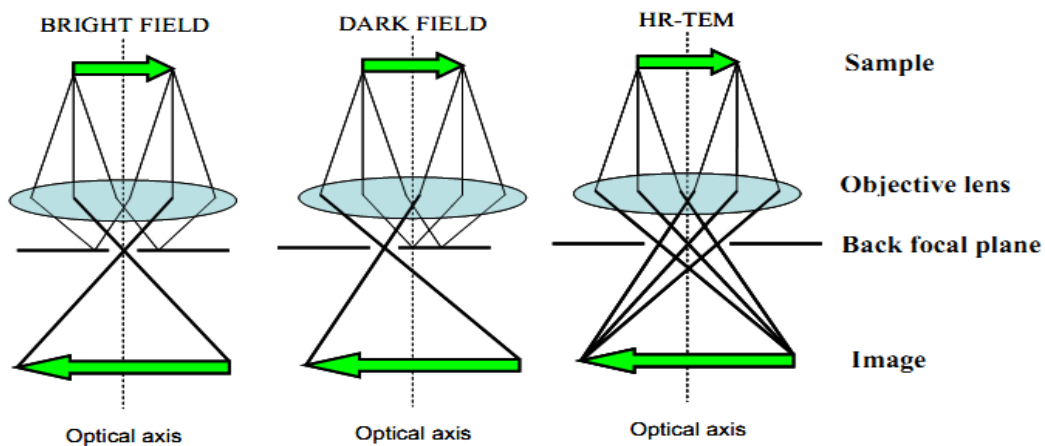


**Figure 2.8.** Generalized description of the three main imaging modes in TEM <sup>22</sup>

## **2.7. Photoluminescence (PL) spectroscopy**

Photoluminescence spectroscopy involves monitoring of emitted light from atoms or molecules after their excitation by absorbing photons followed by deexcitation [23, 24]. This technique can be used for the materials which can exhibit photoluminescence. Similar to the UV-Vis spectroscopy PL spectroscopy can also be used for the identification of both organic and inorganic materials with any size and in any form such as solid, liquid, or gas. In PL spectra, UV and visible light can be used as light source. The PL properties of a sample can be characterized by four important parameters such as intensity, emission wavelength, bandwidth of the emission peak, and the emission stability [25]. Moreover it is found that the PL properties of a material may change with the different environments and presence of other impurities. Furthermore, as the size of the material decreases to nano range one can observe differences in PL emission properties such as shift in the emission wavelength. Moreover, because the emitted photon matches to the energy difference between the states from PL spectroscopy one can determine the material properties such as band gap, recombination mechanisms, and impurity levels. In PL spectroscopy liquid samples can be analyzed by placing the solution in a quartz cuvette with a known path length. In PL technique double beam optics is generally employed from which the first beam passes through an excitation filter or monochromator, then through the sample and onto a detector. This incident light causes photoluminescence, which can emit in all directions. The emitted light can be collected by the detector and allowed to pass through a monochromator [26]. On the other hand the second reference beam is attenuated and compared with the beam obtained from the sample. In PL spectra solid samples can be analyzed by impinging the incident beam on the material (thin film, powder etc.). An emission spectrum is recorded, when the sample is irradiated with a single wavelength and the intensity of the luminescence emission is recorded as a function of wavelength. If the fluorescence of a sample is monitored as a function of time after the initial excitation by a flash of light the technique is called as time resolved fluorescence spectroscopy.

## **2.8. Gas chromatography**

Gas chromatography (GC) is an analytical technique used for the quantitative analysis of gases. In general, chromatography techniques are widely used for the separation of mixtures into pure substances and can be used for both gases and liquids. In gas chromatography (GC), the mobile phase is usually an inert carrier gas such as helium, N<sub>2</sub> or argon. The carrier gas is continuously allowed to flow through a column containing the stationary phase. Generally the columns used for the chromatography techniques consists of

a tube containing a packing of solid support material with various liquid or solid coatings based on the type of mixture under the analysis.

The basic operating mechanism involved in a gas chromatography is to vaporize the sample in a heated injector followed by separation of the components in a column and then analyze the components with a detector. The detector used for the detection of gases is thermal conductivity detector (TCD). In the present thesis work  $N_2$  gas was employed as the carrier gas, a packed column (Porapak Q packed column followed by Hysep Q column, with 2 m length each, 1/8" OD and 2.1 mm ID) and TCD detector. During the photocatalytic experiments, the volume of hydrogen produced from water splitting reaction was quantified by periodically withdrawing gas from reaction vessel using a 500  $\mu$ L gas tight syringe and injecting it into the gas chromatograph (Shimadzu gas chromatography (GC-2014)). Different gas species pass through the column at different rates depending on the strength of electrostatic interactions with the mobile and stationary phases present in the column based on their retention times. This causes the gas mixture to become separated into individual components that reach the end of the column and are detected at different times. By measuring the retention time of each species in the column, the component gases can be identified by comparison with chromatograms for known species. Retention times are affected by the gas concentration, flow rate and pressure as well as the column material and temperature. The signal produced by each gas as it reaches the detector results in a peak on the chromatogram at a residence time that is characteristic for that gas. The peak area is proportional to the gas concentration.

## **2.9. Raman spectroscopy**

Raman spectroscopy is an important spectroscopic technique which is based on inelastic scattering of monochromatic light, generally from a laser source. During an inelastic scattering the frequency of photons in monochromatic light undergo changes upon interaction with the sample. Photons of the laser light are absorbed by the sample and then reemitted. Frequency of these emitted photons is shifted up or down in comparison with original monochromatic frequency, which is called the Raman effect. This shift provides information about vibrational, rotational and other low frequency transitions in molecules [27]. Raman spectroscopy can be used to study solid, liquid and gaseous samples. In the present thesis work the Raman spectra of the samples were recorded on Bruker senterra dispersive Raman microscope (laser excitation of wavelength of 532 nm) equipped with a confocal microscope and liquid-nitrogen cooled charge-coupled device (CCD) detector.

## 2.10. Electrochemical Impedance Spectroscopy

Electrochemical techniques involve the application of an electric perturbation (current, potential) to an electric circuit, causing the appearance of a response. Electrochemical Impedance Spectroscopy (EIS) is an electrochemical technique which involves the study of the system response to the application of a periodic small amplitude AC signal. Generally the measurements in EIS spectroscopy are carried out at different AC (alternative current) frequencies and therefore the name impedance spectroscopy has been adopted [28]. Being at the steady state and the investigations can be carried out for a long time and over a large range of potentials highly accurate results can be obtained by using this technique. This technique can be used to obtain information about the interface, its structure and the electrochemical reactions taking place between the interfaces.

Under the the application of an arbitrary (but known) potential  $E(t)$ , the resistance ( $R$ ) can be defined as the tendency of a circuit to oppose the current flow,  $i(t)$ , in direct current (DC) conditions:

$$\text{DC conditions: } R = E(t) / i(t) \quad (2.16)$$

On the contrary, impedance ( $Z$ ) measures how strongly a circuit opposes to current flow in alternating current (AC) conditions:

$$\text{AC conditions: } E(t) = Z i(t) \quad (2.17)$$

Therefore both resistance and impedance are measured in Ohm ( $\Omega$ ).

The applied potential and the current intensity have typical sine wave flow:

$$E(t) = E_0 \sin(\omega t) \quad (2.18)$$

$$i(t) = i_0 \sin(\omega t + \phi) \quad (2.19)$$

where  $\omega$  stands for the frequency and  $\phi$  for the phase angle.

According to the Euler relationship applied to complex numbers, both previous equations may be described by:

$$E = E_0 \exp(j\omega t) \quad (2.20)$$

$$i = i_0 \exp[j(\omega t + \phi)] \quad (2.21)$$

As shown in relation 1.17,  $Z$  is the ratio between the applied potential and the current intensity; applying the complex number property, it can be described as:

$$Z(\omega) = E_0 \exp(j\omega t) / i_0 \exp[j(\omega t + \phi)] = |Z| \exp(j\phi) = |Z| (\cos \phi + j \sin \phi) \quad (2.22)$$

$$|Z| \cos \phi + |Z| j \sin \phi = Z' - jZ'' = \text{Re}(Z) - j\text{Im}(Z) \quad (2.23)$$

Thus, impedance is defined as the transfer function (TF) between  $E(t)$  and  $i(t)$  at any frequencies  $\omega$  and is a complex number containing phase information as well as magnitude.

EIS is based on the transfer function principle, the system is perturbed by a sine wave input signal and the output response produced by the system is recorded. When the input is the current intensity and the output is a potential, the TF is simply the impedance  $Z$ .

Electrochemical impedance spectroscopy (EIS) is a widely available tool to investigate electronic and ionic processes in quantum dot-sensitized solar cells (QDSSCs). A theoretical model has been explained, to understand the frequency response of the device. The high-frequency feature is ascribed to the charge transfer at the counter electrode while the response in the intermediate-frequency region is associated with the electron transport in the mesoscopic  $\text{TiO}_2$  film and the back reaction at the  $\text{TiO}_2$ /electrolyte interface. The low-frequency region reflects the diffusion in the electrolyte. Using an appropriate equivalent circuit, the charge transfer resistance at the counter electrode/electrolyte interface can be obtained from EIS.

In the present thesis work electrochemical impedance spectra (EIS) of the counter electrode samples were obtained by using Autolab PGSTAT 302N Autolab Potentiostat/Galvanostat coupled with Nova 1.9 software with symmetric cell configuration in presence of 0.5 M  $\text{Na}_2\text{S}$  solution containing KCl as the electrolyte. An AC voltage of 10 mV superimposed over a dc potential of 0.0 V was applied to the electrodes and Nyquist plots were obtained over a frequency range of  $10^6$  Hz to  $10^{-3}$  Hz.

### **2.11. Solar simulator**

Solar simulator which is nothing but an artificial sun is a device that provides illumination approximating natural sunlight and the main purpose of the solar simulator is to provide controllable indoor conditions for the testing of solar cells, sunscreens and plastics and other materials and devices.

Solar simulators can be classified into three broad categories such as continuous, flashed, and pulsed based on the type of illumination. Among these continuous illumination is familiar. This type of solar simulators is used mainly for low intensity testing, from less than 1 sun up to several suns. The term 1 sun is typically defined as the nominal full sunlight intensity on a bright clear day on Earth, which measures  $1000 \text{ W/m}^2$ . The light source for this type of solar simulators is generally a combination of several different lamp types (i.e. Xenon and multiple halogen lamps) to extend the spectrum far into the infrared.

**Xenon arc lamp:** This is the most common type of lamp both for continuous and flashed solar simulators. These lamps offer high intensities and an unfiltered spectrum which matches reasonably well to sunlight.

**Metal Halide arc lamp:** Primarily developed for use in film and television lighting where a high temporal stability and daylight color match are required, metal halide arc lamps are also used in solar simulation.

**QTH:** Quartz tungsten halogen lamps offer spectra which very closely match black body radiation, although typically with a lower color temperature than the sun.

**LED:** Light-emitting diodes have recently been used in research laboratories to construct solar simulators, and may offer promise in the future for energy-efficient production of spectrally tailored artificial sunlight.

In the present thesis work current versus voltage characteristics of the fabricated solar cells were measured on a Newport Oriel 3A solar simulator with a digital source meter (Keithley model 2420). A 450 W Xenon arc lamp was used as the light source which provides the light intensity of  $100 \text{ mW cm}^{-2}$  of air mass (AM) 1.5 illumination and the spatial uniformity of irradiance was confirmed by calibrating with a  $2 \text{ cm} \times 2 \text{ cm}$  Si reference cell (NREL). Before collection of I-V data, each electrode was allowed to reach equilibrium at open-circuit.

## References

- [1] S. T. Aruna and K. C. Patil. Synthesis and properties of nanosize titania. *J. Mater. Synth. Process* 4, (1996) 175-179.
- [2] K. Rajeshwar. Electrosynthesized thin films of group II–VI compound semiconductors, alloys and superstructures. *Adv. Mater.* 4, (1992) 23-29.
- [3] S. R. Jain, K. C. Adiga, and V. R. P. Verneker. A new approach to thermochemical calculations of condensed fuel-oxidizer mixtures. *Combust. Flame.* 40, (1981) 71-79.
- [4] D. Liu, Q. Wang, H.L.M. Chang and H. Chen. Variant structure in metal-organic-chemical-vapor-deposition-derived SnO<sub>2</sub> thin films on sapphire (0001). *J. Mater. Res.* 10, (1995) 1516-1522.
- [5] W. I. F. David, K. Shankland, L. B. Mc Cusker and C. Baerlocher. *Structure Determination from Powder Diffraction Data*. Oxford Science Publications, 1992.
- [6] D. L. Bish, J. E. Post and J. E. Modern. *Powder Diffraction* published by The Mineralogical Society of America, 1989.
- [7] L. V. Azaroff and M. J. Buerger. *The Powder Method in X-ray Crystallography*. McGraw Hill Book Company, Inc, 1975.
- [8] M. J. Buerger, *X-ray Crystallography*. J. Wiley, New York, 1942, 20.
- [9] L. Smart and E. A. Moore. *Solid State Chemistry: an introduction*. CRC Press: United States of America, 2005.
- [10] H. P. Klug and L. E. Alexander. *X-ray Diffraction Procedures for Polycrystalline and Amorphous Materials*. 2nd edition. Wiley, New York, 1974, 687.
- [11] H. Seyama, M. Soma and B.K.G. Theng. *X-ray Photoelectron Spectroscopy*. Handbook of Clay Science. Elsevier: Amsterdam, 2006.
- [12] B. J. Clark, T. Frost, and M. A. Russell. *UV spectroscopy: techniques, instrumentation, data handling*. Chapman & Hall, London, UK, 1993.
- [13] H. H. Perkampus. *UV-VIS spectroscopy and its applications*, Springer-Verlag, Berlin, Germany, 1992.
- [14] C. K. Mann, T. J. Vickers and W. M. Gulick. *Instrumental analysis*. Harper & Row, New York, USA, 1974.
- [15] X. Michalet, F. Pinaud, T. D. Lacoste, M. Dahan, M. P. Bruchez, A. P. Alivisatos and S. Weiss. Properties of fluorescent semiconductor nanocrystals and their application to biological labeling. *Single Molecules* 2, (2001) 261-276.
- [16] A. D. Yoffe. Semiconductor quantum dots and related systems: Electronic, optical, luminescence and related properties of low dimensional systems. *Advances in Physics* 50, (2001) 1-208.

- [17] A. P. Alivisatos. Semiconductor Clusters, Nanocrystals, and Quantum Dots. *Science* 271, (1996) 933-937.
- [18] J. H. Park, J. Y. Kim, B. D. Chin, Y. C. Kim, J. K. Kim, and O. O. Park. White emission from polymer/quantum dot ternary nanocomposites by incomplete energy transfer. *Nanotechnol.* 15, (2004) 1217-1220.
- [19] N. Venkatram, D. N. Rao, and M. A. Akundi. Nonlinear absorption, scattering and optical limiting studies of CdS nanoparticles. *Optics Express* 13, (2005) 867- 872.
- [20] J. G. Calvert and J. N. Pitts Jr. *Photochemistry*. Wiley, New York, 1966, 19.
- [21] S. Brunauer, P. H. Emmet and E. Teller. Adsorption of Gases in Multimolecular Layers. *J. Am. Chem. Soc.* 60, (1938) 309-319.
- [22] D. B. Williams and C. B. Carter. *Transmission Electron Microscopy*. Springer, New York, 1, 1996.
- [23] D. A. Skoog and J. J. Leary. *Principles of Instrumental Analysis*. 4th ed. Saunders College Publishing. Orlando, USA, 1992.
- [24] T. H. Gfroerer. in *Encyclopedia of Analytical Chemistry*. edited by R. A. Meyers. John Wiley & Sons Ltd., Chichester, UK, 17, (2000) 9209-9231.
- [25] L. H. Qu and X. G. Peng. *J. Am. Chem. Soc.* 124, (2002) 2049-2055.
- [26] C. K. Mann, T. J. Vickers and W. M. Gulick. *Instrumental analysis*. Harper & Row, New York, USA, 1974.
- [27] B.M. Weckhuysen and R.A. Schoonheydt. Recent progress in diffuse reflectance spectroscopy of supported metal oxide catalysts. *Catal. Today.* 49, (1999) 441-451.
- [28] A. Lasia. *Electrochemical Impedance Spectroscopy and its Applications, Modern Aspects of Electrochemistry*. B.E. Conway, J. Bockris and R.E. White, Eds.. Kluwer Academic/Plenum Publishers. New York, 1999, 32, 143.



# Chapter 3 -Section I

## Optimization of titanyl nitrate synthesis

### 3.1.1. Introduction

Development of heterogeneous photocatalysts with desirable activities, especially visible light activity, for environmental applications such as air and water purification has become a key research in recent years [1-8]. Among the various semiconductor photocatalysts, titania has been proved to be an evergreen photocatalyst due to its chemical and biological inertness, strong oxidizing power, cost effectiveness, and long-term stability against photochemical corrosion [9]. Since the discovery of phenomenon of photocatalytic splitting of water on  $\text{TiO}_2$  electrode under ultraviolet (UV) light by Fujishima, many promising applications in various areas, ranging from photocatalysis, photovoltaics, photo/electrochromics to sensors have been reported [10-15].

A large number of methods such as electrochemical [16], ionized cluster beam deposition [17], aerosol process [18], homogeneous precipitation at low temperatures [HPPLT] [19], sol-gel [20], mechano chemical [21], hydrothermal [22] and combustion synthesis [23-25] have been tested for the preparation of titania. Among these methods, combustion based techniques are reported to be effective and energy saving for the synthesis of a variety of advanced materials [26, 27]. Among the various approaches of combustion synthesis, solution combustion method has specific advantages like mixing of reactants at molecular level, short duration of reaction that allows the formation of nano scaled high crystalline materials with high surface area without the need of further calcination [28].

In a typical solution combustion synthesis, a self-sustained reaction between metal precursors (preferably nitrates) and fuels lead to the formation of desired products. The nitrate precursors are reported to react vigorously with the fuel to provide the high temperatures required for the synthesis. Combustion synthesis has been reported to be an efficient approach for the development of a wide variety of materials like oxides, carbides, nitrides, multi oxides, metals, noble metal ionic catalysts and alloys [29]. For the synthesis of titania ( $\text{TiO}_2$ ) various fuels like urea, glycine, hexamine etc. were tested and the resulting catalyst showed good performance during the degradation of pollutants like dyes, phenols, benzene derivatives, toxic metal ions and noxious gases. [30-38]. Cheng et al studied the effect of preparation conditions on the photocatalytic properties of combustion synthesized  $\text{TiO}_2$  [39]. All the aforementioned reports are based on the effect of fuel and preparation

conditions on the combustion synthesis of  $\text{TiO}_2$ . But there was no report on optimization of oxidant (titanyl nitrate) preparation.

In the present chapter, the effect of synthesis of oxidant (titanyl nitrate) on the physico-chemical and photocatalytic properties of combustion synthesized  $\text{TiO}_2$  were studied. Titanyl nitrate was synthesized in four different ways from Ti (IV) iso-propoxide and  $\text{TiO}_2$  catalysts were prepared by keeping the fuel (glycine) unchanged. The visible light photocatalytic activity of the  $\text{TiO}_2$  catalysts was tested under direct sunlight by taking a textile dye (methylene blue) as a model dye.

### **3.1.2. Experimental**

#### **3.1.2.1. Synthesis**

The oxidant titanyl nitrate was prepared by slow hydrolysis followed by nitration of Ti(IV) iso-propoxide in four different ways. The first method was based on a slight modification of a reported process [40]. In a typical synthesis solution A was prepared in a quartz beaker by mixing 2 ml Ti(IV) iso-propoxide with 9 ml isopropyl alcohol under inert atmosphere. This solution was placed on a constant temperature bath at 273 K. Then solution B was prepared by mixing 0.75 ml de-ionized water and 9 ml isopropyl alcohol. Afterwards solution B was added drop wise to solution A under vigorous stirring at 273 K and the stirring was continued for 24 h. Then nitration was carried out by adding 4.7 ml of 37 wt % nitric acid to above titanyl hydroxide turbid solution to produce titanyl nitrate solution. This solution was then mixed with glycine in such a way that the fuel / oxidant ratio is 1 (9 moles of titanyl nitrate and 10 moles of glycine). After mixing it was introduced into a preheated muffle furnace at 623 K. In 5 min a light brown  $\text{TiO}_2$  powder was obtained after smoky type combustion without the appearance of flame. This was labelled as G- $\text{TiO}_2$ -I.

In the second method, titanyl nitrate was prepared by taking stoichiometric amounts of reagents. In a typical synthesis, 10 ml Ti(IV) iso-propoxide was mixed with 10 ml of isopropyl alcohol under inert conditions. To this 1.8 ml deionized water was added drop wise and vigorously stirred for 24 h to ensure complete hydrolysis of Ti(IV) iso-propoxide. To this 3.0 ml of 1:1  $\text{HNO}_3$  was added, the obtained precipitate was oven dried and stored for further synthesis of  $\text{TiO}_2$ . A combustion mixture was prepared by mixing this powder with glycine according to fuel / oxidant ratio 1 in a quartz beaker. After thorough mixing, the resulting solution was heated on a hot plate until viscous mass was obtained. Afterwards this viscous mass was kept in a preheated furnace kept at 623 K for 5 min and the obtained brown colored powder was labeled as G- $\text{TiO}_2$ -II.

In the third approach, titanyl nitrate was prepared by slow hydrolysis of Ti(IV) isopropoxide followed by nitration with excess of nitric acid. For this purpose, 10 ml of Ti(IV) isopropoxide was mixed with 20 ml of isopropyl alcohol under inert conditions. To this 1.8 ml deionized water was added drop wise under vigorous stirring for 1 h at 273K, followed by dissolving the obtained precipitate in excess of 1:1 nitric acid. Evaporation to dryness on a hot plate resulted titanyl nitrate, which was stored for further synthesis of TiO<sub>2</sub>. Titanyl nitrate was mixed with glycine by maintaining fuel/oxidant ratio 1. After evaporation on a hot plate, the obtained viscous mass was placed in a preheated furnace maintained at 623 K. The resulting brown colored powder was labeled as G-TiO<sub>2</sub>-III.

In the fourth approach, titanyl nitrate was prepared by acid hydrolysis of Ti (IV) isopropoxide. In a typical synthesis, 4.7 ml of Ti (IV) isopropoxide was added to 10 ml of isopropyl alcohol under inert atmosphere. Simultaneous hydrolysis and nitration was carried out by adding 1.4 ml of 1:1 HNO<sub>3</sub> under vigorous stirring under ice cold conditions. This was mixed with glycine by maintaining fuel/oxidant ratio 1 and was introduced into a preheated muffle furnace at 623 K for 5 min and the resulted light brown colored sample was labeled as G-TiO<sub>2</sub>-IV. In all the four methods the pH of the viscous mass was tested and it was found to be close to 1. To summarize the basis of the different approaches: first method was a slight modification of the reported method, whereas for the second method, stoichiometric amounts of the reagents were used. In the third method, excess of nitric acid was used for nitration, as during the second method the obtained titanylhydroxide precipitate did not dissolve completely in stoichiometric amount of nitric acid, whereas, the fourth method proceeds via simultaneous hydrolysis and nitration.

### **3.1.2.2. Characterization**

Powder X-ray diffraction (PXRD) data of combustion synthesized TiO<sub>2</sub> samples were recorded on powder X-ray diffractometer in order to confirm the phase formation and crystallite size. The average crystallite size was calculated by using the Scherrer equation with the full width at half maxima (FWHM) data. In order to confirm the particle size, transmission electron micrographs (TEM) of G-TiO<sub>2</sub>-III was recorded on a TEM instrument.

Surface area of the TiO<sub>2</sub> samples was estimated by using Quantachrome autosorb automated gas sorption system (NOVA 2200 e). The samples were degassed at 573 K for 3 h and Brunauer–Emmett–Teller (BET) equation was used to calculate the surface area from the adsorption isotherm. Diffused reflectance UV-vis spectra of the samples were measured to determine the band gap energy of the photocatalysts. X-ray photoelectron spectroscopy (XPS) studies were carried out in order to determine the C and N doping into the TiO<sub>2</sub> matrix.

### 3.1.2.3. Photocatalytic activity measurements

Photocatalytic studies were performed under the direct Sunlight by taking methylene blue as the model dye. All the experiments were carried out by taking 100 ml of the dye solution in a 250 ml beaker and catalyst was added. No significant dye degradation was observed without catalyst in Sunlight and with catalyst in dark. Before exposure to sunlight, dye solutions along with catalyst were placed in dark for 2 h in order to facilitate adsorption-desorption equilibrium. The study was completely performed under the direct sunlight between 11 am to 1 pm and the average solar Intensity was 500-600 W/m<sup>2</sup>, which was measured with a Newport Optical Power meter/Energy meter (Model 842.PE). For every 15 min small aliquots were collected from the experimental solutions, centrifuged for 5 min at 2000 rpm in order to separate the catalyst particles and the degradation of dye was monitored by using UV-Vis spectrophotometer.

### 3.1.3. Results and discussion

#### 3.1.3.1. Powder X-ray diffraction (PXRD)

The PXRD patterns of combustion synthesized catalysts (Fig. 3.1.1) showed the effect of titanyl nitrate synthesis on the crystal structures and crystallite size for various TiO<sub>2</sub> samples. The four peaks centered at 25.3, 37.8, 48.1 and 75.2° was attributed to the (101), (004), (200) and (215) planes of the anatase TiO<sub>2</sub>, respectively (JCPDS card file no. 89-4921). The crystallite sizes calculated from the full width at half maxima (FWHM) of the most intense diffraction peak by using Scherrer formula was given in Table 1 along with the other physico-chemical properties.

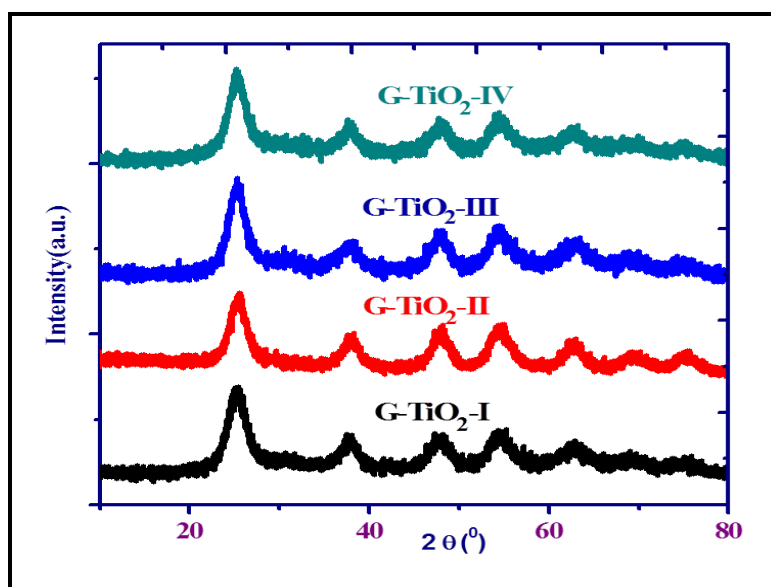


**Fig. 3.1.1.** Powder X-ray diffraction patterns of combustion synthesized TiO<sub>2</sub> samples

### 3.1.3.2. Transmission electron microscopy (TEM)

As shown in figure 3.1.2(a), the crystallites of G-TiO<sub>2</sub>-III were close to 6 nm, which is in good agreement with the XRD results. The inset of figure 3.1.2(a) represents the selected area diffraction pattern (SAED) that confirms the formation of pure anatase phase. The d-spacing values calculated from this SAED pattern are found to be 3.5, 2.4, 1.8, 1.6 Å which are indicative of the (101), (004), (200) and (215) planes of the anatase phase. Figure 3.1.2(b) shows the HRTEM image of G-TiO<sub>2</sub>-III, which further confirmed the anatase phase and crystalline nature of the catalyst.

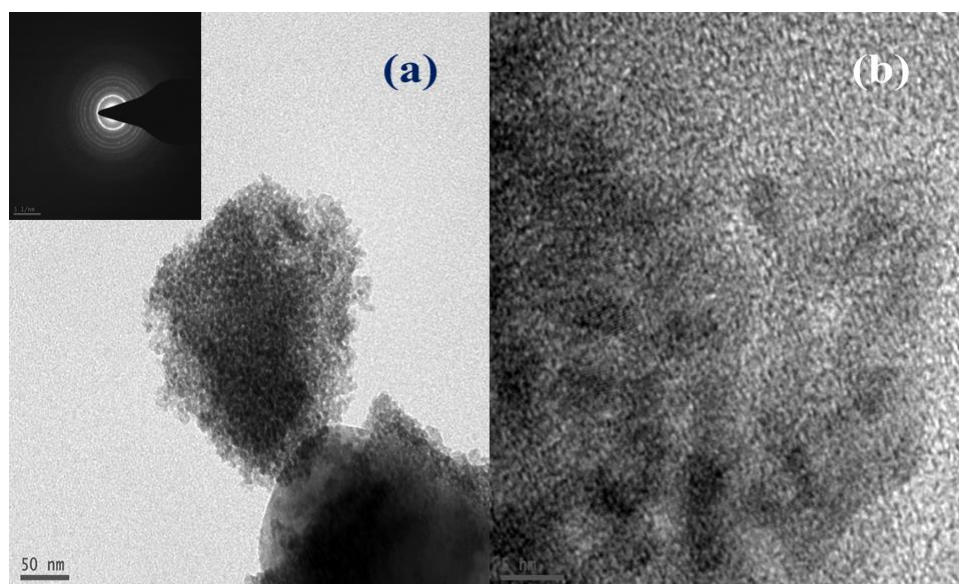


**Fig. 3.1.2.** (a) Transmission electron micrograph of G-TiO<sub>2</sub>-III with selected area diffraction pattern shown in the inset (b) HRTEM image of G-TiO<sub>2</sub>-III

### 3.1.3.3. UV- Visible spectroscopy

It is well-known that the band gap of pure titania anatase phase is around 3.2 eV and doping with various species may change this band gap [41]. The change in electronic property, especially the decrease in optical band gap due to *in-situ* carbon and nitrogen doping was clearly observed in UV-Vis absorption spectra (Fig. 3.1.3). The band gap of the titania samples was calculated by using this UV-Vis DRS spectra transformed to Kubelkamunk mode with the equation,  $E \text{ (eV)} = hc/\lambda$  where E is the band gap energy (eV), h is Planck's constant, c is the velocity of light (m/s) and  $\lambda$  is the wavelength (nm) corresponding to the absorption edge. The G-TiO<sub>2</sub>-I had the band gap of 2.8 eV whereas, G-TiO<sub>2</sub>-II showed absorption edge at 496 nm that corresponds to the band gap of 2.5 eV. The G-TiO<sub>2</sub>-III has two absorption edges at 442 nm and 576 nm, which corresponds to the band gap energies of 2.8 and 2.15 eV respectively, whereas, G-TiO<sub>2</sub>-IV showed an absorption

edge at 420 nm corresponding to the band gap energy of 3.0 eV and also has a considerable absorption up to 600 nm. The weak red shift in the case of G-TiO<sub>2</sub>-IV may be attributed due to the simultaneous hydrolysis and nitration of Ti(IV) iso-propoxide during the synthesis of titanyl nitrate, which may leave some unreacted Ti(IV) iso-propoxide due to the insufficient hydrolysis, which results less efficient combustion compared to the remaining cases and is responsible for the lesser C and N doping and hence the weak red shift.

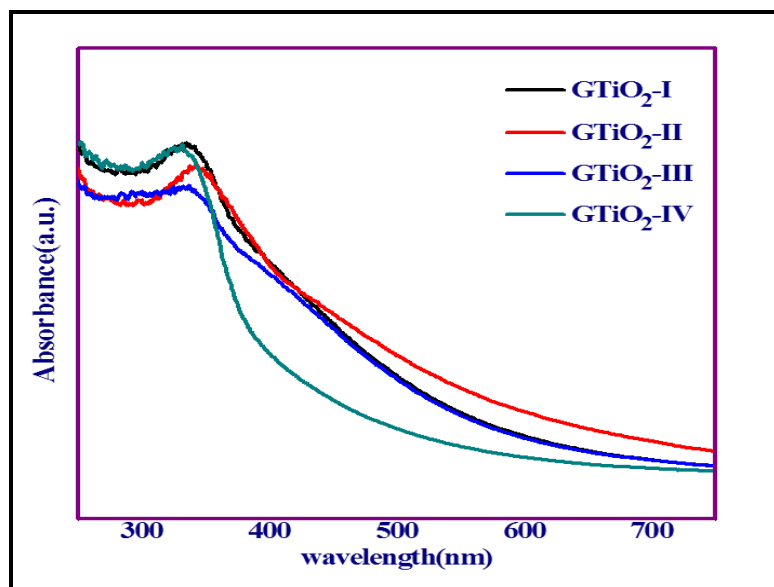


**Fig. 3.1.3.** Diffused reflectance UV-vis spectra of combustion synthesized TiO<sub>2</sub> samples

#### 3.1.3.4. N<sub>2</sub> adsorption

The BET surface area of the synthesized TiO<sub>2</sub> samples was given in Table 3.1.1. The high surface area of G-TiO<sub>2</sub>-III sample may be attributed to the excess of nitric acid used during the titanyl nitrate synthesis, which may lead to evolution of more gaseous products during the synthesis. This in turn may prevent the aggregation of particles leading to the high surface area TiO<sub>2</sub>. The lowest surface area of G-TiO<sub>2</sub>-IV sample may be due to the improper hydrolysis of Ti precursor.

#### 3.1.3.5. X-ray photoelectron spectroscopy (XPS)

XPS spectra of various samples for C 1s, N 1s, Ti 2p and O 2p regions with binding energies at  $458.9 \pm 0.2$ ,  $530.2 \pm 0.2$ ,  $400 \pm 0.3$ ,  $285 \pm 0.2$  eV confirms Ti ( $2p_{3/2}$ ), O (1s), N (1s), C (1s) core level electrons of the TiO<sub>2</sub> samples prepared by four different approaches. The Ti (2p) core level spectra of the four catalysts were given in Fig. 3.1.4. which confirmed Ti ( $2p_{3/2}$ ) and Ti ( $2p_{1/2}$ ) characteristic peaks at binding energies  $458.9 \pm 0.2$  and  $464.5 \pm 0.2$  eV.

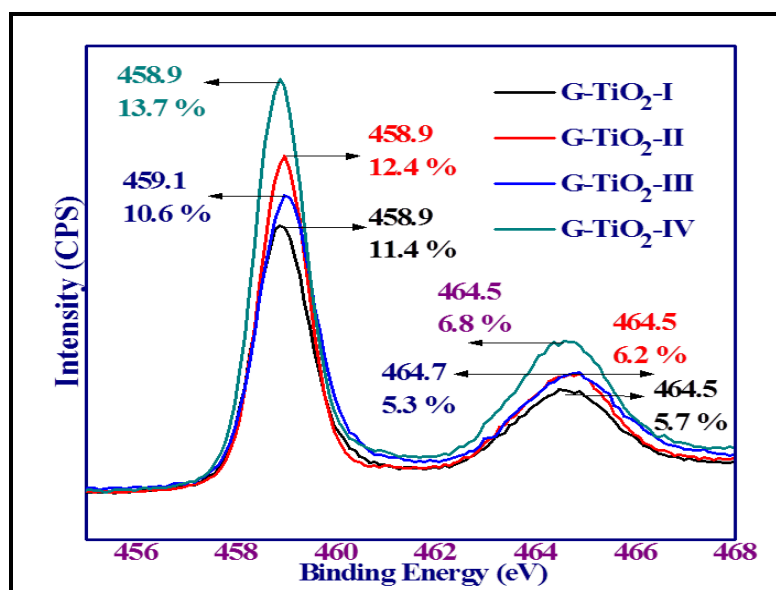


**Fig. 3.1.4.** XPS spectra of Ti 2p core levels of G-TiO<sub>2</sub>-I, G-TiO<sub>2</sub>-II, G-TiO<sub>2</sub>-III and G-TiO<sub>2</sub>-IV

Figure 3.1.5 shows the oxygen 1s spectra of G-TiO<sub>2</sub>-I, G-TiO<sub>2</sub>-II, G-TiO<sub>2</sub>-III and G-TiO<sub>2</sub>-IV. All the catalysts showed a peak at 530 ± 0.2 eV due to the O<sup>2-</sup> ion. Figure 3.1.6 shows peaks at 285 ± 0.2, 286 ± 0.2, 287 ± 0.2, 288.5 ± 0.2, and 289.2 ± 0.2 eV in the C (1s) spectra of the four catalysts.

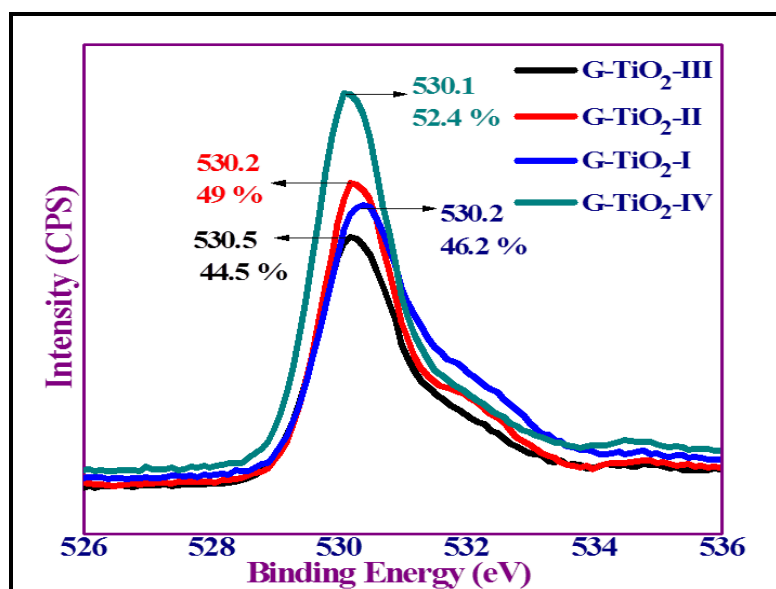


**Fig. 3.1.5.** XPS spectra of O 1s core levels of G-TiO<sub>2</sub>-I, G-TiO<sub>2</sub>-II, G-TiO<sub>2</sub>-III and G-TiO<sub>2</sub>-IV

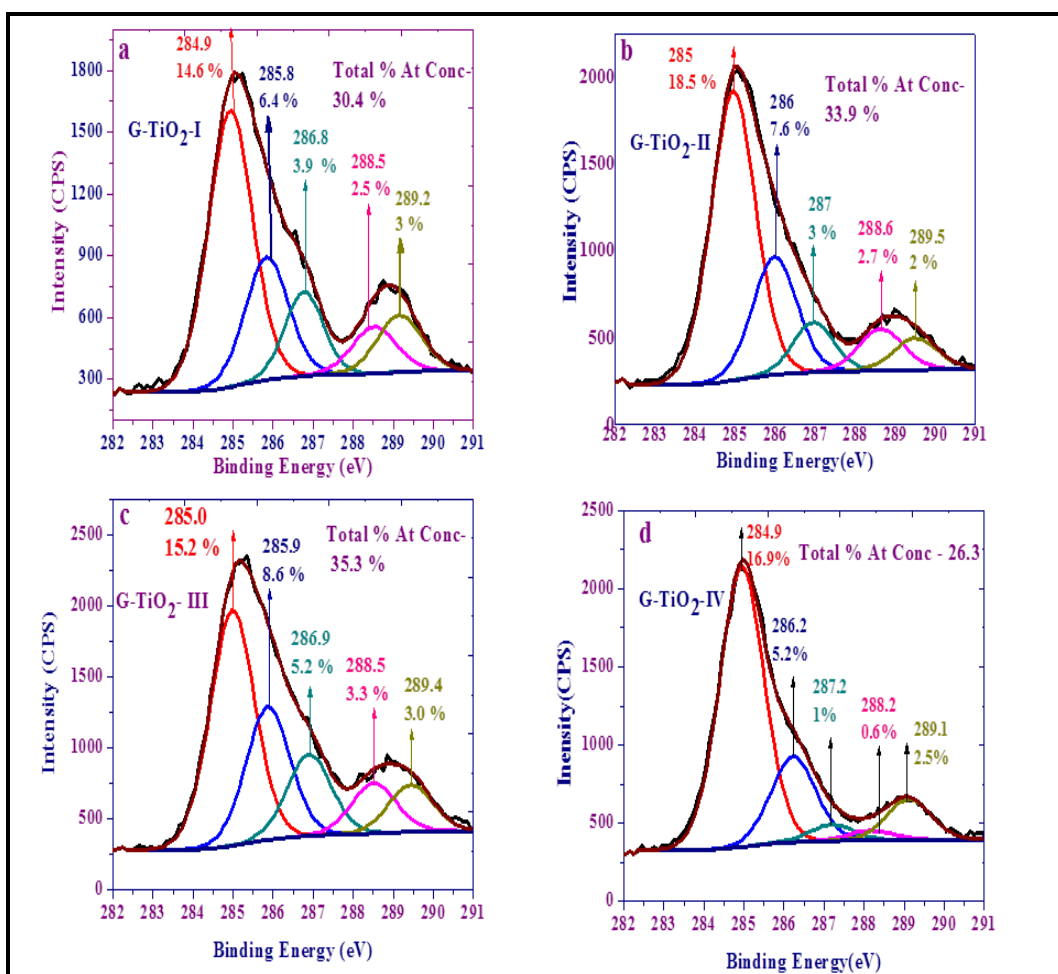


**Fig. 3.1.6.** XPS spectra of C 1s core levels of (a) G-TiO<sub>2</sub>-I (b) G-TiO<sub>2</sub>-II (c) G-TiO<sub>2</sub>-III and (d) G-TiO<sub>2</sub>-IV

The first one corresponds to the aliphatic carbon whereas the other four peaks indicate four different kinds of carbonate linkages. The absence of peak at < 285 eV indicates the absence of metal- carbon linkage. Fig.3.1.7 shows the N (1s) core level spectra of the prepared catalysts. The peak at 400 ±0.2 eV indicates chemisorbed  $\gamma$ -N<sub>2</sub> [42]. The relative intensities indicate the amount of molecular chemisorbed  $\gamma$ -N<sub>2</sub>.



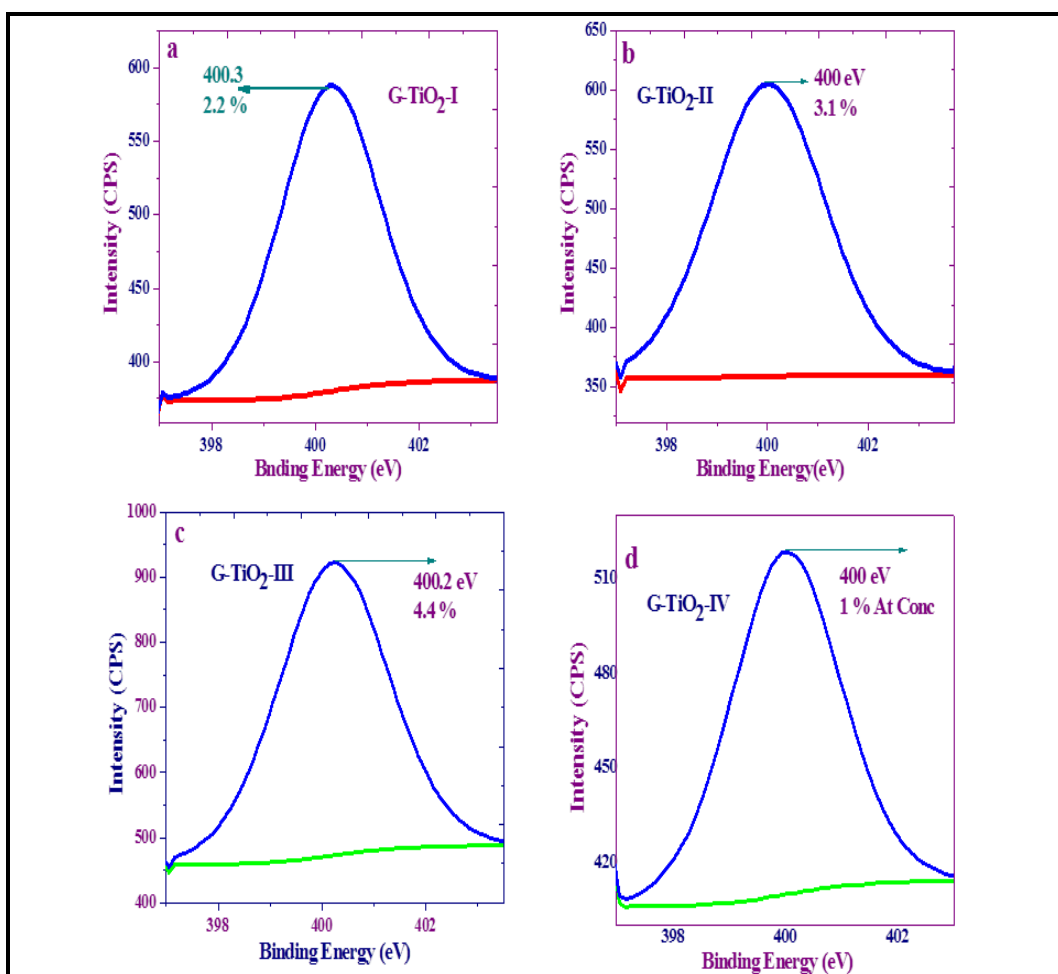


**Fig. 3.1.7.** XPS spectra of N 1s core levels of (a) G-TiO<sub>2</sub>-I (b) G-TiO<sub>2</sub>-II (c) G-TiO<sub>2</sub>-III and (d) G-TiO<sub>2</sub>-IV

**Table 3.1.1.** Physico-chemical characteristics of combustion synthesized TiO<sub>2</sub> samples.

S. No	Sample Name	Crystallite size (nm)	Band Gap (eV)	Surface area (m <sup>2</sup> /g)
1	G-TiO <sub>2</sub> -I	10	2.8	155
2	G-TiO <sub>2</sub> -II	6	2.5	220
3	G-TiO <sub>2</sub> -III	6	2.8, 2.15	250
4	G-TiO <sub>2</sub> -IV	14	3.0	85
5	Evonik P-25	32	3.2	45

### 3.1.3.6. Photocatalytic activity studies under direct sunlight

The visible light photocatalytic activity of the catalysts was tested under direct Sunlight and the results were compared with the commercial Evonik P-25. The percentage of adsorption in the dark was found to be 28, 36, 40, 10 and 2 % for G-TiO<sub>2</sub>-I, G-TiO<sub>2</sub>-II, G-

TiO<sub>2</sub>-III, G-TiO<sub>2</sub>-IV and Evonik P-25, respectively. This adsorption percentage was in agreement with the surface area. All the catalysts showed better activity than Evonik P-25 and among the prepared TiO<sub>2</sub> catalysts, G-TiO<sub>2</sub>-III showed the best photocatalytic activity, whereas, G-TiO<sub>2</sub>-IV showed the least photocatalytic activity and the activity of the catalysts followed the order G-TiO<sub>2</sub>-III > G-TiO<sub>2</sub>-I > G-TiO<sub>2</sub>-II > G-TiO<sub>2</sub>-IV > Evonik P-25. Figure 3.1.8 shows the effect of catalysts (1 gm/l of each catalyst) on the degradation of MB with an initial concentration of 10 mg/l with time. These plots show a decrease of concentration with time and obey first order kinetics. The comparison of initial rates of various catalysts has been shown in the inset of Fig. 3.1.8 which indicated that all the catalysts have better initial rates than Evonik P-25 and among them G-TiO<sub>2</sub>-III showed the best activity.

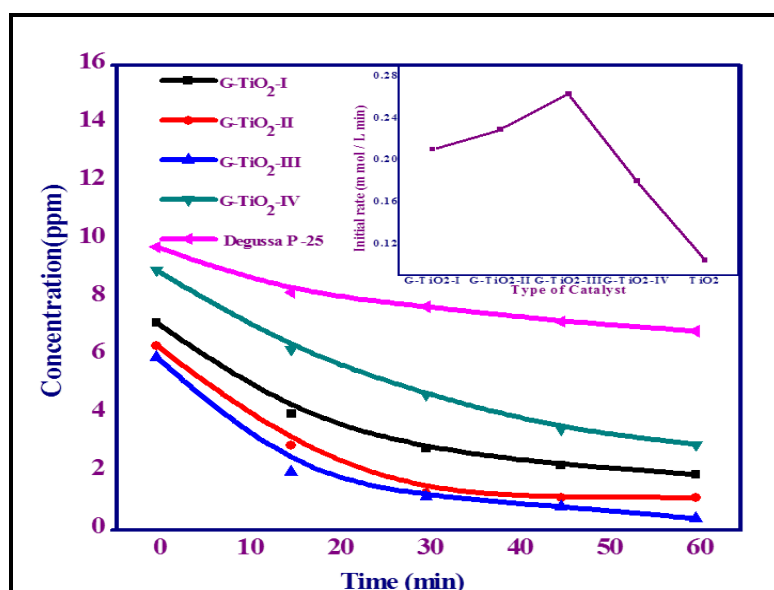


**Fig. 3.1.8.** Photocatalytic degradation of methylene blue concentration with time for all the combustion synthesized catalysts along with Evonik P-25. (inset shows the variation of initial rates with type of the catalyst) ( $C_0 = 10$  mg/l and catalyst amount = 1 gm /l)

### 3.1.3.4. Conclusions

Optimization of titanyl nitrate synthesis for the combustion synthesis of titania with glycine fuel was investigated. It has been observed that titanyl nitrate prepared by slow hydrolysis of Ti (IV) iso-propoxide followed by nitration with excess of nitric acid is found to produce TiO<sub>2</sub> with best characteristics like low band gap (2.8 and 2.1 eV), nano crystalline size and high surface area (250 m<sup>2</sup>/g), which are the prerequisites for the visible light photocatalytic activity. On the other hand, the synthesis involving acid hydrolysis of Ti (IV) iso-propoxide by 1:1 HNO<sub>3</sub> solution is found to have large band gap (3.0 eV) and low surface area (85 m<sup>2</sup>/g). All the catalysts showed better photocatalytic activity than Evonik P-

25 under the direct sun light during the degradation of a model textile dye (MB) and the activity followed the order G-TiO<sub>2</sub>-III > G-TiO<sub>2</sub>-I > G-TiO<sub>2</sub>-II > G-TiO<sub>2</sub>-IV > Evonik P-25.

## Chapter 3-Section II

# Optimization of fuel for the combustion synthesis of C, N doped TiO<sub>2</sub>

### 3.2.1. Introduction

As an alternative strategy, solution combustion synthesis has the unique advantages like low energy requirements due to its self-sustainable exothermic reactions, short reaction time, *in-situ* doping into the oxide matrix and production of high surface area materials [43-46]. The previous section dealt with optimization of titanyl nitrate. In the same context, fuel has a great influence on the properties of combustion synthesized materials. In several cases, the phase transformation and metastable phase formation were found to be aided by the amount and nature of the fuel [47]. It has been well accepted that nitrogen containing compounds i.e. compounds containing N–N bonds were widely used as fuels for combustion synthesis due to their tendency to act as chelating ligands, which may facilitate the formation of complexes with the metal ions [48]. Although a variety of studies have been reported on the combustion synthesis of nanomaterials by employing a single fuel like glycine, urea, oxalyl dihydrazide and hexamine, few studies have been done by using combination of fuels [49-53]. But to the best of our knowledge there was no report that correlated the evolution of gases from the corresponding fuel during the combustion synthesis to its photocatalytic activity.

During the present investigation, the objective was to find the best fuel for the combustion synthesis of TiO<sub>2</sub> and to evaluate the photocatalytic activity. For this purpose, various fuels were tested for the synthesis of C and N doped anatase by using titanyl nitrate as the oxidant. The observed physico-chemical properties have been correlated in terms of number of moles of gases evolved during combustion. The efficient visible light photocatalytic activity of the best TiO<sub>2</sub> sample was asserted from the reduction of Cr (VI) and oxidation of methylene blue from aqueous solutions.

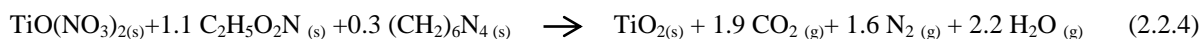
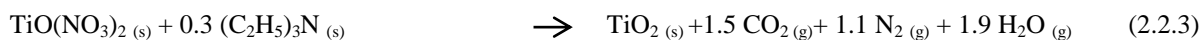
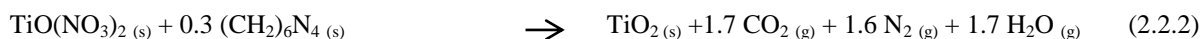
### 3.2.2. Experimental section

#### 3.2.2.1. Synthesis of C and N- co doped TiO<sub>2</sub> catalysts by organic fuels

Titanyl nitrate was used as oxidant in the present solution combustion synthesis of TiO<sub>2</sub>, which was prepared by slow hydrolysis of Ti(IV) iso-propoxide followed by nitration with excess of nitric acid as discussed in the previous study [54]. A primary amine (triethyl

amine) a tetra amine (hexamethylene tetramine) and an amino acid (glycine) were taken as model fuels in order to find out the best fuel for titania. Fuel to oxidant ratio was calculated according to propellant theory and it was maintained at 1 in all the cases. In a typical combustion synthesis 1 mole of titanyl nitrate in each case was mixed with 1.1, 0.28, 0.26 moles of glycine, hexamine and triethyl amine respectively to form the combustion mixture with minimum amount of water. Thus obtained combustion mixtures were preheated at around 80 °C to get dehydrated gels that were introduced into a muffle furnace preheated to 350 °C to get the final product within 5 min after a smoky type of combustion. The obtained products were grounded to get fine powders, which were labeled as G-TiO<sub>2</sub>, H-TiO<sub>2</sub>, and TEA-TiO<sub>2</sub> respectively. Combustion synthesis of TiO<sub>2</sub> with mixture of fuels was also performed in the same manner by taking glycine and hexamine in 1:1 ratio and labeled as GH-TiO<sub>2</sub>. In the same way another mixed fueled TiO<sub>2</sub> by using glycine and triethylamine was prepared and labeled as TEAG-TiO<sub>2</sub>.

The stoichiometric equations are as follows:



From the above stoichiometric equations it can be concluded that the use of glycine as a fuel evolves highest number of moles of gases.

### 3.2.2.2. Characterization

Powder X-ray diffraction data of combustion synthesized TiO<sub>2</sub> samples were collected in order to find out the phase and crystallite size. High-resolution transmission electron microscopy (HRTEM) images of the most active G-TiO<sub>2</sub> among the combustion synthesized catalysts was recorded using the TEM instrument in order to further confirm the phase and crystallite size. Brunauer–Emmett–Teller (BET) sorptometry measurements of the combustion synthesized catalysts have been carried out to estimate the surface area of the samples. UV-Vis reflectance spectra of samples were measured for the dry pressed disk samples between 200 and 800 nm range in order to know the absorption of samples in the visible region and thereby to calculate the band gap energy. X-ray photoelectron

spectroscopy (XPS) data of the combustion synthesized catalysts were collected in order to confirm the C and N doping in to the TiO<sub>2</sub> matrix.

The thermo-gravimetric analysis of the combustion synthesized catalysts was recorded on TG/DTA, TA Instruments SDT Q600 in air flow from room temperature to 900° C with a heating rate of 10° C min<sup>-1</sup>. Percentage of C and N doped into the TiO<sub>2</sub> matrix was determined by using Euro EA elemental analyzer with sulfamethazine as a standard material which consists of 51.78% C, 5.07% H, 20.13% N and 11.52% S.

Photocatalytic studies were performed under direct sunlight by taking methylene blue (MB) as a model dye. Before exposing to sunlight the dye solutions along with catalyst were placed in dark for 30 min in order to achieve adsorption desorption equilibrium. The concentration after this dark reaction was taken as initial concentration. For every 15 min small aliquots were collected from the experimental solutions, centrifuged and the degradation of dye was monitored by using UV-Vis spectrophotometer.

The best photocatalytic activity of G-TiO<sub>2</sub> has also been tested for the photocatalytic reduction of Cr (VI) under the Sunlight. A 10 ppm solution of potassium dichromate was taken as Cr (VI) source. Before the exposure to Sunlight, the Cr (VI) solutions with photocatalyst were placed in dark in order to achieve equilibrium conditions. At a regular intervals of 15 min the samples were collected and throughout the reaction Cr (VI) was estimated by forming a purple coloured complex with 1, 5- Diphenyl hydrazide solution in acidic media [54]. The concentration of Cr (VI) was estimated from the absorbance at 540 nm by using UV-Vis spectrophotometer.

### **3.2.3. Results and discussion**

#### **3.2.3.1. Powder X-ray diffraction (PXRD)**

Powder X-ray diffraction patterns of the as prepared samples were shown in Fig. 3.2.1. The peaks centered at 25.3, 37.8, 48.1, 54.4, 62.9 and 75.2° with corresponding d-spacing values of 3.5, 2.4, 1.8, 1.7, 1.4 and 1.2 Å represents (101), (103), (200), (105), (204) and (215) planes respectively of the anatase phase for all the samples (JCPDS card file no. 89-4921). The crystallite size was calculated from the full width at half maxima (FWHM) of the most intense diffraction peak by using Scherrer formula and the values were given in Table 3.2.1. The crystallite sizes are found to be 4, 10, 17, 20, 6 nm for G-TiO<sub>2</sub>, H-TiO<sub>2</sub>, TEA-TiO<sub>2</sub>, GH-TiO<sub>2</sub> and TEAG-TiO<sub>2</sub>, respectively and the corresponding number of moles of gases evolved during the synthesis is 3.8, 3.3, 2.6, 3.5 and 3.2. Thus the number of moles of gases evolved and crystallite sizes are in good agreement in case of single fueled catalysts. These gases may prevent the agglomeration of particles that may lead to smaller particle size. Thus more is the evolved gases smaller is the particle size. Whereas in case of

mixed fueled catalysts GH-TiO<sub>2</sub> and TEAG-TiO<sub>2</sub> the number of moles of gases evolved and crystallite sizes were not in good agreement. This may be due to the difference in the affinities of the two fuels towards the titanium ion. In the case of GH-TiO<sub>2</sub>, hexamine may have higher affinity than glycine, which can be attributed due to the four coordinating N atoms of hexamine compared to the only one carboxyl and one amine of glycine. So GH-TiO<sub>2</sub> may have the characteristics similar to H-TiO<sub>2</sub>. In a similar manner, for TEAG-TiO<sub>2</sub> catalyst, glycine might bind strongly to the titanium and hence it resembles G-TiO<sub>2</sub>.

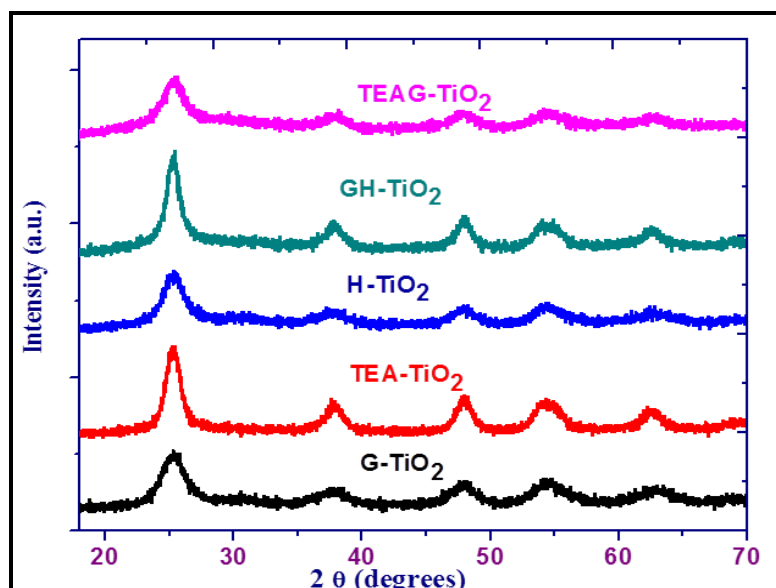


**Fig.3.2.1.** Powder X-Ray Diffraction patterns of combustion synthesized TiO<sub>2</sub> samples

### 3.2.3.2. TEM

The crystallite size of G-TiO<sub>2</sub> was also revealed by the TEM image as shown in Fig. 3.2.2(a). As observed in Fig. 3.2.2(b) the planes present in the HR-TEM image with d-spacing values of 2.4 and 3.5 Å represents (004) and (101) planes of anatase phase respectively. The selected area electron diffraction pattern (Fig. 3.2.2(c)) given in the inset also confirms the anatase phase.

### 3.2.3.3. Diffuse UV- Vis reflectance spectral analyses

The C and N doping into the TiO<sub>2</sub> matrix was clearly evidenced from the red shift in the UV-Vis diffuse reflectance spectra of the as prepared samples as shown in Fig. 3.2.3. The band gap energy values as calculated from the absorption spectra were shown in Table 1, which clearly indicated the band gap of 2.7, 2.8, 3.1, 3.2, 3.2 and 3.2 eV for G-TiO<sub>2</sub>, TEAG-TiO<sub>2</sub>, GH-TiO<sub>2</sub>, H-TiO<sub>2</sub>, TEA-TiO<sub>2</sub> and commercial TiO<sub>2</sub> respectively. From Fig. 3.2.3 it was also evident that G-TiO<sub>2</sub> has a broad absorption in the entire visible region compared to other catalysts. TEAG-TiO<sub>2</sub> also has significant absorption from 400-750 nm.

From the literature reports it is well accepted that C and N doping can cause red shift in the onset absorption for C and/or N doped TiO<sub>2</sub> samples [55, 56].

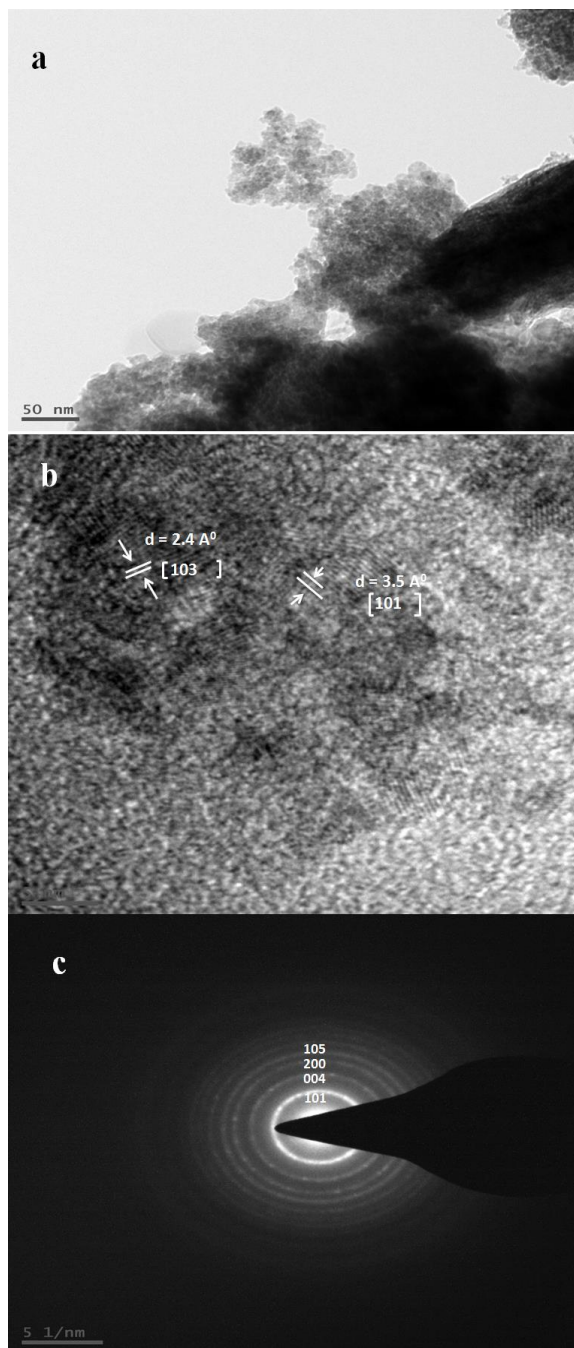


**Fig.3.2.2.** (a) TEM image of combustion synthesized G -TiO<sub>2</sub> catalyst (b) HRTEM image of G-TiO<sub>2</sub> showing planes of G-TiO<sub>2</sub> (c) Selected area electron diffraction pattern of G-TiO<sub>2</sub>



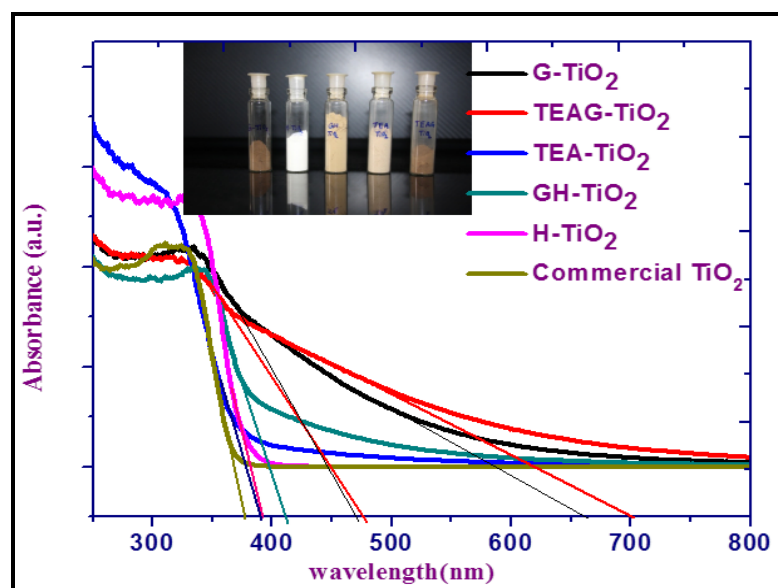


**Fig.3.2.3.** Diffused Reflectance UV-Vis spectra of combustion synthesized TiO<sub>2</sub>

The observed visible light activity of the catalysts may be either due to decrease of the band gap due to overlap of O 2p with N/C 2p orbitals or the presence of dopant energy states in the band gap. Asahi et al. reported that N-doped TiO<sub>2</sub> showed improved visible light activity than undoped TiO<sub>2</sub> which they assigned due to band-gap narrowing due to mixing of N 2p states with O 2p states. On the other hand, theoretical calculations by Irie et al. suggested that the visible-light response in N-doped TiO<sub>2</sub> may be due to N 2p states present as dopant levels above the valence band of TiO<sub>2</sub>. Similarly, the red-shift in C-doped TiO<sub>2</sub> has been observed by Choi et al. Hence, increasing dopant may favor visible light response which can be observed by the red shift in onset absorption. Thus different band gap values of the prepared samples may be due to different percentage of C and N inclusion into the TiO<sub>2</sub> matrix.

#### 3.2.3.4. BET sorptometry studies

The BET surface area of the combustion synthesized TiO<sub>2</sub> samples were given in Table 3.2.1. The specific surface area values of the as prepared samples were found to be 250, 230, 140, 130 and 110 m<sup>2</sup>/g for G-TiO<sub>2</sub>, TEAG-TiO<sub>2</sub>, H-TiO<sub>2</sub>, TEA-TiO<sub>2</sub>, and GH-TiO<sub>2</sub> respectively.

#### 3.2.3.5. XPS

The XPS spectra of the as prepared TiO<sub>2</sub> samples were shown in Fig.3.2.4. The position of characteristic bands and atomic ratios from the XPS spectra were shown in Table 3.2.1. The characteristic bands at binding energies 458.9±0.2 and 464.5±0.2 eV as shown in Fig. 3.2.4 indicate the presence of Ti<sup>+4</sup> (2p<sub>3/2</sub>) and Ti<sup>+4</sup> (2p<sub>1/2</sub>).

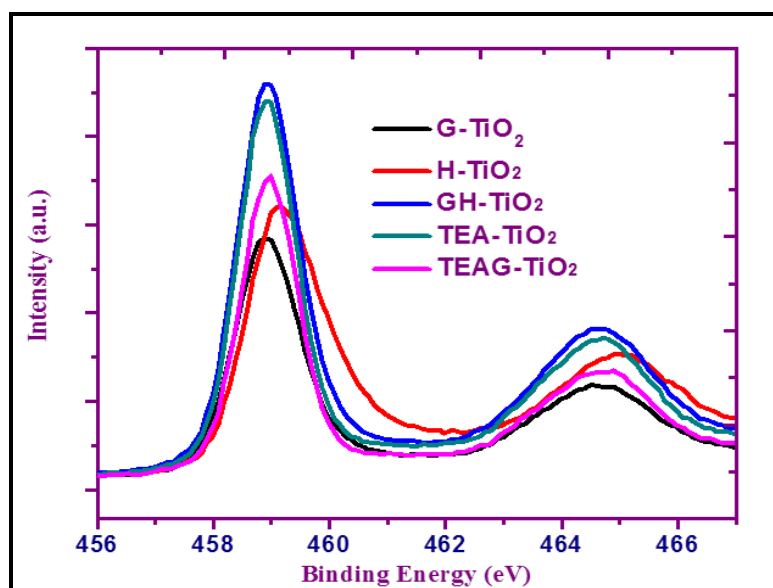


**Fig.3.2.4.** XPS spectra of Ti 2p core levels of G-TiO<sub>2</sub>, H-TiO<sub>2</sub>, TEA-TiO<sub>2</sub>, GH-TiO<sub>2</sub> and TEAG TiO<sub>2</sub>

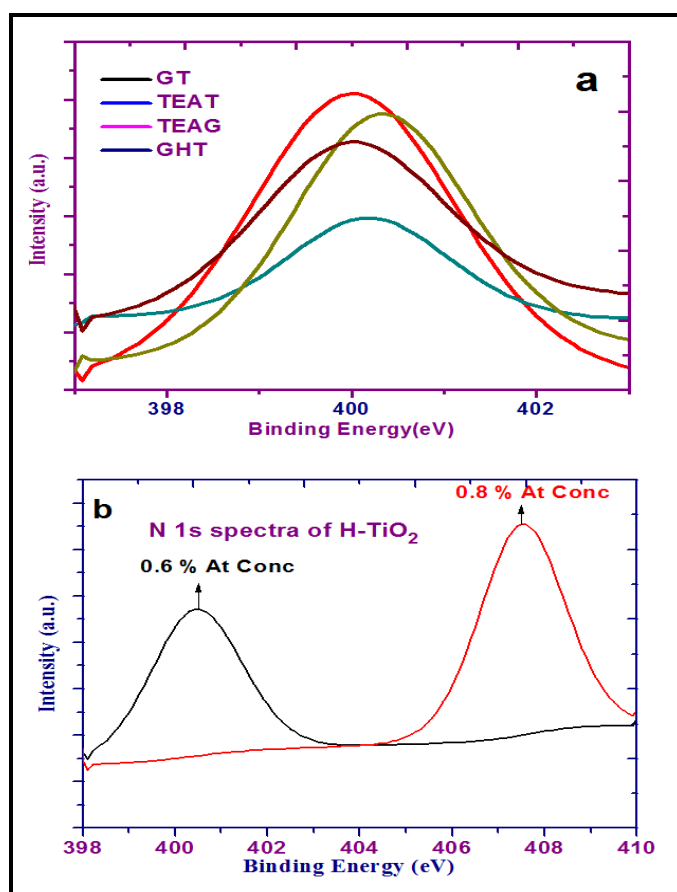


**Fig.3.2.5.** (a) XPS spectra of N 1s core levels of G-TiO<sub>2</sub>, TEA-TiO<sub>2</sub>, GH-TiO<sub>2</sub> and TEAG TiO<sub>2</sub>. (b) XPS spectra of N 1s core levels of H-TiO<sub>2</sub> showing additional peak at 407.5 eV which is indicative of M-N bonding

As reviewed by Emeline et al., [57] the attribution of the N 1s binding energies is still remains as a controversial topic. As shown in Fig. 3.2.5 (a) the peak centered at 400 eV for the N 1s spectra of all the samples can be attributed to the molecular species whereas the additional peak observed at 407.5 eV in Fig. 3.2.5(b) can be attributed due to the metal nitrogen linkage [58].

The peak positions observed at different binding energies for the C 1s spectra of all the samples can be divided into 3 segments as shown in Fig. 3.2.6. The C–(C, H) contribution at 285.0 eV is a classical aliphatic carbon. At a relatively higher binding energy (286.3 eV) we can find C involved in a simple binding with O or N. The peaks at still higher binding energy values of about 288-290 eV may be attributed to the C involved in either a double bond or two single bonds with N and/or O. Quantitative determination of % of C and N doped into the TiO<sub>2</sub> matrix has been calculated and shown in Table 3.2.1.

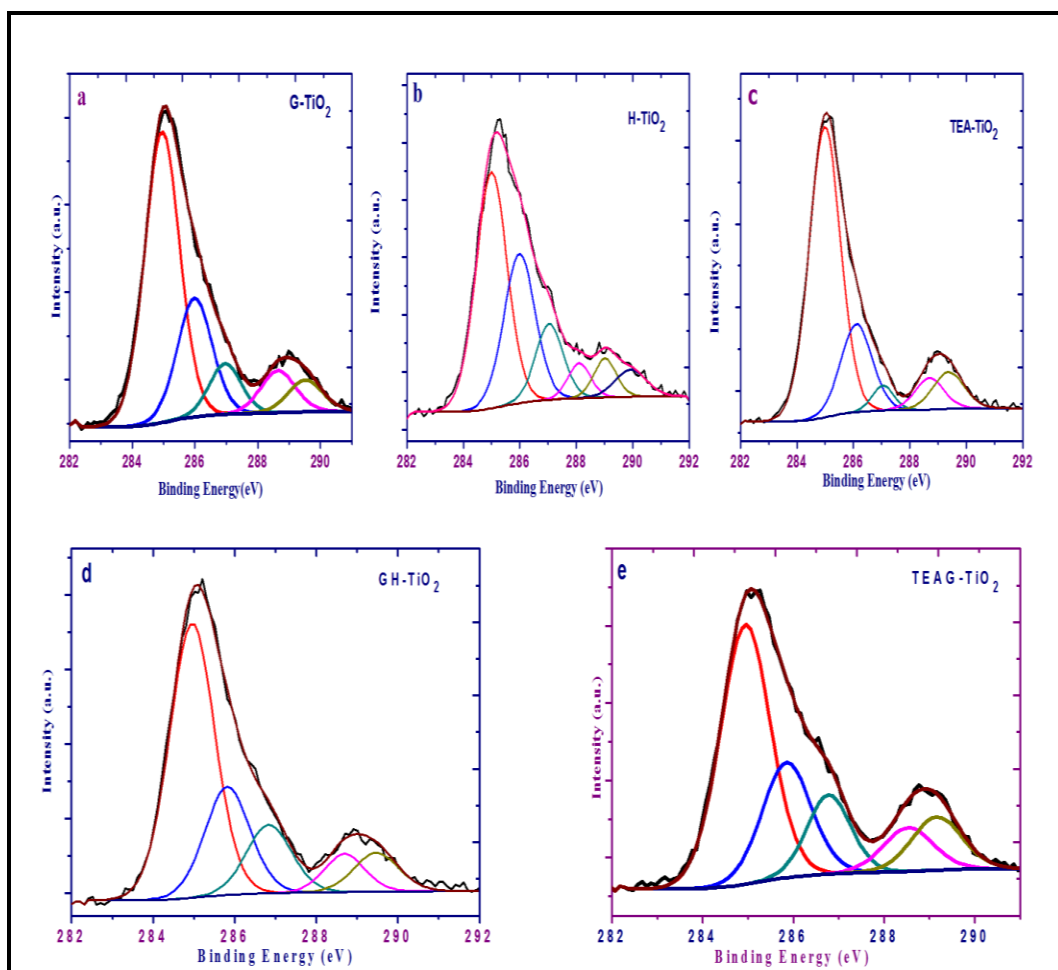


**Fig.3.2.6.** XPS spectra of C 1s core levels of (a) G-TiO<sub>2</sub> (b) H-TiO<sub>2</sub> (c) TEA-TiO<sub>2</sub> (d) GH-TiO<sub>2</sub> and TEAG-TiO<sub>2</sub>.

### 3.2.3.6. TGA studies

In order to further confirm the presence of carbon in the combustion synthesized samples TGA spectra have been recorded under air atmosphere and the plots are shown in Fig. 3.2.7. There were three regions of weight loss in all the samples except for commercial  $\text{TiO}_2$ . The first region of weight loss below  $200^\circ\text{C}$  may be due to the physically adsorbed water and the second region of weight loss between  $200\text{-}450^\circ\text{C}$  may be attributed owing to the strongly bound water. The third region of weight loss between  $450\text{-}800^\circ\text{C}$  is due combustion of C present in the sample [31]. The percentage weight of C calculated from the third region of weight loss was 1.57, 1.54, 1.23, 0.97 and 0.96, respectively for G- $\text{TiO}_2$ , TEAG- $\text{TiO}_2$ , TEA- $\text{TiO}_2$ , GH- $\text{TiO}_2$  and H- $\text{TiO}_2$ . Hence the presence of C in all the combustion synthesized samples was confirmed.

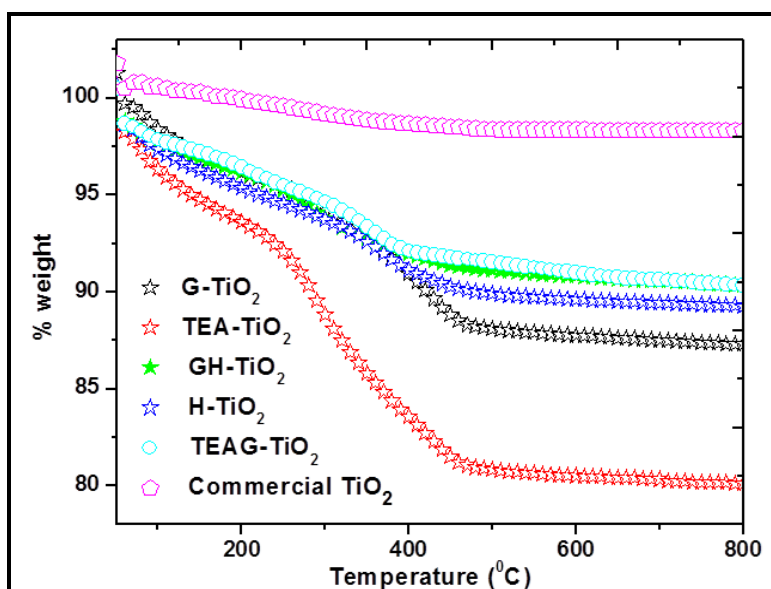


**Fig.3.2.7.** TGA spectra of combustion synthesized samples under air atmosphere

### 3.2.3.7. CHNS Elemental Analyses

In order to analyze the weight percentage of C and N present in the combustion synthesized photocatalysts CHNS elemental analysis was carried out. The % C was found to be 1.52, 1.50, 1.18, 0.93, and 0.91 respectively for G- $\text{TiO}_2$ , TEAG- $\text{TiO}_2$ , TEA- $\text{TiO}_2$ , GH- $\text{TiO}_2$  and H- $\text{TiO}_2$ . The % of N was found to be 0.65, 0.51, 0.46, 0.49 and 0.32 respectively for G- $\text{TiO}_2$ , TEAG- $\text{TiO}_2$ , TEA- $\text{TiO}_2$ , H- $\text{TiO}_2$  and GH- $\text{TiO}_2$ . Thus the C and N doping in all the photocatalysts was also evidenced by elemental analyses.

**Table 3.2.1.** Physico-chemical characteristics of combustion synthesized TiO<sub>2</sub> samples

S. No	Sample Name	Crystallite size (nm)	Band Gap (eV)	Surface area (m <sup>2</sup> /g)	% weight of C	% weight of N
1	G-TiO <sub>2</sub>	4	2.7	250	1.52	0.65
2	H-TiO <sub>2</sub>	10	3.2	140	0.91	0.49
3	TEA-TiO <sub>2</sub>	17	3.2	130	1.18	0.46
4	GH-TiO <sub>2</sub>	20	3.1	110	0.93	0.32
5	TEAG-TiO <sub>2</sub>	6	2.8	230	1.50	0.51

### 3.2.3.8. Photocatalytic activity

#### 3.2.3.8.1. Photocatalytic activity of various combustion synthesized photocatalysts

It has been reported that the absorption of light and the charge separation are the important factors during photocatalysis [59,60]. In order to achieve these two factors, several C and N doped TiO<sub>2</sub> samples were synthesized. During the present study, visible light activity of synthesized TiO<sub>2</sub> photocatalysts were evaluated for the degradation of 20 ppm of MB under direct solar irradiation with 1 gm/L each of TiO<sub>2</sub> catalysts. It is worth mentioning that no detectable degradation of MB was observed either without TiO<sub>2</sub> or without visible irradiation.

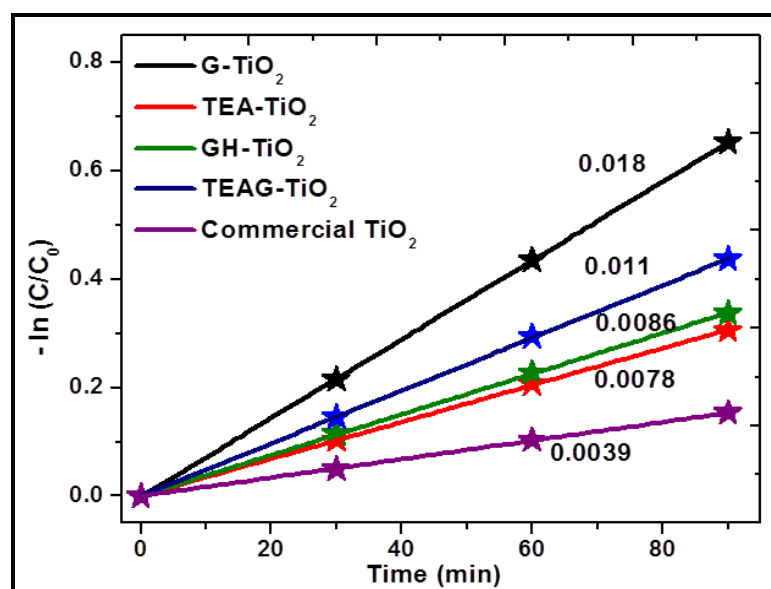
**Fig.3.2.8.** First order kinetic plots for the photocatalytic degradation of MB in presence of different combustion synthesized photocatalysts ( $C_0 = 20$  ppm, Catalyst amount = 0.25gm/l)

Fig. 3.2.8 presents the first order kinetic plot of MB degradation over various catalysts and the comparison was also made with a commercial TiO<sub>2</sub> catalyst. As stated

earlier, the samples were stirred in dark for 30 min prior to the exposure to solar radiation. For 20 ppm MB, the adsorption capacity of G-TiO<sub>2</sub>, TEAG-TiO<sub>2</sub>, TEA-TiO<sub>2</sub>, H-TiO<sub>2</sub>, GH-TiO<sub>2</sub> and commercial TiO<sub>2</sub> was 12, 10, 4, 5, 2, and 1 %, respectively, which is consistent with the BET surface area values (Table 1). As seen in Fig. 3.2.8, the photocatalytic activity of combustion synthesized samples i.e. G-TiO<sub>2</sub>, TEAG-TiO<sub>2</sub>, TEA-TiO<sub>2</sub> and GH-TiO<sub>2</sub> is higher than that of commercial TiO<sub>2</sub>, which may be assigned due to the absorption in visible light region, as confirmed by UV-Vis spectroscopy and/or high surface area. Among combustion synthesized samples, H-TiO<sub>2</sub> showed no photocatalytic activity under the direct sunlight even up to 60 min of irradiation, which is in agreement with the band gap of 3.2 eV that demands UV irradiation.

As evident from Fig. 3.2.8, the photodegradation of MB followed the first-order kinetics that obeys the equation  $\ln(C_0/C) = kt$ , where  $k$  is the rate constant,  $t$  is the irradiation time,  $C_0$  and  $C$  are the initial and concentration at time  $t$ . The first order rate constant values calculated from the slopes obtained from Fig. 3.2.8 were found to be 0.018, 0.011, 0.0086, 0.0078 and 0.0039 min<sup>-1</sup>, respectively for G-TiO<sub>2</sub>, TEAG-TiO<sub>2</sub>, GH-TiO<sub>2</sub>, TEA-TiO<sub>2</sub> and commercial TiO<sub>2</sub> and among the catalysts, G-TiO<sub>2</sub> has the highest rate constant. Since among the photocatalysts G-TiO<sub>2</sub> has highest activity, further studies were carried out by using the same catalyst.

#### **3.2.3.8.2. Effect of photocatalytic amount on degradation rate**

Fig. 3.2.9 (a) shows the effect of G-TiO<sub>2</sub> catalytic amount on the degradation of 20 ppm of MB for 60 min run. It may be observed that increasing the G-TiO<sub>2</sub> amount from 0.5 g to 1 g/L, the rate constant increased from 0.008 to 0.018 min<sup>-1</sup>. With further increase of the catalyst amount to 1.5 g/L, rate constant decreases slightly to 0.012 min<sup>-1</sup>. This indicated the optimum catalyst dosage of 1 g/L. Increasing catalytic dosage provides more active sites for MB degradation. However, the decrease in the rate constant for catalyst dosage higher than 1 g/L may be due to the shadowing effect due to high turbidity of the solution that decreases the penetration depth of solar radiation [61].

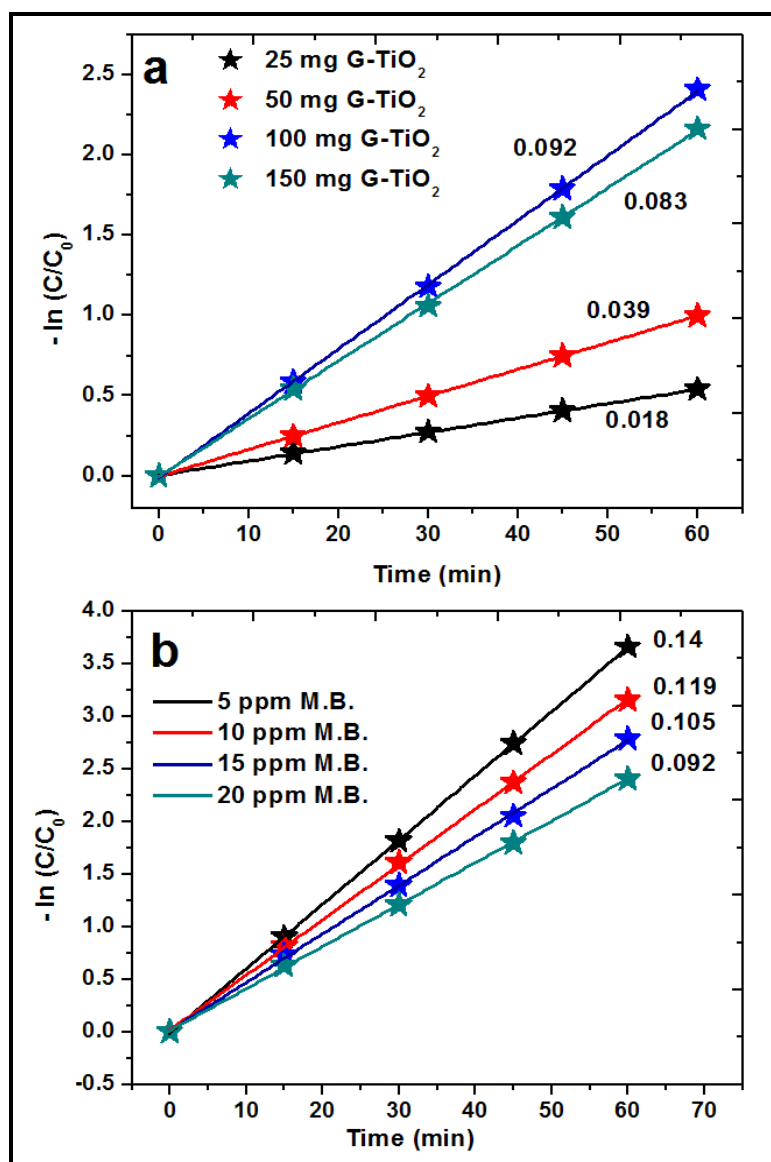


**Fig.3.2.9.** (a) First order kinetic plots showing the effect of catalytic amount on degradation of MB in presence of G-TiO<sub>2</sub> (C<sub>0</sub> = 20 ppm). (b) First order kinetic plots representing the effect of initial concentration of MB on its degradation in presence of G-TiO<sub>2</sub> (Catalytic amount- 1 gm/L)

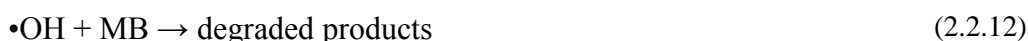
### 3.2.3.8.3. Effect of initial concentration of MB on photocatalytic degradation

In order to understand the influence of dye initial concentration, photocatalytic degradation of MB was studied in the concentration range of 5 to 20 ppm with G-TiO<sub>2</sub> and the results are shown in Fig. 3.2.9 (b). As seen in Fig. 3.2.9 (b), the concentration has a significant effect on the degradation of MB. After illumination for 60 min, the rate constant 'k' for 5, 10, 15 and 20 ppm was found to be 0.14, 0.119, 0.105, 0.092 min<sup>-1</sup> which clearly shows that as the concentration decreases rate constant increases. This can be attributed to

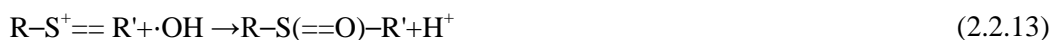
the hindering of photons with the increase in concentration of MB to reach the surface of photocatalyst. Moreover, as the concentration of dye (MB) increases, the molecules adsorbed on the surface of photocatalyst might increase. This decreases the active sites on the photocatalyst which results in a decrease in generation of hydroxyl radical, and hence the lower activity [62].

### 3.2.3.8.4. Photocatalytic degradation mechanism on TiO<sub>2</sub> samples

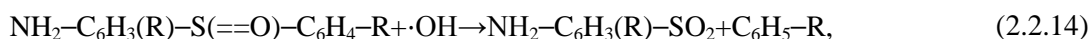
It has been reported that irradiation of a photocatalyst with energy corresponds to the band gap promotes a valance band electron to the conduction band, leaving a hole in the valance band (Eq. 6). The adsorbed water molecules react with the holes to form hydroxyl radicals, whose oxidation potential (2.8 V) is higher than many conventional oxidants like H<sub>2</sub>O<sub>2</sub>, ozone, etc [63]. On the other hand, in the conduction band the electron reduces the adsorbed oxygen to superoxide anion radical (O<sub>2</sub><sup>•-</sup>), which then reacts with water to form •OH radical, as given in (Eqs. (10) and (11)). The reaction of •OH radical with MB degrades the pollutant (Eq. (12)) [31, 64].



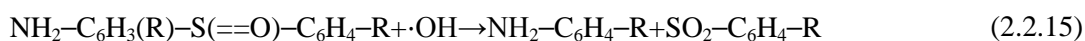
Hence, •OH initiated MB degradation may be proposed as follows [65, 66]. Since the MB is cationic dye, MB degradation may proceed via •OH initiated cleavage of the C-S<sup>+</sup>==C functional group of MB:



The sulfoxide group undergoes a second attack by second •OH producing the sulfone and causing the definitive dissociation of two benzenic rings (Eq. 2.2.14-2.2.15)



and/or

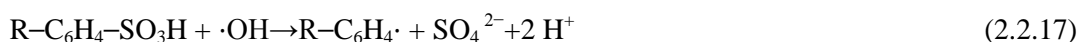


Subsequently, attack of the sulfone by a third •OH to form sulfonic acid

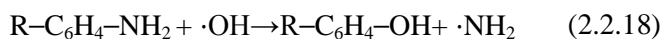


Finally the release of SO<sub>4</sub><sup>2-</sup> ions may be due to the attack of the fourth •OH (Eq. 2.2.17)





In addition, the amino group in MB can be substituted by a  $\cdot\text{OH}$  that leads to the formation of corresponding phenol and released  $\text{NH}_2\cdot$  may generate ammonia and ammonium ions (Eq 2.2.18-2.2.20)



The other two symmetrical dimethyl phenyl amino groups in MB undergo a progressive oxidation of one methyl group by  $\cdot\text{OH}$  radical, producing an alcohol, followed by aldehyde, acid that decarboxylates into  $\text{CO}_2$ .

### 3.2.3.8.5. Photocatalytic reduction of Cr (VI)

Photocatalytic activity of G-TiO<sub>2</sub> has also been evaluated by the photo reduction of Cr (VI) in aqueous solution under natural sunlight. Fig. 3.2.10 (a) shows the first order kinetic plots of Cr (VI) reduction for various catalytic amounts. As shown in Figure 3.2.10 (a) the rate constant of photocatalytic reduction of Cr (VI) was 0.014, 0.035, 0.053, 0.069 min<sup>-1</sup> respectively for a catalyst loading of 0.25, 0.50, 0.75 and 1 gm/L. As the rate constant stabilizes around 1 gm/L, the effect of pH was carried out with this catalytic amount.

Fig. 3.2.10 (b) shows the effect of pH (2-11) on the photocatalytic reduction of Cr (VI). As seen in the Fig. 3.2.10 (b), the photo reduction of Cr (VI) was 100 % within 15 min under highly acidic conditions (pH < 2). As shown in Fig. 3.2.10 (b), the rate constant was found to be 1.2, 0.17, 0.069, 0.013 and 0.002 min<sup>-1</sup> respectively at pH of 2, 4, 7, 9 and 11. As pointed out by Chen and Cao [67], increasing pH decreases the adsorption capacity of the catalyst for dichromate ions. In general, Cr (VI) occurs in the forms of oxy anions like  $\text{HCrO}_4^-$ ,  $\text{Cr}_2\text{O}_7^{2-}$ ,  $\text{CrO}_4^{2-}$ ,  $\text{CrO}_3$ , etc. The predominant form of Cr(VI) was the acid chromate species ( $\text{HCrO}_4^-$ ) at lower pH that on increasing the pH, changes to other forms like  $\text{CrO}_4^{2-}$  and  $\text{Cr}_2\text{O}_7^{2-}$  [67, 68]. Therefore, the ionic forms of Cr (VI) in solution and the charge of G-TiO<sub>2</sub> surface depend on the pH of the solution. Under acidic conditions, the surface of the catalyst may be predominantly protonated and attracts the negatively charged Cr (VI) ions. In addition, under basic conditions, Cr (OH)<sub>3</sub> may be precipitated and cover the surface of the catalyst and decreases the activity of the catalyst.

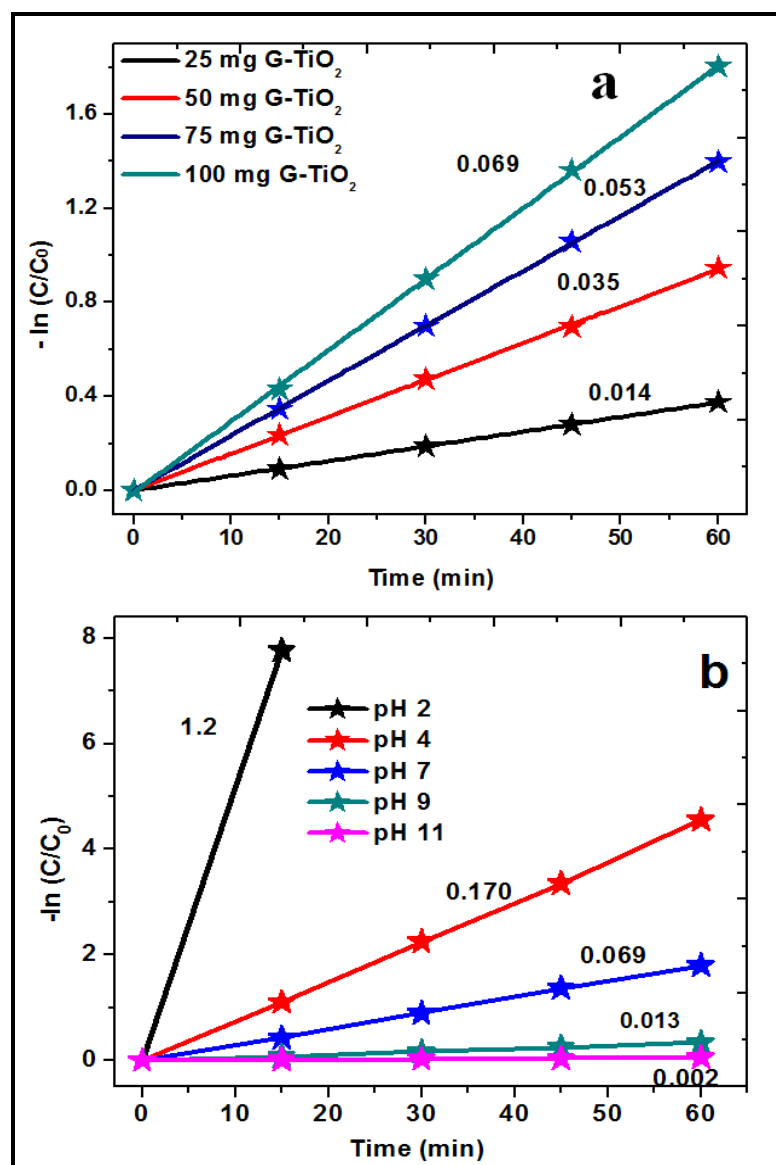


**Fig.3.2.10.** (a) Photocatalytic reduction of Cr(VI) in presence of various catalytic dosages of G-TiO<sub>2</sub> (C<sub>0</sub> = 20 ppm). (b) First order kinetic plots representing the effect of pH on photocatalytic reduction of Cr(VI) with G-TiO<sub>2</sub> photocatalyst (Catalytic amount- 1 gm/L)

### 3.2.3.8.6. Mechanism of photocatalytic reduction of Cr (VI)

The mechanism of Cr (VI) reduction may be explained as follows. On irradiation of sunlight, electron (e<sup>-</sup>) and hole (h<sup>+</sup>) pairs were produced in the valence and conduction band and the corresponding reactions of these excitons are summarized in Eq 2.2.21-2.2.23



The overall reaction under acidic conditions ( $\text{pH} \leq 2$ ) may be summarized as follows:



#### **3.2.4. Conclusions**

A facile one pot synthesis of C and N doped  $\text{TiO}_2$  catalysts have been achieved by using titanium nitrate as oxidant and with various fuels as reductants. Study of combustion with various fuels indicated the high surface area and best activity for glycine fuel derived  $\text{TiO}_2$  under direct sunlight, which was correlated due to more number of evolved gases. However for mixed fuel, the interaction between the coordinating atoms and Ti metal ion may be responsible for the properties observed. The visible light photocatalytic activity was tested under the direct Sunlight for the degradation of a textile dye methylene blue and for the reduction of Cr (VI) that confirmed the better activity of all the catalysts compared to commercial  $\text{TiO}_2$ . Study of effect of pH revealed that the acidic pH favors the reduction Cr (VI) due to better interactions between  $\text{TiO}_2$  surface and Cr (VI).

# Chapter 3-Section III

## Optimization of fuel for combustion

### synthesis of C doped TiO<sub>2</sub>

#### 3.3.1. Introduction

Increasing water pollution due to the rapid industrialization, increase of automobiles and excessive use of pesticides is threatening the entire globe [69,70]. Some of the major pollutants are heavy metal ions, dyes and organic compounds etc.. Chromium (VI) is one of the toxic heavy metal ions released into the aqueous streams through tanning, bricks, pigment photography, steel, galvanizing, cement industries, mining industries etc. The conventional methods in practice for the removal of heavy metal ions are precipitation, coagulation, cementation, ion exchange, reverse osmosis, electro-dialysis, electro-winning and electro-coagulation [71]. These methods are not so effective due to incomplete removal of the metal ions and generation of toxic by-products.

On the other hand phenol is one of the extremely toxic organic pollutants that have a high solubility in water. It is used in the manufacture of polymeric resins, herbicides, fungicides, etc. In addition to this it is widely used in several industries such as oil refining, paper mills and in the pharmaceutical industries [72]. Phenol is also one of the most widely used petrochemical products and its usage is increasing day by day [73]. Since 2001 there is a tremendous increase in demand for the phenol derivative bisphenol A for the production of polycarbonate resins used in the manufacture of CDs, CD-ROMs and DVDs [74]. Production of phenolic formaldehyde resins for circuit boards, coatings and adhesives is another major contribution of phenol [75]. It is hazardous, corrosive and its cellular uptake is rapid and can cause respiratory, nervous and cardiovascular problems [76]. As a result, there are strict recommendations for controlling the levels of phenol in drinking and bathing water. The best way to remove phenol is by advanced oxidation process, where hydroxyl radical oxidizes phenol [77].

In the present study, by employing SCS, C-doped anatase TiO<sub>2</sub> nanomaterials with high surface area and low band gap have been synthesized by using titanium nitrate as oxidant and citric acid, ascorbic acid as fuels. Present study excludes N-doping due to the usage of N-free fuels and provides an understanding on whether both C, N doping offers any advantage over mere carbon doping in to TiO<sub>2</sub>. The as synthesized catalysts were

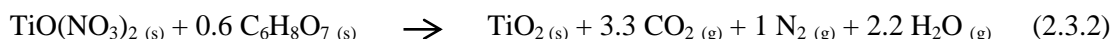
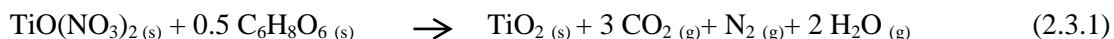
characterized and the visible light photocatalytic activity was asserted from the simultaneous oxidation of phenol and reduction of Cr(VI) under simulated solar light. Plausible mechanism for the enhanced activity during the simultaneous removal of pollutants has been proposed.

### 3.3.2. Experimental section

#### 3.3.2.1. Synthesis of catalyst

The chemicals used in the present study are as follows: Ti(IV) iso-propoxide (Sigma–Aldrich), isopropyl alcohol (Merck), nitric acid (Merck), citric acid (Merck) and ascorbic acid (Merck). The oxidant titanyl nitrate was prepared by the slow hydrolysis of titanium iso-propoxide followed by nitration with excess of nitric acid [53]. Citric acid ( $C_6H_8O_7$ ) and ascorbic acid ( $C_6H_8O_6$ ) were selected as the two fuels that can act as effective carbon sources. Oxidant/fuel ratio was calculated according to propellant theory and it was maintained at 1 in all the cases [77,78]. In a typical synthesis 1gm of titanyl nitrate, 2.013 gm of citric acid or 1.875 gm of ascorbic acid (oxidant to fuel ratio of 1) were mixed with 15 ml of water in a quartz beaker. This solution was preheated on a hot plate for initial dehydration. Thereafter the obtained thick mass was transferred to a preheated furnace maintained at  $350^\circ C$ . Chocolate brown colored materials were obtained after 10 min of combustion in both the cases and were labeled as Cit-TiO<sub>2</sub> and Asc-TiO<sub>2</sub> respectively for citric acid and ascorbic acid used TiO<sub>2</sub> samples.

The stoichiometric equations are as follows:



Above equations show the stoichiometric reactions between titanyl nitrate and ascorbic acid ( $C_6H_8O_6$ ), citric acid ( $C_6H_8O_7$ ) respectively. From this it can be concluded that the combustion reaction between titanyl nitrate and citric acid involves the evolution of more number of gases, which might have a positive impact on the physico-chemical properties [79].

#### 3.3.2. 2. Photocatalytic activity measurement

Photocatalytic experiments were carried out in a photo reactor which consists of three 250 W halogen lamps. The intensity of light falling on the sample cells was found to be  $850-900 W/m^2$  as measured by using Newport optical power/energy meter (Model 842. PE). Visible light activity of the TiO<sub>2</sub> samples was assessed by simultaneous and individual study of oxidation of phenol and reduction of Cr(VI) from aqueous streams. Before exposing to light source the sample solutions along with catalysts were allowed to attain

adsorption desorption equilibrium by stirring in dark for a period of 30 min. Experiments were carried out in the absence of light and without catalyst and it was observed that there was no considerable oxidation of phenol or reduction of Cr(VI). During the light exposure for every 15 min small aliquots were collected, centrifuged at an rpm of 2000 and the catalysts particles were separated by filtering with milli Q membrane filters. Thereafter phenol and Cr(VI) were estimated by using UV-Vis spectrophotometer.

Before spectrophotometric analysis, phenol was converted into a complex by adding 1ml of buffer (pH-9) followed by 1 ml of 0.05 M 4-aminoantipyrene and 1ml of 0.05 M potassium ferricyanide aqueous solution [80,81]. Then the obtained brownish red antipyrene dye was estimated with UV-Vis spectrometer (Shimadzu UV-Vis spectrophotometer (UV-3600)) at 504 nm. Cr(VI) was estimated at 540 nm by forming a purple coloured complex with 1, 5- Diphenyl hydrazide solution in acidic media [54].

### 3.3.3. Results and Discussion

#### 3.3.3.1. XRD

X-ray diffraction patterns of the C-doped TiO<sub>2</sub> samples are shown in Fig. 3.3.1. The peaks centered at 25.3, 37.8, 48.1, 54.4, 62.9 and 75.2° with corresponding d-spacing values of 3.5, 2.4, 1.8, 1.7, 1.4 and 1.2 Å represent (101), (103), (200), (105), (204) and (215) planes, respectively of the anatase phase for both the samples (JCPDS card file no. 89-4921). The relatively broad peaks observed for both the samples as shown in Fig. 3.3.1. can be attributed to the nano crystallite size of the samples. The crystallite sizes calculated by using Scherrer formula were found to be around 4-6 nm for both Cit-TiO<sub>2</sub> and Asc-TiO<sub>2</sub>.

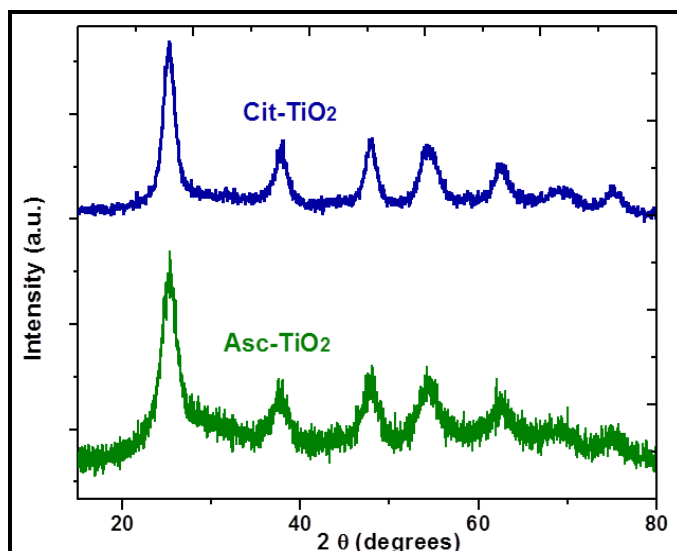


**Fig.3.3.1.** Powder X-ray diffraction patterns of the C-doped TiO<sub>2</sub> samples

### 3.3.3.2. TEM

The crystalline phase and size of the C-doped anatase TiO<sub>2</sub> samples were further confirmed by the TEM image as shown in fig. 3.3.2(a) that confirms the nanoparticles of around 4 nm for Asc-TiO<sub>2</sub>. The inset of fig. 3.3.2(a) shows the selected area diffraction (SAED) pattern, which confirms the anatase phase. Figure 3.3.2 (b) shows the HRTEM image of the Asc-TiO<sub>2</sub> which clearly shows the lattice spacing of 3.5 and 2.4 Å characteristic of (101) and (103) planes of anatase TiO<sub>2</sub>. Figure 3.3.2(c) shows the TEM image of Cit-TiO<sub>2</sub> which also shows the nanoparticles of size 4 nm. The inset of Figure 3.3.2(c) shows the SAED pattern of Cit-TiO<sub>2</sub> which reveals the polycrystalline nature and anatase phase of the sample. Figure 3.3.2(d) shows the HRTEM image of Cit-TiO<sub>2</sub>, which also confirms the anatase phase TiO<sub>2</sub>.

### 3.3.3.3. Diffuse UV-Visible spectral analyses

In general, the light absorption capabilities of TiO<sub>2</sub> can be altered by doping of TiO<sub>2</sub> and the diffuse reflectance UV-Vis spectra is generally used to investigate the shift in the absorption spectra of TiO<sub>2</sub> [82]. In the present study the UV-Vis absorption spectra of C-doped TiO<sub>2</sub> samples and commercial TiO<sub>2</sub> are shown in Fig. 3.3.3. It is well known that incorporation of C species in the TiO<sub>2</sub> structure causes shift in the optical absorption into the visible region, probably through the formation of intra gap energy states. In correlation with the above statement, the C-doped TiO<sub>2</sub> samples exhibit a red shift in the absorption spectra as shown in Fig. 3.3.3. probably due to the C doping in to TiO<sub>2</sub>. The C 2p levels are believed to interact with O 2p states thereby forming a valence band which is higher in energy than the valance band of undoped TiO<sub>2</sub>. Thus the visible light activity may be expected.

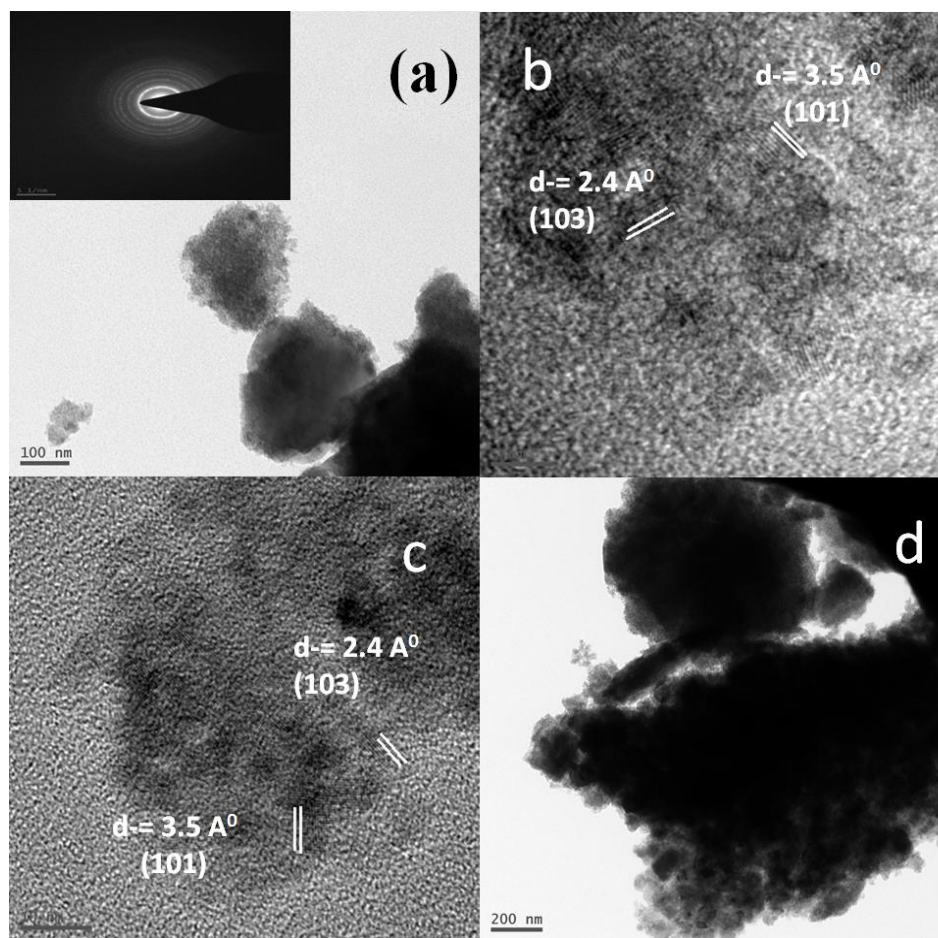


**Fig.3.3.2.** (a) TEM image of Asc -TiO<sub>2</sub> (inset shows the SAED pattern) (b) HRTEM image of Asc-TiO<sub>2</sub> showing lattice fringes characteristic of anatase phase TiO<sub>2</sub> (c) TEM image of Cit -TiO<sub>2</sub> (inset shows the SAED pattern) (d) HRTEM image of Asc-TiO<sub>2</sub> showing lattice fringes characteristic of anatase phase TiO<sub>2</sub>

The band gap energies as calculated from the absorption spectra were found to be 2.6, 3.1 and 3.2 eV for Cit-TiO<sub>2</sub>, Asc-TiO<sub>2</sub> and commercial TiO<sub>2</sub>, respectively. From Fig. 3.3.3, it is also evident that Cit-TiO<sub>2</sub> has a broad absorption in the entire visible region, whereas Asc-TiO<sub>2</sub> has significant absorption between 400 to 600 nm. It is reported that carbon doping can introduce new states (C 2p) close to the valence band edge of TiO<sub>2</sub> (i.e. O 2p states) and as a result, the valence band edge shifts to higher energy compared with the reference TiO<sub>2</sub>. The energy shift of the valence band depends on the overlap of carbon states and O 2p states. A higher doping concentration of carbon results in higher energy shift due to significant overlap of carbon and oxygen states and this leads to narrower band gap in the compound [55]. Thus from Fig. 3.3.3., it is clear that the extent of doping is high in Cit-TiO<sub>2</sub> compared to Asc-TiO<sub>2</sub>.



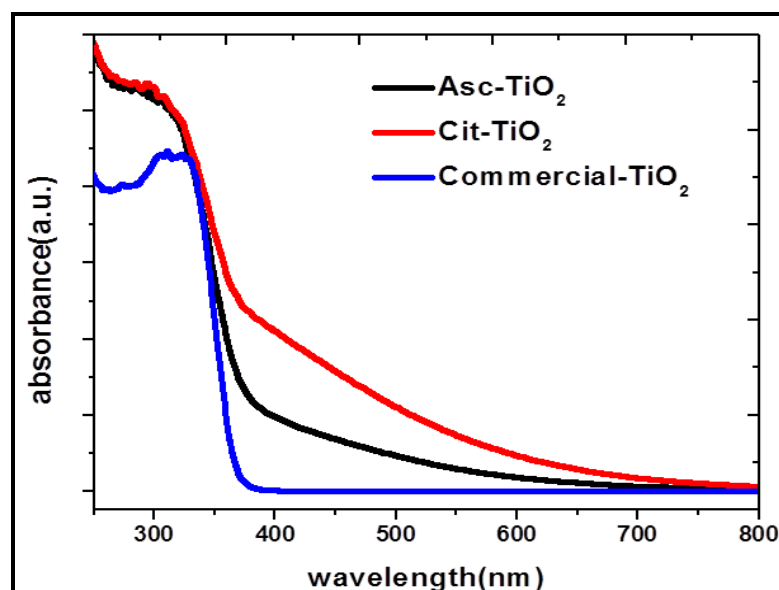


**Fig.3.3.3.** Diffused reflectance UV-Vis spectra of C-doped TiO<sub>2</sub> samples along with commercial TiO<sub>2</sub> sample

### 3.3.3.4. N<sub>2</sub> adsorption studies

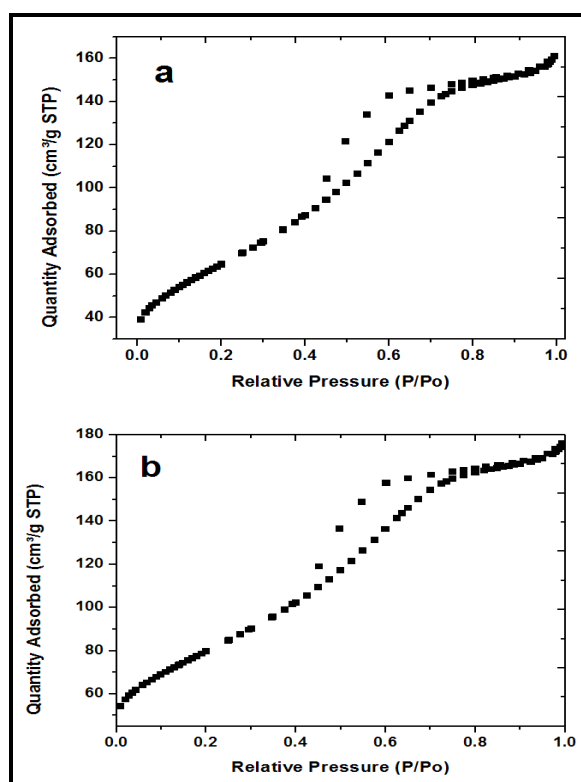


**Fig. 3.3.4.** N<sub>2</sub> adsorption isotherms of (a) Asc-TiO<sub>2</sub> (b) Cit-TiO<sub>2</sub>

Figure 3.3.4(a) and (b) shows the adsorption desorption isotherm of Cit-TiO<sub>2</sub> and Asc-TiO<sub>2</sub> samples respectively. The surface area was found to be 290 m<sup>2</sup>/g and 230 m<sup>2</sup>/g, which is higher than commercial anatase TiO<sub>2</sub>.

### 3.3.3.5. XPS

The Ti 2p spectra (Fig. 3.3.5a) of both Cit-TiO<sub>2</sub> and Asc-TiO<sub>2</sub> samples clearly shows two peaks corresponding to Ti<sup>4+</sup> (2p<sub>3/2</sub>) and Ti<sup>4+</sup> (2p<sub>1/2</sub>) with peaks centered at 458.9±0.2 and 464.5±0.2 eV. Figure 3.3.5(b) shows the spectra of O 1s of both Cit-TiO<sub>2</sub> and Asc-TiO<sub>2</sub>, which shows a peak at 530 eV characteristic of O 1s. In order to investigate the carbon states in the photocatalysts, XPS spectra of C 1s core levels was recorded and shown in Fig. 3.3.5(c). and 3.3.5(d) respectively for Cit-TiO<sub>2</sub> and Asc-TiO<sub>2</sub>. Deconvolution of the C 1s spectrum of both samples revealed three distinct environments at 284.5 eV, 288.0 eV and 290.3 eV. The peak centered at 284.5 eV was due to C 1s of elemental carbon. At a relatively higher binding energy (286.3 eV) the peak observed was due to the C-OH groups. Sakthivel and Kwasch observed the two kinds of carbonate species at binding energies of 287.5 and 288.5 eV [31]. In a similar manner, Ohno et al. observed only one kind of carbonate species with a binding energy of 288.0 eV, and they thought that C<sup>4+</sup> ions were incorporated into the bulk phase of TiO<sub>2</sub> [83]. On the other hand Li et al. also observed only one kind of carbonate species at a binding energy of 288.2 eV [84]. Recently, Ren et al. observed only a single carbonate species with binding energies of 288.6 eV that was assigned to carbon substituted for some of the lattice titanium atoms forming Ti-O-C structure [82]. These results indicated that the C 1s XPS peak observed at 287.5 and 288.6 eV could be assigned to Ti-O-C structure in the present study. In addition, the peak centered at 289.7 eV was attributed to O=C-O components [85].

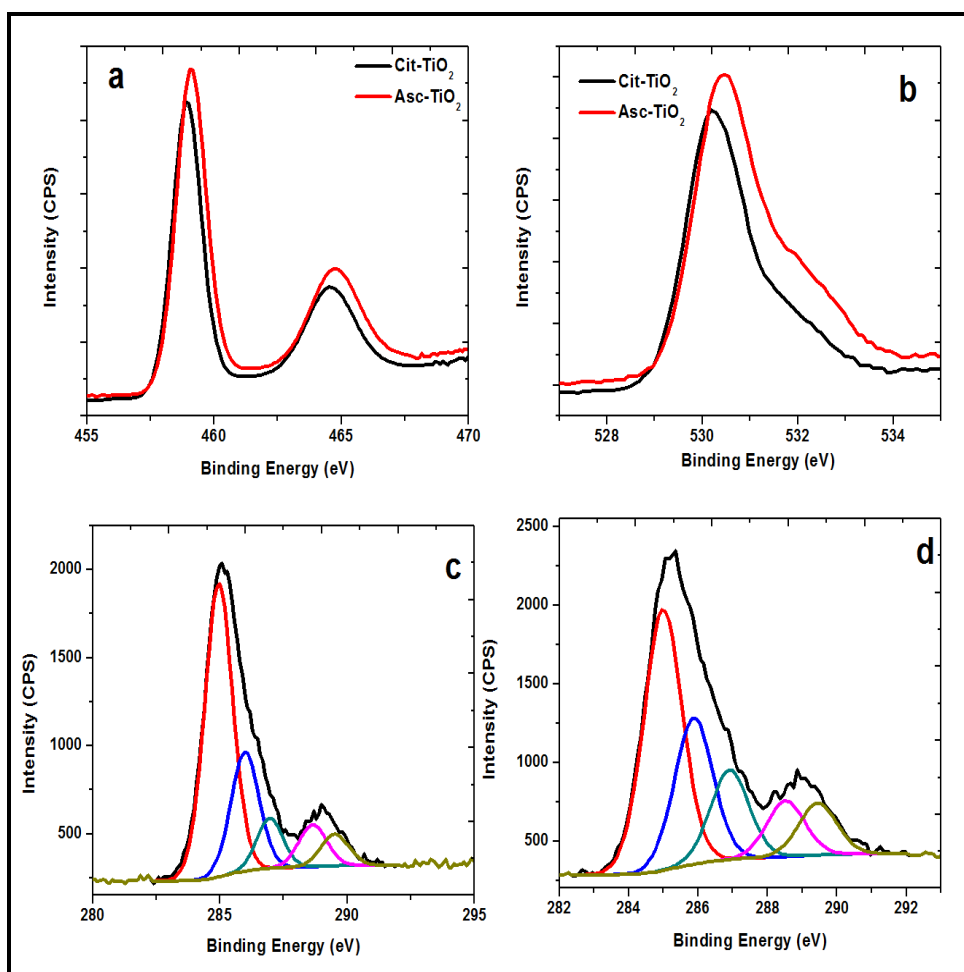


**Fig.3.3.5.** (a) XPS spectra of Ti 2p core levels of Asc-TiO<sub>2</sub> and Cit- TiO<sub>2</sub>. (b) XPS spectra of O 1s core levels of Asc-TiO<sub>2</sub> and Cit- TiO<sub>2</sub>. (c) XPS spectra of C 1s core levels of Asc-TiO<sub>2</sub> (d) XPS spectra of C 1s core levels of Cit- TiO<sub>2</sub>

### 3.3.3.6. TGA studies

In order to further confirm the presence of carbon in C-doped TiO<sub>2</sub> samples, TGA spectra have been recorded under air atmosphere and the plots were shown in Fig. 3.3.6, which shows three regions of weight loss. As reported by Nagaveni et. al. the first region of weight loss below 473 K corresponds to the physically adsorbed water on the catalyst surface, whereas the second weight loss between 473-723 K could be attributed to the strongly bound water on the surface of TiO<sub>2</sub> and the third region of weight loss between 723-1073 K is due to combustion of C present in the sample [86]. For the samples synthesized during the present study, the weight % of C calculated from the third region is 1.59 and 1.56, respectively for Cit -TiO<sub>2</sub> and Asc-TiO<sub>2</sub>. It is worth mentioning that there was no weight loss in case of commercial TiO<sub>2</sub> in the region of 723-1073 K.

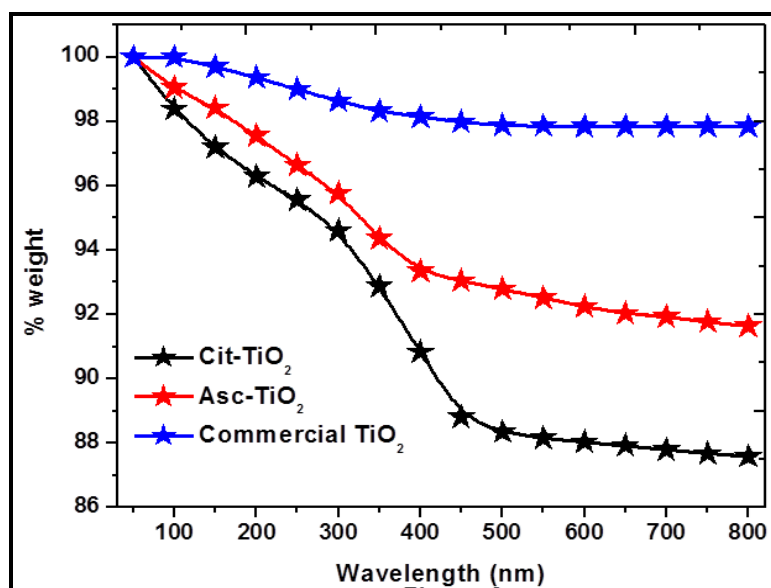


Fig.3.3.6. TGA spectra of C-doped TiO<sub>2</sub> samples under air atmosphere

### 3.3.3.7. Photocatalytic studies

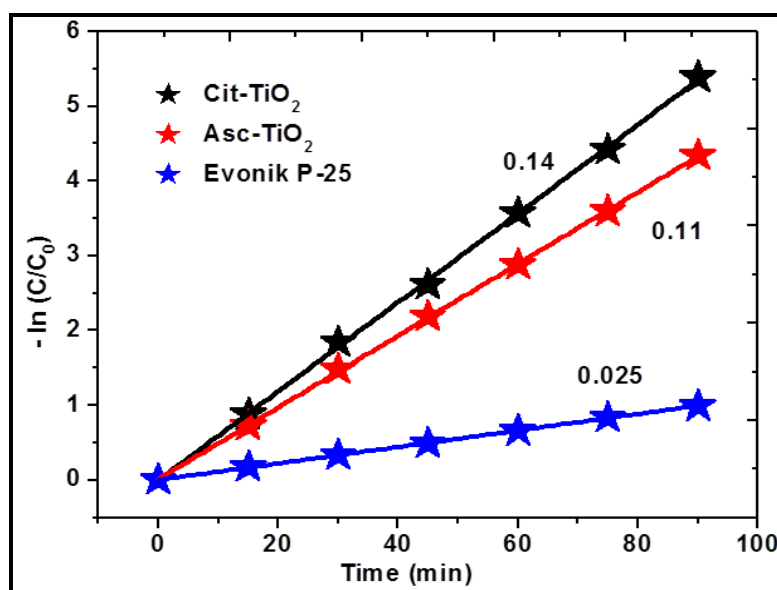


Fig.3.3.7. Comparison of photocatalytic activities of C-doped TiO<sub>2</sub> samples and commercial TiO<sub>2</sub> sample for the reduction of Cr(VI) under simulated solar light. (Catalyst amount = 1gm/l, C<sub>Cr(VI)</sub> = 100 ppm)

In order to understand the visible light photocatalytic activity of the C-doped TiO<sub>2</sub> samples, a test reaction was carried out for the reduction of 100 ppm of Cr(VI) with 100 mg of each catalyst and the results along with commercial TiO<sub>2</sub> studies are shown in figure 3.3.7. The first order rate constants observed were found to be 0.14, 0.11, and 0.025 min<sup>-1</sup> respectively for Cit-TiO<sub>2</sub>, Asc-TiO<sub>2</sub> and commercial TiO<sub>2</sub> samples. It is clear that both the C-doped TiO<sub>2</sub> samples have higher activity and among the C-doped TiO<sub>2</sub> samples Cit-TiO<sub>2</sub>

has best activity than Asc-TiO<sub>2</sub> and Evonik-P25. Therefore the further catalytic studies were carried out by using Cit-TiO<sub>2</sub>.

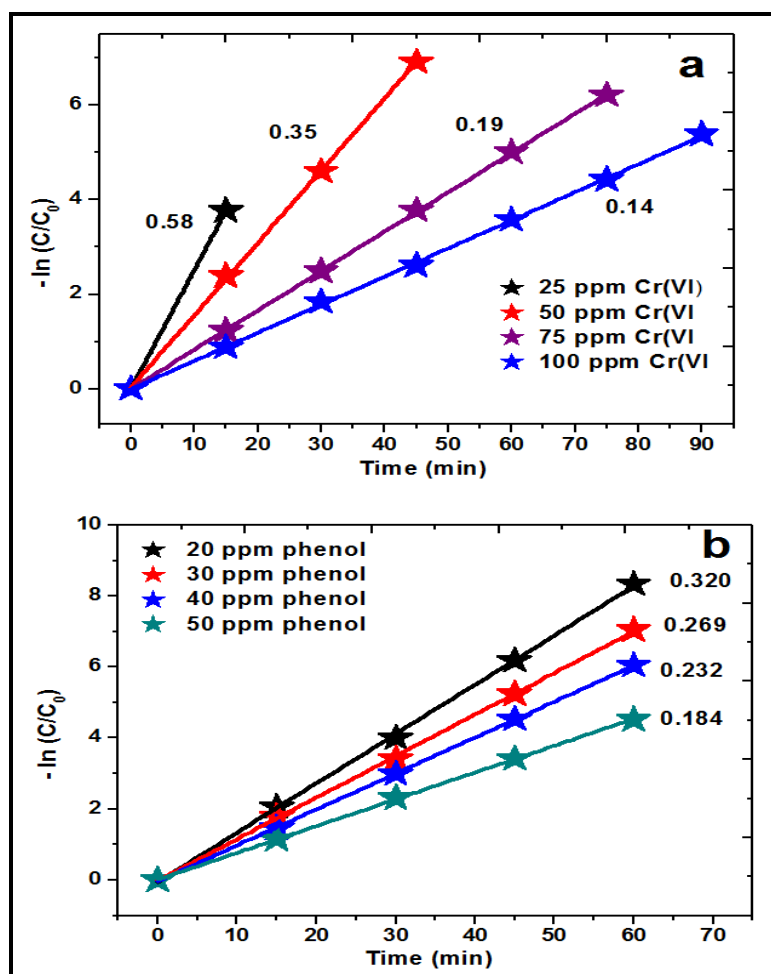
#### **3.3.3.7.1. Effect of Cr(VI) concentration**

Figure 3.3.8 (a) shows the first order kinetic plots of the photocatalytic reduction of Cr(VI) at different initial concentrations. The rate constants calculated from the slopes of first order plots were found to be 0.58, 0.35, 0.19 and 0.14 min<sup>-1</sup> respectively for 25, 50, 75 and 100 ppm of Cr(VI) aqueous solution. From the above observations it is clear that the rate constant increases with the decreasing concentration of Cr(VI). This can be explained based on the hindering effect imposed with the increasing concentration of Cr(VI), which prevents the photons to reach the surface of photocatalyst [62]. In addition to this, with increasing concentration of Cr(VI), the molecules adsorbed on the surface of photocatalyst might increase. This might decrease the active sites on the photocatalyst which effects the generation of hydroxyl radical, and hence lowers the activity [62].

#### **3.3.3.7.2. Photocatalytic oxidation of phenol**

The effect of phenol concentration on the activity of the photocatalyst is presented in Fig. 3.3.8(b). Concentrations were varied between 20 and 50 ppm using 1g/L of catalyst. It has been observed that with increasing concentration of phenol rate constant decreases. The rate constants observed are found to be 0.32, 0.27, 0.23 and 0.18 min<sup>-1</sup> respectively for 20,30,40 and 50 ppm initial concentration of phenol. This can be explained as follows: At higher concentration of phenol, there might be a greater number of phenol molecules adsorbed on the surface and they may form a “passive” monolayer [87]. This inhibits additional phenol molecules to reach the TiO<sub>2</sub> surface, hence, the reduction in photocatalytic degradation.

Simultaneous utilization of redox properties of a photocatalyst can decrease the cost of water treatment. In addition to this, simultaneous redox reaction also prevents the recombination of the excitons. In order to understand the advantageous of a simultaneous reaction, reduction of Cr(VI) and oxidation of phenol were carried out under visible light.



**Fig. 3.3.8** (a). First order kinetic plots for the photocatalytic reduction of Cr(VI) in presence of Cit- TiO<sub>2</sub> photocatalyst at different initial concentrations of Cr(VI) (Catalyst amount = 1gm/l). (b) First order kinetic plots for the photocatalytic oxidation of phenol in presence of Cit- TiO<sub>2</sub> photocatalyst at different initial concentrations of phenol (Catalyst amount = 1gm/l)

### 3.3.3.7.3. Simultaneous oxidation of phenol and reduction of Cr(VI)

Since the industrial waste water consists of mixture of pollutants, simultaneous oxidation and reduction of phenol and Cr(VI) respectively may be advantageous. In addition, simultaneous treatment reduces the cost of the water treatment. Figure 3.3.9 shows the first order kinetic plots for the simultaneous oxidation and reduction of phenol and Cr(VI), respectively. 50 ppm of Cr(VI) aqueous solution and 30 ppm of phenol were taken as a combination of pollutants. It is worth mentioning that there is no reaction in the dark or without catalyst.

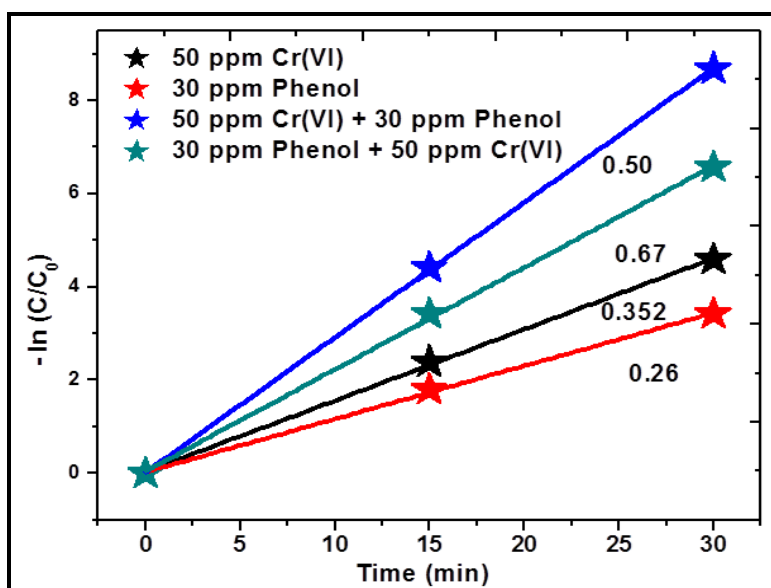
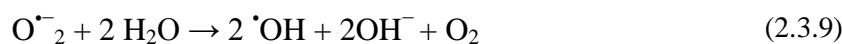


**Fig.3.3.9.** Comparison of first order kinetics of the individual and simultaneous oxidation of phenol and reduction of Cr(VI) in presence of Cit-TiO<sub>2</sub> photocatalyst ( $C_{Cr(VI)} = 50$  ppm,  $C_{phenol} = 30$  ppm, Catalyst amount = 1gm/l)

From the rate constants, it is concluded that in case of simultaneous reaction the rate constant was found to be two times higher than that of the individual reactions, which was explained based on the plausible mechanism as described in the following sections.

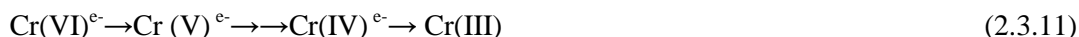
#### 3.3.3.7.4. Photocatalytic reaction mechanism for the removal of individual pollutants

Irradiation of a photocatalyst with suitable energy that corresponds to the band gap excites a valence band electron to the conduction band, leaving a hole in the valence band (Eq. 3). These holes react with adsorbed water molecules to form hydroxyl radicals, whose oxidation potential (2.8 V) is higher than many conventional oxidants like Cl<sub>2</sub>, H<sub>2</sub>O<sub>2</sub>, ozone, etc [63]. On the other hand, the electron present in the conduction band reduces the adsorbed oxygen to superoxide anion radical (O<sub>2</sub><sup>•-</sup>), which then reacts with water to form <sup>•</sup>OH radical, as given in (Eqs. (2.3.7) and (2.3.9)). The reaction of <sup>•</sup>OH radical with phenol converts it into non-toxic products such as CO<sub>2</sub> and H<sub>2</sub>O (Eq. (2.3.10)) [64].





The photocatalytic reduction of Cr(VI) can be explained as follows by using the following mechanism. On irradiation of sunlight, electron ( $e^-$ ) and hole ( $h^+$ ) pairs were produced in the valence and conduction band and the corresponding reactions of these excitons are summarized in Eq (2.3.11 and 2.3.12)



### 3.3.3.7.5. Mechanism for the simultaneous oxidation of phenol and reduction of Cr(VI)

#### (a) Photocatalytic oxidation of phenol in the presence of Cr(VI)

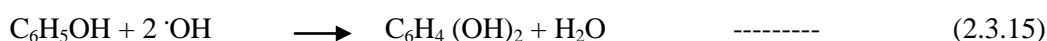
As shown in equations (2.3.4-2.3.9) the exposure of aqueous pollutants along with  $\text{TiO}_2$  photocatalyst to radiation of suitable wavelength produces excitons that may react with water molecules on the surface of the photocatalyst to produce hydroxyl radicals. These hydroxyl radicals ( $\cdot\text{OH}$ ) are reactive due to high oxidation potential (2.8 V). For phenol aqueous solutions,  $\cdot\text{OH}$  radical can act as an electrophile and attacks the aromatic ring of phenol to form the corresponding cyclohexadienyl radicals ( $\cdot\text{C}_6\text{H}_5(\text{OH})_2$ ) [88,89]:



In the absence of external oxidants, the cyclohexadienyl radicals ( $\cdot\text{C}_6\text{H}_5(\text{OH})_2$ ) may disproportionate to dihydroxybenzene and the starting material as shown below [88]:

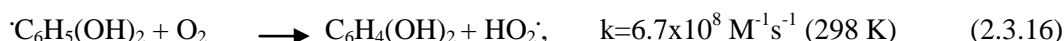


Thus from reactions (2.3.13) and (2.3.14), the stoichiometry of phenol oxidation by  $\cdot\text{OH}$  radical can be written as follows:



From equation (2.3.15), it may be observed that the oxidation of each phenol molecule utilizes two  $\cdot\text{OH}$  radicals.

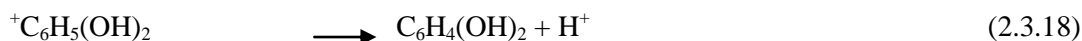
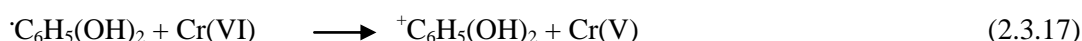
Generally, cyclohexadienyl radicals have reducing nature [89] and can be oxidized by using proper oxidants like oxygen [90], transition metal ions ( $\text{Fe}^{3+}$  or  $\text{Cu}^{2+}$ ) etc. [91,92]. In the presence of suitable oxidant, phenol molecule may consume only one  $\cdot\text{OH}$  radical. For example, the reaction of  $\cdot\text{C}_6\text{H}_5(\text{OH})_2$  with oxygen may be written as given in Eq. 2.3.16 [90]:



However, reaction shown in Eq. 2.3.16 is very rare in photocatalytic systems due to the low solubility of oxygen. In this context, Cr(VI) has been selected to promote the phenol

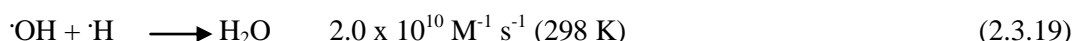


oxidation during the presence study. As Cr(VI) is a powerful oxidant,  $\bullet\text{C}_6\text{H}_5(\text{OH})_2$  radicals can be readily oxidized by Cr(VI), according to the following reactions [92-94].

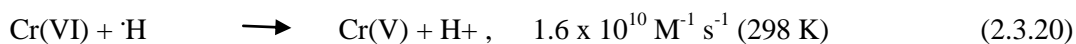


Reaction (2.3.17) is found to be the rate-determining step. No phenol oxidation was observed without photocatalyst and light source in the presence of Cr(VI) which suggests that the direct phenol oxidation by Cr(VI) was negligible.

In a typical photocatalytic process, the resulted  $\bullet\text{OH}$  and  $\bullet\text{H}$  may recombine to form water as shown in Eq. 2.3.19 [95]:



However, in the presence of Cr(VI), the  $\bullet\text{H}$  atoms can also be rapidly oxidized by Cr(VI) as in Eq. 2.3.20 [96]:



Clearly, reaction (2.3.20) suppressed the back reaction (2.3.19) and as a result, more  $\bullet\text{OH}$  are available for phenol oxidation. Reduction of Cr(VI) in the absence of phenol under basic conditions supports the above assumptions [97]. Moreover the presence of Cr(VI) can reduce the recombination of electron and hole by trapping electrons efficiently as shown in equations (2.3.6 and 2.3.11). Hence, it may be assumed that the effects of Cr(VI) on phenol oxidation is three-fold: decreases the consumption of  $\bullet\text{OH}$  radical for phenol oxidation, increases the concentration of  $\bullet\text{OH}$  radical by scavenging the  $\bullet\text{H}$  atoms and traps the photoelectrons in the conduction band.

#### (b) Effect of phenol on photocatalytic reduction of Cr(VI)

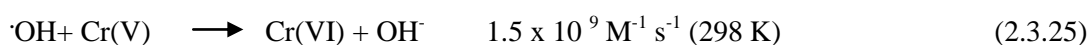
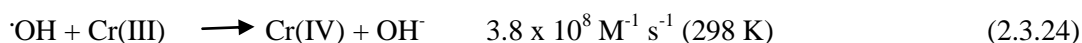
Reaction shown in Eq. 2.3.20 indicates that  $\bullet\text{H}$  can reduce Cr(VI) to Cr(V), which can be further reduced to Cr(III) by the following sequence [97]:



From reactions (2.3.20), (2.3.21) and (2.3.22), the stoichiometric reduction reaction of Cr(VI) to Cr(III) by  $\bullet\text{H}$  atoms is:



In a similar manner, there is a possibility for the reaction between Cr(III) or Cr(V) to give back Cr(IV) and Cr(VI) by the  $\bullet\text{OH}$  radicals, respectively [53].



Although the rate constants of the reactions (2.3.24) and (2.3.25) are small when compared to that of reaction (2.3.20), they cannot be neglected, as the concentration of  $\bullet\text{OH}$

radicals that can be produced during photocatalytic reaction are higher than  $\cdot\text{H}$  atoms. In order to prevent the reaction of  $\cdot\text{OH}$  with the Cr(V) and Cr(III), phenol was used as an  $\cdot\text{OH}$  scavenger (reaction (2.3.13)). The reaction rate constant of  $\cdot\text{OH}$  with phenol is  $1.2 \times 10^{10} \text{ M}^{-1} \text{ s}^{-1}$ , which is almost ten times the rate constant to the reaction of  $\cdot\text{OH}$  with Cr(V). More  $\cdot\text{OH}$  radicals can be trapped with higher phenol concentration and thereby preventing the re-oxidation of Cr(III) and Cr(V). The net reaction is that each  $\cdot\text{OH}$  radical is converted to an  $\cdot\text{C}_6\text{H}_5(\text{OH})_2$  radical that reduces one equivalent of Cr(VI) to Cr(V) or one third that of Cr(VI) to Cr(III).

#### 3.3.4. Conclusions

A facile solution combustion synthesis of carbon doped anatase  $\text{TiO}_2$  photocatalysts with very high surface area and visible light response is reported. Citric acid and ascorbic are used as fuels as well as carbon sources. The visible light photocatalytic activity of the samples is studied in simulated solar light and typical results indicated the better performance of C-doped  $\text{TiO}_2$  than commercial  $\text{TiO}_2$  for the oxidation of phenol and reduction of Cr(VI). It has been observed that simultaneous treatment of phenol and chromium (VI) is advantageous over individual treatments. Among the C-doped  $\text{TiO}_2$  samples Cit- $\text{TiO}_2$  found to have highest activity than Asc- $\text{TiO}_2$ , which can be attributed to the more C doping and high surface area of Cit- $\text{TiO}_2$  compared to Asc- $\text{TiO}_2$ . Plausible mechanism of simultaneous removal of phenol and Cr(VI) has been proposed. In case of Cr(VI) reduction in presence of phenol the selective trapping of  $\cdot\text{OH}$  by phenol can prevent the re-oxidation of Cr(III) and thereby enhances Cr(VI) reduction. On the other hand phenol oxidation in presence of Cr(VI) was found to be enhanced due to the oxidizing power of Cr(VI) and also the capability of trapping  $\cdot\text{H}$  to provide more number of  $\cdot\text{OH}$  for phenol oxidation.

## References

- [1] A. Fujishima, X. Zhang and D.A. Tryk. Heterogeneous photocatalysis: From water photolysis to applications in environmental cleanup. *Int. J. Hydrogen Energ.* 32, (2007) 2664–2672.
- [2] M. Hegedus, A. Dombi. Gas-phase heterogeneous photocatalytic oxidation of chlorinated ethenes over titanium dioxide: perchloroethene. *Appl. Catal. B: Environ.* 53, (2004) 141–151.
- [3] L. Zhang, S. Sawell, C. Moralejo and W.A. Anderson. Heterogeneous photocatalytic decomposition of gas-phase chlorobenzene. *Appl. Catal. B: Environ.* 71, (2007) 135–142.
- [4] M.J. Lopez-Munoz, J. Aguado, A. Arencibia and R. Pascual. Mercury removal from aqueous solutions of  $\text{HgCl}_2$  by heterogeneous photocatalysis with  $\text{TiO}_2$ . *Appl. Catal. B: Environ.* 104, (2011) 220–228.
- [5] S. Malato, P. Fernandez-Ibanez, M.I. Maldonado, J. Blanco and W. Gernjak. Decontamination and disinfection of water by solar photocatalysis: Recent overview and trends. *Catal. Today.* 147, (2009) 1–59.
- [6] C. P. Rodrigues, R. L. Ziolli and J. R. Guimaraes. Inactivation of *Escherichia coli* in Water by  $\text{TiO}_2$ -assisted Disinfection using Solar Light. *J. Braz. Chem. Soc.* 18, (2007) 126–134.
- [7] C. Tizaoui, K. Mezughi and R. Bickley. Heterogeneous photocatalytic removal of the herbicide clopyralid and its comparison with UV/ $\text{H}_2\text{O}_2$  and ozone oxidation techniques. *Desalination.* 273, (2011) 197–204.
- [8] T.E. Doll and F.H. Frimmel. Removal of selected persistent organic pollutants by heterogeneous photocatalysis in water. *Catal. Today.* 101, (2005) 195–202.
- [9] M.R. Hoffmann, S.T. Martin, W. Choi and D.W. Bahnemann. Environmental Applications of Semiconductor Photocatalysis. *Chem. Rev.* 95, (1995) 69–96.
- [10] A. Fujishima and K. Honda. Electrochemical Photolysis of Water at a Semiconductor Electrode. *Nature.* 238, (1972) 37–38.
- [11] A. Fujishima, T.N. Rao and D.A. Tryk. Titanium dioxide photocatalysis. *J. Photochem. Photobiol. C.* 1, (2000) 1–21.
- [12] A. Hagfeldt, M. Gratzel. Light-Induced Redox Reactions in Nanocrystalline Systems. *Chem. Rev.* 95, (1995) 49–68.
- [13] A.L. Linsebigler, G. Lu and J.T. Yates. Photocatalysis on  $\text{TiO}_2$  Surfaces: Principles, Mechanisms, and Selected Results. *Chem. Rev.* 95, (1995) 735–758.
- [14] A. Millis, S.L. Hunt. An overview of semiconductor photocatalysis. *J. Photochem. Photobiol. A.* 108, (1997) 1–35.

- [15] M. Gratzel. Conversion of sunlight to electric power by nanocrystalline dye-sensitized solar cells. *J. Photochem. Photobiol. A.* 164, (2004) 3-14.
- [16] B.R. Sankapal, S.D. Sartale, M.C. Lux-Steiner and A. Ennaoui. Chemical and electrochemical synthesis of nanosized TiO<sub>2</sub> anatase for large-area photon conversion. *C. R. Chimie.* 9, (2006) 702–707.
- [17] M. Takeuchi, K. Sakamoto, K. Tsujimaru and M. Anpo. Photo-induced Superhydrophilicity on TiO<sub>2</sub> Thin Films Prepared by an Ionized Cluster Beam Deposition Method. *Catal. Lett.* 131, (2009) 189–193.
- [18] G-T. Lim, K.H. Kim, J. Park, S-H. Ohk, J-H. Kim and D.L. Cho. Synthesis of carbon-doped photocatalytic TiO<sub>2</sub> nanopowders by AFD process. *J. Ind. Eng. Chem.* 16, (2010) 723–727.
- [19] K-Y. Chen, Y-W. Chen. Synthesis of Spherical Titanium Dioxide Particles by Homogeneous Precipitation in Acetone Solution. *J. Sol-Gel Sci. Techn.* 27, (2003) 111–117.
- [20] N. Shahruz, M.M. Hossain. Synthesis and size control of TiO<sub>2</sub> photocatalyst nanoparticles preparation using sol-gel method. *World Applied Sciences Journal*, 12, (2011) 1981-1986.
- [21] P. Billik, G. Plesch. Mechanochemical synthesis of anatase and rutile nanopowders from TiOSO<sub>4</sub>. *Mater. Lett.* 61, (2007) 1183–1186.
- [22] Y.V. Kolenko, B.R. Churagulov, M. Kunst, L. Mazerolles and C. Colbeau-Justin. Photocatalytic properties of titania powders prepared by hydrothermal method. *Appl. Catal. B: Environ.* 54, (2004) 51–58.
- [23] K.C. Patil, S.T. Aruna and T. Mimani. Combustion synthesis: an update. *Curr. Opin. Solid St. M.* 6, (2002) 507–512.
- [24] Y. Kitamura, N. Okinaka, T. Shibayama, O.O.P. Mahaney, D. Kusano, B. Ohtani and T. Akiyama. *Powder Technol.* 176, (2007) 93–98.
- [25] J.J. Moore, H.J. Feng. Combustion Synthesis of Advanced Materials: Part I. Reaction Parameters. *Prog. Mater. Sci.* 39, (1995) 243-273.
- [26] V. Hlavacek, J. Puszynski. Chemical Engineering Aspects of Advanced Ceramic Materials. *Ind. Eng. Chem. Res.* 35, (1996) 349–377.
- [27] K. Deshpande, A.S. Mukasyan and A. Varma. Direct Synthesis of Iron Oxide Nanopowders by the Combustion Approach: Reaction Mechanism and Properties. *Chem. Mater.* 16, (2004) 4896–4904.
- [28] C.M. Wang, H. Wu and S.L. Chung. Optimization of experimental conditions based on Taguchi robust design for the preparation of nano-sized TiO<sub>2</sub> particles by solution combustion method. *J. Porous Mater.* 13, (2006) 307-314.

- [29] M. S. Hedge, Giridhar Madras, K. C. Patil, Noble metal ionic catalysts. *Accounts. Chem. Res.* 42, (2009) 704-712.
- [30] G. Sivalingam, M.S. Hegde and G. Madras. Photocatalytic degradation of various dyes by combustion synthesized nano anatase TiO<sub>2</sub>. *Appl. Catal. B.* 45, (2003) 23-28.
- [31] K. Nagaveni, M.S. Hegde, N. Ravishankar, G.N. Subbanna and G. Madras. Synthesis and Structure of Nanocrystalline TiO<sub>2</sub> with Lower Band Gap Showing High Photocatalytic Activity. *Langmuir.* 20, (2004) 2900-2907.
- [32] C.H. Jung, J.Y. Park, S.J. Oh, H.K. Park, Y.S. Kim, D.K. Kim and J.H. Kim. Synthesis of Li<sub>2</sub>TiO<sub>3</sub> ceramic breeder powders by the combustion process. *J. Nucl. Mater.* 253, (1998) 203-212.
- [33] K. Nagaveni, G. Sivalingam, M.S. Hegde and G. Madras. Solar photocatalytic degradation of dyes: high activity of combustion synthesized nano TiO<sub>2</sub>. *Appl. Catal. B: Environ.* 48, (2004) 83-93.
- [34] G. Sivalingam, M.H. Priya and G. Madras. Kinetics of the photodegradation of substituted phenols by solution combustion synthesized TiO<sub>2</sub>. *Appl. Catal. B: Environ.* 51, (2004) 67-76.
- [35] M.H. Priya, Giridhar Madras. Kinetics of Photocatalytic Degradation of Phenols with Multiple Substituent Groups. *J Photoch. Photobio. A.* 179, (2006) 256-262.
- [36] Sounak Roy, T. Aarthi, M.S. Hegde and Giridhar Madras. Kinetics of Photocatalytic reduction of NO by CO with Pd<sup>2+</sup> ion substituted nano-TiO<sub>2</sub>. *Ind. Eng. Chem. Res.* 46, (2007) 5798-5802.
- [37] T. Aarthi, Giridhar Madras. Photocatalytic reduction of Metals in presence of Combustion Synthesized nano-TiO<sub>2</sub>. *Cat. Comm.* 9, (2008) 630-634.
- [38] G. Sivalingam, K. Nagaveni, Giridhar Madras and M.S. Hegde. Kinetics of Catalytic Degradation of Polycarbonate in Solution. *Ind. Eng. Chem. Res.* 42, (2003), 687- 691.
- [39] C. Youping, S. Hongqi, J.W Wanqin, X.U Nanping and Chin. *J. Chem. Eng.* 15, (2007) 178-183.
- [40] Shyan-Lung Chung, Ching-Mei Wang. Effect of Preparation Conditions on Visible Photocatalytic Activity of Titania Synthesized by Solution Combustion Method. *J Sol-Gel Sci Technol.* 57, (2011) 76-85.
- [41] M. Sathish, B. Viswanathan, R. P. Viswanath and Chinnakonda S. Gopinath. Synthesis, characterization, electronic structure, and photocatalytic activity of nitrogen-doped TiO<sub>2</sub> nanocatalyst. *Chem. Mater.* 17, (2005) 6349- 6353.
- [42] R. Asahi, T. Morikawa, T. Ohwaki, K. Aoki and Y. Taga. Visible-Light Photocatalysis in Nitrogen-Doped Titanium Oxides. *Science.* 293, (2001) 269-271.

- [43] X.Y. Tao, X.N. Wang and X. D. Li. Nanomechanical Characterization of One-Step Combustion-Synthesized  $\text{Al}_4\text{B}_2\text{O}_9$  and  $\text{Al}_{18}\text{B}_4\text{O}_{33}$  Nanowires. *Nano Lett.* 7, (2007) 3172-3176.
- [44] M.S. Hegde, G. Madras and K.C. Patil. Noble Metal Ionic Catalysts. *Acc. Chem. Res.* 42, (2009) 704-712.
- [45] A.S. Prakash, P. Manikandan, K. Ramesha, M. Sathiya, J.M. Tarascon and A.K. Shukla. Solution-Combustion Synthesized Nanocrystalline  $\text{Li}_4\text{Ti}_5\text{O}_{12}$  As High-Rate Performance Li-Ion Battery Anode. *Chem. Mater.* 22, (2010) 2857-2863.
- [46] N. Kalaiselvi, A. Manthiram. One-pot, glycine-assisted combustion synthesis and characterization of nanoporous  $\text{LiFePO}_4/\text{C}$  composite cathodes for lithium-ion batteries. *J. Power Sources.* 195, (2010) 2894-2899.
- [47] H-K. Ma, H-A. Yang. Combustion synthesis of titania nanoparticles in a premixed methane flame. *J. Alloys. Compd.* 504, (2010) 115–122.
- [48] S.T. Aruna, K.S. Rajam. Mixture of fuels approach for the solution combustion synthesis of  $\text{Al}_2\text{O}_3\text{-ZrO}_2$  nanocomposite. *Mater. Res. Bull.* 39, (2004) 157–167.
- [49] S. Sasikumar, R. Vijayaraghavan. Solution combustion synthesis of bioceramic calcium phosphates by single and mixed fuels-A comparative study. *Ceram. Int.* 34, (2008) 1373–1379.
- [50] R. Ianos, I. Lazau, C. Pacurariu and P. Barvinschi. Solution combustion synthesis of  $\text{MgAl}_2\text{O}_4$  using fuel mixtures. *Mater. Res. Bull.* 43, (2008) 3408–3415.
- [51] G. Sivalingam, M.H. Priya and Giridhar Madras. Kinetics of the photodegradation of substituted phenols by solution combustion synthesized  $\text{TiO}_2$ . *Appl. Catal. B: Environ.* 51, (2004) 67–76.
- [52] M.H. Priya, G. Madras. Photocatalytic degradation of nitrobenzenes with combustion synthesized nano- $\text{TiO}_2$ . *J. Photochem. Photobiol. A: chem.* 178, (2006) 1-7.
- [53] A. Daya Mani, V. Laporte, P. Ghosal and Ch. Subrahmanyam. Combustion synthesized  $\text{TiO}_2$  for enhanced photocatalytic activity under the direct sunlight-optimization of titanyl nitrate synthesis. *Mater. Res. Bull.* 47, (2012) 2415–2421.
- [54] N. M. Stover. Diphenyl Carbazide as a test for chromium. *J. Am. Chem. Soc.* 50, (1928) 2363-2366.
- [55] H. Irie, Y. Watanabe and K. Hashimoto. Nitrogen-concentration dependence on photocatalytic activity of  $\text{TiO}_{2-x}\text{N}_x$  powders. *J. Phys. Chem. B*, 107, (2003) 5483-5486.
- [56] Y. Choi, T. Umabayashi and M. Yoshikawa. Fabrication and characterization of C-doped anatase  $\text{TiO}_2$  photocatalysts. *J. Mater. Sci.* 39, (2004) 1837-1839.

- [57] A. V. Emeline, V. N. Kuznetsov, V. K. Rybchuk and N. Serpone. Visible-Light-Active Titania Photocatalysts: The Case of N-Doped TiO<sub>2</sub>S—Properties and Some Fundamental Issues, *Intern. J. Photoenergy*. 2008, 258394, DOI: 10.1155/2008/258394.
- [58] N. C. Saha, H. G. Tomkins. Titanium nitride oxidation chemistry: An x- ray photoelectron spectroscopy Study. *J. Appl. Phys.* 72, (1992) 3072-3079.
- [59] H. Zhang, X. J. Lv, Y. M. Li, Y. Wang and J. H. Li. P25-Graphene Composite as a High Performance Photocatalyst. *ACS Nano*, 4, (2010) 380-386.
- [60] X. J. Liu, L. K. Pan, T. Lv, T. Lu, G. Zhu, Z. Sun and C. Q. Sun. Microwave-assisted synthesis of ZnO–graphene composite for photocatalytic reduction of Cr(VI). *Catal.Sci. Technol.* 1, (2011) 1189-1193.
- [61] K. Nagaveni, G. Sivalingam, M.S. Hegde and Giridhar Madras. *Applied Catalysis B: Environmental*, 48 (2004) 83–93.
- [62] Fa-tang Li, Ye Zhao, Ying Liu, Ying-juan Hao, Rui-hong Liu and Di-shun Zhao. Solution combustion synthesis and visible light-induced photocatalytic activity of mixed amorphous and crystalline MgAl<sub>2</sub>O<sub>4</sub> nanopowders. *Chem. Eng. J.* 173, (2011) 750–759.
- [63] P.R. Gogate, A.B. Pandit. A review of imperative technologies for wastewater treatment I: oxidation technologies at ambient conditions. *Adv. Environ. Res.* 8, (2004) 501-551.
- [64] X.Q. Zhu, J.L. Zhang and F. Chen. Study on visible light photocatalytic activity and mechanism of spherical Bi<sub>12</sub>TiO<sub>20</sub> nanoparticles prepared by low-power hydrothermal method. *Appl. Catal. B: Environ.* 102, (2011) 316–322.
- [65] Houas A, Lachheb H and Ksibi M. Photocatalytic Degradation Pathway of Methylene Blue in Water. *Appl. Catal. B: Environ.* 31, (2001) 145–157.
- [66] FU Ping-feng, ZHAO Zhuo, PENG Peng and DAI Xue-gang. Photodegradation of Methylene Blue in a Batch Fixed Bed Photoreactor Using Activated Carbon Fibers Supported TiO<sub>2</sub> Photocatalyst. *The Chinese J Process Eng.* 8, (2008) 65-71.
- [67] S. F. Chen, G.Y. Cao. Study on the photocatalytic reduction of dichromate and photocatalytic oxidation of dichlorvos. *Chemosphere.* 60, (2005) 1308–1315.
- [68] N. Tewari, P. Vasudevan and B.K. Guha. Study on biosorption of Cr (VI) by *Mucor hiemalis*. *Biochem. Eng. J.* 23, (2005) 185–192.
- [69] G. Aragay, F. Pino and A. Merkoci. Nanomaterials for Sensing and Destroying Pesticides. *Chem. Rev.* 112, (2012) 5317–5338.
- [70] K.-H. Kim, S.-K. Ihm. Heterogeneous catalytic wet air oxidation of refractory organic pollutants in industrial wastewaters: A review. *J. Haz. Mater.* 186, (2011) 16–34.

- [71] F. Fu, Q. Wang. Removal of heavy metal ions from wastewaters: A review. *J. Environ. Manage.* 92, (2011) 407-418.
- [72] C.-H. Chiou, R.-S. Juang. Photocatalytic degradation of phenol in aqueous solutions by Pr doped TiO<sub>2</sub> nanoparticles. *J. Hazard. Mater.* 149, (2007) 1–7.
- [73] W. Kujawski, A. Warszawsk, W. Ratajczak, T. Porebski, W. Capata and I. Ostrowska. Removal of phenol from wastewater by different separation techniques. *Desalination.* 163, (2004) 287–296.
- [74] M.F. Fernandez, J.P. Arrebola, J. Taoufiki, A. Navalon, O. Ballesteros, R. Pulgar, J.L. Vilchez and N. Olea. Bisphenol-A and chlorinated derivatives in adipose tissue of women, *Reprod. Toxicol.* 24, (2007) 259–264.
- [75] M. Wang, M. Leitch and C. C. Xu. Synthesis of phenol–formaldehyde resol resins using organosolv pine lignins. *Eur. Polym. J.* 45, (2009) 3380–3388.
- [76] D. Fabbri, A. B. Prevot and E. Pramauro. Effect of surfactant micro structures on photocatalytic degradation of phenol and chlorophenols. *Appl. Catal. B- Environ.* 62, (2006) 21–27.
- [77] K. C. Patil. Combustion synthesis and properties. *Bull. Mater. Sci.* 16, (1993) 533-542.
- [78] S. R. Jain, K. C. Adiga and V. R. P. Verneker. A new approach to thermochemical calculations of condensed fuel-oxidizer mixtures. *Combust. Flame.* 40, (1981) 71-79.
- [79] A. D. Mani, B. R. Raju, N. Xanthopoulos, P. Ghosal, B. Sreedhar and Ch. Subrahmanyam. Effect of fuels on combustion synthesis of TiO<sub>2</sub> – Towards efficient photocatalysts for methylene blue oxidation and Cr (VI) reduction under natural sunlight. *Chem. Eng. J.* 228, (2013) 545–553.
- [80] B. Naik, K. M. Parida and C. S. Gopinath. Facile Synthesis of N- and S-Incorporated Nanocrystalline TiO<sub>2</sub> and Direct Solar-Light-Driven Photocatalytic Activity. *J. Phys. Chem. C.* 114, (2010) 19473-19482.
- [81] E. A. Clesceri, A. Greenberg. *Standard Methods For Examinations of Water and Wastewater.* 19th edn, APHA, AWWA and WEF, Washington, DC, 1995.
- [82] W. J. Ren, Z. H. Ai, F. L. Jia, L. Z. Zhang, X. X. Fan and Z. G. Zou. Low temperature preparation and visible light photo catalytic activity of mesoporous carbon-doped crystalline TiO<sub>2</sub>. *Appl. Catal. B- Environ.* 69, (2007) 138-144.
- [83] S. Sakthivel, H. Kwasch. Daylight Photocatalysis by Carbon-Modified Titanium Dioxide. *Angew. Chem. Int. Ed.* 42, (2003) 4908-4911.
- [84] T. Ohno, T. Tsubota, M. Toyofukum and R. Inaba. Photocatalytic Activity of a TiO<sub>2</sub> Photocatalyst Doped with C<sup>4+</sup> and S<sup>4+</sup> Ions Having a Rutile Phase Under Visible Light. *Catal. Lett.* 98, (2004) 255-258.



- [85] Y. Li, D.-S. Hwang, N. H. Lee and S.-J. Kim. Synthesis and characterization of carbon-doped titania as an artificial solar light sensitive photocatalyst. *Chem. Phys. Lett.* 404, (2005) 25-29.
- [86] Y.-H. Tseng, C.-S. Kuo, C.-H. Huang, Y.-Y. Li, P.-W. Chou, C.-L. Cheng and M.-S. Wong. Visible-light-responsive nano-TiO<sub>2</sub> with mixed crystal lattice and its photocatalytic activity. *Nanotechnol.* 17, (2006) 2490-2497.
- [87] S. Bekkouche, M. Bouhelassa, N.H. Salah and F.Z. Meghlaoui. Study of adsorption of Phenol on titanium oxide (TiO<sub>2</sub>), *Desalination.* 166, (2004) 355–362.
- [88] H. Kusic, N. Koprivanac, A.L. Bozic and I. Selanec. Photo-assisted Fenton type processes for the degradation of phenol: a kinetic study. *J. Hazard. Mater. B* 136, (2006) 632–644.
- [89] Y. Liu. Simultaneous oxidation of phenol and reduction of Cr(VI) induced by contact glow discharge electrolysis. *J. Haz. Mater.* 168, (2009) 992–996.
- [90] P. Neta, J. Grodkowski and A.B. Ross. Rate constants for reactions of aliphatic carbon-centered radicals in aqueous solution. *J. Phys. Chem. Ref. Data.* 25, (1996) 709–1050.
- [91] N. Narita, T. Tezuka. On the mechanism of oxidation of hydroxy cyclohexadienyl radicals with molecular oxygen. *J. Am. Chem. Soc.* 104, (1982) 7316–7318.
- [92] C. Walling. Intermediates in the reactions of Fenton type reagents. *Acc. Chem. Res.* 31, (1998) 155–157.
- [93] G.V. Buxton, J.R. Langan and J.R.L. Smith. Aromatic hydroxylation. 8. A radiation chemical study of the oxidation of hydroxycyclohexadienyl radicals. *J. Phys. Chem.* 90, (1986) 6309–6313.
- [94] A.K. Pikaev, L.I. Kartasheva, T.P. Zhestkova, T.K. Yurik, V.N. Chulkov, O.A. Didenko, D.K. Kim, Y. Kim and B. Han. Removal of heavy metals from water by electron-beam treatment in the presence of an hydroxyl radical scavenger. *Mendeleev Commun.* 7, (1997) 52–53.
- [95] M.K. Eberhardt. Radiation-induced homolytic aromatic substitution. IV. Effect of metal ions on the hydroxylation of nitrobenzene. *J. Phys. Chem.* 79, (1975) 1913–1916.
- [96] A. Hickling, M.D. Ingram. Contact glow-discharge electrolysis. *Trans. Faraday Soc.* 60, (1964) 783–793.
- [97] M. Al-Sheikhly, W.L. McLaughlin. The mechanisms of the reduction reactions of Cr(VI) in the radiolysis of acidic potassium and silver dichromate solutions in the presence or absence of acetic acid. *Int. J. Radiat. Appl. Instrum. C* 38, (1991) 203–221.

# Chapter 4-Section I

## Combustion synthesis of cadmium sulfide nanomaterials for efficient hydrogen production from water

### 4.1.1. Introduction

Emission of oxides of carbon due to the combustion of fossil fuels made the global warming a difficult task to handle [1]. As the fossil fuel reserves are depleting at a faster rate, there is an immediate need to look for renewable and/or clean energy sources that are free of carbon. In this context, research on direct utilization of solar energy has been increasing [2]. It is believed that in future, hydrogen may supersede the current non-renewable resources [3, 4]. The traditional steam methane reforming for hydrogen production is not an environmental friendly method and there is an immediate need to look for eco-friendly alternatives. Among the several methods for hydrogen production [5-7], photocatalytic water splitting is gaining much attention due to its sustainable and environmental benign nature [8]. However, the design of suitable materials that are active under sunlight still remains as a challenge.

Among the materials for harvesting solar energy, semiconductor nanostructures are gaining importance owing to their unique optical, electronic and catalytic properties. Cadmium sulfide with a direct band gap of 2.4 eV is one of the first semiconductors to be discovered. It is perhaps one of the most important electronic and optoelectronic materials with proven applications in solar cells, nonlinear optical devices and electronic devices [9-11]. CdS has been extensively studied as a photocatalyst for the degradation of organic dyes, but its usage in hydrogen production studies are rather limited due to its photo-corrosive nature [12,13].

Designing CdS nanomaterials with matching redox potentials for the aforementioned applications is of great interest in material science. Although a variety of techniques such as thermal evaporation, hydrothermal method, chemical vapor deposition, template method, thermal decomposition method and solvothermal process are reported for the preparation of CdS quantum dots, many of them demand complicated procedures, inert

conditions and longer reaction times [14,15]. In this context, combustion synthesis with less energy payback time (A key parameter in life cycle analyses of solar energy materials and devices) is receiving more attention, especially for the synthesis of oxides [16-18].

However, application of combustion synthesis for the synthesis of metal chalcogenides is not fully explored. To the best of our knowledge, this is probably the first attempt of metal sulfide synthesis by using solution combustion method. Present section discusses about the facile synthesis of C and N doped CdS nanomaterials. Synthesized CdS nanomaterials have been tested for the visible light driven hydrogen production from water in presence of sacrificial reagents.

#### **4.1.2. Experimental section**

The required quantities of precursors were calculated based on the oxidant/fuel (O/F) ratio obtained by using propellant theory. In a typical synthesis, aqueous solutions of cadmium nitrate and thiourea were mixed to form a homogeneous solution. Dehydration followed by combustion in a preheated furnace at 573 K resulted the product. Different oxidant/fuel ratios (O/F -1, 2, 3, 4 and 10) have been studied and the resulting CdS samples were labelled as CdS(1), CdS(2), CdS(3), CdS(4) and CdS(10), respectively.

##### **4.1.2.1. Characterization**

Cadmium sulfide samples were characterized to examine its structural, morphological, and optical properties. Phase purity and crystallinity of the as synthesized CdS samples were obtained from powder X-ray diffraction (PXRD) technique. Transmission electron microscopic images of the CdS(2) sample were recorded in order to further confirm the formation of hexagonal CdS and the particle size. Diffuse UV-Vis reflectance spectra of the prepared samples were recorded to understand the absorption of light in the visible region and to calculate the band gap of the materials. X-ray photoelectron spectroscopy studies were performed in order to confirm the C and N doping into the TiO<sub>2</sub> matrix. Raman spectra of the as synthesized samples were carried out to further confirm the formation of TiO<sub>2</sub>.

##### **4.1.2.2. Photocatalytic studies**

Photocatalytic water splitting under simulated visible light radiation was performed in a quartz round bottomed flask containing 100 ml water and 100 mg of the catalyst. The study was carried out in the presence of 1 M Na<sub>2</sub>S and 1M Na<sub>2</sub>SO<sub>3</sub> as the sacrificial reagents. Before addition of CdS catalyst, N<sub>2</sub> was bubbled for 30 min, followed by evacuation for 15 min to remove the dissolved gases. After adding CdS catalyst, the solution was stirred in dark for 30 min in order to facilitate the adsorption of water molecules on the CdS surface. It is worth mentioning that there is no appreciable reaction in the dark. All

studies were carried out under simulated visible light radiation with light intensity around 800-900 W/m<sup>2</sup>, as measured by Newport power meter. Hydrogen produced in the reaction was analyzed by using a Shimadzu gas chromatography (GC-2014) with a packed column. Every hour a 500 µl hydrogen gas was collected in a gas tight syringe (Hamilton) and analyzed.

### **4.1.3. Results and discussion**

#### **4.1.3.1. Powder X-ray diffraction (PXRD)**

Cadmium sulfide samples synthesized at various O/F ratios from 1 to 10 were characterized by PXRD to identify the phase purity and crystallite size. As shown in figure 4.1.1, except in the case of O/F ratio 1, pure CdS was observed for other ratios. CdS(1) with more intense diffraction peaks at d-spacing of 2.7, 2.4 and 1.7 Å confirms the existence of CdO. This can be attributed to insufficient fuel, thiourea. CdS(2) shows major peaks at  $2\theta = 28.2, 24.8, 43.7, 26.5$  and  $47.9^\circ$  corresponding to 101, 100, 110, 002 and 103 planes with the corresponding d- spacings of 3.6, 3.4, 3.2, 2.1 and 1.9 Å respectively representing the hexagonal phase of CdS. From the figure 4.1.1 it was observed that CdS(3) and CdS(4) also has diffraction peaks corresponding to the hexagonal phase. However in the case of CdS(3) the peaks corresponding to (101), (100) and (002) planes seem overlapped due to the small crystallite size (around 14 nm). However, for CdS(4) and CdS(10), these peaks are distinguishable due to large crystallite size (around 25 nm). Generally, broadening of diffraction peak may be due to one of the following factors such as micro strain (deformations of the lattice), crystalline faults (extended defects), crystalline size and domain size distribution [19-21]. The average crystallite sizes of the CdS samples calculated by using scherrer formula were found to be 58, 70, 14, 20 and 25 nm for CdS(1), CdS(2), CdS(3), CdS(4) and CdS(10), respectively. Larger crystallite size in case of CdS (2) may be explained on the basis of optimum O/F ratio, which facilitates the combustion and provides high temperatures for the crystal growth [13].

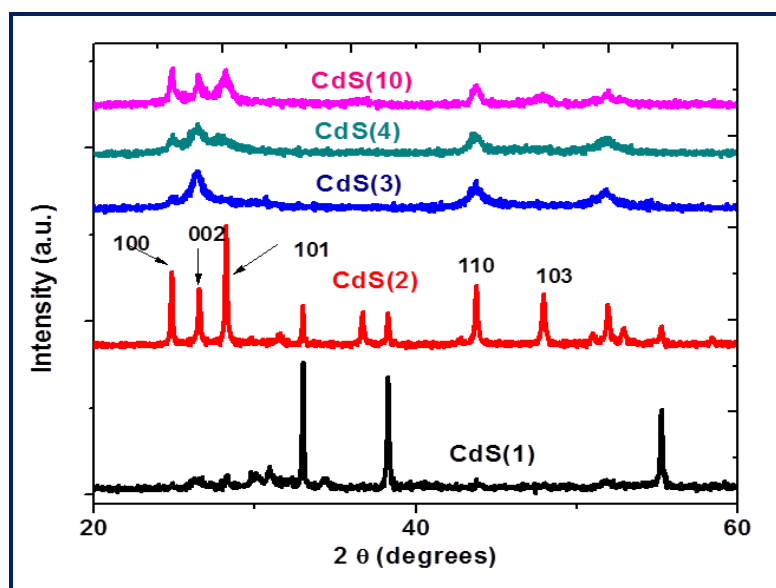


**Figure 4.1.1.** Powder X-ray diffraction patterns of the cadmium sulfide samples  
**4.1.3.2. Transmission electron microscopy (TEM)**

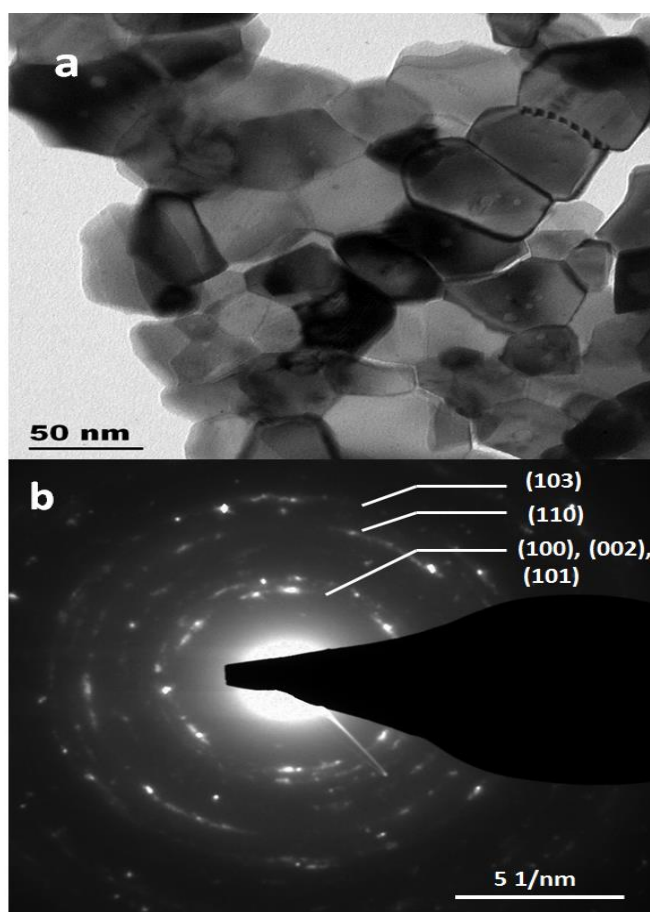


**Fig.4.1.2.** (a) TEM images of the best active CdS(2) sample (b) Selected area electron diffraction pattern of CdS(2) sample.

In order to confirm the phase and crystallite size, TEM studies were carried out for CdS(2) sample. From figure 2(a) it was clear that CdS(2) sample consists of some irregular shaped crystalline nanoparticles. The particle size was found to be around 70 nm which is in good agreement with the PXRD results. The selected area electron diffraction pattern (figure 2(b)) with the d-spacing corresponding to the planes (100), (002), (103) and (110) confirmed the hexagonal CdS phase which is also good agreement with the PXRD results.

#### 4.1.3.3. Diffuse reflectance UV-Vis spectral studies

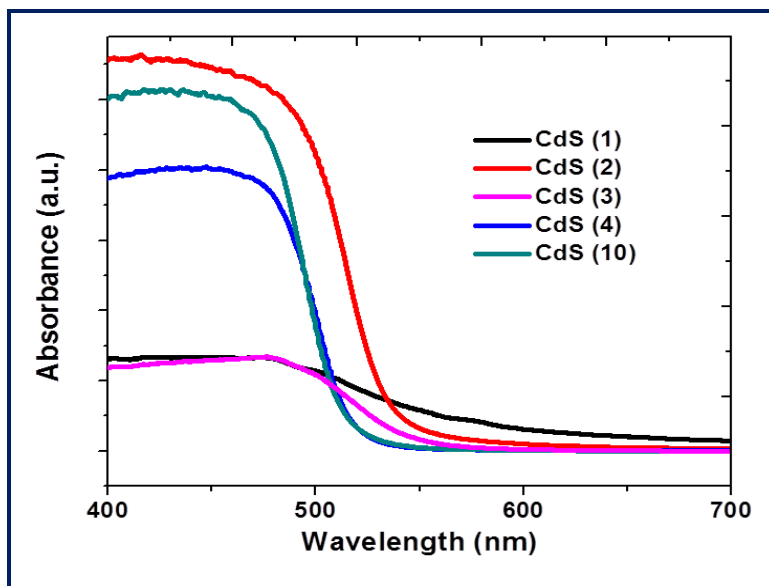


**Figure 4.1.3.** Diffuse reflectance UV-Vis spectra of CdS samples

It is well known that CdS is a direct band gap semiconductor with band gap energy of 2.4 eV. A red shift in the absorption due to the C and N doping was recognized from the absorption spectra of the combustion synthesized CdS samples (Fig. 4.1.3). Band gap energies of CdS(1), CdS(2), CdS(3), CdS(4) and CdS(10) samples were found to be 2.0, 2.2, 2.3, 2.4 and 2.4 eV, respectively. The band gap energy of 2.0 eV in case of CdS(1) could be attributed to the C and N doped CdO (band gap of CdO is 2.16 eV). Among CdS(2), CdS(3), CdS(4) and CdS(10) samples, CdS(2) was found to have a low band gap of 2.2 eV, probably due to more C and N doping compared to the rest of the samples and with increasing O/F ratio from 3 to 10 band gap again increased to the original value of 2.4 eV due to fuel rich conditions, which hindered proper combustion.

#### 4.1.3.4. X-ray photoelectron spectroscopy (XPS)

In order to confirm the presence of C and N as dopants, XPS study of CdS (2) sample was carried out and the spectra are shown in Fig. 4.1.4. As evident from figure 4.1.4(a), Cd (3d) spectra showed two peaks centered at 405.2 and 411.9 eV characteristic of Cd 3d<sub>5/2</sub> and Cd 3d<sub>3/2</sub>, respectively [22-25]. Whereas the S 2p peak observed at 161.5 eV

and 162.7 eV as shown in Fig. 4.1.5(b) inferred the existence of sulfides. The absence of peaks centered at 165 and 170 eV reveals the existence of sulfur in the non-oxidized form.

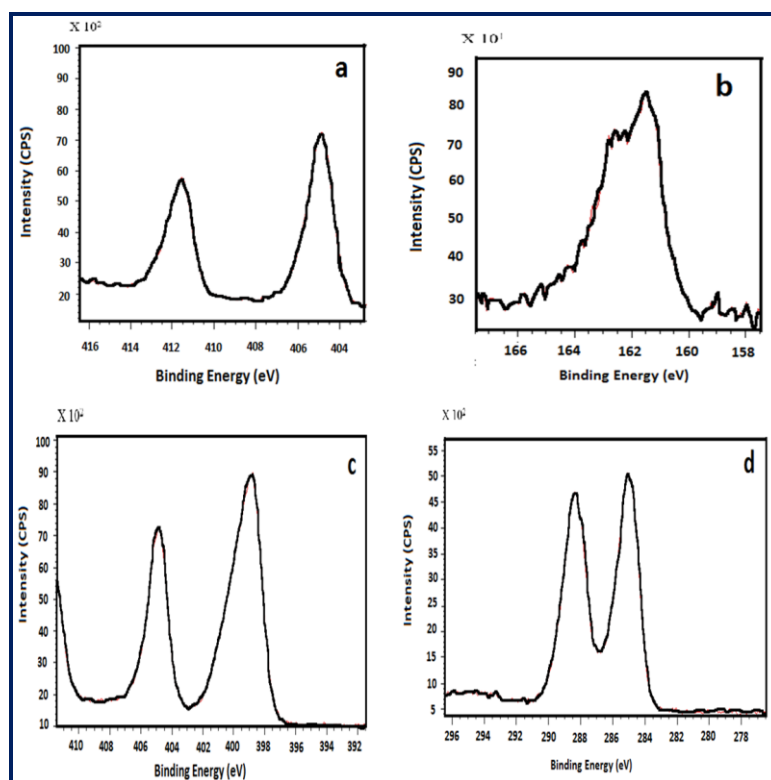


**Figure 4.1.4.** XPS spectra of (a) Cd 3d core levels (b) S 2p core levels (c) C 1s core levels (d) N 1s core levels of CdS (2) sample

Presence of C as a dopant was clearly shown by the peaks at 285 and 289 eV in the C 1s spectra as represented in Fig. 4.1.4(c). The former peak might be due to the aliphatic carbon whereas the latter one was due to the C bonded with O and/or S either with a double bond or two single bonds [26]. Similarly, evidence for nitrogen doping was provided from the N(1s) spectra that showed two peaks at 399.7 eV and 405 eV (Fig. 4.1.4(d)). Literature data confirmed that the binding energy of the N1s was very sensitive to the chemical environment of the nitrogen and it varies from 396 to 408 eV [27]. The peaks observed at 399.7 eV corresponds to the terminally bonded well screened molecular nitrogen ( $\gamma$ -N<sub>2</sub>), whereas, the 405 eV peak might be due to terminally bonded poorly screened molecular nitrogen ( $\gamma$ -N<sub>2</sub>) [28].

#### 4.1.3.5. Raman spectra

Hexagonal CdS is one of the simple uniaxial structures that can be analyzed by Raman scattering phenomena [29]. Figure 4.1.5(a) presents the Raman spectra of the synthesized CdS samples, whereas figure 4.1.5(b) and 4.1.5(c) showed the enlarged views of the A11LO and AL2LO phonon modes of CdS, respectively.

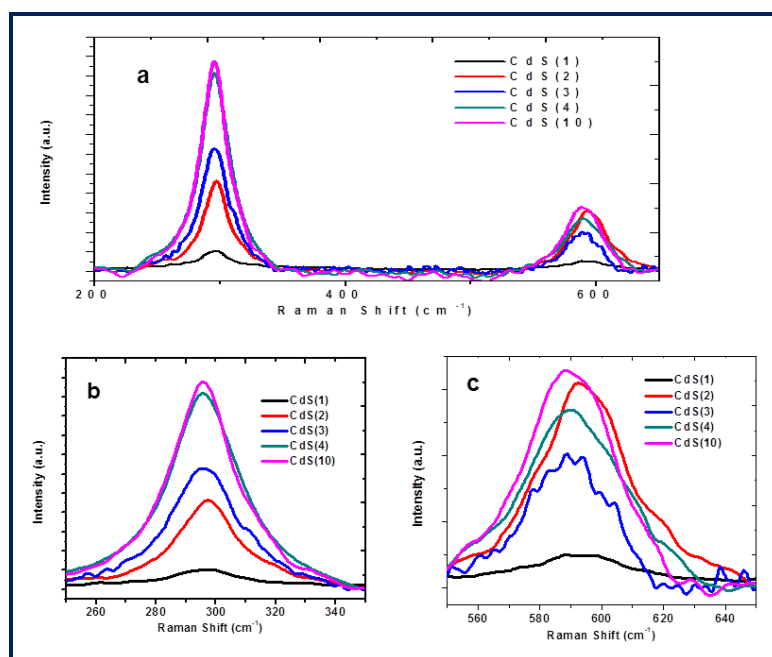


**Figure 4.1.5.** (a) Raman spectra of CdS samples (b) Enlarged view of A1 1LO phonon mode of CdS samples (c) Enlarged view of A1 2LO phonon mode of CdS samples

It represents two distinct Raman bands in the spectral region of 200 to 700  $\text{cm}^{-1}$ . The Raman bands at 299 and 600  $\text{cm}^{-1}$  correspond to the A1 1LO (longitudinal optical) and A1 2LO phonons, respectively [29-33] and the intensity of A1 2LO phonon at 600  $\text{cm}^{-1}$  was lower compared to the intensity of A1 1LO mode at 299  $\text{cm}^{-1}$  [34]. As seen clearly from Fig. 4.1.5(b) and 4.1.5(c) that with increasing O/F ratio, the peak shifted to lower frequency region and FWHM increased due to the difference in the crystallite sizes.

#### 4.1.3.6. Photocatalytic studies

Since CdS is well known for its visible light activity and also the in-situ doping of C and N into the CdS has been confirmed, visible light activity of the CdS was tested for hydrogen production from water. Although CdS has good absorption in the visible region, its photo corrosive nature limits its application in  $\text{H}_2$  production [35]. In order to reduce the photocorrosion of CdS and to prevent the recombination of excitons, 1M  $\text{Na}_2\text{S}$  and 1M  $\text{Na}_2\text{SO}_3$  are used as sacrificial reagents. These sacrificial reagents may interact with the holes that prevent the photocorrosion of CdS catalyst [35].  $\text{H}_2$  production studies were carried out with all the CdS samples and the typical results shown in Fig. 4.1.6 confirmed the formation of 1215, 2135, 1800, 1590 and 1345  $\mu\text{mol/h}$  of hydrogen, respectively for CdS(1), CdS(2), CdS(3), CdS(4) and CdS(10). These results confirmed that the highest hydrogen evolution was achieved for CdS(2). In order to assess the stability of CdS(2) photocatalyst for hydrogen production, the activity was monitored for 25 hours by



evacuating the reactor after every 5 h and the results are shown in Fig. 4.1.7. After 25 h, the decrease in H<sub>2</sub> production was found to be approximately 10 % confirming the reasonable stability of the catalyst. The best activity of CdS(2) can be attributed to the higher crystallinity and low band gap, due to which it has the best absorption in the visible region.

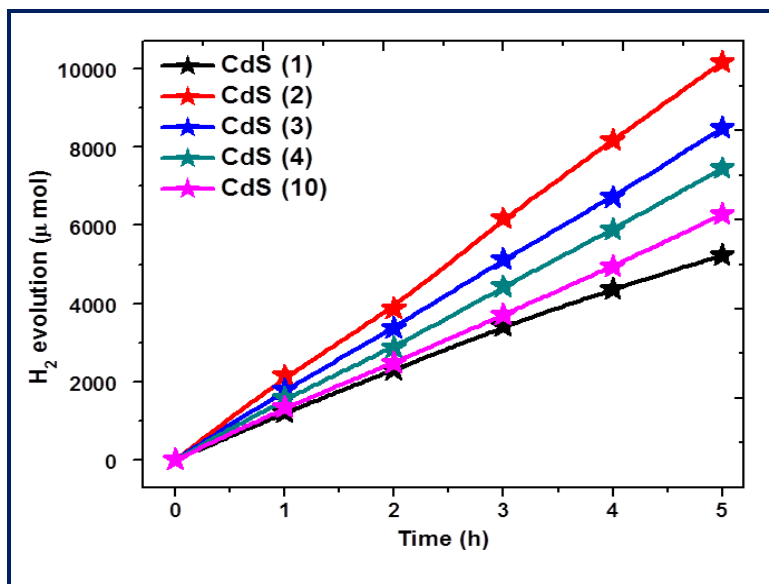


**Fig.4.1.6.** Rate of photocatalytic H<sub>2</sub> evolution from splitting of water containing Na<sub>2</sub>S and Na<sub>2</sub>SO<sub>3</sub> sacrificial reagents under visible light in the presence of different CdS samples

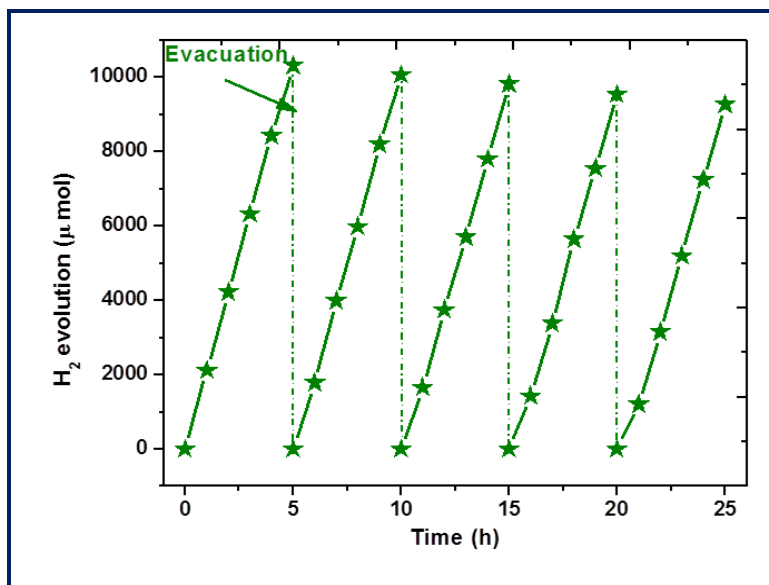


**Fig.4.1.7.** Rate of H<sub>2</sub> evolution profiles from water containing Na<sub>2</sub>S and Na<sub>2</sub>SO<sub>3</sub> sacrificial agents in the presence of CdS (2) (five runs in a continuous reaction were shown)

#### 4.1.4. Conclusions

Synthesis of C and N doped nanocrystalline CdS has been reported by using solution combustion synthesis without using any surfactants and tedious procedure.

Variation of O/F ratios between 1 and 10 revealed that the sample synthesized at O/F ratio of 2 had the best photocatalytic activity. Efficient hydrogen production of 2120  $\mu\text{mol/h}$  from water containing 1M  $\text{Na}_2\text{S}$  and 1M  $\text{Na}_2\text{SO}_3$  as sacrificial agent under visible irradiation complemented the synthesis approach. The best activity of CdS(2) may be attributed to the good absorption in the visible region, resistance to photocorrosion and prevention of exciton recombination by the dopant energy levels.

# **Chapter 4- Section II**

## **Efficient C, N doped ZnS with rice grain morphology for visible light photocatalytic activity**

### **4.2.1. Introduction**

Although  $\text{TiO}_2$  is proved to be the best photocatalyst under UV radiation, development of highly active photocatalysts that are active under the natural sunlight is still remains as a difficult task. There is a great demand for the synthesis of oxide and sulfide semiconductors that have high absorption in the visible radiation. Among them, ZnS is gaining interest owing to its favorable conduction band energy levels, and high theoretical efficiency of photo carrier generation than  $\text{TiO}_2$  [36,37].

Even though ZnS nanomaterials with different morphologies have been reported by chemical or physical methods, these methods either use the expensive templates or the process is limited by low production yields [38-40]. In spite of the preferred negative reduction potential of zinc sulfide that favors hydrogen production, its high band gap becomes a thorn for its photocatalytic activity under solar light. Several studies have been carried out to increase visible light activity of ZnS by doping with metal ions and nonmetals [41, 42].

Combustion synthesis, a known method for the synthesis of oxide materials is gaining interest due to several advantages like shorter reaction times, non-expensive precursors, high surface area materials and in-situ anion doping [16, 43-47]. In the previous section combustion synthesis of CdS nanomaterials has been reported. In this section the technique has been extended to wide band gap sulfide i.e. ZnS. Therefore the present section deals with the synthesis of C and N doped zinc sulfide nanomaterials that are active under visible light. The visible light activity is assessed by the individual as well as simultaneous removal of Cr(VI) and methylene blue (MB) from aqueous solutions under natural sunlight. Also,  $\text{H}_2$  production from water containing  $\text{Na}_2\text{S}$  and  $\text{Na}_2\text{SO}_3$  sacrificial reagents was studied under simulated solar light.

## **4.2.2. Experimental section**

### **4.2.2.1. Synthesis of C, N doped ZnS nanomaterials**

The instant synthesis of zinc sulfide is as follows: Different ratios (1:2 to 1:6) of zinc and sulfur precursors were used to prepare ZnS nanomaterials. In a typical synthesis aqueous solutions of zinc nitrate (oxidant) and thio urea (fuel) were mixed in a quartz bowl and preheated on a hot plate until a viscous mass has been obtained, which was then transferred to a preheated furnace at 623 K. In 5 min a yellow color material was obtained that is ready to be used for further photocatalytic studies. The samples were labeled as ZnS(1:2), ZnS(1:3), ZnS(1:4), ZnS(1:5) and ZnS(1:6).

### **4.2.2.2. Characterization**

Powder X-ray diffraction (PXRD) patterns of the as prepared zinc sulfide nanomaterials were recorded to know the formation of zinc sulfide and crystallite size. The average crystallite sizes of the ZnS photocatalysts were calculated with the scherrer equation with the full width at half maxima (FWHM) data. High resolution transmission electron microscopy (HRTEM) images of the combustion synthesized zinc sulfide photocatalysts were recorded in order to further confirm the particle size, morphology and phase formation. Diffuse UV-Vis reflectance spectra of the samples were measured to know the band gap of the materials.

The thermo-gravimetric analyses (TGA) of the as synthesized catalysts were recorded on TG/DTA, TA Instruments SDT Q600 in air flow from room temperature to 1173 K at a heating rate of 283 K min<sup>-1</sup>. Percentage of C and N doped into the ZnS matrix was determined by using Euro EA elemental analyzer with sulfamethazine as a standard material which consists of 51.8 % C, 5.1 % H, 20.1 % N and 11.5 % S. X-ray photoelectron spectroscopic analysis of the samples were performed on Axis Ultra instrument under ultra-high vacuum condition (<10<sup>-8</sup> Torr) and by using a monochromatic Al K $\alpha$  X-ray source (1486.6 eV).

Photocatalytic activity of the rice grain shaped zinc sulfide nano structures has been investigated by the individual and simultaneous removal of MB and Cr(VI) pollutants under the sunlight between 11 am to 1 pm. Before the exposure to sunlight, test solutions with photocatalyst were placed in dark in order to achieve equilibrium conditions. During the light exposure, every 15 min small aliquots were collected, centrifuged at an rpm of 2000 and the catalyst particles were separated by filtering with milli Q membrane filters. Thereafter MB and Cr(VI) were estimated by using UV-Vis spectrophotometer. At regular intervals of time the degradation of dye was monitored by the absorbance at 664 nm by

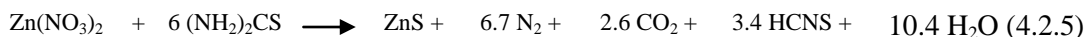
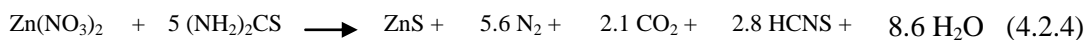
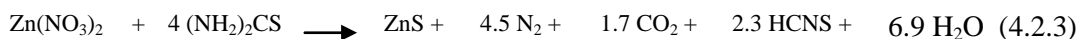
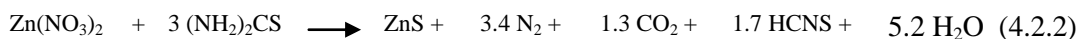
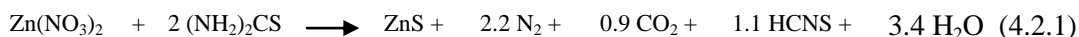
using UV-Vis absorption spectroscopy. Cr(VI) was estimated at 540 nm by forming a purple coloured complex with 1, 5- diphenyl hydrazide solution in acidic media [48].

The visible light activity of the ZnS photocatalysts was also estimated by the H<sub>2</sub> production experiments from water containing 1 M Na<sub>2</sub>S and 1 M Na<sub>2</sub>SO<sub>3</sub> as sacrificial agents under simulated solar light. H<sub>2</sub> production experiments were carried out in a photo reactor which consists of three 250 W halogen lamps. The intensity of the light falling on the sample cells was found to be 850-900 W/m<sup>2</sup> as measured by using Newport optical power/energy meter (Model 842. PE). The reaction cell was a quartz round bottomed flask containing 100 ml water and 100 mg of catalyst. Before addition of ZnS catalyst, N<sub>2</sub> was bubbled for 15 min, followed by evacuation for 15 min to remove the dissolved gases. After addition of the catalyst, the solution was stirred in dark for 30 min in order to facilitate the adsorption of water molecules on the ZnS surface. Hydrogen produced in the reaction was analyzed by using gas chromatography (GC-2014) with packed column by using N<sub>2</sub> as the carrier gas. Every hour a 500 µl hydrogen gas was collected in a gas tight syringe (Hamilton) and injected into the GC column. The experiments performed both in dark and without catalyst in presence of light did not produce any hydrogen.

### 4.2.3. Results and discussion

#### 4.2.3.1. Formation mechanism of C and N doped ZnS

The synthesis of ZnS may proceed via the formation and decomposition of the zinc thiourea complex (Zn-(SC(NH<sub>2</sub>)<sub>2</sub>)<sub>2</sub>(NO<sub>3</sub>)<sub>2</sub>). Therefore, in a typical tetrahedral or distorted tetrahedral Zn thiourea complex, SC(NH<sub>2</sub>)<sub>2</sub> is coordinated to zinc through the sulfur atom, forming ZnS<sub>4</sub> groups [49]. As the nitrate is a monodentate ligand, it may be coordinated to zinc through the oxygen atom. Since the first coordination sphere of zinc complex contains, along with thiourea, the NO<sub>3</sub><sup>-</sup> anion, under the experimental conditions, thermal decomposition of Zn(SC-(NH<sub>2</sub>)<sub>2</sub>)(NO<sub>3</sub>)<sub>2</sub> complexes results in the formation of C and N doped ZnS nanomaterials through the following reactions [50,52]. From the following reactions it is clear that with increasing ratio of sulfur precursor, the evolved gases also increases that also increases the amount of C and N doping in the ZnS matrix. This is consistent with the elemental analysis data.



#### 4.2.3.2. PXRD

Powder X-ray powder diffraction (PXRD) patterns of the ZnS samples as shown in figure 4.2.1 reveal the phase and crystallinity of ZnS nanostructures. The diffraction patterns of ZnS (1:2) to ZnS (1:6) can be indexed to the hexagonal ZnS (JCPDS card no 80-0007). From figure 4.2.1 it is observed that the diffraction peaks of (100) and (101) were overlapped with (002) diffraction peak due to peak broadening. The significant broadening of the diffraction peaks is ascribed to the very small crystallite size with in the rice grain morphology. Moreover it is observed that the crystallinity of the ZnS samples also increased from ZnS (1:2) to ZnS (1:6).

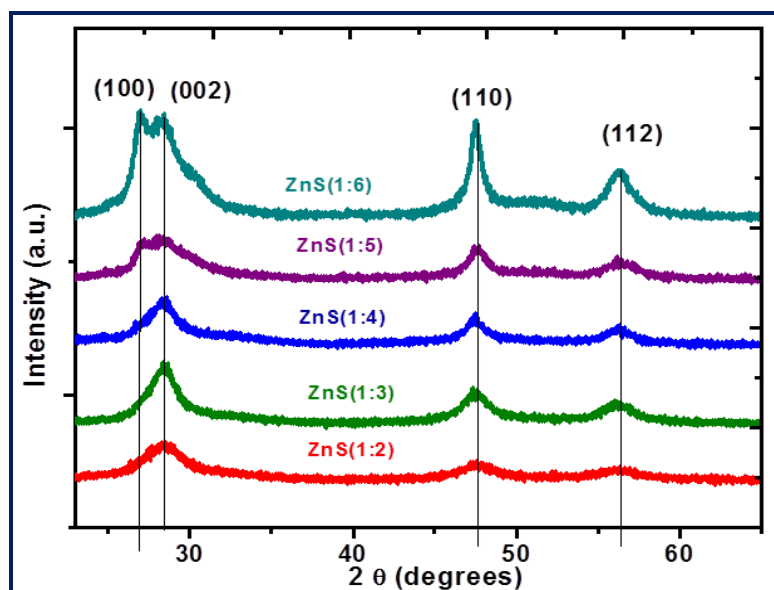


Fig.4.2.1. Powder X-ray diffraction patterns of zinc sulfide samples

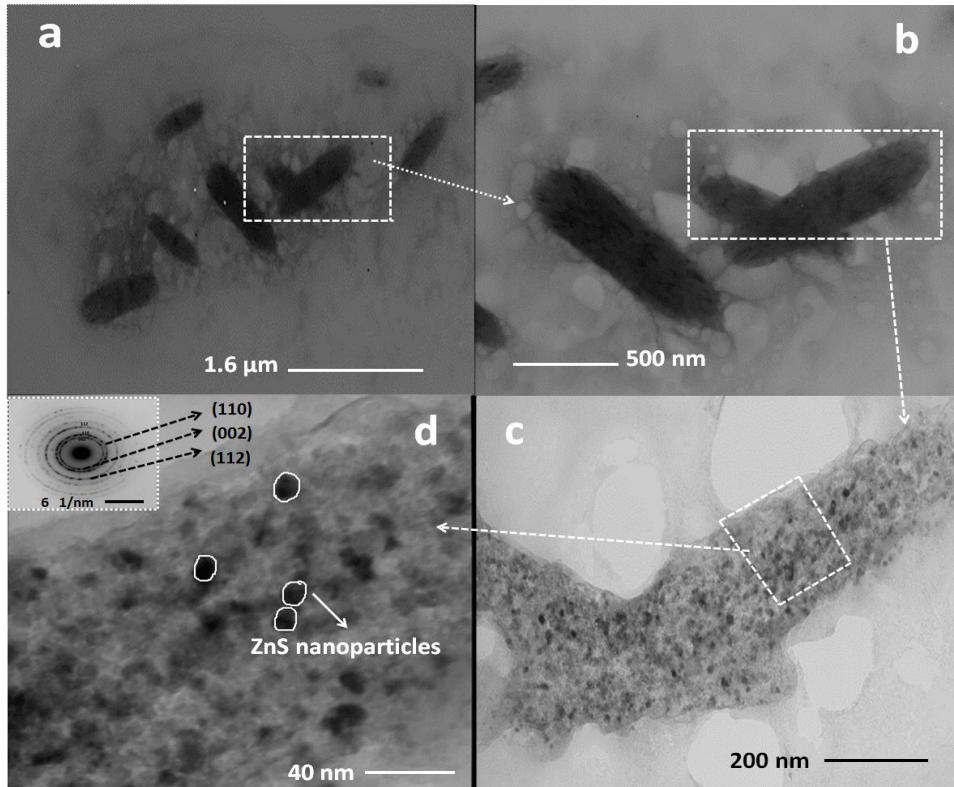
#### 4.2.3.3. TEM

Figure 4.2.2(a) shows a low magnification TEM image of the ZnS(1:5) sample. It clearly shows that the sample is composed of well dispersed rice grain shaped microstructures which consist of several nanoparticles of ZnS. The average size of the rice grain structure was around 1 $\mu$ m as observed from Fig. 4.2.2 (b). The high magnification TEM image, as shown from Fig. 4.2.2(c) to 2(d) shows that the rice grain shaped microstructures consist of several nanoparticles with a size of 10 nm which are assembled in a rice grain shaped structural configuration. Selected area electron diffraction (SAED) pattern of ZnS rice grain structures presented in the inset of Fig. 4.2.2(d) confirms (002), (110) and (112) planes which are characteristic of hexagonal ZnS phase.

#### 4.2.3.4. Diffuse reflectance UV-Vis spectral analyses

Diffuse reflectance UV-Vis spectra of the ZnS samples are shown in Fig.4.2.3. A red shift in the absorption edge when compared to the conventional ZnS (3.7 eV) may be

due to the in-situ C and N doping into the ZnS matrix during the combustion synthesis. The absorption onsets of all the combustion synthesized nano ZnS samples (430–460 nm) show significant red shifts ( $DE = 0.7\text{--}0.9\text{ eV}$ ) with respect to that of bulk ZnS (onset- 350 nm) [52]. The onset edges for ZnS (1:2), ZnS (1:3), ZnS (1:4) ZnS (1:5) and ZnS (1:6) were calculated to be 3.0, 2.8, 2.8, 2.8 and 2.8 eV, respectively.



**Figure 4.2.2.** TEM image of ZnS rice grain microstructures (b) Enlarged view of the selected portion from figure 2(a). (c) Enlarged portion of rice grain shaped ZnS showing several nanoparticles (d) Further magnified view of the selected portion in figure 2(c) showing distinct nanoparticles of ZnS (inset shows selected area diffraction pattern of ZnS)

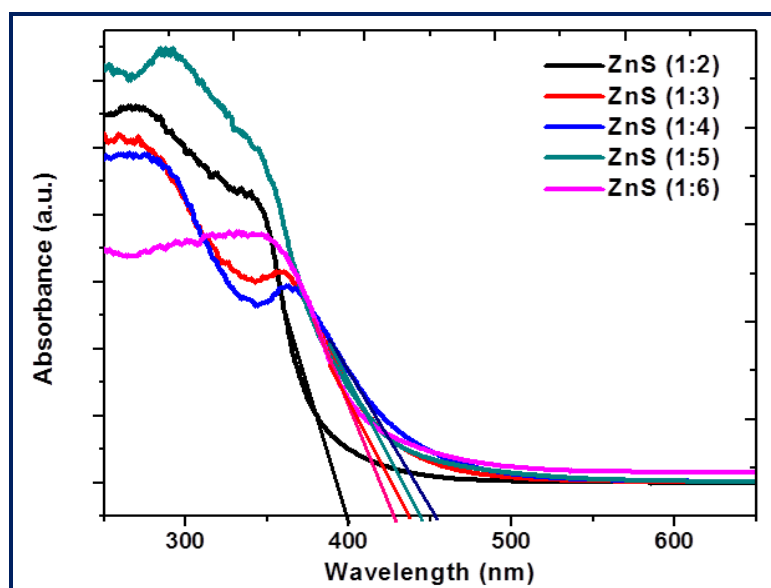


**Fig.4.2.3.** Diffused reflectance UV-Vis spectra of ZnS samples

#### 4.2.3.5. X-ray photoelectron spectroscopy (XPS)

The composition and C, N doping in the ZnS matrix was further investigated by XPS. Figure 4.2.4 shows the XPS spectra of ZnS (1:5) sample. The observed binding energies at 1045.0 and 1022.31 eV respectively corresponds to the Zn 2p<sub>1/2</sub> and Zn 2p<sub>3/2</sub> peaks (Fig. 4.2.4(a)) whereas S 2p spectra shown in figure 4.2.4(b) confirms a peak at 160.86 eV corresponding to the existence of sulfides [53].

XPS studies also revealed the presence of both C and N in ZnS nanomaterials. The N 1s (Fig. 4.2.4(c)) spectrum indicated two peaks which appeared at around 399.3 and 402.2eV that were attributed to Zn-N and/or C≡N bonds [54-57]. This is consistent with the literature observations, where the Zn-N bond of Zn<sub>3</sub>N<sub>2</sub> and ZnO<sub>1-x</sub>N<sub>x</sub> was observed at 396.2 and 399.1 eV, respectively. [56,57]. Therefore, the peak at 399.3 eV in Fig. 4.2.4(c) may be due to the Zn-N bond of ZnS<sub>1-x</sub>N<sub>x</sub> [42]. The slight chemical shift might be due to the surface strain and lattice distortion induced by the incorporation of nitrogen and carbon [58]. The peak appeared at 402.2 eV, may be attributed to an oxidized form of nitrogen or molecularly chemisorbed nitrogen ( $\gamma$ -N<sub>2</sub>) [56,59].

Figure 4.2.4(d) shows the C 1s spectra of ZnS (1:5) catalyst. The peaks observed at 286.0 and 287.5 eV in Fig. 4.2.4(d) can be attributed to C-N and C≡N bonds, respectively. The absence of peaks between 289.4 and 292.5 eV revealed the absence of C-O and O=C-O bonds, which is consistent with XRD observations that ZnS is free of ZnO impurity [55, 60]. The peak at 284.5 eV may be attributed to the elemental carbon (C-C) bond [61].

From the XPS studies it is concluded that the doping of carbon and nitrogen may be interstitial doping since the concentrations of dopants are relatively higher in the catalysts as



observed from the CHNS analysis. Therefore XPS results and the higher N:C ratio observed in the elemental analysis suggests the possibility of Zn-N-C-N type linkage. Both the Zn and S atoms in the wurtzite structure are four coordinated and the structure is composed of alternating planes of four coordinated  $S^{2-}$  and  $Zn^{2+}$  ions [62]. Therefore we speculate that the N-C-N linkage could bond with zinc and/or sulfur atom in the same plane or two adjacent planes and could also exist in the interface of the planes, which may open a door for the possibility that N and C induce a higher energy band contributed by the localized N 2p and C 2p states. The amount of nitrogen and carbon is relatively higher in the synthesized catalysts, which reflects in the red shift in the band gap of ZnS from 3.6 to 2.8 eV.

#### 4.2.3.6. CHNS elemental analyses

In order to analyze the weight percentage of C and N present in the combustion synthesized ZnS photocatalysts CHNS elemental analysis was carried out. The % C was found to be 6.8, 9.2, 13.1, 16.2, and 18.3 respectively for ZnS (1:2), ZnS (1:3), ZnS (1:4), ZnS (1:5) and ZnS (1:6) and the corresponding % of N was 10.4, 14.7, 22.8, 27.7 and 29.1. Thus the C and N doping in all the photocatalysts was also evidenced by elemental analyses.

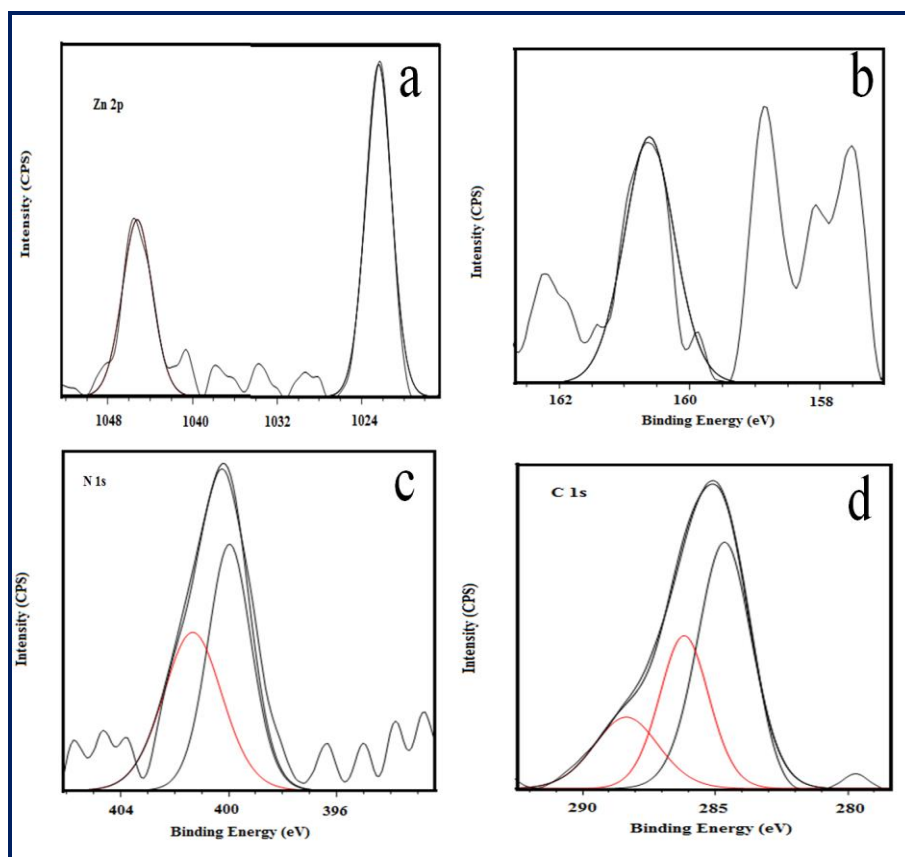


**Fig.4.2.4.** XPS spectra of (a) Zn 2p (b) S 2p (c) N 1s and (d) C 1s core levels

#### **4.2.3.7. Photocatalytic activity**

##### **4.2.3.7.1. Photocatalytic oxidation of MB**

Photocatalytic activity of ZnS was estimated for the oxidation of methylene blue and reduction of chromium(VI) and the results are compared with a commercial photocatalyst (Evonik P25 TiO<sub>2</sub>). Figure 4.2.5(a) shows the first order kinetic plots for the oxidation of methylene blue under natural sunlight and the first order rate constant calculated was found to be 0.0039, 0.013, 0.015, 0.02, 0.026 and 0.021 min<sup>-1</sup> respectively for Evonik P-25 TiO<sub>2</sub>, ZnS(1:1), ZnS(1:2), ZnS(1:3), ZnS(1:4), ZnS(1:5) and ZnS(1:6). From this, it can be concluded that from ZnS (1:2) to ZnS (1:5) the activity steadily increased and thereafter it decreased slightly for ZnS(1:6). It clearly shows that ZnS(1:5) has highest activity among the ZnS samples.

##### **4.2.3.7.2. Effect of pH on photocatalytic oxidation of MB**

It is well known that pH of the medium can influence the rate of photocatalytic degradation of organic pollutants present in waste water. Figure 4.2.5(b) shows first order kinetic plots for the photocatalytic oxidation of MB at different pH of the solution. The observed rate constants are found to be 0.25, 0.12, 0.026, 0.01 and 0.007 min<sup>-1</sup> respectively at pH 11, 9, 7, 4 and 2. From this, it may be concluded that basic pH favors the degradation of MB. This observation can be explained as follows: The pH of the solution affects the formation of hydroxyl radical, the primary oxidant during the photocatalytic process. It is well known that at higher pH the concentration of OH<sup>-</sup> ions will be more, which favors the formation of the HO<sup>•</sup>, thereby resulting in an increased photocatalytic degradation efficiency of MB [63]. On the other hand pH may also modify the electrical double layer of the solid electrolyte interface, which affects the adsorption-desorption processes and separation of the photogenerated electron-hole pairs on the surface of catalyst particles [64]. In general the surface of photocatalysts are found to be positively charged in acidic solutions and negatively charged in alkaline solutions [65]. As a result, the efficiency of the MB degradation is expected to increase with pH owing to the electrostatic interaction between the negatively charged photocatalyst surface and MB cations. In addition to the above explanations higher pH also proved to be favorable for the oxidation of sulfur containing organic pollutants (MB) and hence may decrease the deactivation of catalyst [66].

##### **4.2.3.7.3. Photocatalytic reduction of Cr(VI)**

The photocatalytic activity of ZnS catalysts was also tested for the photocatalytic reduction of Cr(VI) under natural sunlight and the results are presented in Fig. 4.2.6 (a), which confirms first order kinetics. The corresponding first order rate constants were found

to be 0.028, 0.036, 0.058, 0.1, 0.07  $\text{min}^{-1}$  respectively for ZnS (1:2), ZnS (1:3), ZnS (1:4), ZnS (1:5) and ZnS(1:6). Thus during the reduction process also ZnS (1:5) shows higher activity.

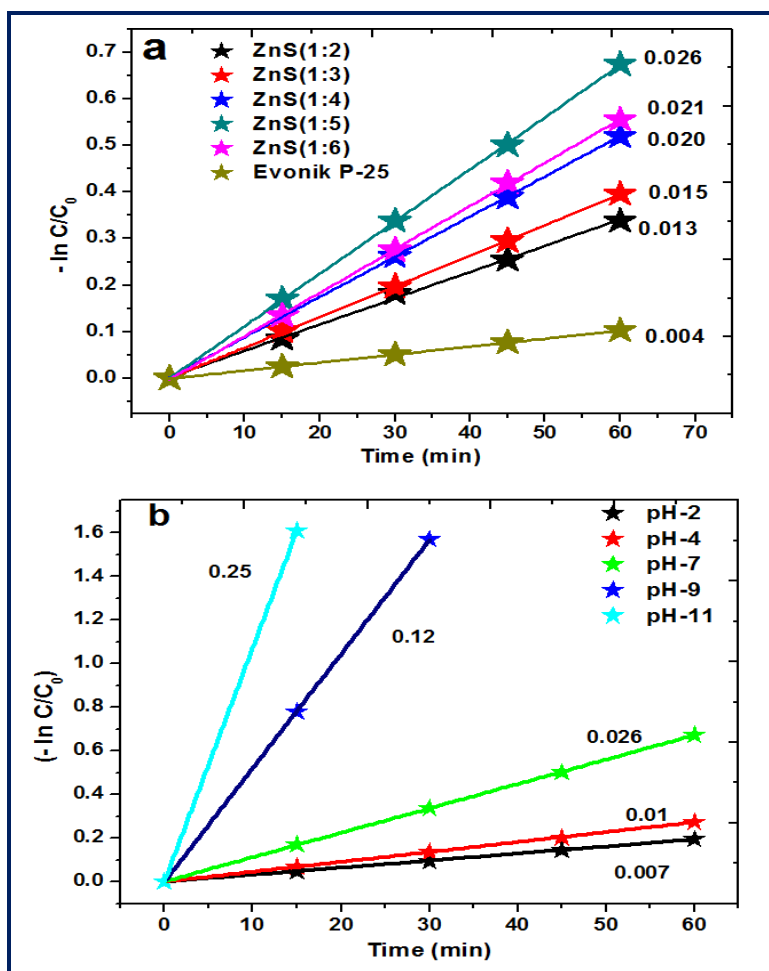


**Fig.4.2.5.** (a) First order kinetic plots for the oxidation of MB by ZnS samples and commercial  $\text{TiO}_2$  sample ( $C_0$  (MB) = 20 ppm, catalytic amount=100 mg) (b) First order rate plots for oxidation of MB at different pH values ( $C_0$  (MB) = 20 ppm, catalyst amount=100 mg, pH (2,4,7,9,11))

#### 4.2.3.7.4. Effect of pH on photocatalytic reduction of Cr(VI)

Fig. 4.2.6 (b) shows the effect of pH (2-11) on the photocatalytic reduction of Cr (VI). As shown in the Fig. 4.2.6 (b), the photo reduction of Cr(VI) was 100 % within 15 min under acidic conditions ( $\text{pH} < 2$ ). As shown in Fig. 4.2.6 (b), the rate constants were found to be 1.34, 0.23, 0.1, 0.06 and 0.04  $\text{min}^{-1}$  respectively at pH of 2, 4, 7, 9 and 11. As reported by Chen and Cao [67], increasing pH decreases the adsorption capacity of the catalyst for dichromate ions. In general, Cr(VI) occurs in the forms of oxy anions like  $\text{HCrO}_4^-$ ,  $\text{Cr}_2\text{O}_7^{2-}$

,  $\text{CrO}_4^{2-}$ ,  $\text{CrO}_3$ , etc. The predominant form of Cr(VI) was the acid chromate species ( $\text{HCrO}_4^-$ ) at lower pH which on increasing the pH, changes to other forms like  $\text{CrO}_4^{2-}$  and  $\text{Cr}_2\text{O}_7^{2-}$  [46, 47]. Therefore, the ionic forms of Cr(VI) in solution and the charge of ZnS surface depend on the pH of the solution. Under the acidic conditions, the surface of the catalyst may be predominantly protonated and attracts the negatively charged Cr(VI) ions. In addition, under basic conditions,  $\text{Cr}(\text{OH})_3$  may be precipitated which cover the surface of the catalyst and decreases the activity of catalyst.

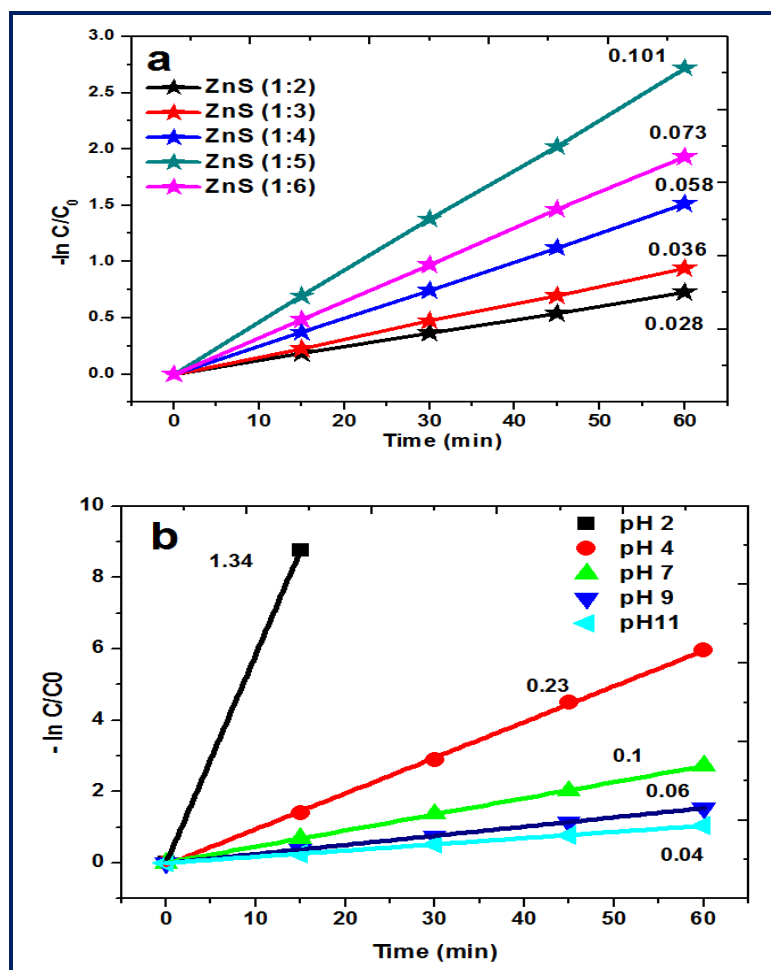


**Fig.4.2.6.** (a) First order kinetic plots for the reduction of Cr(VI) by ZnS samples ( $C_0$  (Cr(VI)) = 10 ppm, catalytic amount=100 mg) (b) Effect of pH on photocatalytic reduction of Cr(VI) ( $C_0$  (Cr(VI)) = 10 ppm, catalytic amount=100 mg, pH (2,4,7,9,11))

#### 4.2.3.7.5. Simultaneous oxidation of MB and reduction of Cr(VI)

Generally industrial waste waters consist of mixture of pollutants and simultaneous removal of these pollutants is beneficial. In addition, simultaneous treatment reduces the cost of water treatment. Figure 4.2.7 shows the first order kinetic plots for the simultaneous oxidation and reduction of MB and Cr(VI), respectively. A 50 ppm of Cr(VI) aqueous

solution and 100 ppm of MB were taken as the combination of pollutants. It is worth mentioning that there is no reaction in the dark or without catalyst. From the rate constants, it is concluded that in case of simultaneous reaction the rate constant was found to be almost doubled than the individual reactions, which can be due to the suppression of electron hole recombination. Therefore simultaneous redox reactions not only decreases the water treatment cost but also increases the efficiency of the reaction.

The best activity of ZnS(1:5) during the photocatalytic oxidation and reduction can be explained as follows: With the increase of sulfur precursor from ZnS(1:2) to ZnS(1:5) there may be free sulfide ions which can't find a zinc ion due to the insufficient zinc precursor which can act like a polysulfide ion and thereby can enhance both oxidation and reduction reactions on the surface of ZnS catalyst. But as observed in case of ZnS(1:6) the reduced activity might be due to the covering of active sites of ZnS by the far excess of sulfide residue. Thus the optimum ratio of oxidant and fuel might be achieved at 1:5.

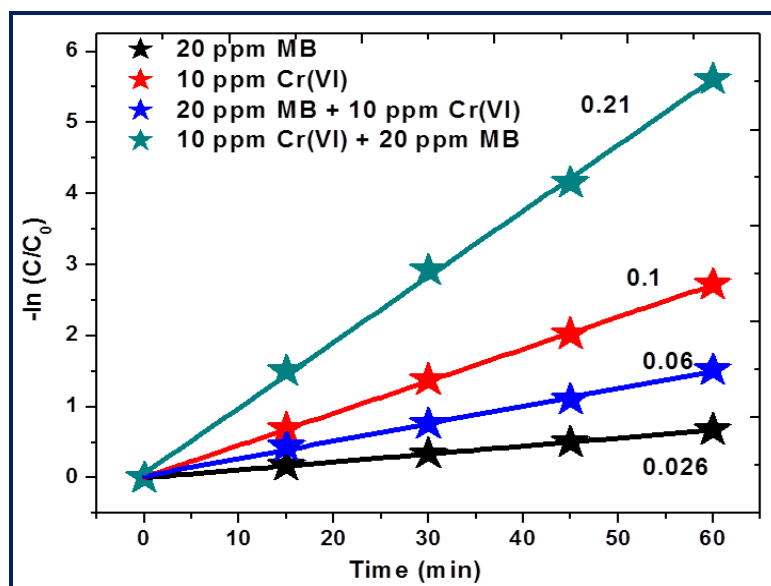
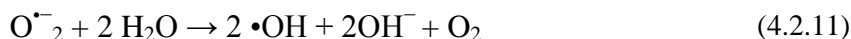
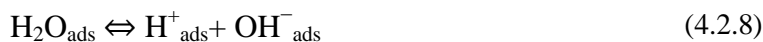


**Fig.4.2.7.** First order kinetic plots for the simultaneous removal of MB and Cr(VI) ( $C_0$  (Cr(VI)) = 10 ppm,  $C_0$  (MB) = 20 ppm catalytic amount=100 mg)

#### 4.2.3.7.6. Photocatalytic degradation mechanism of MB on C, N doped ZnS samples

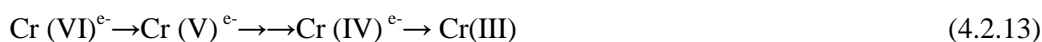
The mechanism of pollutant degradation has been given in one of our publications [47]. Generally irradiation of photocatalyst with energy suitable to that of band gap may promote a VB electron to the CB, leaving a hole in the VB (Eq. 4.2.6). Thereafter adsorbed water molecules on the photocatalyst surface react with these holes to form hydroxyl radicals, whose oxidation potential (2.8 V) is higher than many conventional oxidants like  $H_2O_2$ , ozone, etc [48]. On the other hand, in the conduction band the electron reduces the adsorbed oxygen to superoxide anion radical ( $O_2^{\cdot-}$ ), which then reacts with water to form

•OH radical, as given in (Eqns. (4.2.10) and (4.2.11)). Consequently the reaction of •OH radical with MB degrades the pollutant (Eq. (4.2.12)) [70].



#### 4.2.3.7.7. Mechanism of photocatalytic reduction of Cr(VI)

The mechanism of Cr(VI) reduction may be explained as follows. The excitons produced upon irradiation of ZnS with suitable irradiation and the corresponding reactions of these excitons may be as follows (Eq 4.2.13-4.2.15).



The overall reaction under acidic conditions ( $\text{pH} \leq 2$ ) may be summarized as follows:



#### 4.2.3.7.8. Hydrogen production from water

In order to evaluate the visible light activity of ZnS photocatalysts  $\text{H}_2$  production studies from water were performed. The studies were carried out in the presence of  $\text{Na}_2\text{S}$  and  $\text{Na}_2\text{SO}_3$  as sacrificial reagents in order to prevent the photocorrosion of metal sulfide in presence of light. The studies were carried out continuously for 5 h without evacuation and the results are shown in figure 4.2.8(a). The observed rate of  $\text{H}_2$  evolution was found to be 440, 580, 750, 999 and 870  $\mu\text{mol/h}$ , respectively for ZnS(1:2), ZnS(1:3), ZnS(1:4), ZnS(1:5) and ZnS(1:6). In order to study the stability of the photocatalyst under visible irradiation  $\text{H}_2$  evolution studies were carried out for the most active ZnS(1:5) sample by studying five successive runs (25 h). The rate of  $\text{H}_2$  evaluation with respect to time was given in figure 4.2.8(b). From figure 4.2.8(b) it is clearly observed that around 1000  $\mu\text{mol/h}$  of  $\text{H}_2$  was evolved and for every five hours of duration the reaction flask was evacuated to facilitate the empty space for the  $\text{H}_2$  evolution. Five successive cycles of  $\text{H}_2$  production were carried out and the decrease in  $\text{H}_2$  production rate was found to be very less (approximately 7%) which indicates the good stability of the ZnS sample.

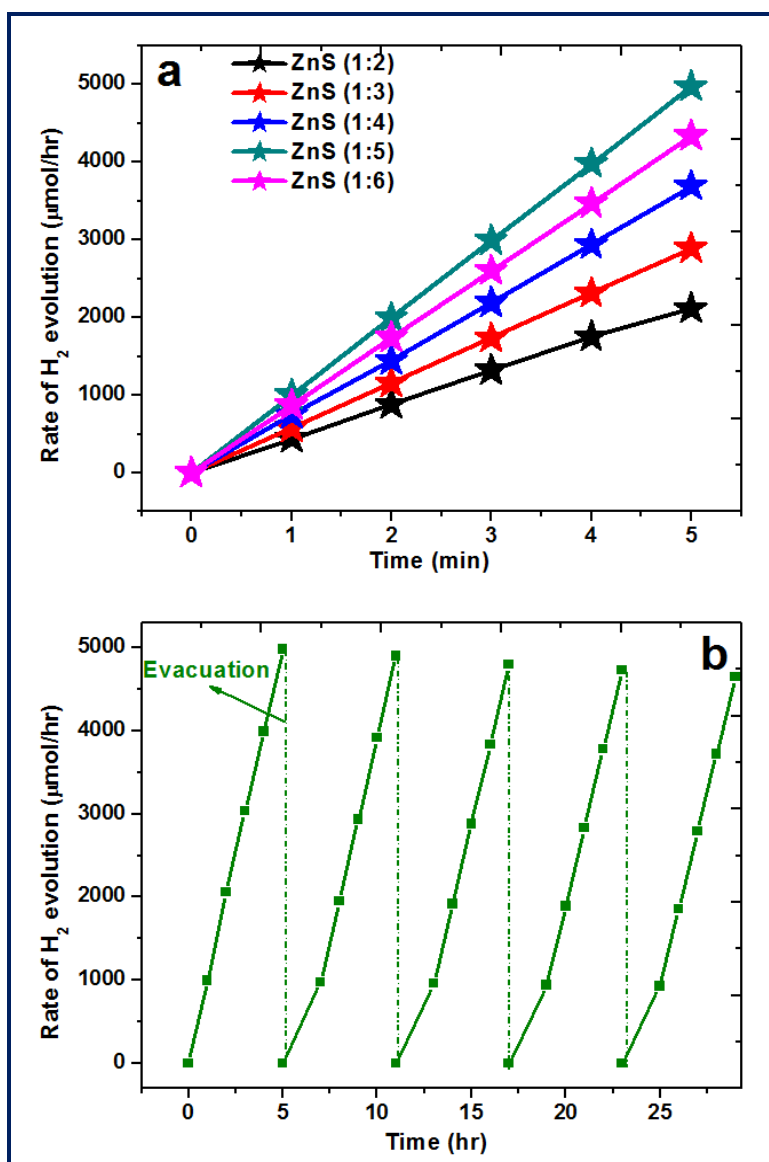


**Fig.4.2.8.** (a) Rate of H<sub>2</sub> evolution profiles from water containing 1M Na<sub>2</sub>S and 1 M Na<sub>2</sub>SO<sub>3</sub> sacrificial agents in the presence of all combustion synthesized ZnS samples for a period of 5 hr. (b) Rate of H<sub>2</sub> evolution profiles from water containing 1M Na<sub>2</sub>S and 1 M Na<sub>2</sub>SO<sub>3</sub> sacrificial agents in the presence of ZnS (1:5) (five runs in a continuous reaction were shown)

#### 4.2.4. Conclusions

The important findings may be summarized as follows:

- 1) Combustion synthesis offers a rapid one pot synthesis of C, N doped ZnS nanomaterials without the need of costly precursors, surfactants and/or capping agents. A plausible formation mechanism has been proposed for the C and N doped ZnS nanomaterials.

- 2) ZnS nanomaterials showed excellent activity under visible radiation. A high activity for the H<sub>2</sub> production (upto 10000 μmol/h/g) was achieved from water containing Na<sub>2</sub>S and Na<sub>2</sub>SO<sub>3</sub> sacrificial agents under visible light.
- 3) It has been observed that simultaneous removal of Cr(VI) and MB is more beneficial than mitigation of individual pollutants.
- 4) Studies on the effect of pH indicated that acidic conditions favor the reduction of Cr(VI), whereas, basic conditions favor MB oxidation.



## References

- [1] M. C. Peter, A. B. Richard, D. J. Chris, A. S. Steven, J. T. Ian. Acceleration of global warming due to carbon-cycle feedbacks in a coupled climate model. *Nature*. 408, (2000) 184-187.
- [2] B. Coelho, A. C. Oliveira, A. Mendes. Concentrated solar power for renewable electricity and hydrogen production from water—a review. *Energy Environ. Sci.* 3, (2010) 1398-1405.
- [3] M. Z. Jacobson, W. G. Colella, D. M. Golden. Cleaning the Air and Improving Health with Hydrogen Fuel-Cell Vehicles. *Science*. 308, (2005) 1901-1905.
- [4] I.P. Jain. Hydrogen the fuel for 21st century. *Int. J. Hydrogen Energ.* 34, (2009) 7368-7378.
- [5] C. Li, H. P. F. Herbert. Fermentative Hydrogen Production from Wastewater and Solid Wastes by Mixed Cultures. *Crit. Rev. Env. Sci. Tec.* 37, (2007) 1-39.
- [6] J. D. Holladay, J. Hu, D. L. King, Y. Wang. An overview of hydrogen production technologies. *Catal. Today*. 139, (2009) 244-260.
- [7] O. Kaoru, K. Shinji, T. Atsuhiko, S. Nariaki, H. Ryutaro. Thermochemical water-splitting cycle using iodine and sulfur. *Energy Environ. Sci.* 2, (2009) 491-497.
- [8] W. Xinchun, M. Kazuhiko, T. Arne, T. Kazuhiro, X. Gang, M. C. Johan, D. Kazunari, A. Markus. A metal-free polymeric photocatalyst for hydrogen production from water under visible light. *Nat. Mater.* 8, (2009) 76-80.
- [9] H. Pan, C. K. Poh, Y. W. Zhu, G. C. Xing, K. C. Chin, Y. P. Feng, J. Y. Lin, C. H. Sow, W. Ji, A.T.S. Wee. Novel CdS Nanostructures: Synthesis and Field Emission. *J. Phys. Chem. C*. 112, (2008) 11227-11230.
- [10] Y. F. Lin, J. H. Song, Y. Ding, S.Y. Lu, Z. L. Wang. Alternating the Output of a CdS Nanowire Nano generator by a White-Light-Stimulated Optoelectronic Effect. *Adv. Mater.* 20, (2008) 3127-3130.
- [11] G. Z. Shen, J. H. Cho, J. K. Yoo, G. C. Yi, C. J. Lee. Synthesis of Single-Crystal CdS Micro belts Using a Modified Thermal Evaporation Method and Their Photoluminescence. *J. Phys. Chem. B*. 109, (2005) 9294-9298 .
- [12] K. A. Sanjay, N. G. Sunil, P. M. Gurudas, V. Ajayan, D. N. Sonali, P. A. Dinesh, B. K. Bharat. A Facile Template-Free Approach for the Large-Scale Solid-Phase Synthesis of CdS Nanostructures and Their Excellent Photocatalytic Performance. *Small*. 7, (2011) 957-964.
- [13] N. Bao, L. Shen, T. Takata, K. Domen, A. Gupta, K. Yanagisawa and C. A. Grimes. *J. Phys. Chem. C*. 111, (2007) 17527.

- [14] Q. Q. Wang, G. Xu, G. R. Han. Synthesis and Characterization of Large-Scale Hierarchical Dendrites of Single-Crystal CdS. *Cryst. Growth Des.* 6, (2006) 1776-1780.
- [15] R. Thiruvengadathan, O. Regev. Hierarchically Ordered Cadmium Sulfide Nanowires Dispersed in Aqueous Solution. *Chem. Mater.* 17, (2005) 3281-3287.
- [16] K. Rajeshwar, N. R. de Tacconi. Solution combustion synthesis of oxide semiconductors for solar energy conversion and environmental remediation. *Chem. Soc. Rev.* 38, (2009) 1984-1998.
- [17] X. Guo, D. Mao, S. Wang, G. Wu and G. Lu. Combustion synthesis of CuO–ZnO–ZrO<sub>2</sub> catalysts for the hydrogenation of carbon dioxide to methanol. *Cat. Commun.* 10, (2009) 1661.
- [18] Z. Zhang, W. Wang, M. Shang and W. Yin. Photocatalytic degradation of rhodamine B and phenol by solution combustion synthesized BiVO<sub>4</sub> photocatalyst. *Cat. Commun.* 11, (2010) 982.
- [19] H. P. Klug, L. E. Alexander. 1954. X-ray Diffraction Procedures for Polycrystalline and Amorphous Materials, 1st ed. Chapter 9. Wiley: New York.
- [20] L. Shen, N. Bao, K. Yanagisawa, K. Domen, A. Gupta, C. A. Grimes. Direct synthesis of ZnO nanoparticles by a solution-free mechano chemical reaction. *Nanotechnol.* 17, (2006) 5117-5123.
- [21] L. Shen, N. Bao, K. Yanagisawa, Y. Zheng, K. Domen, A. Gupta, C. A. Grimes. Organic Molecule-Assisted Hydrothermal Self-Assembly of Size-Controlled Tubular ZnO Nanostructures. *J. Phys. Chem. C.* 111, (2007) 7280-7287.
- [22] T. Zhai, X. Fang, Y. Bando, Q. Liao, X. Xu, H. Zeng, Y. Ma, J. Yao, D. Golberg. Morphology-Dependent Stimulated Emission and Field Emission of Ordered CdS Nanostructure Arrays. *ACS Nano.* 3, (2009) 949-959.
- [23] S. Xiong, X. Zhang, Y. Qian. CdS with Various Novel Hierarchical Nanostructures by Nanobelts/Nanowires Self-Assembly: Controllable Preparation and Their Optical Properties. *Cryst. Growth. Des.* 9, (2009) 5259-5265.
- [24] J. E. B. Katari, V. L. Colvin, A. P. Alivisatos. X-ray Photoelectron Spectroscopy of CdSe Nanocrystals with Applications to Studies of the Nanocrystal Surface. *J. Phys. Chem.* 98, (1994) 4109-4117.
- [25] D. Wang, D. Li, L. Guo, F. Fu, Z. Zhang, Q. Wei. Template-Free Hydrothermal Synthesis of Novel Three-Dimensional Dendritic CdS Nanoarchitectures. *J. Phys. Chem. C.* 113, (2009) 5984-5990.

- [26] Y. Li, D.-S. Hwang, N. H. Lee, S.-J. Kim. Synthesis and characterization of carbon-doped titania as an artificial solar light sensitive photocatalyst. *Chem. Phys. Lett.* 404, (2005) 25-29.
- [27] J.F. Moulder, W.F. Stickle, P.E. Sobol, K.D. Bomben, J. Chastain. *Handbook of X-ray Electron Spectroscopy*. 1992. Perkin-Elmer Corp, Eden Prairie, MN.
- [28] N.D. Shinn, K.L. Tsang. Raman Effect in Cadmium Sulfide. *J. Vac. Sci. Technol. A* 9, (1991) 1558-1562.
- [29] M. A. Nusimovici, J. L. Birman. Lattice Dynamics of Wurtzite: CdS. *Phys. Rev.* 156, (1967) 925-938.
- [30] C. A. Arguello, D. L. Rousseau, S. P. S. Porto. First-Order Raman Effect in Wurtzite-Type Crystals. *Phys. Rev.* 181, (1969) 1351-1363.
- [31] B. Tell, T. C. Damen, S. P. S. Porto. Raman Effect in Cadmium Sulfide, *Phys. Rev.* 144, (1966) 771-774.
- [32] A. Pan, R. Liu, Q. Yang, Y. Zhu, G. Yang, B. Zou, K. Chen. Stimulated Emissions in Aligned CdS Nanowires at Room Temperature. *J. Phys. Chem. B* 109, (2005) 24268-24272.
- [33] H. M. Fan, Z. H. Ni, Y. P. Feng, X. F. Fan, J. L. Kuo, Z. X. Shen, B. S. Zou. Anisotropy of electron-phonon coupling in single wurtzite CdS nanowires. *Appl. Phys. Lett.* 91, (2007) 171911-171913.
- [34] A. Yamamoto, H. Endo, N. Matsuura, A. Ishizumi, Y. Kanemitsu. Raman scattering spectra of CdS nanocrystals fabricated by a reverse micelle method. *Phys. Stat. Sol. C* 6, (2009) 197-200.
- [35] M. Muruganandham, R. Amutha, K. Yoshihumi, S. Miki. Are dopant-stabilized visible light-responsive photocatalysts efficient and stable?. *Phys. Chem. Chem. Phys.* 12, (2010) 14677-14681.
- [36] J. S. Hu, L. L. Ren, Y.G. Guo, H. P. Liang, A.M. Cao, L. J. Wan, C. L. Bai. Mass Production and High Photocatalytic Activity of ZnS Nanoporous Nanoparticles, *Angew. Chem. Int. Ed.*, 44, (2005) 1269–1273.
- [37] S. L. Xiong, B. J. Xi, C. M. Wang, D. C. Xu, X. M. Feng, Z. C. Zhu and Y. T. Qian, Tunable Synthesis of Various Wurtzite ZnS Architectural Structures and Their Photocatalytic Properties, *Adv. Funct. Mater.* 17, (2007) 2728–2738
- [38] Y. Jiang, X.-M. Meng, J. Liu, Z.-Y. Xie, C.-S. Lee, S.-T. Lee, Hydrogen-Assisted Thermal Evaporation Synthesis of ZnS Nanoribbons on a Large Scale, *Adv. Mater.* 15, (2003) 323–327.

- [39] H. Zhou, T. Fan, D. Zhang, Q. Guo, H. Ogawa, Novel Bacteria-Templated Sonochemical Route for the in Situ One-Step Synthesis of ZnS Hollow Nanostructures, *Chem. Mater.* 19, (2007) 2144-2146.
- [40] Q. Zhao, L. Hou, R. Huang, Synthesis of ZnS nanorods by a surfactant-assisted soft chemistry method, *Inorg. Chem. Commun.* 6, (2003) 971–973.
- [41] S. Biswas, S. Kar, S. Chaudhuri, Optical and Magnetic Properties of Manganese-Incorporated Zinc Sulfide Nanorods Synthesized by a Solvothermal Process, *J. Phys. Chem. B.* 109, (2005) 17526 -17530.
- [42] M. Muruganandham, Y. Kusumoto, Synthesis of N, C Codoped Hierarchical Porous Microsphere ZnS As a Visible Light-Responsive Photocatalyst, *J. Phys. Chem. C.* 113, (2009) 16144–16150.
- [43] M.S. Hegde, G. Madras, K.C. Patil, Noble Metal Ionic Catalysts, *Acc. Chem. Res.* 42, (2009) 704-712.
- [44] K.C. Patil, S.T. Aruna, T. Mimani, Combustion synthesis: an update, *Curr. Opin. Solid State Mater. Sci.* 6, (2002) 507–512.
- [45] X.M. Guo, D.S. Mao, G.Z. Lu, S. Wang, G.S. Wu, Glycine–nitrate combustion synthesis of CuO–ZnO–ZrO<sub>2</sub> catalysts for methanol synthesis from CO<sub>2</sub> hydrogenation, *J. Catal.* 271, (2010) 178-185.
- [46] A. D. Mani, V. Laporte, P. Ghosal, Ch. Subrahmanyam, Combustion synthesized TiO<sub>2</sub> for enhanced photocatalytic activity under the direct sunlight-optimization of titanyl nitrate synthesis, *Mater. Res. Bull.* 47, (2012) 2415–2421.
- [47] A. D. Mani, B. R. Raju, N. Xanthopoulos, P. Ghosal, B. Sreedhar, Ch. Subrahmanyam, Effect of fuels on combustion synthesis of TiO<sub>2</sub> – Towards efficient photocatalysts for methylene blue oxidation and Cr (VI) reduction under natural sunlight, *Chem. Eng. J.* 228, (2013) 545–553.
- [48] N. M. Stover., Diphenyl Carbazide as a test for chromium, *J. Am. Chem. Soc.* 50, (1928) 2363-2366.
- [49] A.V. Naumov, V. N. Semenov, E. G. Goncharov, Properties of CdS Films Prepared from Thiourea Complexes of Cadmium Salts, *Inorg. Mater.* 37, (2001) 539-543.
- [50] V. N. Semenov, A.V. Naumov, Thermal Decomposition of Cadmium Thiourea Coordination Compounds, *Russ. J. Gen. Chem.* 71, (2001) 495-499.
- [51] A. A. Uritskaya, G. A. Kitaev, N. S. Belova, Kinetics of Cadmium Sulfide Precipitation from Aqueous Thiourea Solutions, *Russ. J. Appl. Chem.* 75, (2002) 846-848.

- [52] K. Suzuki, K. Ikari, H. Imai, Synthesis of Silica Nanoparticles Having a Well-Ordered Meso structure Using a Double Surfactant System, *J. Am. Chem. Soc.* 126, (2004) 462 – 463.
- [53] K. Sooklal, B. S. Cullum, S. M. Angel and C. J. Murphy, Photophysical Properties of ZnS Nanoclusters with Spatially Localized  $Mn^{2+}$ , *J. Phys.Chem.*, 100, (1996) 4551-4555.
- [54] G. L. Chen, Y. Li, J. Lin, C. H. Huan, Y. P. Guo, The effect of thermal annealing on reactive radio-frequency magnetron-sputtered carbon nitride films, *J. Phys. D:Appl. Phys.* 32, (1999) 195-199.
- [55] Y. H. Cheng, B. K. Tay, S. P. Lau, X. Shi, H. C. Chua, X. L. Qiao, J. G. Chen, Y. P. Wu, C. S. Xie, Deposition of carbon nitride films by filtered cathodic vacuum arc combined with radio frequency ion beam source, *Diamond Relat. Mater.* 9, (2000) 2010-2018.
- [56] N. Tabet, M. Faiz, A. Al-Oteibi, XPS study of nitrogen-implanted ZnO thin films obtained by DC-Magnetron reactive plasma, *J. Electron Spectroc. Relat.Phenom.* 163, (2008) 15-18.
- [57] M. Mapa, C. S. Gopinath, Combustion Synthesis of Triangular and Multifunctional  $ZnO_{1-x}N_x$  ( $x \leq 0.15$ ) Materials, *Chem. Mater.* 21, (2009) 351-359.
- [58] J. Yang, H. Bai, X. Tan, J. Lian, IR and XPS investigation of visible-light Photocatalysis-Nitrogen-carbon-doped  $TiO_2$  film, *Appl. Surf. Sci.* 253, (2006) 1988-1994.
- [59] L.-C.Chen, Y.-J. Tu, Y.-S. Wang, R.-S. Kan,C.-M. Huang, Characterization and photoreactivity of N-, S-, and C-doped ZnO under UV and visible light illumination, *J. Photochem. Photobiol. A* 199, (2008) 170-178.
- [60] Y.-H. Tseng, C.-S. Kuo, C.-H. Huang, Y.-H. Li, P.-W. Chou, C.-L. Cheng, M.-S. Wong, Visible-light-responsive nano- $TiO_2$  with mixed crystal lattice and its photocatalytic activity, *Nanotechnology*, 17, (2006) 2490-2497.
- [61] H. Pan, J. B. Yi, L. Shen, R. Q. Wu, J. H. Yang, J. Y. Lin, Y. P. Feng, J. Ding, L. H. Van, J. H. Yin, Room-Temperature Ferromagnetism in Carbon-Doped ZnO, *Phys. Rev. Lett.* 99, (2007) 127201-127204.
- [62] D. Moore, Z. L. Wang, Growth of anisotropic one-dimensional ZnS nanostructures, *J. Mater. Chem.* 16, (2006) 3898-3905.
- [63] K.M. Parida, N. Sahu, N.R. Biswal, B. Naik, A.C. Pradhan,Preparation, characterization, and photocatalytic activity of sulfate-modified titania for degradation of methyl orange under visible light, *J. Colloid. Interface Sci.* 318, (2008) 231–237.
- [64] A. Franco, M.C. Neves, M.M.L.R. Carrott, M.H. Mendonça, M.I. Pereira, O.C. Monteiro, Photocatalytic decolorization of methylene blue in the presence of  $TiO_2/ZnS$  nanocomposites. *J. Hazard. Mater.* 161, (2009) 545–550.

- [65] W.Z. Tang, C.P. Huang, Inhibitory effect of thioacetamide on CdS dissolution during photocatalytic oxidation of 2,4-dichlorophenol. *Chemosphere* 30, (1995) 1385–1399.
- [66] A.P. Davis, C.P. Huang, The photocatalytic oxidation of sulfur-containing organic compounds using cadmium sulfide and the effect on CdS photocorrosion. *Water Res.* 25, (1991) 1273–1278.
- [67] S. F. Chen, G.Y. Cao, Study on the photocatalytic reduction of dichromate and photocatalytic oxidation of dichlorvos, *Chemosphere*. 60, (2005) 1308–1315.
- [68] N. Tewari, P. Vasudevan, B.K. Guha, Study on biosorption of Cr (VI) by *Mucor hiemalis*. *Biochem. Eng. J.* 23, (2005) 185–192.
- [69] P.R. Gogate, A.B. Pandit, A review of imperative technologies for wastewater treatment I: oxidation technologies at ambient conditions, *Adv. Environ. Res.* 8, (2004) 501-551.
- [70] X.Q. Zhu, J.L. Zhang, F. Chen, Study on visible light photocatalytic activity and mechanism of spherical Bi<sub>12</sub>TiO<sub>20</sub> nanoparticles prepared by low-power hydrothermal method, *Appl. Catal. B: Environ.* 102, (2011) 316–322.

# Chapter 5

## One pot synthesis of CdS/ TiO<sub>2</sub> nanostructures for H<sub>2</sub> Production from water and removal of pollutants

### 5.1. Introduction

Increasing CO<sub>2</sub> levels in the atmosphere due to fossil fuel burning has stimulated tremendous research on renewable energy utilization [1]. In order to meet the global energy demand, large amounts of carbon free energy will be required [2,3]. Even though hydrogen is an environmental friendly efficient energy carrier, it is primarily produced from hydrocarbon reforming, which is accompanied by the emission of oxides of carbon [4, 5]. In this respect photocatalytic hydrogen generation by water splitting appears to be the best alternative [6, 7].

Among the several photocatalysts, TiO<sub>2</sub> has remained the best due to its high absorption crosssection, easy availability, photostability and matching band positions for H<sub>2</sub> evolution [8-11]. However, as a wide band gap semiconductor (e.g. 3.2 eV for anatase), TiO<sub>2</sub> can be activated mainly under UV irradiation, which accounts to only a small portion of the solar radiation reaching the Earth [12,13]. To overcome this limitation, many attempts like doping with anion, cation, dye sensitization and coupling with small band gap semiconductor have been attempted to decrease the band gap of TiO<sub>2</sub> so as to make it active under visible light [14-16]. Sensitizing TiO<sub>2</sub> with a small band gap semiconductor like CdS, CdSe, PbS, SnS<sub>2</sub>, SnS, Bi<sub>2</sub>S<sub>3</sub>, In<sub>2</sub>S<sub>3</sub>, CuInS<sub>2</sub>, etc. is gaining increasing interest because of their matching conduction band levels that can prevent recombination of hole and photoelectron [17–20]. Moreover, these hybrid photocatalysts may have the potential to mimic the natural photosynthesis [21]. CdS is one of the most suitable metal chalcogenides for photocatalytic H<sub>2</sub> production due to its high activity under visible light and reasonable negative flat-band potential [22,23]. Such coupled semiconductor hetero structures (or nanocomposites) offer the advantages like synergetic effect, efficient charge separation and migration, expanded visible light response and improved photostability over the individual components. TiO<sub>2</sub> plays a dual role in the hybrid system as it prevents the aggregation of CdS and also enhances the charge separation by forming a potential gradient at the interface

of CdS and TiO<sub>2</sub>. It has been reported that the rate of photo induced electron transfer at CdS increases by tenfold in the presence of TiO<sub>2</sub>, and thereby photocatalytic efficiency [24-26].

Various preparation strategies, such as precipitation, micro emulsion process, chemical bath deposition (CBD), chemical vapor deposition, and electrochemical deposition have been studied to synthesize CdS/TiO<sub>2</sub> nano composites [27-31]. Many of these techniques involve the separate preparation of TiO<sub>2</sub> nanostructures and thereby sensitization with low band gap semiconductor. It is well-known that the contact between quantum dots (QDs) and TiO<sub>2</sub> is less strong when compared with metal and TiO<sub>2</sub>. Hence synthesis of stable and active QDs/TiO<sub>2</sub> composite materials still remains as a challenge [32].

This chapter deals with a single step combustion synthesis of CdS/TiO<sub>2</sub> hetero nanostructures without using molecular linkers, expensive precursors under ambient atmospheric conditions. The as prepared composites were characterized by several techniques to understand the physico-chemical properties. The visible light photocatalytic activity was evaluated by H<sub>2</sub> production from water containing sacrificial agents and also for the removal of model aqueous organic pollutants (methylene blue and Cr(VI)).

## **5.2. Experimental Section**

Cadmium nitrate tetra hydrate and thiourea were purchased from Merck and used as received. The oxidant titanium nitrate was prepared according to the method mentioned in our previous report [33]. Different molar ratios of titanium and cadmium precursors (0.5:1, 1:1, 1:0.5 moles of cadmium and titanium precursors respectively) were taken in order to obtain the composites with best characteristics. In an optimized synthesis, aqueous solutions of cadmium nitrate, titanium nitrate and thiourea were mixed to form a homogeneous solution. Dehydration followed by combustion in a preheated furnace at 350 °C results the product in few minutes. The resulting composites were labeled as CdS/TiO<sub>2</sub> (0.5:1), CdS/TiO<sub>2</sub> (1:1), CdS/TiO<sub>2</sub> (1:0.5) respectively. The specific advantage of the present method is less time required for the synthesis and the samples do not need any post treatments such as washing, calcination etc. before testing catalytic activity.

### **5.2.1. Characterization**

The synthesized CdS/TiO<sub>2</sub> hetero nanostructures were characterized to examine its structural, morphological and optical properties. Confirmation of the material formation and crystallite size of the CdS/TiO<sub>2</sub> composites were obtained from powder X-ray diffractometer. Transmission electron microscopic image of the CdS/TiO<sub>2</sub> samples were recorded in order to understand the morphology and particle size of the samples, whereas, diffuse UV-Vis reflectance spectra of the prepared composite samples were collected using Shimadzu UV-Vis spectrophotometer (UV-3600) to calculate the band gap energies. X-ray



photoelectron spectroscopic study was performed to understand the surface chemical composition. Fluorescence quenching studies of the CdS/TiO<sub>2</sub> hetero nanostructures were carried out on fluorescence spectrometer by dispersing the samples in ethanol. Raman spectra of the as synthesized samples were recorded using a dispersive Raman spectroscope to further confirm the formation of CdS/TiO<sub>2</sub> hetero nanostructures, whereas, surface area of the CdS/TiO<sub>2</sub> nano hetero structures were recorded with BET surface area analyzer.

Photocatalytic H<sub>2</sub> production experiments were carried out in a quartz round bottomed flask containing 100 ml water and 100 mg of the catalyst. The study was carried out in the presence of 1 M Na<sub>2</sub>S and 1M Na<sub>2</sub>SO<sub>3</sub> as the sacrificial reagents. It is worth mentioning that there is no reaction in the dark. All the studies were carried out under simulated visible light radiation with light intensity around 800-900 W/m<sup>2</sup>. Hydrogen produced in the reaction was analyzed by using a Shimadzu gas chromatography (GC-2014) with a packed column. Every hour a 500 µl of the gas was collected in a gas tight syringe (Hamilton) and analyzed.

Oxidation of methylene blue, an aqueous pollutant was performed under the direct sunlight between 11 am to 2 pm (Intensity of light ~ 600-700 W/m<sup>2</sup>). In a typical reaction, a 100 ml of dye solution was taken in a 250 ml beaker and 100 mg of the catalyst was dispersed in the solution by constant stirring and exposed to the sunlight. It is observed that there is no oxidation of dye either in the absence of sunlight or catalyst. Before keeping in sunlight, dye solutions along with catalyst were placed in dark for 30 min in order to facilitate adsorption-desorption equilibrium. For every 15 min, required amount of dye sample has been collected from the experimental solution and the catalyst particles were separated by centrifugation. Then the solution was monitored by using UV-vis spectrophotometer in order to observe the degradation of dye. In a similar manner, the reduction ability of the CdS/TiO<sub>2</sub> photocatalysts was also tested by taking a 30 ppm solution of potassium dichromate as the model pollutant and keeping in sunlight. For every 15 min a small aliquots of the Cr(VI) sample was collected and the reduction of Cr (VI) was estimated by forming a purple colored complex with 1, 5-diphenyl hydrazide solution in acidic media [34]. The decrease in concentration of Cr (VI) was monitored from the absorbance at 540 nm by using UV-vis spectrophotometer.

### **5.3. Results and discussion**

#### **5.3.1. Powder X-ray diffraction (PXRD)**

Figure 5.1 presents the PXRD patterns of CdS/TiO<sub>2</sub> composites along with the reference TiO<sub>2</sub> and CdS samples for comparison. It was observed that the peaks observed at d-spacing of 3.5, 2.4, 1.8, 1.7 and 1.4 Å represent (101), (103), (200), (105), (204) and (215)

planes, respectively of anatase titania highlighting the absence of rutile phase (JCPDS card file no. 89-4921). On the other hand for pure CdS, the peaks observed at d-spacing values of 3.6, 3.4, 3.2, 2.1 and 1.9 Å confirmed (101), (100), (110), (002) and (103) planes, indicating the hexagonal CdS phase. It was observed that all the composites have the peaks corresponding to the both anatase phase TiO<sub>2</sub> and hexagonal CdS phases with varying intensities, which confirm the coexistence of both the phases. The dotted lines in the figure correspond to the diffraction peaks of hexagonal CdS whereas the dark lines indicated that of anatase. In the case of CdS/TiO<sub>2</sub> (0.5:1) the XRD patterns shows rather weak CdS peaks, probably due to the low loading of CdS. A similar observation was found in case of CdS/TiO<sub>2</sub> (1:0.5) where the XRD pattern showed rather weak TiO<sub>2</sub> peaks, due to the low amount of TiO<sub>2</sub>. On the other hand, for CdS/TiO<sub>2</sub> (1:1), the diffraction peaks correspond to both TiO<sub>2</sub> and CdS were observed, which can be attributed to the proper dispersion and optimum loading of CdS on TiO<sub>2</sub>.

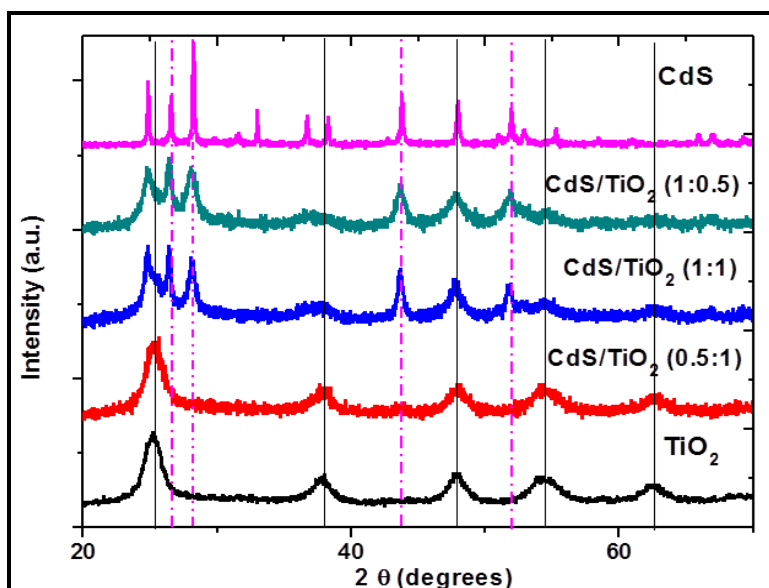
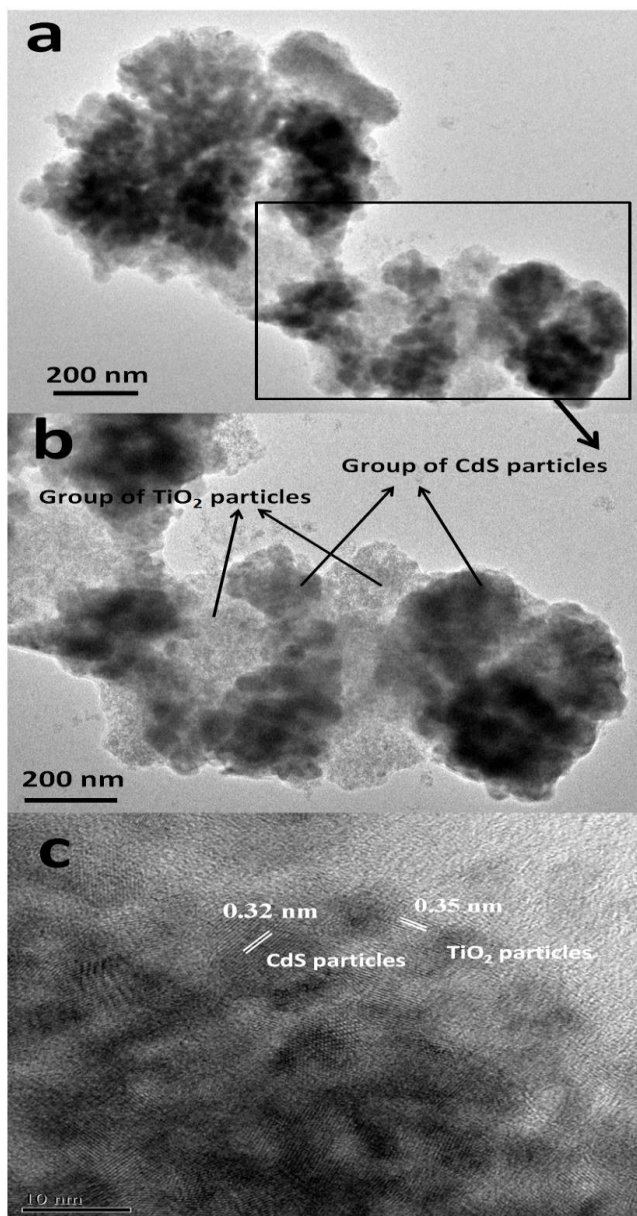


**Figure 5.1.** X-ray diffraction patterns of CdS/TiO<sub>2</sub> hetero nanostructures along with pure TiO<sub>2</sub> and pure CdS

### 5.3.2. TEM

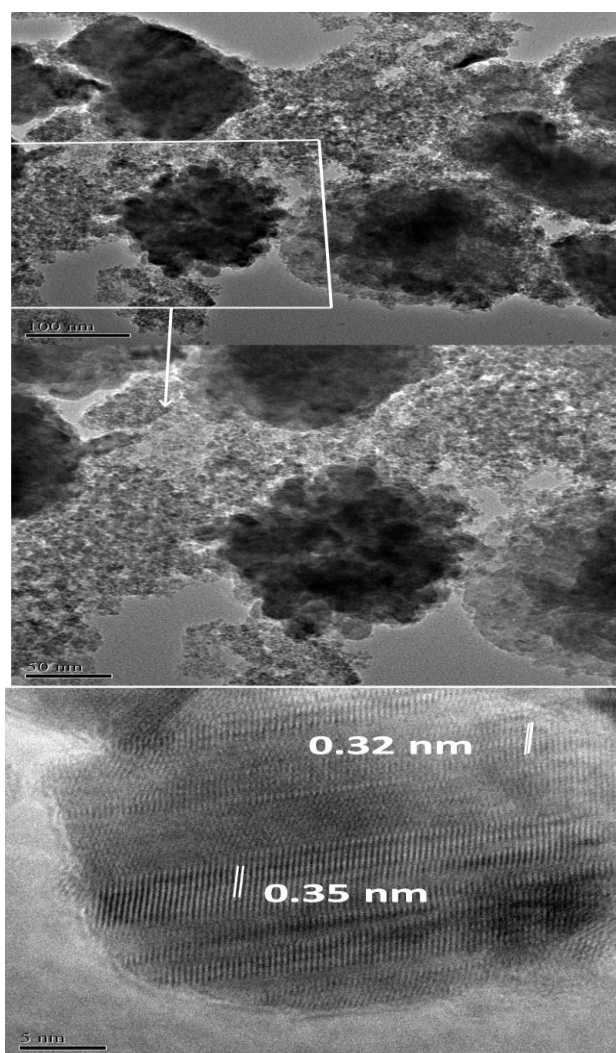
Figure 5.2 shows the high resolution transmission electron microscopy (HRTEM) image of the CdS/TiO<sub>2</sub> (0.5:1) sample, confirmed two different materials with different sizes that are well connected to each other. From Fig. 5.2(b), it was observed that the size of CdS particles (70 nm) is larger than the size of TiO<sub>2</sub> particles (5 nm). Also CdS particles are well decorated on TiO<sub>2</sub> particles which confirm the advantage of the combustion synthesis, especially for composite materials. In Fig. 5.2(b), in some regions only TiO<sub>2</sub> particles are visible which may be attributed to the higher content of TiO<sub>2</sub> than CdS in the sample

CdS/TiO<sub>2</sub>(0.5:1). In some other regions of Fig. 5.2(b) only CdS particles are visible clearly which may be due to its bigger particle size which covers the TiO<sub>2</sub> particles. Figure 5.2 (c) shows the high magnification HRTEM image of CdS/ TiO<sub>2</sub> (0.5:1) sample. The lattice spacing calculated for the crystalline planes observed in Fig. 5.2(c) is found to be 0.35 and 0.31 nm which can be assigned to (101) and (101) planes of anatase TiO<sub>2</sub> (JCPDS file No. 84-1286) and hexagonal CdS (JCPDS file No. 77-2306), respectively.



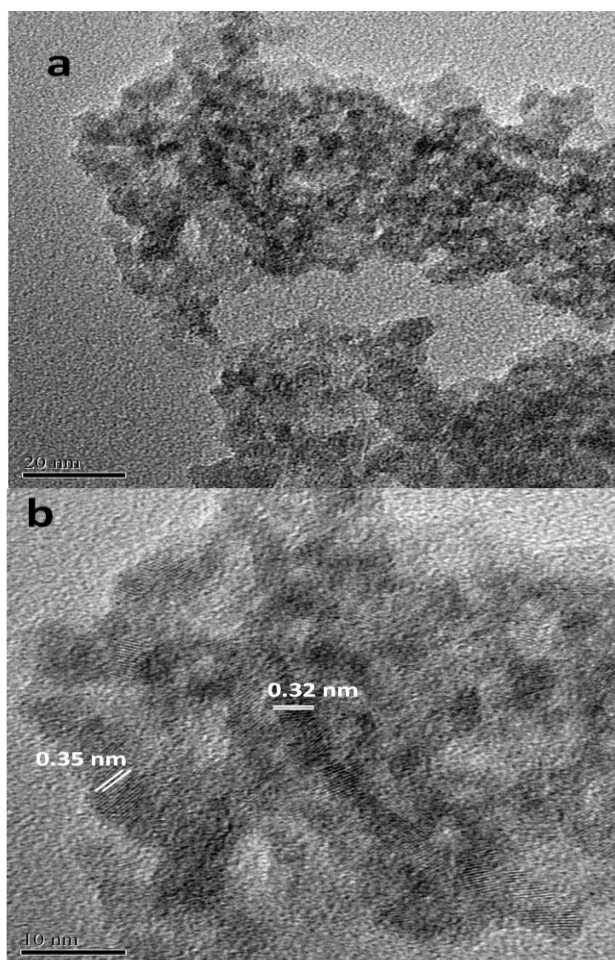
**Figure 5.2.** (a) Low magnification HRTEM image of CdS/TiO<sub>2</sub> (0.5:1) (b) Enlarged view of the marked portion in figure 5.2(a). (c) High magnification HRTEM image of CdS/TiO<sub>2</sub> (0.5:1).

Figure 5.3 shows the HRTEM image of CdS/TiO<sub>2</sub> (1:1) sample. It shows closely connected CdS and TiO<sub>2</sub> particles. As explained in the case of CdS/TiO<sub>2</sub> (0.5:1) for this sample also the size of CdS was found to be larger than TiO<sub>2</sub> and in some places of image only CdS particles are more visible. However the particle size was found to be slightly different than the CdS/TiO<sub>2</sub> (0.5:1). The particle size of TiO<sub>2</sub> remains the same but CdS particle size was reduced from 70 nm to 25 nm in case of CdS/TiO<sub>2</sub> (1:1). The lattice spacing calculated for the crystalline planes in figure 6.3(d) was 0.32 and 0.35nm which confirms the presence of both CdS and TiO<sub>2</sub> (101) planes.



**Figure 5.3.** (a) Low magnification HRTEM image of CdS/TiO<sub>2</sub> (1:1) (b) Enlarged view of the marked portion in figure 5.3(a). (c) High magnification HRTEM image of CdS/TiO<sub>2</sub> (1:1)

Figure 5.4 shows the HRTEM image of CdS/TiO<sub>2</sub> (1:0.5) sample, which shows well decorated CdS particles on TiO<sub>2</sub>. The particles size of CdS was reduced further in case of CdS/TiO<sub>2</sub> (1:0.5) sample as evidence from the HRTEM image as shown in figure 5.4. The particle size of both TiO<sub>2</sub> and CdS are found to be 5 nm. The HRTEM image (figure 5.4(d)) confirms the d-spacing of 0.32 and 0.35 nm, which confirms the formation of anatase TiO<sub>2</sub> and CdS, respectively.



**Figure 5.4.** (a) HRTEM image of CdS/TiO<sub>2</sub> (1:0.5) (b) High magnification HRTEM image of CdS/TiO<sub>2</sub> (1:0.5)

### 5.3.3. Diffuse reflectance UV-Vis spectral studies

The composite nature of CdS/TiO<sub>2</sub> may be further evidenced by the diffuse reflectance UV-vis spectra as shown in Fig. 5.5. Pure TiO<sub>2</sub> only absorbs in the UV region with a band edge of approximately 380 nm ( $E_g = 3.2$  eV). But the composite sample exhibited two distinct absorption edges corresponding to TiO<sub>2</sub> (around 380-400 nm) and a strong absorbance in the visible-light region CdS (around 550-570 nm). The studies show

that the CdS/TiO<sub>2</sub> hetero nano structures absorb the visible as well as in the UV region of the solar spectrum.

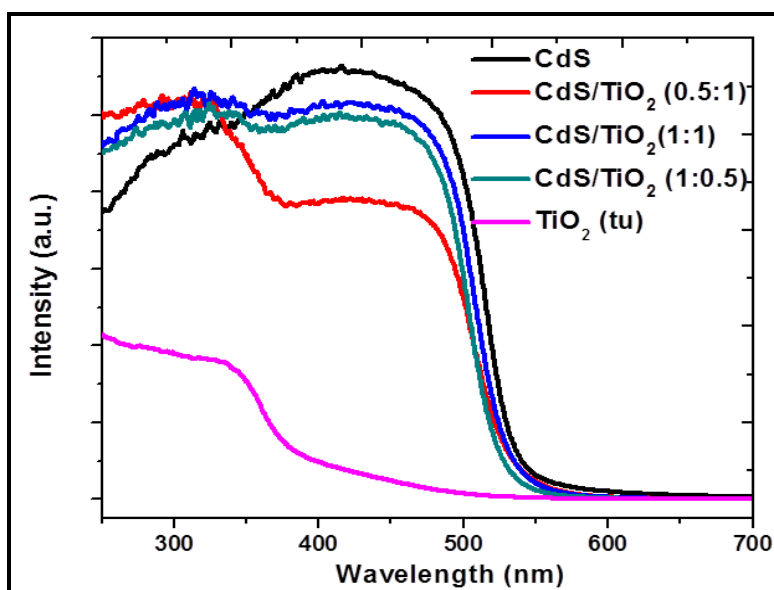


**Figure 5.5.** Diffuse reflectance UV-Vis spectra of CdS/TiO<sub>2</sub> hetero nanostructures along with pure TiO<sub>2</sub> and pure CdS

#### 5.3.4. XPS

The presence of Ti, Cd, O, S, C and N elements in the CdS/TiO<sub>2</sub> composites and their surface composition, valence states were determined by using XPS. Figure 5.6 presents the XPS spectra of Ti 2p, Cd 3d, S 2p, O1s, C 1s and N 1s core levels. As shown in Fig. 5.6(a), the two peaks centered at 405.2 and 412.1 eV with a spin-orbit separation of 6.7 eV were the characteristic peaks of Cd 3d<sub>5/2</sub> and Cd 3d<sub>3/2</sub> states of CdS [35-38]. On the other hand, the peaks centered at 161.5 eV and 162.7 eV confirmed the S<sub>2p</sub> (figure 5.6(b)) present in non-oxidized form. The two peaks located at 459.0 and 463.9 eV correspond to Ti 2p<sub>3/2</sub> and Ti 2p<sub>1/2</sub> of Ti<sup>4+</sup> in TiO<sub>2</sub>, respectively and the absence of peak at around 457.0 eV indicate the absence of Ti<sup>3+</sup> (Fig. 5.6 (c)). Figure 5.6(d) shows the O1s spectra with a narrow peak at a binding energy of 530.4 eV can be attributed to the crystal lattice oxygen of Ti-O.

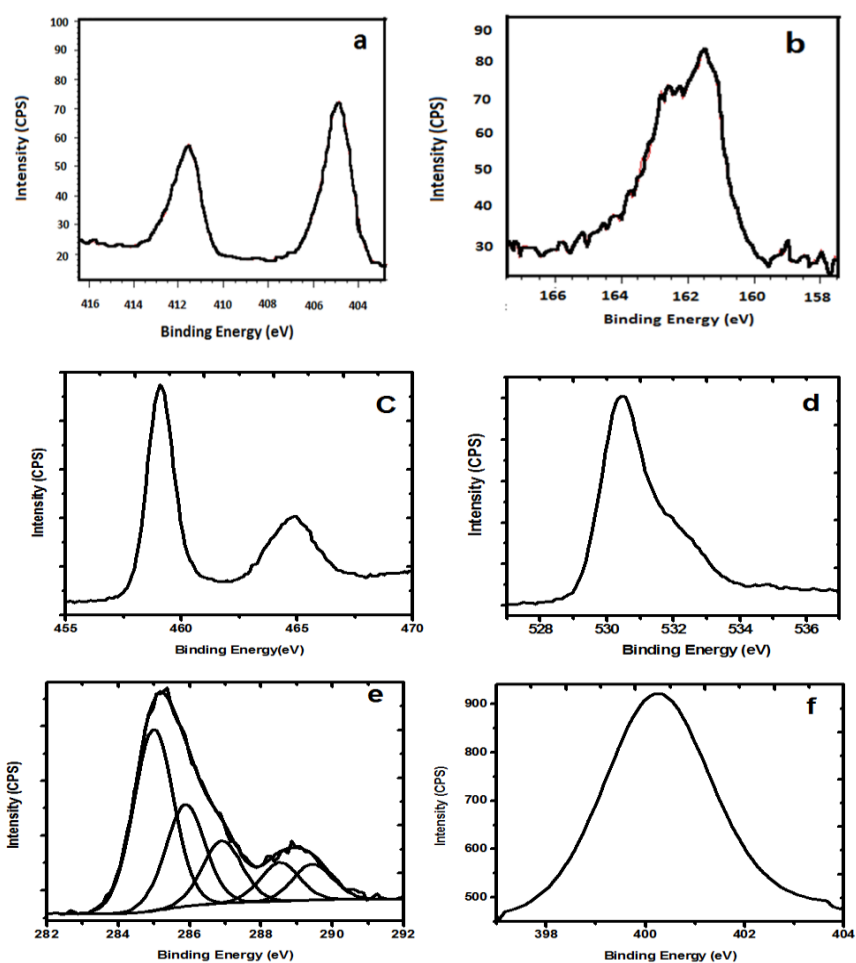


**Figure 5.6.** XPS spectra of CdS/TiO<sub>2</sub> hetero nanostructures (a) Cd 3d spectra (b) S 2p spectra (c) Ti 2p core level spectra (d) O 1s spectra (e) C 1s spectra (f) N 1s spectra.

The evidence of C1s doping was obtained from the spectrum (Fig. 5.6(e)) from the peaks centered at 284.5 eV, 288.0 eV and 290.3 eV. The peak centered at 284.5 eV was due to elemental carbon, whereas, the peak at 286.3 eV may be due to the C-OH groups. Sakthivel and Kwasch et. al. has reported two kinds of carbonate species at binding energies of 287.5 and 288.5 eV [39]. In a similar manner, Ohno et al. detected only one kind of carbonate species with a binding energy of 288.0 eV, and they concluded that C<sup>4+</sup> ions might be incorporated into the bulk phase of TiO<sub>2</sub> [40]. Li et al. confirmed only one kind of carbonate species at a binding energy of 288.2 eV [41], which is confirmed by Ren et al. [42]. These results indicated that the peak at 287.5 and 288.6 eV in the C 1s spectrum could be due to Ti-O-C structure, whereas, the peak centered at around 289.7 eV may be attributed to the O=C-O components [43].

The evidence for nitrogen doping was obtained from the N (1s) spectra, which clearly show two peaks at 399.7 eV and 405 eV (Fig. 5.6(f)). It is well known that the



binding energy of the N 1s is very sensitive to the chemical environment of the nitrogen and it varies between 396-408 eV [44]. The peaks observed at 399.7 eV can be attributed to the terminally bonded well screened molecular nitrogen ( $\gamma$ -N<sub>2</sub>), whereas, the 405 eV peak might be due to terminally bonded poorly screened molecular nitrogen ( $\gamma$ -N<sub>2</sub>) [45].

### 5.3.5. Raman spectroscopy

It has been accepted that Raman spectroscopy is a powerful technique for the investigation of the structural properties of nanoparticles. Decreasing particle size influences the force constants and vibrational amplitudes. Figure 5.7 shows the Raman spectra of the CdS/TiO<sub>2</sub> hetero nanostructures. The peaks at 149, 400, 517 and 637 cm<sup>-1</sup> can be assigned to the Eg, B1g, A1g, and Eg modes of the anatase phase, respectively and the absence of band located at 242 cm<sup>-1</sup> confirms the absence of rutile phase and complements the XRD results [46–48]. From Fig. 5.7 it is also clear that the Raman peaks at 300 cm<sup>-1</sup> and 600 cm<sup>-1</sup> for pure CdS correspond to the first-order and second order transverse optical phonon modes [49]. The relatively broad and symmetric nature of Raman peaks of CdS indicates the lower crystallinity of CdS, which is also consistent with the XRD observations. The intensity of Raman peaks for CdS/TiO<sub>2</sub> hetero nanostructures is lower than either pure TiO<sub>2</sub> or pure CdS. This may be attributed to the scattering losses due to the defects at the hetero junction. In all the CdS/TiO<sub>2</sub> composites, Raman peaks corresponding to CdS are predominant, probably due to the high dispersion of CdS over TiO<sub>2</sub>.

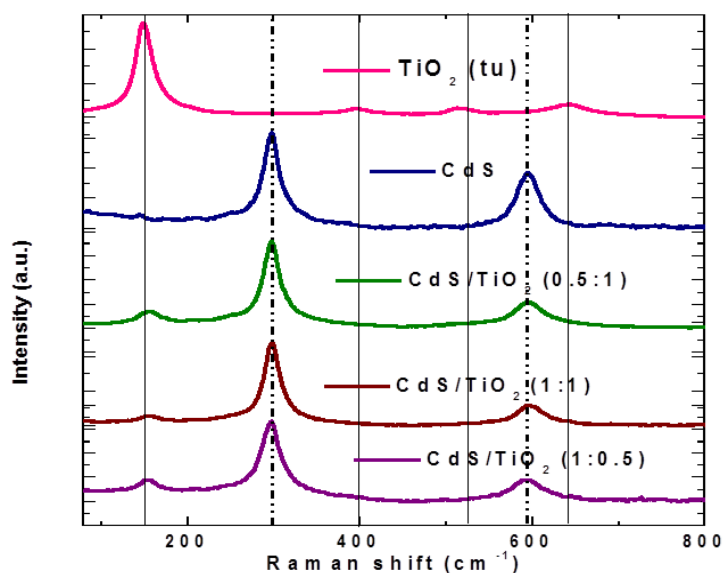


**Figure 5.7.** Raman spectra of CdS/TiO<sub>2</sub> hetero nanostructures along with pure TiO<sub>2</sub> and pure CdS



### 5.3.6. N<sub>2</sub> adsorption studies

The specific surface area of the CdS/TiO<sub>2</sub> samples was obtained from the N<sub>2</sub> adsorption-desorption isotherms by using BET method. The observed specific surface area values are found to be 82, 152, 67, 12, 185 m<sup>2</sup>g<sup>-1</sup> for CdS/TiO<sub>2</sub> (0.5:1), CdS/TiO<sub>2</sub> (1:1), CdS/TiO<sub>2</sub> (1:0.5), CdS, TiO<sub>2</sub> respectively. From these, it may be concluded that TiO<sub>2</sub> has more surface area than the composites and among the composites CdS/TiO<sub>2</sub> (1:1) have higher surface area.

### 5.3.7. Fluorescence quenching

In general the recombination of excitons in semiconductor and the charge trapping phenomenon can be understood by using the concept of fluorescence quenching. It is well known that the conduction band (CB) of TiO<sub>2</sub> is less negative than that of CdS and can facilitate the transfer of electrons from the conduction band of CdS to TiO<sub>2</sub>. Therefore, the separation of charge carriers is improved and the lifetime of the carriers can be prolonged in CdS/ TiO<sub>2</sub> nanostructures compared to the bare CdS nanomaterials.

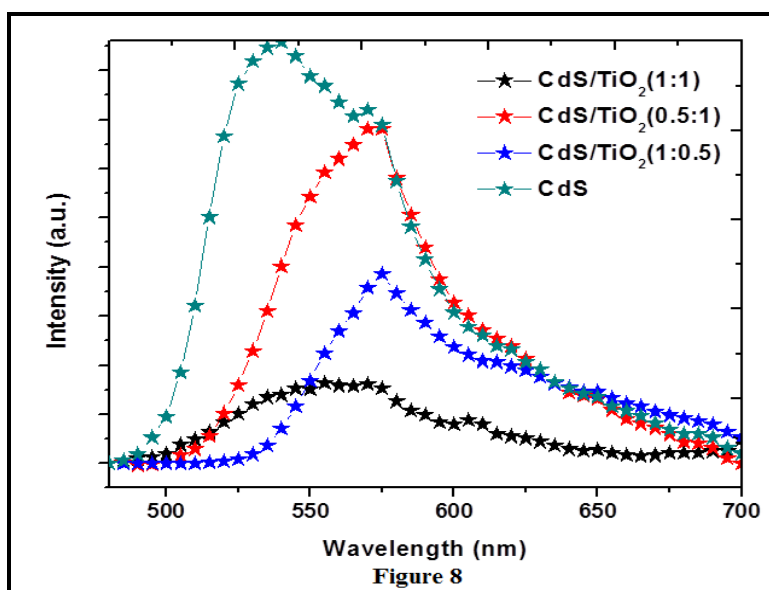


**Figure 5.8.** PL spectra of CdS and CdS/TiO<sub>2</sub> hetero nanostructures

Figure 5.8 represents the emission spectra of combustion synthesized CdS, CdS/TiO<sub>2</sub> (0.5:1), CdS/TiO<sub>2</sub> (1:1) and CdS/TiO<sub>2</sub> (1:0.5) hetero nanostructures which are excited at a wavelength of 350 nm. A broad emission peak centered at around 550 nm was observed for all the samples with varying intensities. This peak can be attributed to the band edge emission [50,51]. The intensity of this broad band edge emission peak is quenched drastically for CdS/TiO<sub>2</sub> samples. The extent of photoluminescence quenching is higher for CdS/TiO<sub>2</sub> (1:1) followed by CdS/TiO<sub>2</sub> (1:0.5) and CdS/TiO<sub>2</sub> (0.5:1), which provides the evidence for the efficient charge transfer from the conduction band edge of CdS to the

conduction band of TiO<sub>2</sub>. Therefore the recombination of the photo-induced electrons and holes can be minimized, due to the facile charge transfer from CdS to TiO<sub>2</sub> [52,53].

## 5.4. Photocatalytic Studies

### 5.4.1. Photocatalytic oxidation of MB

Due to the improved visible light absorption and reduced exciton recombination, composites are expected to show promising photocatalytic activity. In order to understand this, photocatalytic activity was assessed for oxidation of methylene blue and reduction of Cr (VI) as model aqueous organic pollutants and the results are compared with standard Evonik TiO<sub>2</sub>. Figure 5.9 shows the first order kinetic plots of the photocatalytic oxidation of 20 ppm of MB in the presence of all the photocatalysts. The first order rate constants are found to be 0.101, 0.067, 0.048, 0.041, 0.018, 0.005 min<sup>-1</sup> respectively for CdS/TiO<sub>2</sub> (1:1), CdS/TiO<sub>2</sub> (0.5:1), CdS/TiO<sub>2</sub> (1:0.5), CdS, TiO<sub>2</sub> (tu) and Evonik TiO<sub>2</sub>, highlighting the best activity of CdS/TiO<sub>2</sub> (1:1) and the activity was in the following order: CdS/TiO<sub>2</sub> (1:1) > CdS/TiO<sub>2</sub> (0.5:1) > CdS/TiO<sub>2</sub> (1:0.5) > CdS > TiO<sub>2</sub> (tu) > Evonik TiO<sub>2</sub>.

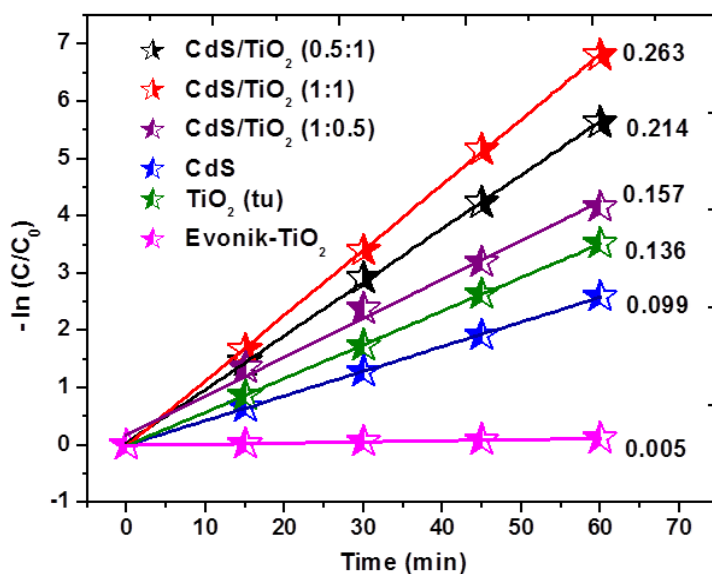


**Figure 5.9.** First order kinetic profiles of oxidation of MB over CdS/TiO<sub>2</sub> hetero nanostructures (C<sub>MB</sub>= 20 ppm)

### 5.4.2. Photocatalytic reduction of Cr(VI)

Photocatalytic reduction of Cr (VI) has also been studied under visible light irradiation and the results are shown in Fig. 5.10. Typical results during the degradation of 30 ppm of Cr (VI) indicated a similar trend to that of MB oxidation. Cr(VI) reduction followed first order kinetics and the corresponding rate constants were found to be 0.263, 0.214, 0.157, 0.136, 0.099 and 0.005 min<sup>-1</sup> respectively for CdS/TiO<sub>2</sub> (1:1), CdS/TiO<sub>2</sub>

(0.5:1), CdS/TiO<sub>2</sub> (1:0.5), CdS, TiO<sub>2</sub> (tu) and Evonik TiO<sub>2</sub>. From these results, it was concluded that CdS/TiO<sub>2</sub> (1:1) shows best activity amongst the photocatalysts tested.

The best activity of CdS/TiO<sub>2</sub> composites when compared to the bare CdS and TiO<sub>2</sub> can be attributed to the facile electron transfer from CdS to TiO<sub>2</sub> due to higher conduction band edge of CdS is than TiO<sub>2</sub>. Under visible light irradiation CdS undergo excitation and the photo generated electrons transfer from the conduction band of CdS to TiO<sub>2</sub> while holes accumulate in the valence band of CdS. Thus the exciton recombination was prevented effectively.

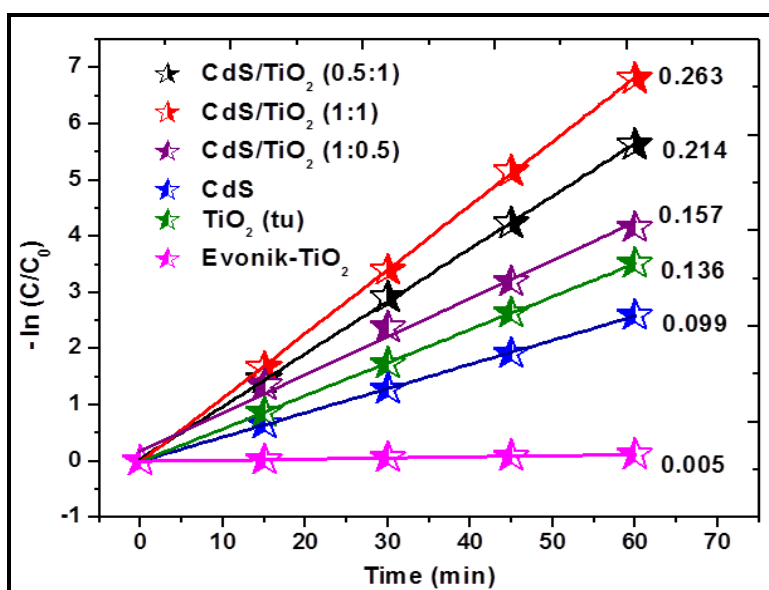


**Figure 5.10.** First order kinetic profiles of reduction of Cr(VI) over CdS/TiO<sub>2</sub> hetero nanostructures ( $C_{Cr(VI)} = 30$  ppm)

#### 5.4.3. Hydrogen production from water

Photocatalytic H<sub>2</sub> production from water splitting was carried out by using CdS/TiO<sub>2</sub> composites and the results are shown in Fig. 5.11. To prevent the photocorrosion of metal sulfide in presence of light, studies were carried out in the presence of Na<sub>2</sub>S and Na<sub>2</sub>SO<sub>3</sub> as sacrificial reagents. The observed rate of H<sub>2</sub> evolution was found to be 9.1, 7.4, 11.8, 2.5 and 1.6 mmol/h, respectively for CdS/TiO<sub>2</sub> (0.5:1), CdS/TiO<sub>2</sub> (1:0.5), CdS/TiO<sub>2</sub> (1:1), CdS and TiO<sub>2</sub> (tu).

In order to study the stability of the photocatalyst under visible irradiation H<sub>2</sub> evolution studies were carried out for the most active CdS/TiO<sub>2</sub> (1:1) upto 25 h. The rate of H<sub>2</sub> evolution with respect to time was given in Fig. 5.12. From figure 6.12 it is clearly observed that around 11.8 mmol/h H<sub>2</sub> was evolved. After every five hours, the reaction flask was evacuated. Five successive runs of H<sub>2</sub> production were carried out and the decrease in

H<sub>2</sub> production rate is approximately 14 % which indicates the reasonable stability of the CdS/TiO<sub>2</sub> (1:1) sample.

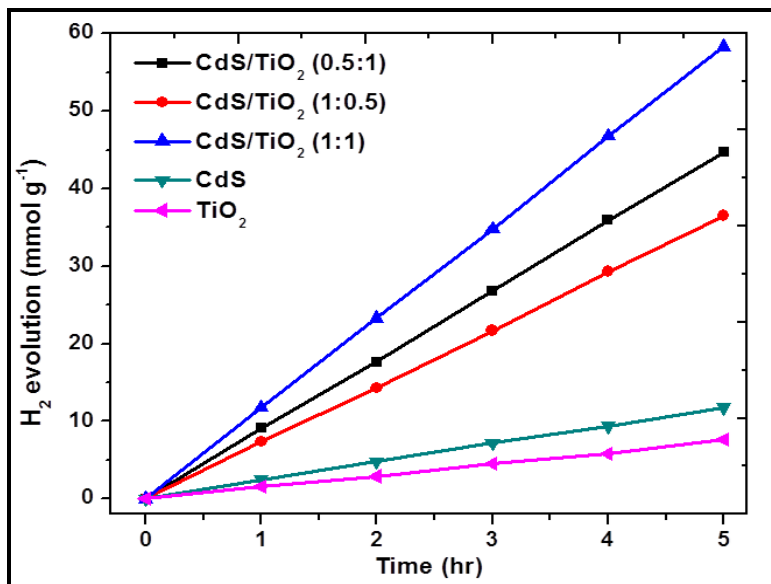


**Fig.5.11.** H<sub>2</sub> evolution with respect to time from water containing 1M Na<sub>2</sub>S and 1 M Na<sub>2</sub>SO<sub>3</sub> sacrificial agents in the presence of CdS and CdS/TiO<sub>2</sub> composites for a period of 5 hr

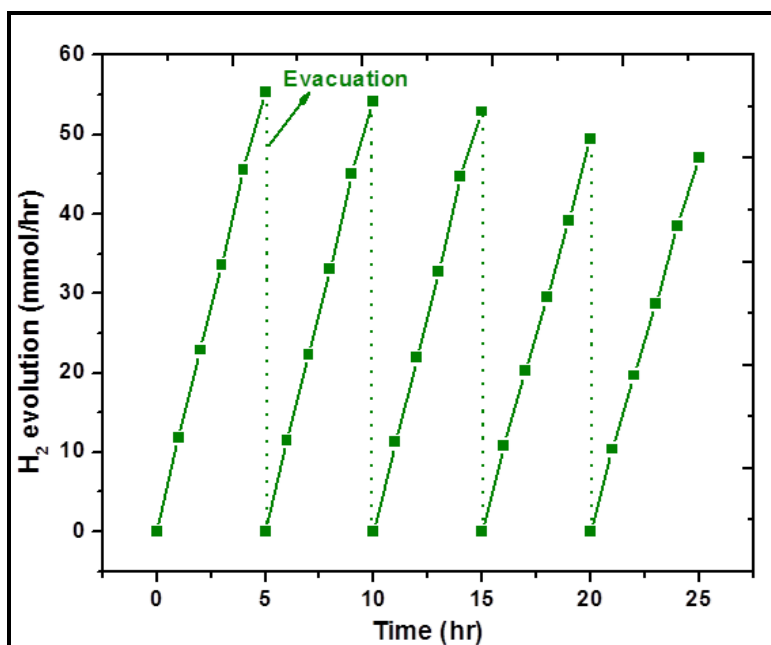


**Fig.5.12.** Five successive cycles of H<sub>2</sub> production from water containing 1M Na<sub>2</sub>S and 1 M Na<sub>2</sub>SO<sub>3</sub> sacrificial agents to assess the stability of the photocatalyst CdS/TiO<sub>2</sub>(1:1)

## 5.5. Conclusions

A novel single step combustion synthesis was developed to prepare CdS/TiO<sub>2</sub> hetero nanostructures. Various physico-chemical studies confirmed the formation of TiO<sub>2</sub> anatase and CdS, the best adsorption in the visible region and suppression of exciton recombination. Photocatalytic activity of the composites was assessed from the oxidation of methylene blue and reduction of Cr(VI), whereas, photocatalytic water splitting without the need of any noble metal indicated the promising nature of CdS/TiO<sub>2</sub> system for H<sub>2</sub> production.

## References

- [1] J. Quaas. The soot factor. *Nature* 471, (2011) 456-457.
- [2] X. Chen, S. Shen, L. Guo and S. S. Mao. Semiconductor-based photocatalytic hydrogen generation. *Chem. Rev.* 110, (2010) 6503-6570.
- [3] X. Chen, L. Liu, P. Y. Yu and S. S. Mao. Increasing Solar Absorption for Photocatalysis with Black Hydrogenated Titanium Dioxide Nanocrystals. *Science* 331, (2011) 746-749.
- [4] A. Midilli, M. Ay, I. Dincer and M. A. Rosen. On hydrogen and hydrogen energy strategies: I: current status and needs. *Renew Sust Energ Rev* 9, (2005) 255–271.
- [5] A. Zuttel, A. Remhof, A. Borgschulte, O. Friedrichs. Hydrogen: the future energy carrier. *Phil Trans R Soc A* 368, (2010) 3329–3342.
- [6] T. R. Cook, D. K. Dogutan, S. Y. Reece, Y. Surendranath, T. S. Teets and D. G. Nocera. Solar Energy Supply and Storage for the Legacy and Nonlegacy Worlds. *Chem. Rev.* 110, (2010) 6474–6502.
- [7] Y. Yu, G. Chen, G. Wang and Z. Lv. Visible-light-driven  $\text{ZnIn}_2\text{S}_4/\text{CdIn}_2\text{S}_4$  composite photocatalyst with enhanced performance for photocatalytic  $\text{H}_2$  evolution. *Int. J. Hydrogen Energ.* 38, (2013) 1278-1285.
- [8] K. M. Parida, S. Pany, B. Naik. Green synthesis of fibrous hierarchical meso-macroporous N doped  $\text{TiO}_2$  nano photocatalyst with enhanced photocatalytic  $\text{H}_2$  production. *Int J Hydrogen Energ.* 38, (2013) 3545-3553.
- [9] A. L. Linsebigler, G. Lu and J. T. Yates. Photocatalysis on  $\text{TiO}_2$  Surfaces: Principles, Mechanisms, and Selected Results. *Chem. Rev.* 95, (1995) 735-758.
- [10] K. Hadjiivanov and D. G. Klissurski. Surface chemistry of titania (anatase) and titania-supported catalysts. *Chem. Soc. Rev.* 25, (1996) 61-69.
- [11] D. P. Serrano, G. Calleja, P. Pizarro and P. Galvez. Enhanced photocatalytic hydrogen production by improving the Pt dispersion over mesostructured  $\text{TiO}_2$ . *Int. J. Hydrogen Energ.* 39, (2014) 4812-4819.
- [12] H. G. Yang, C. H. Sun, S. Z. Qiao, J. Zou, G. Liu, S. C. Smith, H. M. Cheng, G. Q. Lu. Anatase  $\text{TiO}_2$  single crystals with a large percentage of reactive facets. *Nature.* 453, (2008) 638-641.
- [13] H. G. Yang, G. Liu, S. Z. Qiao, C. H. Sun, Y. G. Jin, S. C. Smith, J. Zou, H. M. Cheng, and G. Q. Lu. Solvothermal Synthesis and Photoreactivity of Anatase  $\text{TiO}_2$  Nanosheets with Dominant {001} Facets. *J. Am. Chem. Soc.* 131, (2009) 4078-4079.
- [14] (a) Y-C. Nah, I. Paramasivam, P. Schmuki. Doped  $\text{TiO}_2$  and  $\text{TiO}_2$  Nanotubes: Synthesis and Applications. *Chem. Phys. Chem.* 11, (2010) 2698–2713. (b) C. W. Dunnill, I. P.

Parkin. Nitrogen-doped TiO<sub>2</sub> thin films: photocatalytic applications for healthcare environments. *Dalton Trans.* 40, (2011) 1635–1640.

[15] (a) S. K. Choi, H. S. Yang, J. H. Kim, H. Park. Organic dye-sensitized TiO<sub>2</sub> as a versatile photocatalyst for solar hydrogen and environmental remediation. *Appl Catal B: Environ* 121–122, (2012) 206–213. (b) X. Zhang, L. Yu, C. Zhuang, T. Peng, R. Li, X. Li. Highly efficient visible/near-IR-light-driven photocatalytic H<sub>2</sub> production over asymmetric phthalocyanine-sensitized TiO<sub>2</sub>. *RSC Adv* 3, (2013) 14363–14370.

[16] (a) S. B. Rawal, S. Bera, D. Lee, D.-J. Jang, W. I. Lee. Design of visible-light photocatalysts by coupling of narrow bandgap semiconductors and TiO<sub>2</sub>: effect of their relative energy band positions on the photocatalytic efficiency. *Catal Sci Technol* 3, (2013) 1822–1830. (b) X. Cui, G. Jiang, M. Zhu, Z. Zhao, L. Du, Y. Weng, C. Xu, D. Zhang, Q. Zhang, Y. Wei, A. Duan, J. Liu, J. Gao. TiO<sub>2</sub>/CdS composite hollow spheres with controlled synthesis of platinum on the internal wall for the efficient hydrogen evolution. *Int. J. hydrogen energ.* 38, (2013) 9065–9073.

[17] S Ding, X Yin, X Lu, Y Wang, F Huang and D Wan. One-Step High-Temperature Solvothermal Synthesis of TiO<sub>2</sub>/Sulfide Nanocomposite Spheres and Their Solar Visible-Light Applications. *ACS Appl. Mater. Interfaces.* 4, (2012) 306–311.

[18] Y. Xie, G. Ali, S. H. Yoo, S. O. Cho. Sonication-Assisted Synthesis of CdS Quantum-Dot-Sensitized TiO<sub>2</sub> Nanotube Arrays with Enhanced Photoelectrochemical and Photocatalytic Activity. *ACS Appl. Mater. Interfaces.* 2, (2010) 2910–2914.

[19] J. Hensel, G. Wang, Y. Li, J. Z. Zhang. Synergistic Effect of CdSe Quantum Dot Sensitization and Nitrogen Doping of TiO<sub>2</sub> Nanostructures for Photoelectrochemical Solar Hydrogen Generation. *Nano Lett.* 10, (2010) 478–483.

[20] G. Wang, X. Yang, F. Qian, J. Z. Zhang, Y. Li. Double-Sided CdS and CdSe Quantum Dot Co-Sensitized ZnO Nanowire Arrays for Photoelectrochemical Hydrogen Generation. *Nano Lett.* 10, (2010) 1088–1092.

[21] H. Tada, T. Mitsui, T. Kiyonaga, T. Akita, K. Tanaka. All-solid-state Z-scheme in CdS-Au-TiO<sub>2</sub> three-component nanojunction system. *Nat. Mater.* 5, (2006) 782–786.

[22] M. Matsumura, S. Furukawa, Y. Saho, H. Tsubomura. Cadmium sulfide photocatalyzed hydrogen production from aqueous solutions of sulfite: effect of crystal structure and preparation method of the catalyst. *J Phys Chem* 89, (1985) 1327–1329.

[23] J. F. Reber, K. Meier. Photochemical hydrogen production with platinized suspensions of cadmium sulfide and cadmium zinc sulfide modified by silver sulfide. *J Phys Chem* 90, (1986) 824–834.

- [24] L. Spanhel, H. Weller and A. Henglein. Photochemistry of semiconductor colloids. 22. Electron ejection from illuminated cadmium sulfide into attached titanium and zinc oxide particles. *J Am Chem Soc* 109, (1987) 6632–6635.
- [25] P. A. Sant, P. V. Kamat. Interparticle electron transfer between size-quantized CdS and TiO<sub>2</sub> semiconductor nanoclusters. *Phys Chem Chem Phys* 4, (2002) 198–203.
- [26] L. Wu, J. C. Yu, X. Fu, Characterization and photocatalytic mechanism of nanosized CdS coupled TiO<sub>2</sub> nanocrystals under visible light irradiation. *J Mol Catal A: Chem* 244, (2006) 25–32.
- [27] L. M. Peter, D. J. Riley, E. J. Tull, K. G. Wijayantha. Photosensitization of nanocrystalline TiO<sub>2</sub> by self-assembled layers of CdS quantum dots. *Chem Commun* (2002) 1030–1031.
- [28] L. J. Diguna, Q. Shen, J. Kobayashi, T. Toyoda. High efficiency of CdSe quantum-dot-sensitized TiO<sub>2</sub> inverse opal solar cells. *Appl Phys Lett* 91, (2007) 023116-023116-3.
- [29] Y. Bessekhoad, D. Robert, J. V. Weber. Bi<sub>2</sub>S<sub>3</sub>/TiO<sub>2</sub> and CdS/TiO<sub>2</sub> heterojunctions as an available configuration for photocatalytic degradation of organic pollutant. *J Photochem Photobiol A* 163, (2004) 569–580.
- [30] M. Nanu, J. Schoonman, A. Goossens. Solar-Energy Conversion in TiO<sub>2</sub>/CuInS<sub>2</sub> Nanocomposites. *Adv Funct Mater* 15, (2005) 95–100.
- [31] W. Zhu, X. Liu, H. Q. Liu, D. L. Tong, J. Y. Yang, J. Y. Peng. Coaxial Heterogeneous Structure of TiO<sub>2</sub> Nanotube Arrays with CdS as a Super thin Coating Synthesized via Modified Electrochemical Atomic Layer Deposition. *J Am Chem Soc* 132, (2010) 12619–12626.
- [32] R. S. Dibbell, D. F. Watson. Distance-Dependent Electron Transfer in Tethered Assemblies of CdS Quantum Dots and TiO<sub>2</sub> Nanoparticles. *J Phys Chem C* 113, (2009) 3139–3149.
- [33] A. D. Mani, V. Laporte, P. Ghosal, Ch. Subrahmanyam. Combustion synthesized TiO<sub>2</sub> for enhanced photocatalytic activity under the direct sunlight-optimization of titanyl nitrate synthesis. *Mater Res Bull* 47, (2012) 2415–2421.
- [34] N. M. Stover. Diphenyl carbazide as a test for chromium. *J Am Chem Soc* 50, (1928) 2363–2366.
- [35] T. Zhai, X. Fang, Y. Bando, Q. Liao, X. Xu, H. Zeng, Y. Ma, J. Yao, D. Golberg. Morphology-Dependent Stimulated Emission and Field Emission of Ordered CdS Nanostructure Arrays. *ACS Nano* 3, (2009) 949-959.



- [36] S. Xiong, X. Zhang, Y. Qian. CdS with Various Novel Hierarchical Nanostructures by Nanobelts/Nanowires Self-Assembly: Controllable Preparation and Their Optical Properties. *Cryst Growth Des* 9, (2009) 5259-5265.
- [37] J. E. B. Katari, V. L. Colvin, A. P. Alivisatos. X-ray Photoelectron Spectroscopy of CdSe Nanocrystals with Applications to Studies of the Nanocrystal Surface. *J Phys Chem* 98, (1994) 4109-4117.
- [38] D. Wang, D. Li, L. Guo, F. Fu, Z. Zhang and Q. Wei. Template-Free Hydrothermal Synthesis of Novel Three-Dimensional Dendritic CdS Nanoarchitectures. *J Phys Chem C* 113, (2009) 5984-5990.
- [39] S. Sakthivel, H. Kwasch. Daylight Photocatalysis by Carbon-Modified Titanium Dioxide, *Angew Chem Int Ed* 42, (2003) 4908-4911.
- [40] T. Ohno, T. Tsubota, M. Toyofukum, R. Inaba. Photocatalytic Activity of a TiO<sub>2</sub> Photocatalyst Doped with C<sup>4+</sup> and S<sup>4+</sup> Ions Having a Rutile Phase Under Visible Light. *Catal Lett* 98, (2004) 255-258.
- [41] Y. Li, D-S. Hwang, N. H. Lee, S-J. Kim. Synthesis and characterization of carbon-doped titania as an artificial solar light sensitive photocatalyst. *Chem Phys Lett* 404, (2005) 25-29.
- [42] W. J. Ren, Z. H. Ai, F. L. Jia, L. Z. Zhang, X. X. Fan, Z. G. Zou. Low temperature preparation and visible light photo catalytic activity of mesoporous carbon-doped crystalline TiO<sub>2</sub>. *Appl Catal B-Environ* 69, (2007) 138-144.
- [43] Y-H. Tseng, C-S. Kuo, C-H. Huang, Y-Y. Li, P-W. Chou, C-L. Cheng, M-S. Wong. Visible-light-responsive nano-TiO<sub>2</sub> with mixed crystal lattice and its photocatalytic activity. *Nanotechnol.* 17, (2006) 2490-2497.
- [44] J. F. Moulder, W. F. Stickle, P. E. Sobol, K. D. Bomben and J. Chastain. *Handbook of X-ray Electron Spectroscopy*. Perkin-Elmer Corp. Eden Prairie: MN; 1992.
- [45] N. D. Shinn, K. L. Tsang. Raman Effect in Cadmium Sulfide. *J. Vac. Sci. Technol. A.* 9, (1991) 1558-1562.
- [46] Z. Q. Wang, J. F. Gong, J. H. Duan, H. B. Huang, S. G. Yang, X. N. Zhao, R. Zhang and Y. W. Du. Direct synthesis and characterization of CdSnanobelts. *Appl Phys Lett.* 89, (2006) 033102-05.
- [47] X. P. Shen, A. H. Yuan, F. Wang, J. M. Hong, Z. Xu. Fabrication of well-aligned CdS nanotubes by CVD-template method. *Solid State Commun* 133, (2005) 19-22.
- [48] F. Chen, R. J. Zhou, L. G. Yang, N. Liu, M. Wang, H. Z. Chen. Large-Scale and Shape-Controlled Syntheses of Three-Dimensional CdS Nanocrystals with Flowerlike Structure. *J Phys Chem C* 112, (2008) 1001-1007.

- [49] B. Tell, T. C. Damen, S. P. S. Porto. Raman Effect in Cadmium Sulfide. *Phys Rev* 144, (1966) 771-774.
- [50] Z. A. Peng, X. G. Peng. Nearly Monodisperse and Shape-Controlled CdSe Nanocrystals via Alternative Routes: Nucleation and Growth. *J Am Chem Soc* 124, (2002) 3343-3353.
- [51] S. Karan and B. Maw. Tunable visible-light emission from CdS nanocrystallites prepared under microwave irradiation. *J Phys Chem C* 111, (2007) 16734-16741.
- [52] J. Liqiang, Q. Yichun, W. Baiqi, L. Shudan, J. Baojiang, Y. Libin, F. Wei, F. Honggang, S. Jiazhong. Review of photoluminescence performance of nano-sized semiconductor materials and its relationships with photocatalytic activity. *Solar Energ. Materials and Solar Cells*. 90, (2006) 1773–1787.
- [53] H. Zhu, B. Yang, J. Xu, Z. Fu, M. Wen, T. Guo, S. Fu, J. Zuo and S. Zhang. Construction of Z-scheme type CdS-Au-TiO<sub>2</sub> hollow nanorod arrays with enhanced photocatalytic activity. *Applied Catalysis B*, 90, (2009) 463–469.

# Chapter 6-Section I

## One pot stoichiometric synthesis of nickel sulfide nanomaterials as counter electrode materials in QDSSCs

### 6.1.1. Introduction

Solar energy is the ultimate solution to the rapidly increasing energy demand. Solar cells, the perceptive idea of converting solar energy into electricity is gaining paramount interest in the field of energy conversion [1]. The electrodes made up of semiconductor nanostructures decorated on conducting surfaces, are receiving attention for the design of next generation solar cells [2,3]. Amongst, quantum dot sensitized solar cells (QDSSCs) are receiving importance owing to the best absorption in the visible region and easy fabrication methods [4-7]. Especially, QDSSCs have emerged as potential candidates that are expected to supersede DSSCs. The intrinsic properties of quantum dots (QDs) like tunable band gap [8], high molar extinction coefficients [9], large intrinsic dipole moment [10], etc. makes them a viable alternative to expensive organic dyes that are traditionally used in DSSCs.

A typical QDSSC consists of a wide band gap semiconductor sensitized with semiconductor quantum dots (CdS, CdSe, PbS, PbSe etc.), which act as the working electrode, a poly sulfide electrolyte as redox electrolyte and a counter electrode. Various procedures like SILAR (successive ionic layer adsorption and reaction), chemical bath deposition, electrochemical deposition, electrophoresis, and linker assisted binding, etc. have been reported for the sensitization of CdS or CdSe quantum dots on a wide band gap semiconductor support [11-20]. But all the above methods are either expensive or time consuming techniques. In this context, recently reported solar paint approach appears to be a suitable alternative [21].

In addition, there is an urgent need to reduce the processing cost and develop facile methods for fabrication of counter electrode materials [22, 23]. Therefore, there is a need for Pt-free counter electrodes, without compromising the performance. Hitherto, several materials such as carbonaceous materials [24-29], conducting polymers [30, 31], metal sulfides [32-35] and carbides, nitrides of transition metals [36] have been reported for Pt substitution.

Present section deals with the stoichiometric synthesis of nickel sulfide nanomaterials by solution combustion synthesis, which allows the possibility of large scale synthesis and in-situ C and N doping. The CdS nanomaterials prepared by combustion synthesis as reported in the previous chapter were used as photoanode materials in QDSSCs. A different sensitization approach i.e. physical grinding of CdS and TiO<sub>2</sub> in different ratios was used rather than the SILAR technique for CdS sensitization on a wide band gap semiconductor. Nickel sulfide nanomaterials prepared by combustion synthesis were used as counter electrode materials. A paint approach was used for the deposition of working and counter electrodes on FTO glass plates and the solar cell performance was compared with Pt counter electrode.

### **6.1.2. Experimental Section**

Cadmium sulfide was synthesized by using solution combustion synthesis as described in chapter 4. In a typical synthesis, cadmium nitrate tetra hydrate and thiourea are mixed by maintaining an oxidant/fuel (O/F) ratio of 2 to form a homogeneous solution, which on dehydration followed by combustion at 573 K for 5 min resulted in the desired product.

#### **5.1.2.1. Synthesis of nickel sulfide nanomaterials**

The amount of precursors required for the synthesis were calculated based on the oxidant/fuel (O/F) ratio according to the propellant theory. Different O/F ratios (1, 2, 3, 4 and 10) have been scrutinized in order to get the different stoichiometric compositions of nickel sulfides with best characteristics. In a typical synthesis, aqueous solutions of nickel nitrate and thiourea were mixed to form a homogeneous solution. Dehydration of the gel followed by combustion in a preheated furnace at 573 K formed the product in a few minutes. The samples prepared at different O/F ratios of 1, 2, 3, 4 and 10 were labeled as CE 1, CE 2, CE 3, CE 4 and CE 5 respectively.

#### **5.1.2.2. Preparation of solar paint and electrode materials**

CdS powder and Evonik P25 TiO<sub>2</sub> samples were grounded (1:1, 2:1, and 1:2 weight ratios) in an agate mortar and were made into a paste by adding minimum volume of ethanol followed by sonication for 30 min. The obtained thick yellow paste was directly applied with a paint brush on FTO glass plates pretreated by TiCl<sub>4</sub> solution. Then the plate was annealed to 673 K for 30 min. In a similar manner, nickel sulfide paste was prepared and painted. Pt counter electrode was prepared by thermal decomposition of H<sub>2</sub>PtCl<sub>4</sub> solution in ethanol on FTO glass plate at 673 K. A 0.5 M Na<sub>2</sub>S solution consisting of KCl was employed as the electrolyte. The solar cell assembly consisted of the working electrode, an aqueous electrolyte of 0.5 M Na<sub>2</sub>S containing KCl and either Nickel sulfide/FTO or Pt/FTO

as the counter electrode placed in a glass cell. Figure 6.1.1 shows the diagrammatic representation of different steps involved in the preparation of photoanode and counter electrode materials in a facile manner.

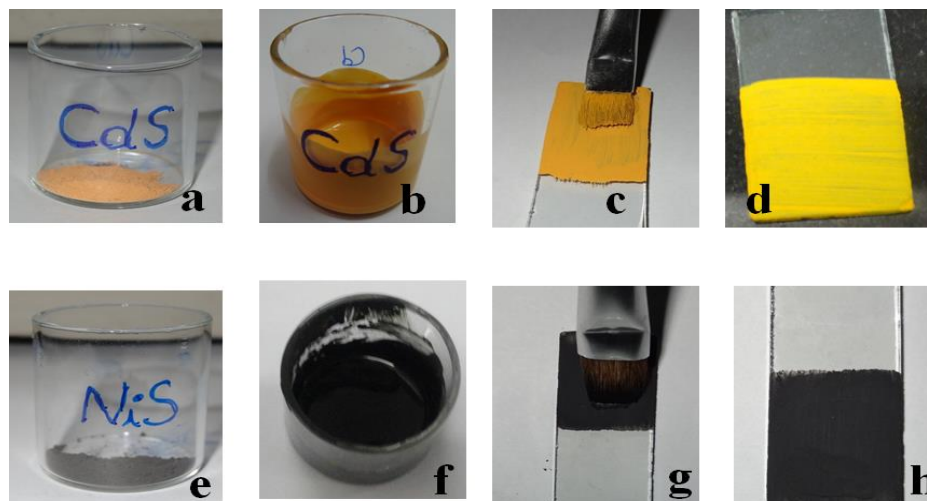


**Figure 6.1.1.** (a) Combustion synthesized CdS powder mixed with PVDF binder  
(b) CdS paint after 30 min of sonication in ethanol  
(c) Application of CdS paint on FTO glass plate, pretreated with  $\text{TiCl}_4$   
(d) CdS working electrode after annealing at 673 K  
(e) Combustion synthesized nickel sulfide powder mixed with PVDF binder  
(f) Nickel sulfide paint after 30 min of sonication in ethanol  
(g) Nickel sulfide paint on FTO glass plate (h) Nickel sulfide counter electrode after annealing at 673 K

### 6.1.2.3. Characterization

As prepared nickel sulfide samples were characterized by various physico-chemical characterization techniques in order to understand the structural, morphological, optical and electrocatalytic properties. Phase purity and crystallinity of the as synthesized nickel sulfide samples were obtained from powder X-ray diffraction. High resolution transmission electron microscopy (HRTEM) images of the best counter electrode (CE 2) among the synthesized samples were recorded using the TEM instrument. Diffuse reflectance UV-Vis spectra of the CdS/  $\text{TiO}_2$  powders were collected with spectral grade  $\text{BaSO}_4$  as the reference. Photoluminescence spectra of the CdS/ $\text{TiO}_2$  samples mixed at different ratios were recorded fluorescence spectrometer after dispersing the samples in ethanol. Current versus voltage characteristics of the fabricated solar cells were measured on solar simulator with a digital source meter. Before collection of I-V data, each electrode was allowed to reach equilibrium at open-circuit. Electrochemical impedance spectra (EIS) of the counter

electrode samples were obtained under symmetric cell configuration in presence of 0.5 M Na<sub>2</sub>S solution containing KCl as the electrolyte. An AC voltage of 10 mV superimposed over a dc potential of 0.0 V was applied to the electrodes and Nyquist plots were obtained over a frequency range of 10<sup>6</sup> Hz to 10<sup>-3</sup> Hz.

### 6.1.3. Results and discussion

#### 6.1.3.1. Photoluminescence spectral studies (PL)

Figure 6.1 shows the photoluminescence spectra of the working electrodes CdS, CdS/TiO<sub>2</sub> (1:1), CdS/TiO<sub>2</sub> (1:2) and CdS/TiO<sub>2</sub> (2:1) at an excitation wavelength of 350 nm that showed a sharp emission peak at 425 nm with a shoulder at 405 nm and a broad band at 575 nm for all the samples. In general, PL spectra of the semiconductor nanoparticles provide the information on energy and dynamics of excitons produced as well as on the nature of emitting states.

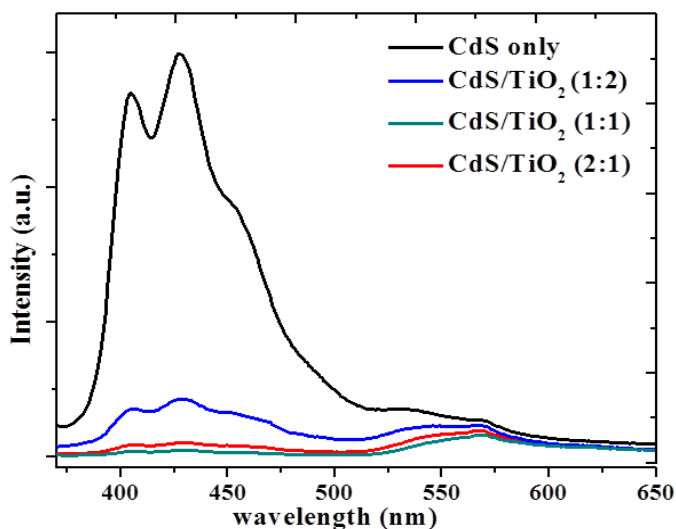


**Figure 6.1.2.** Photoluminescence spectra of combustion synthesized CdS and physically grounded CdS/TiO<sub>2</sub> samples

PL results when an electron undergoes radiative recombination either from a valence band (band edge luminescence) or from surface/trap states within the forbidden gap [37, 38]. In the present case, a broad emission observed in the range of 425 nm to 525 nm with a  $\lambda_{\text{max}}$  at 425 nm may be attributed to the band edge emission due to recombination of excitons at the delocalized states of nanoparticles. Generally, in CdS the defect sites may be either due to cadmium vacancies, sulfur vacancies, interstitial sulfur or cadmium atoms adsorbed on the surface. Shoulder peak observed at the 405 nm may be due to the recombination of charge carriers in deep traps of surface localized states [37, 38-41]. From the PL spectra, it may be seen that the intensity of emission peak observed at 425 nm got quenched upon sensitization with TiO<sub>2</sub> at different ratios. But maximum quenching was

observed for the CdS/TiO<sub>2</sub> (1:1) sample, which indicates a lesser exciton recombination compared to the CdS, CdS/TiO<sub>2</sub> (1:2) and CdS/TiO<sub>2</sub> (2:1). The intense emission peak for CdS shows fast exciton recombination due to the small band gap. This quenching may be due to the proper injection of excited electron in to the conduction band of TiO<sub>2</sub> upon illumination in the CdS/TiO<sub>2</sub> samples.

### 6.1.3.2. Diffuse reflectance UV-Vis spectral analyses

Diffuse reflectance UV-Vis spectra of CdS/TiO<sub>2</sub> samples are shown in Fig. 6.1.3 along with TiO<sub>2</sub> and pure CdS. It was observed that all the samples showed two absorption edges at 390 and 560 nm that may be assigned to TiO<sub>2</sub> and CdS, respectively (Fig. 6.1.3.).

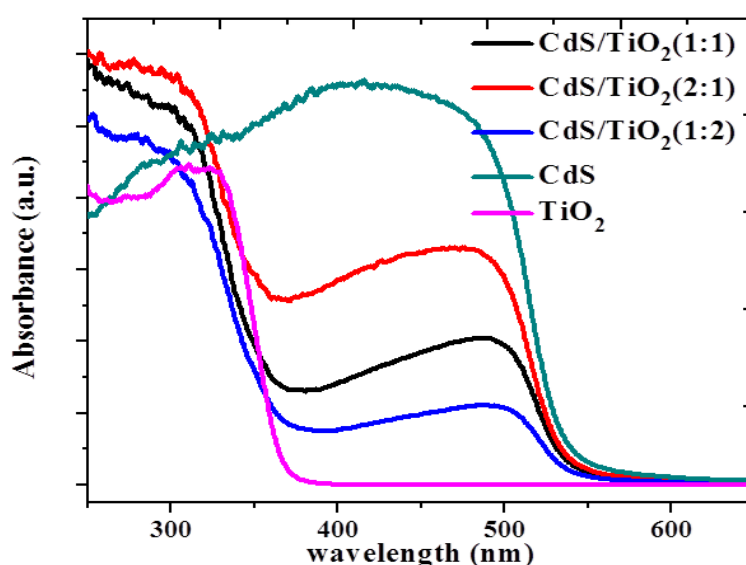


**Figure 6.1.3.** Absorbance spectra of the combustion synthesized CdS and physically grounded CdS/TiO<sub>2</sub> samples

### 6.1.3.3. XRD

Since nickel sulfide exists in several stoichiometric compositions such as Ni<sub>3</sub>S<sub>2</sub>, Ni<sub>7</sub>S<sub>6</sub>, Ni<sub>9</sub>S<sub>8</sub>,  $\alpha$ -NiS,  $\beta$ -NiS, Ni<sub>3</sub>S<sub>4</sub>, and NiS<sub>2</sub>, in order to understand the phase and crystallite size of the nickel sulfide samples, XRD patterns were recorded for nickel sulfide samples prepared at various O/F ratios (1, 2, 3, 4 and 10). From Fig. 6.1.4 it is observed that in case of CE 1, the diffraction peaks observed at d-spacing of 2.4, 2.1 and 1.5 Å correspond to the (222), (400) and (440) planes, of the cubic phase of NiO. From this it is concluded that at O/F ratio of 1, the fuel may not be sufficient to form the predominant nickel sulfide phase. Upon increasing the O/F ratio to 2, the nickel sulfide phase begins to form and the diffraction peaks observed at d-spacing of 4.1, 2.8, 2.4, 1.8 and 1.7 Å confirm the formation of the rhombohedral Ni<sub>3</sub>S<sub>2</sub> stoichiometry in CE 2 sample. As shown in Fig. 3, the CE 3 sample shows diffraction peaks at d-spacings of 2.9, 2.6, 1.9, and 1.7 Å which correspond to

the NiS stoichiometry. This can be attributed to the increase in sulfur source which favors the formation of a sulphur rich sulfide. In case of CE 4 and CE 5, the peaks corresponding to the cubic NiS<sub>2</sub> stoichiometry appeared at d-spacing of 2.8, 2.5, 2.3, 2.0 and 1.7 Å which matches with the (200), (311), (210), (220) and (211) planes respectively. From the above observations it may be concluded that under sulfur rich conditions, nickel sulfide changes from Ni<sub>3</sub>S<sub>2</sub> to NiS and finally to NiS<sub>2</sub>. The above observations reveal the instant stoichiometry selective synthesis of nickel sulfide on varying the ratio of metal to sulfur precursor. The average crystallite sizes calculated by using Scherrer formula were found to be 92, 8, 35, 16 and 35 nm respectively for CE1, CE2, CE3, CE4 and CE 5.

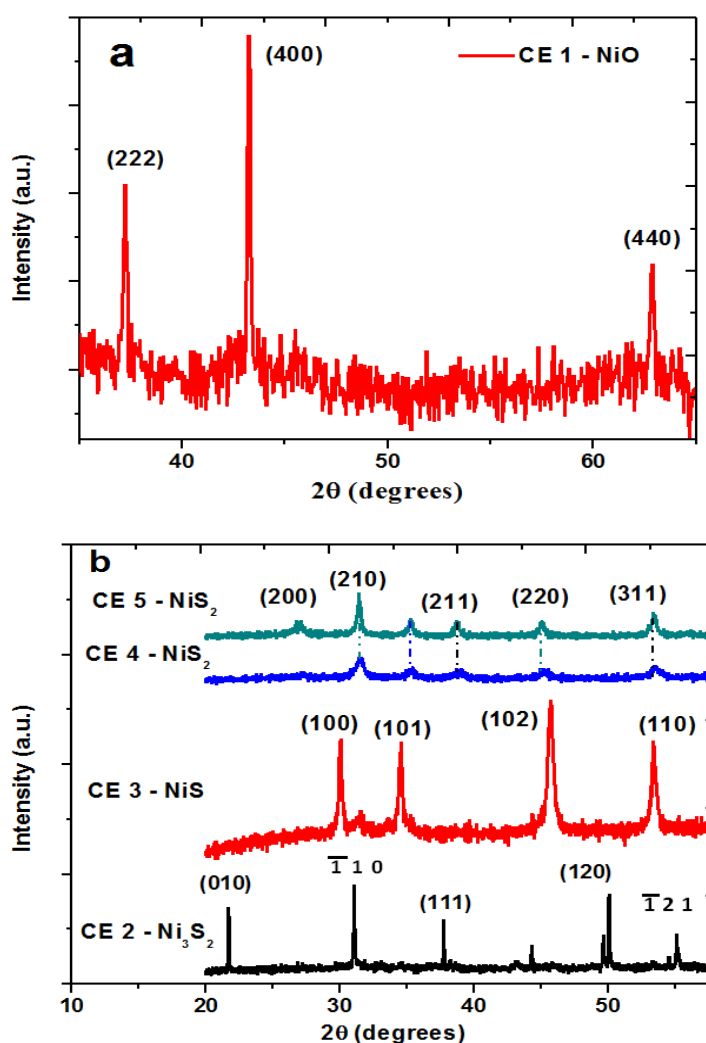


**Figure 6.1.4.** X-ray diffraction patterns of combustion synthesized nickel sulfide samples (a) XRD pattern of CE 1 sample which was found to consist of NiO. (b) XRD patterns of CE 2, CE 3, CE 4 and CE 5 samples which were found to consists of Ni<sub>3</sub>S<sub>2</sub>, NiS, NiS<sub>2</sub> and NiS<sub>2</sub> stoichiometries respectively.



#### 6.1.3.4. Transmission electron microscopy (TEM)

High resolution transmission electron microscopy (HRTEM) images of the CE 2 ( $\text{Ni}_3\text{S}_2$ ) sample are shown in Fig. 6.1.5. From the low magnification HRTEM image shown in figure 6.1.5(a) it is clear that the  $\text{Ni}_3\text{S}_2$  sample consists of roughly spherical shaped particles with approximately 10 nm in size. Figure 6.1.5(b) shows the high magnification HRTEM image of the CE 2 sample which clearly shows crystalline planes with a d-spacing of 0.28 nm that is characteristic of (101) plane of  $\text{Ni}_3\text{S}_2$ .

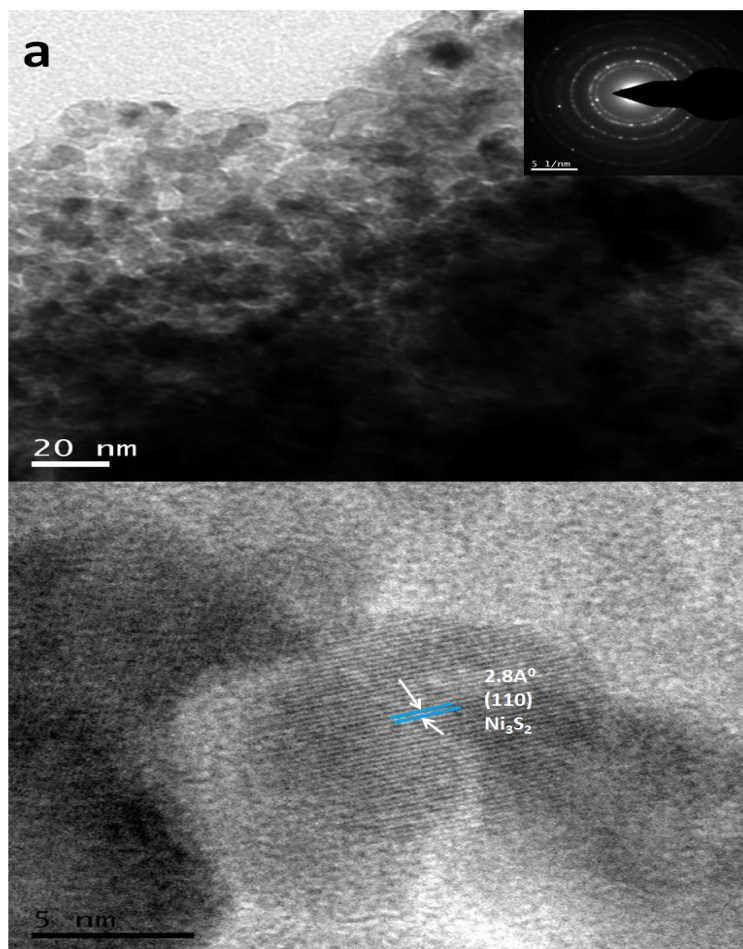


**Figure 6.1.5.** (a) TEM image of CE 2 sample (inset shows the selected area diffraction pattern) (b) HRTEM image of the CE 2 sample.

#### 6.1.3.5. X-ray photoelectron spectroscopy (XPS)

Figure 6.1.6 shows the XPS spectra of CE 2 sample, for which XRD confirmed  $\text{Ni}_3\text{S}_2$  phase. As shown in Fig. 6.1.6 (a) the peak located at 853.1 eV can be assigned to  $\text{Ni}^{2+}$  of  $\text{Ni}_3\text{S}_2$  [45, 46]. Absence of peak at 852.6 eV confirms the absence of metallic Ni [46], whereas, the presence of peak at 162 eV in the S 2p spectra (figure 6.1.6(b)) indicates the

presence of S. In addition to this, an additional peak at 168 eV indicates the presence of S as sulfur oxides which may be attributed to the surface oxidation [47].

Presence of C as a dopant was evident by the peaks at 285 and 289 eV in the C 1s spectra shown in figure 6.1.6 (c). The former peak may be attributed to the aliphatic carbon whereas the latter one may be due to the C involved in either double binding or in a bridging position with O and/or S. Similarly evidence for in-situ nitrogen doping was provided from the N (1s) spectra that showed a peak at 400 eV in Fig. 6.1.6 (d). Literature reports show that the binding energy of the N 1s is very sensitive to the chemical environment of the nitrogen and it varies from 396 to 408 eV [48]. The peak observed at 400 eV in the present case corresponds to the terminally bonded well screened molecular nitrogen ( $\gamma$ -N<sub>2</sub>) [49].

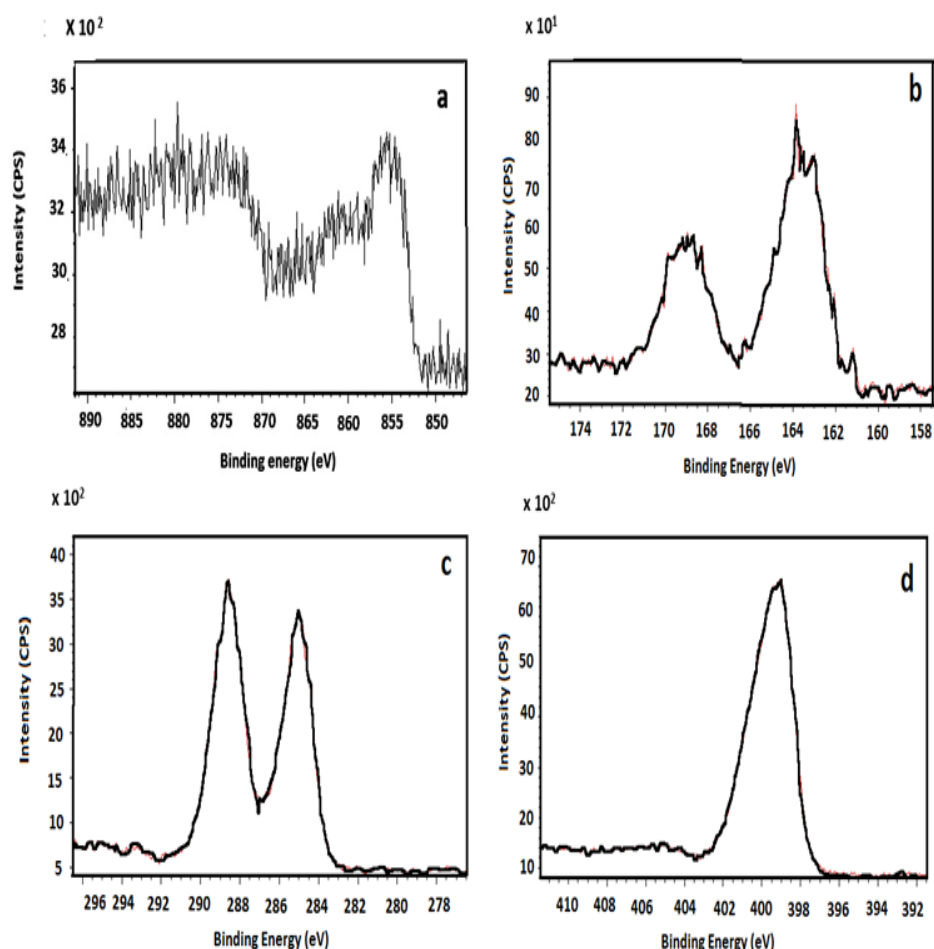


**Figure 6.1.6.** X-ray photoelectron spectra of CE 2 sample (a) Cd 3d electrons (b) S 2p electrons (c) C 1s electrons (d) N 1s electrons

### 6.1.3.5. Photoelectrochemical Measurements

The performance of the synthesized nickel sulfide samples as counter electrodes was investigated by using pure CdS as the working electrode and nickel sulfide samples as counter electrodes in the presence of Na<sub>2</sub>S containing KCl as the redox electrolyte. Current density versus photo voltage curves of the typical solar cells fabricated are shown in Fig. 6.1.7 (a) and the obtained solar cell parameters are given in table 6.1.1. The efficiency values are found to be 0.22, 0.48, 0.33, 0.31 and 0.24 for CE 1, CE 2, CE 3, CE 4 and CE 5 samples respectively, which clearly shows the best performance of CE 2 sample, which has Ni<sub>3</sub>S<sub>2</sub> composition.

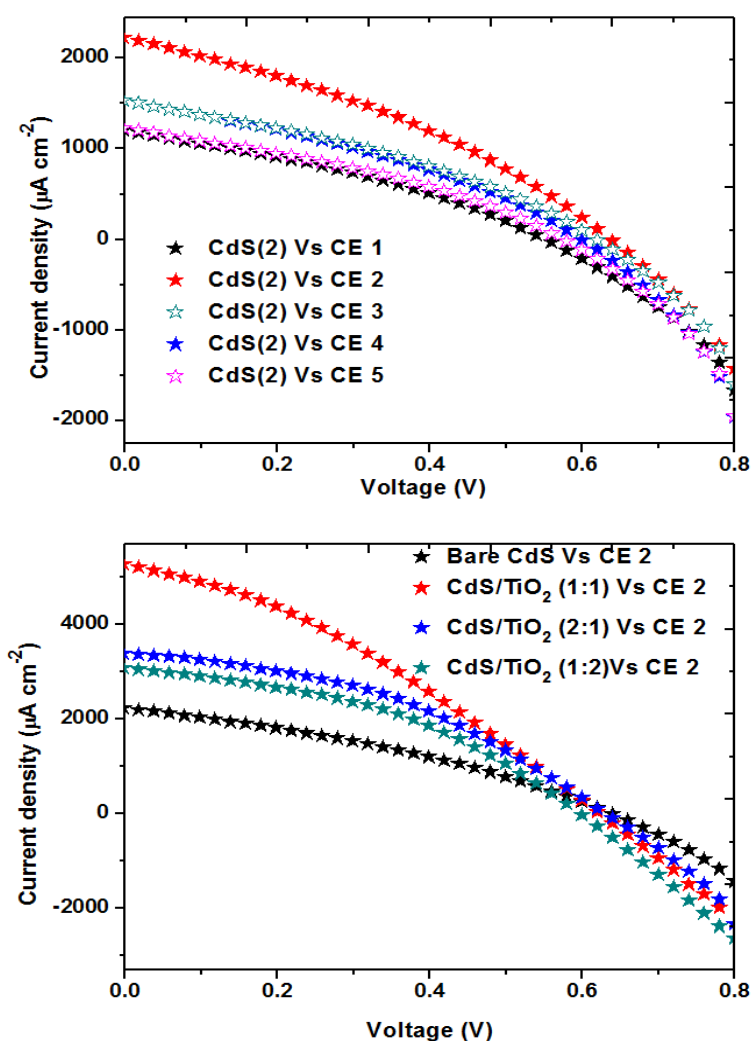


**Figure 6.1.7.** (a) J-V characteristics of photoelectrochemical cells based on bare CdS photoanode and different nickel sulfide samples as counter electrodes (b) Comparison of J-V characteristics of photoelectrochemical cells based on bare CdS and different physically grounded CdS/TiO<sub>2</sub> samples versus combustion synthesized CE 2 as counter electrode.

**Table 6.1.1. Solar cell parameters for various QDSSC fabricated by using different CE and the various impedance parameters**

CE	$V_{OC}$ (V)	$J_{SC}$ ( $\mu A\ cm^{-2}$ )	FF	$\eta$ (%)	$R_{ct}/\Omega cm^{-2}$	$Y_0$ ( $m\Omega^{-1}$ )
CE 1 (NiO)	550	1202	0.32	0.22	113	6.35
CE 2 (Ni <sub>3</sub> S <sub>2</sub> )	636	2223	0.37	0.48	37	21.8
CE 3 (NiS)	617	1535	0.36	0.33	45	21.1
CE 4 (NiS <sub>2</sub> )	597	1539	0.35	0.31	65	25.0
CE 5 (NiS <sub>2</sub> )	572	1231	0.35	0.24	193	0.98
Pt/FTO	439	706	0.26	0.11	272	0.149

Further studies were carried out only with CE 2 counter electrode whereas, for the working electrode optimization, CdS was sensitized on TiO<sub>2</sub> by physical mixing/grinding method. Interestingly, an increase in the efficiency was observed, which may be due to the reduced exciton recombination in the working electrode material. As shown in Fig. 6.1.7 (b), among the different working electrodes i.e. CdS/TiO<sub>2</sub> (1:2), CdS/TiO<sub>2</sub> (1:1) and CdS/TiO<sub>2</sub> (2:1) used in the present study, CdS/TiO<sub>2</sub> (1:1) showed highest  $V_{OC}$  and  $J_{SC}$  and thereby best efficiency ( $\eta$ ), which may be attributed to the best sensitization of CdS on TiO<sub>2</sub>. The best efficiency of 1.1% with CE 2 counter electrode was compared with the conventional Pt electrode and the results are shown in Fig. 6.1.8. The four fold increase in efficiency of CE 2 counter electrode was confirmed. The solar cell parameters for the different CdS sensitized TiO<sub>2</sub> electrodes versus CE 2 and Pt counter electrodes are tabulated in Table 6.1.2.

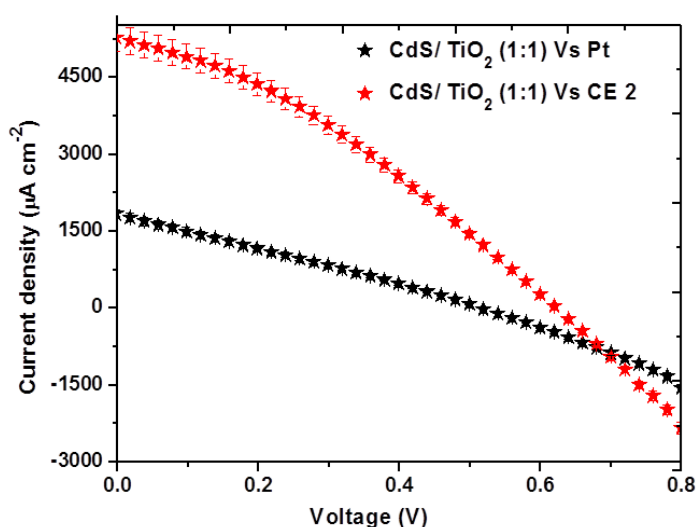


**Figure 6.1.8.** Comparison of J-V characteristics of photoelectrochemical solar cells constructed by using CdS/TiO<sub>2</sub>(1:1) as photoanode versus Pt and CE 2 as counter electrodes

### 6.1.3.6. Electrochemical Impedance Spectroscopy

It is known that the performance of QDSSC depends on the electrical conductivity of the CEs used [50]. In this context in order to analyze the performances of different nickel sulfide samples synthesized in the present study and also to study the nature of charge transfer between the corresponding counter electrode and electrolyte, electrochemical impedance spectroscopy (EIS) was recorded. Typical Nyquist plots are shown in Fig. 6.1.9 (a). Symmetrical electrodes were used for EIS analysis in order to avoid the influence of TiO<sub>2</sub> working electrode and 0.5 M Na<sub>2</sub>S solution containing KCl electrolyte. In general, the intercept of the real axis at high frequency region represents the series resistance (R<sub>s</sub>) that includes the sheet resistance of two identical counter electrodes and the electrolytic resistance. The semicircle at high frequency gives the magnitude of the charge transfer resistance (R<sub>ct</sub>) at the electrolyte/counter electrode interface. The constant phase element (CPE) is a circuit element that often used as a substitute for the capacitor in an equivalent circuit to fit the impedance behavior of the electrical double layer more precisely when the double layer does not behave like an ideal capacitor [51]. The R<sub>ct</sub> and Y<sub>0</sub> values of the electrodes have been obtained by fitting the experimental data with the equivalent circuit (Fig. 6.1.9(b)) and shown in Table 6.1.1 The observed R<sub>ct</sub> values of CE 1, CE 2, CE 3, CE 4, CE 5 and Pt are found to be 113, 37, 45, 65, 193 and 272 Ω cm<sup>2</sup> respectively. These values clearly indicate that the charge transfer resistance for nickel sulfide samples is much lower than the R<sub>ct</sub> of Pt, which highlights the best electrocatalytic activity of the nickel sulfide samples than Pt. In addition it was also observed that among the nickel sulfide samples the R<sub>ct</sub> of CE 2 (Ni<sub>3</sub>S<sub>2</sub>) was least which is in good agreement with the best efficiency of (0.48%). On the other hand, due to high R<sub>ct</sub>, Pt working electrode shows lowest performance of 0.1 % under similar experimental conditions. The lowest performance of Pt counter electrode can also be due to the poisoning effect of S in the polysulfide solution that increases the charge transfer resistance [52]. On the other hand the values of Y<sub>0</sub> represent the charge conduction ability of the electrode. The values of Y<sub>0</sub> are given in table 1 and it was observed that Y<sub>0</sub> was high for samples CE 2, CE 3 and CE 4 indicating that CE 2 can promote faster charge transport. The low value of Y<sub>0</sub> (0.149 mΩ<sup>-1</sup>) for Pt/FTO indicates the charge transport was not facile.

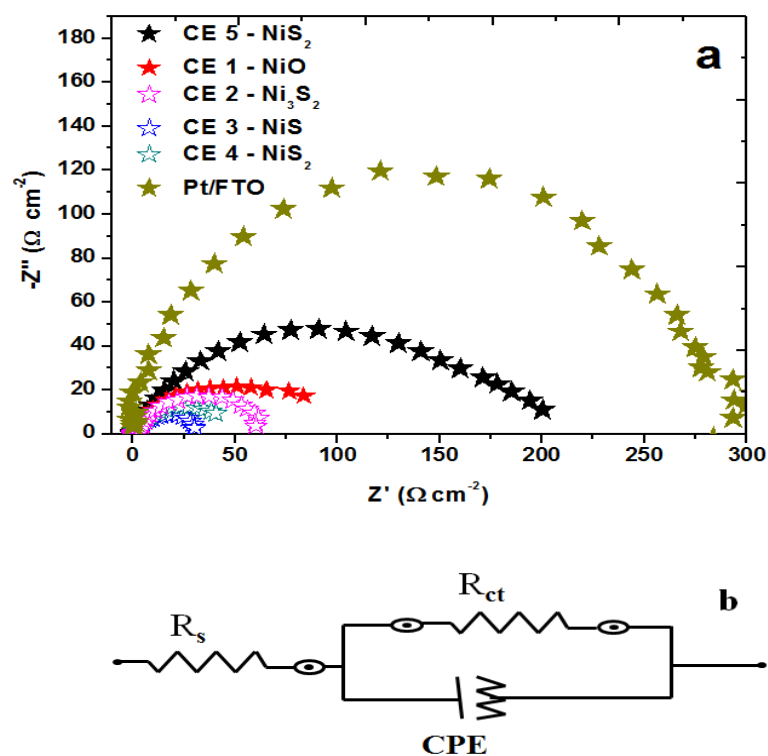


**Figure 6.1.9.** (a) Comparison of electro chemical impedance spectra of different combustion synthesized nickel sulfides and Pt/FTO counter electrode (b) Equivalent circuit used for fitting the EIS data of the symmetric cells.  $R_s$  is the series resistance, CPE is the constant phase element,  $R_{ct}$  is the charge transfer resistance.

**Table 6.1.2.** Solar cell parameters for various QDSSC fabricated by using different working electrodes used in this study with CE 2 ( $\text{Ni}_3\text{S}_2$ ) and Pt as counter electrodes.

Working electrode Vs CE 2	$V_{oc}$ (mV)	$J_{sc}$ ( $\mu\text{A cm}^{-2}$ )	Fill Factor	Efficiency (%)
CdS / $\text{TiO}_2$ (1:1) Vs CE 2	622	5253	0.33	1.08
CdS / $\text{TiO}_2$ (2:1) Vs CE 2	631	3366	0.37	0.87
CdS / $\text{TiO}_2$ (1:2) Vs CE 2	596	3074	0.36	0.76
CdS / $\text{TiO}_2$ (1:1) Vs Pt	516	1825	0.27	0.25

#### **6.1.4. Conclusions**

Phase selective synthesis of in-situ C and N doped nickel sulfide nanomaterials was achieved by using combustion synthesis. Different O/F ratios have been studied in order to obtain phase selective nickel sulfide and were studied as counter electrode materials in QDSSC. An efficient method of sensitization of CdS quantum dots on TiO<sub>2</sub> was developed. A simple paint approach has been used for the fabrication of electrode materials. All nickel sulfide nanomaterials developed instantly in the present study were found to supersede the expensive Pt as the counter electrode in QDSSC with an efficiency of ~1.1%, which was four fold higher than the efficiency achieved for conventional Pt counter electrode. Interestingly, among the different phases of nickel sulfides identified in the present study, CE 2 (Ni<sub>3</sub>S<sub>2</sub>) showed superior activity, which may be attributed to the facile charge transfer between the redox electrolyte and the counter electrode, as evidenced by electrochemical impedance spectral studies. Thus the present study presents a novel approach for the phase selective synthesis of efficient nickel sulfide counter electrode materials and a simple fabrication procedure for electrode preparation.

## Chapter 6-Section II

# One pot synthesis of metal (Pb, Cu, Co) sulfide nanomaterials as efficient counter electrodes in QDSSCs

### 6.2.1. Introduction

The present study provides a novel and facile method for the selective stoichiometric synthesis of various metal sulfides without using expensive surfactants, capping agents at ambient conditions. A paint approach has been developed to fabricate the counter electrode materials in a facile manner and their performance has been tested against Pt counter electrode in QDSSC.

### 6.2.2. Experimental section

Metal nitrates (oxidants) such as  $\text{Pb}(\text{NO}_3)_2$ ,  $\text{Cu}(\text{NO}_3)_2$ ,  $\text{Co}(\text{NO}_3)_2$  and thiourea (fuel) are purchased from Merck and used as received. The amount of precursors required for the synthesis were calculated based on the oxidant/fuel (O/F) ratio according to the propellant theory [46,47] and it was varied between 1 to 10 in order to obtain various stoichiometric compositions. In a typical synthesis, metal nitrate solutions and thiourea were mixed in a quartz bowl followed by preheating to get a thick gel that was transferred to a preheated furnace at  $300^\circ\text{C}$  to get metal sulfide powder in less than 5 min. The samples were labeled as MS(x) (where M is Cu, Pb and Co and x is 1,2,3,4 and 10). For the synthesis of CdS, calculated quantities of cadmium nitrate and thiourea (O/F ratio 2) were mixed in minimum water and preheated on a hot plate to get thick gel. The thick gel was transferred to the preheated furnace maintained at  $300^\circ\text{C}$  to get CdS nanomaterial in 5 min.

#### 6.2.2.1. Preparation of solar paint and electrodes

Working electrode was prepared by mixing 1:1 CdS powder and commercial  $\text{TiO}_2$  in minimum amount of ethanol followed by sonication for 30 min. A paint brush approach was used for the fabrication of electrodes and then annealed at 673 K for 30 min. As obtained yellow paint was applied on FTO glass plates, which were pretreated by  $\text{TiCl}_4$  solution. In a similar manner, counter electrodes of lead, copper and cobalt sulfides with different stoichiometry were made. For comparison Pt counter electrode was prepared by thermal decomposition of  $\text{H}_2\text{PtCl}_4$  solution in ethanol on FTO glass plate at 673 K [48]. In



general a common in-situ prepared  $\text{Cu}_2\text{S}$  electrode on brass sheet has been widely used as the counter electrode for quantum dot sensitized solar cells. Therefore in order to realize the advantage of present synthetic strategy for the synthesis of metal sulfide counter electrodes,  $\text{Cu}_2\text{S}$  electrode on brass was prepared by following a reported method and the results are compared with the counter electrodes prepared in the present report [49,50]. A 0.5 M  $\text{Na}_2\text{S}$  solution consisting of KCl was used as the electrolyte. The solar cell assembly consisted of the working electrode, an aqueous electrolyte of 0.5 M  $\text{Na}_2\text{S}$  containing KCl and either metal sulfide/FTO or Pt/FTO as the counter electrode placed in a glass cell. Schematic representation of electrodes fabrication is shown in Fig. 6.2.1.

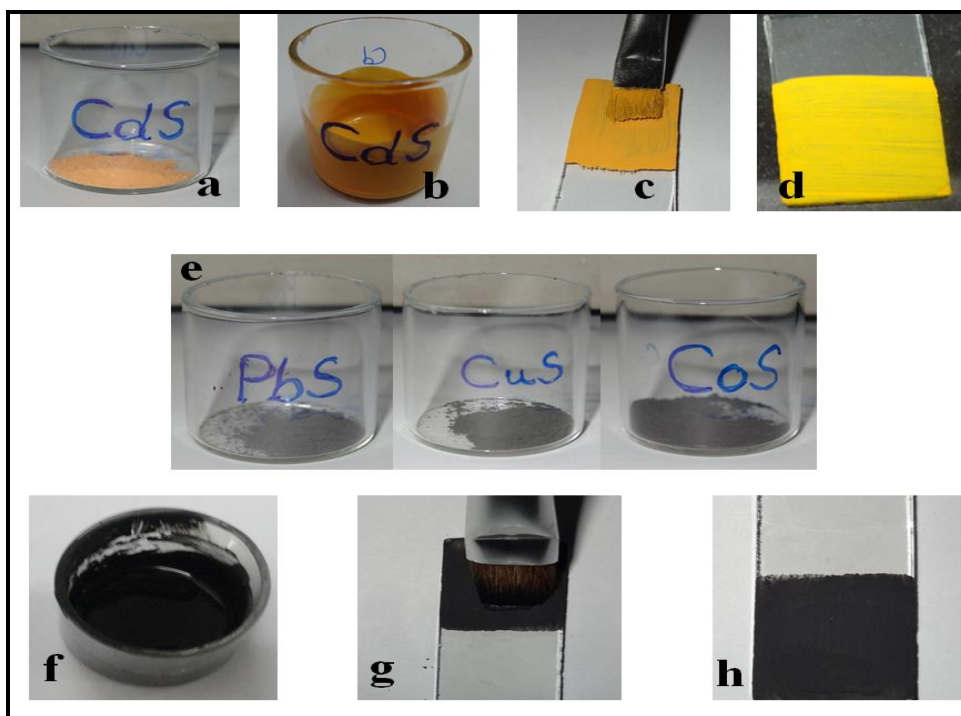


**Figure 6.2.1.** (a) Combustion synthesized CdS powder mixed with PVDF binder  
 (b) CdS paint after 30 min of sonication in ethanol  
 (c) Application of CdS paint on FTO glass plate, pretreated with  $\text{TiCl}_4$   
 (d) CdS working electrode after annealing at 673 K  
 (e) Combustion synthesized metal (Pb, Cu, Co) sulfide powders mixed with PVDF binder  
 (f) Metal sulfide paint after 30 min of sonication in ethanol  
 (g) Application of metal sulfide paint on FTO glass plate (h) Metal sulfide counter electrode after annealing at 673 K

#### 6.2.2.2. Characterization

Lead, copper and cobalt sulfide samples were characterized by various physico-electrochemical techniques in order to understand the structural, morphological, optical and

electrocatalytic properties. Stoichiometry, phase purity and crystallinity of the as synthesized lead, copper and cobalt sulfide samples were analyzed by using powder X-ray diffraction (PXRD). High resolution transmission electron microscopy (HRTEM) images of the metal sulfide samples were recorded in order to confirm the phase, particle size and morphology. Current versus voltage characteristics of the fabricated solar cells were measured on solar simulator with a digital source meter. Before collection of I-V data, each electrode was allowed to reach equilibrium at open-circuit. Electrochemical impedance spectra (EIS) of the counter electrode samples were obtained under symmetric cell configuration in presence of 0.5 M Na<sub>2</sub>S solution containing KCl as the electrolyte. An AC voltage of 10 mV superimposed over a dc potential of 0.0 V was applied to the electrodes and Nyquist plots were obtained over a frequency range of 10<sup>6</sup> Hz to 10<sup>-3</sup> Hz.

### 6.2.3. Results and discussion

#### 6.2.3.1. Powder X-ray diffraction (PXRD)

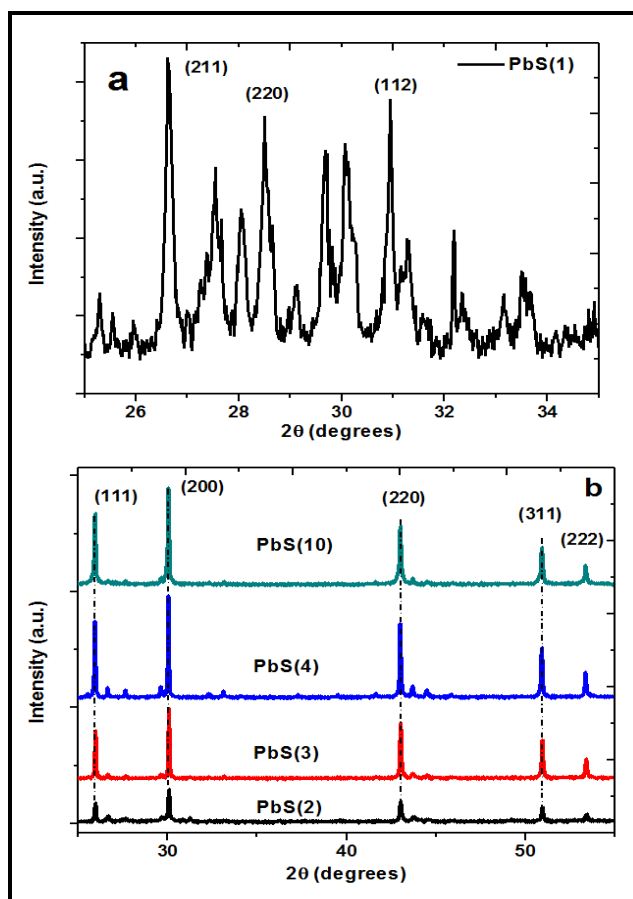


**Figure 6.2.2.** (a) PXRD spectra of PbS(1) sample showing the presence of Pb<sub>3</sub>O<sub>4</sub> (b) PXRD spectra of PbS(2), PbS(3), PbS(4) and PbS(10) samples showing the presence of PbS stoichiometry in all the samples.

Figure 6.2.2 shows the X-ray diffraction patterns of the lead sulfide samples synthesized at various O/F ratios. As shown in Fig. 6.2.2(a), PbS (1) shows major peaks at d-spacing of 3.4, 3.1 and 2.9 Å representing (211), (220) and (112) planes of Pb<sub>3</sub>O<sub>4</sub>. The formation of oxide phase is expected as the reaction was carried out at atmospheric conditions. However, as shown in Fig. 6.2.2(b), by increasing the O/F ratio, formation of sulfide phase (PbS) was observed in PbS (2), PbS (3), PbS (4) and PbS (10), as confirmed by the diffraction peaks with d-spacing of 3.4, 2.9, 2.1, 1.8 and 1.7 Å representing (111), (200), (220), (311) and (222) planes, respectively. The crystallite size calculated was around 8±2 nm for all the samples.

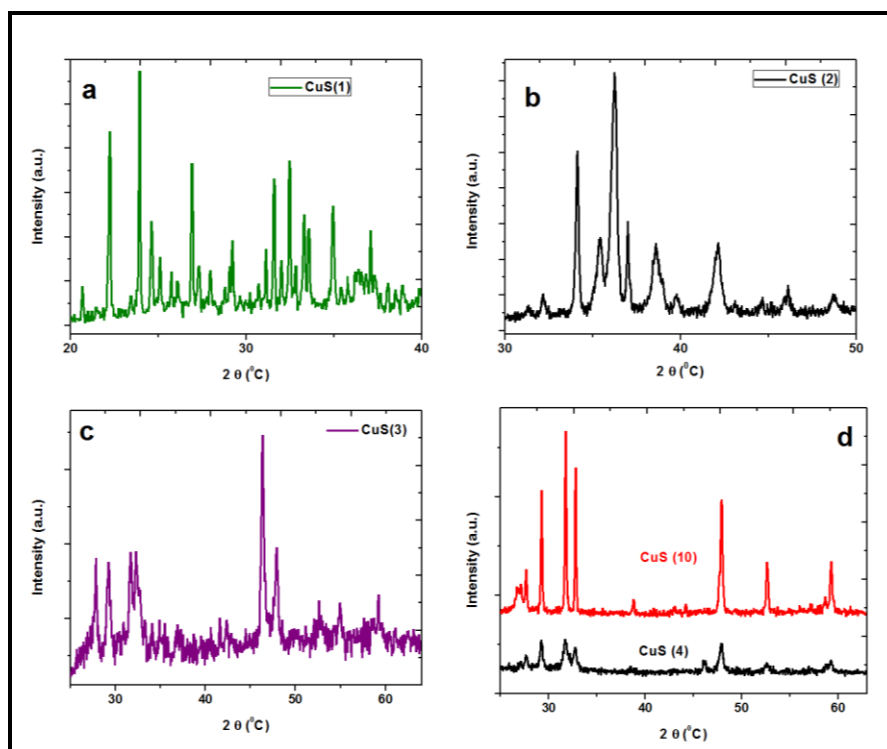


**Figure 6.2.3.** (a) PXRD spectra of CuS(1) sample showing the presence of CuO (b) PXRD spectra of CuS(2) sample showing the presence of Cu<sub>2</sub>O stoichiometry (c) PXRD spectra of CuS(3) sample showing the presence of Cu<sub>2</sub>S stoichiometry (d) PXRD spectra of CuS(4) and CuS(10) samples showing the presence of CuS stoichiometry.

Figure 6.2.3 presents the X-ray diffraction patterns of the copper sulfide samples. As seen in Fig. 6.2.3(a), CuO phase dominates for CuS (1), as confirmed by d-spacing of 3.6, 2.7, 2.5, 2.3, 2.1, 1.8 and 1.4 Å. On increasing O/F ratio, Cu<sub>2</sub>O followed by Cu<sub>2</sub>S and CuS were identified. Diffraction peaks at 2θ of 36.2, and 42.1° with corresponding d-spacing of 2.4 and 2.1 Å as seen in Fig. 6.2.3(b) indicated Cu<sub>2</sub>O phase of CuS(2). It may be concluded that oxygen lean conditions favored the formation of metal sulfides (Fig. 6.2.3(c) and 6.2.3(d)). Peaks at d-spacing of 2.4, 1.9 and 1.8 Å represents the (102), (110) and (103)

planes of the  $\text{Cu}_2\text{S}$  phase for CuS (3) as observed from Fig. 6.2.3(c). In case of CuS (4) and CuS (10) the diffraction peaks observed at d-spacing of 3.0, 2.8, 2.7, 1.9, 1.7 and 1.5 Å represents (102), (103), (006), (110), (108) and (116) planes respectively of CuS stoichiometry (Fig. 6.2.3(d)). The crystallite sizes calculated by using Scherrer formula were found to be 9, 8, 3, 6, and 8 nm respectively for CuS (1), CuS (2), CuS (3), CuS (4) and CuS (10).

Figure 6.2.4 represents the X-ray diffraction patterns of the cobalt sulfide for different O/F ratios which confirms the formation of CoO for O/F=1 that disappeared on changing O/F >2 leading to the formation of  $\text{CoS}_2$  phase. As shown in Fig. 6.2.4(a) diffraction peaks at d-spacing 2.4 and 2.1 Å represents (111) and (200) planes of CoO phase whereas, peaks at d-spacing 2.9, 2.5, 1.9 and 1.7 Å represent (311), (400), (511) and (440) planes of  $\text{Co}_9\text{S}_8$ . As represented in Fig. 6.2.4(b) the peaks with d-spacing 2.7 and 1.6 Å for CoS (3) represents  $\text{CoS}_2$  phase. On the other hand, CoS (4) and CoS (10) shows peaks at d-spacing of 2.7, 2.4, 2.2, 1.9, 1.8 and 1.6 Å, representing  $\text{CoS}_2$  phase (Fig. 6.2.4(b)). The crystallite sizes calculated by using Scherrer formula was around 9 nm for all the samples.

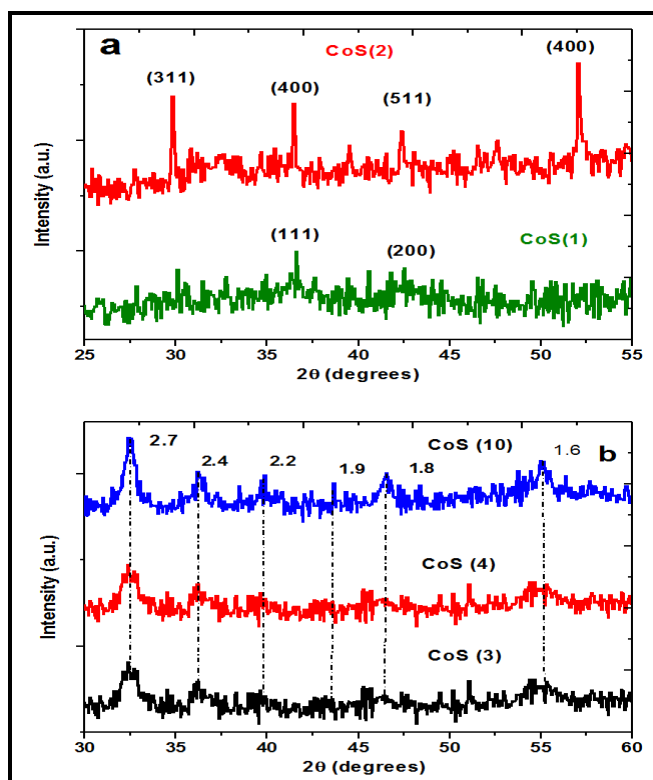


**Figure 6.2.4.** (a) PXRD spectra of CoS (1) and CoS (2) samples showing the presence of  $\text{Co}_3\text{O}_4$  and  $\text{Co}_9\text{S}_8$  stoichiometry respectively (b) PXRD spectra of CoS (3), CoS (4) and CoS (10) samples showing the presence of  $\text{CoS}_2$  stoichiometry.

### 6.2.3.2. TEM

In order to further confirm the stoichiometry and crystallite size of the metal sulfide samples, TEM measurements were carried out for CuS(3) and CoS(2) samples. Figure 6.2.5(a) presents the TEM image of CuS(3) which clearly showed nanoparticles (around 5 nm) and the SAED pattern present in the inset shows the polycrystalline nature of the CuS(3) sample. Figure 6.2.5(b) shows the HRTEM image of the CuS (3) sample with a lattice spacing 1.97 Å, which can be attributed to the Cu<sub>2</sub>S stoichiometry, compliments the XRD observations. In a similar manner, TEM image of CoS (2) (Fig. 6.2.5(c)) confirmed the nanoparticles around 9 nm, whereas, Fig. 6.2.5(d) confirmed the presence of (440) and (311) planes, characteristic of Co<sub>9</sub>S<sub>8</sub>.

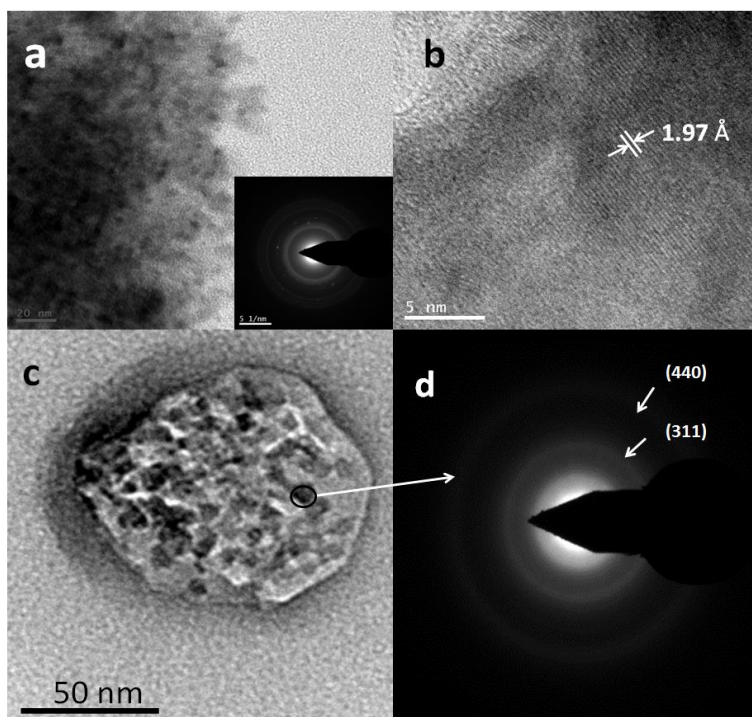


**Figure 6.2.5.** (a) TEM image of CuS(3) sample (inset shows the selected area diffraction pattern) (b) HRTEM image of the CuS(3) sample confirming the Cu<sub>2</sub>S stoichiometry (c) TEM image of CoS(2) sample (d) Selected area diffraction pattern of CoS(2) sample showing the planes corresponding to the Co<sub>9</sub>S<sub>8</sub> stoichiometry

### 6.2.3.3. Photoelectrochemical measurements

Current density (J) and photo voltage (V) characteristics were recorded for the quantum dot solar cells fabricated by using bare CdS as working electrode and various metal sulfide counter electrodes in the presence of 0.5 M Na<sub>2</sub>S as electrolyte. Figure 6.2.6 presents the J-V characteristics for the quantum dot solar cells with lead sulfide counter

electrodes. The J values observed for different lead sulfide samples were 1081, 2291, 2143, 1405 and 924  $\mu\text{A cm}^{-2}$  respectively for PbS(1), PbS(2), PbS(3), PbS(4) and PbS(10), confirming the best activity of PbS(2), which can be explained based on the formation of PbS phase. The decreasing J values at higher O/F ratio may be due to the presence of S in excess that may cover the active sites of the PbS and reduces the electron collecting/transfer ability of the counter electrode from PbS(3), PbS(4) to PbS(10).

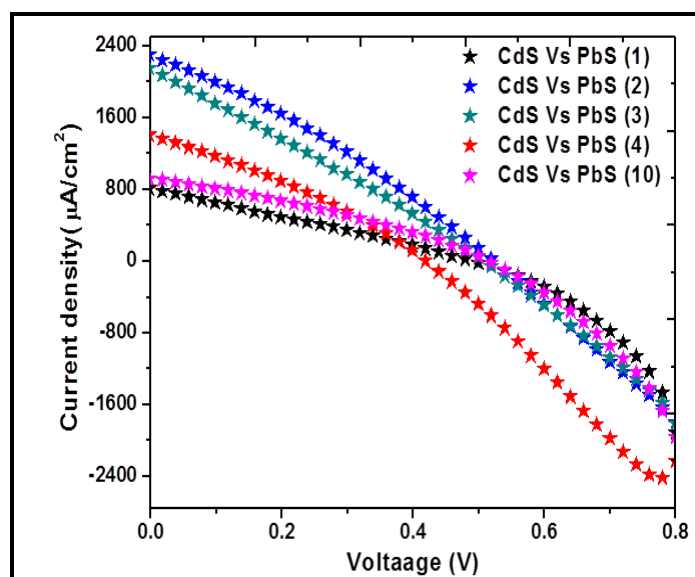


**Figure 6.2.6.** (a) J-V characteristics of photoelectrochemical cells based on bare CdS as working electrode and different combustion synthesized lead sulfide samples as counter electrodes.

Figure 6.2.7 presents the J-V curves of copper sulfide counter electrodes with CdS working electrode. Typical current density values of 1517, 2874, 3507, 2293 and 1535  $\mu\text{A cm}^{-2}$  were observed for CuS (1), CuS (2), CuS (3), CuS (4) and CuS (10) respectively. Lower J values for CuS (1) and CuS (2) may be due to is the presence of oxide phases, as evidenced by XRD, whereas, for CuS (3), the best activity may be due to the formation of  $\text{Cu}_2\text{S}$ , which is known as a good counter electrode [11]. However due to the disappearance of  $\text{Cu}_2\text{S}$  and formation of CuS, higher O/F ratios showed poor activity. From this, it is concluded that the  $\text{Cu}_2\text{S}$  might be the best stoichiometric sulfide to act as the counter electrode.

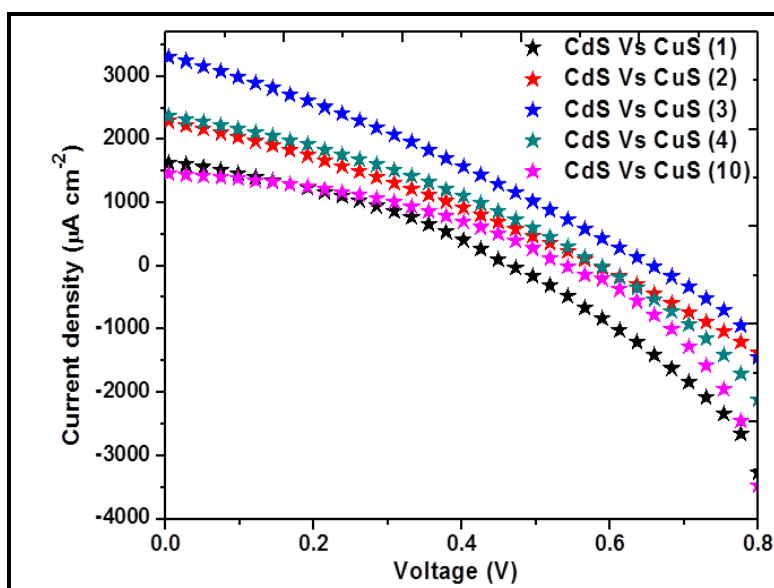


**Figure 6.2.7.** (a) J-V characteristics of photoelectrochemical cells based on bare CdS as working electrode and different combustion synthesized copper sulfide samples as counter electrodes.

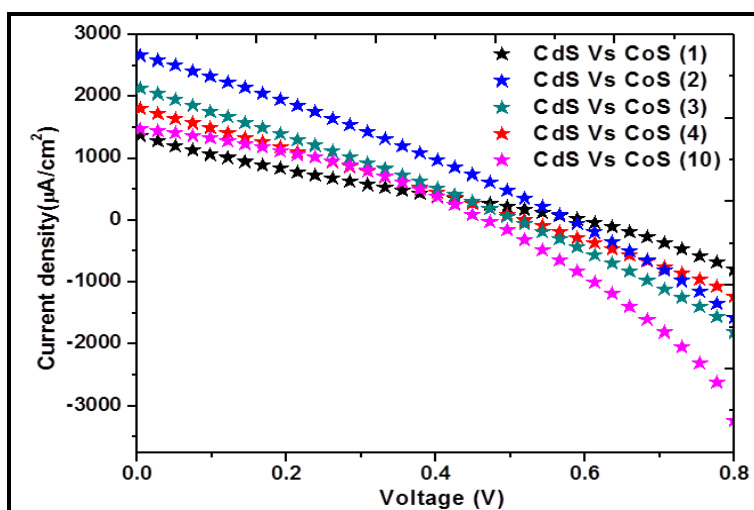


**Figure 6.2.8.** (a) J-V characteristics of photoelectrochemical cells based on bare CdS as working electrode and different combustion synthesized cobalt sulfide samples as counter electrodes.

In a similar manner, the J-V characteristics of cobalt sulfide counter electrodes shown in figure 6.2.8 confirms the current density of 1845, 2672, 2144, 1965 and 1812  $\mu\text{A cm}^{-2}$ , respectively for CoS(1), CoS(2), CoS(3), CoS(4) and CoS(10). Similar to the observations made with copper sulfide, CoS (2) gave highest current density probably due the presence of  $\text{Co}_9\text{S}_8$  [11]. It is worth mentioning that under the same experimental conditions, Pt counter electrode showed J value 700  $\mu\text{A cm}^{-2}$ . Table 6.2.1 summarizes the

comparative activity of various counter electrodes including Pt that confirms that the metal sulfide samples supersede Pt counter electrode.

**Table 6.2.1. Solar cell parameters for various QDSSC fabricated by using different counter electrodes used in this study and the various impedance parameters obtained by fitting in an equivalent circuit.**

CE	V <sub>oc</sub> (V)	J <sub>sc</sub> ( $\mu\text{A cm}^{-2}$ )	FF	$\eta$ (%)	R <sub>ct</sub> / $\Omega\text{cm}^{-2}$	Y <sub>0</sub> ( $\mu\Omega^{-1}$ )
<b>PbS (1)</b>	491	1081	0.26	0.1	427	260
<b>PbS (2)</b>	522	2291	0.28	0.36	187	270
<b>PbS (3)</b>	507	2143	0.27	0.29	209	199
<b>PbS (4)</b>	503	1705	0.26	0.23	292	151
<b>PbS (10)</b>	474	1050	0.26	0.17	317	118
<b>CuS (1)</b>	468	2168	0.28	0.27	3.7	81
<b>CuS (2)</b>	584	2295	0.31	0.40	3.5	11
<b>CuS (3)</b>	656	3324	0.35	0.65	0.7	196
<b>CuS (4)</b>	587	2365	0.33	0.47	2.9	37
<b>CuS (10)</b>	544	1455	0.32	0.31	3.7	204
<b>CoS (1)</b>	593	1845	0.28	0.18	3.4	1.2
<b>CoS (2)</b>	580	2672	0.31	0.44	1.2	34
<b>CoS (3)</b>	506	2144	0.28	0.29	2.9	112
<b>CoS (4)</b>	467	1965	0.28	0.25	2.6	62
<b>CoS (10)</b>	519	1812	0.28	0.25	3.2	68
<b>Pt/FTO</b>	439	706	0.26	0.11	272	0.15

From the above results, it is concluded that PbS (2), CuS (3) and CoS (2) showed best J values with bare CdS working electrode. Thus the best active counter electrodes from each metal sulfide were tested with CdS sensitized TiO<sub>2</sub> as working electrode (QDSSC). For this purpose, CdS/ TiO<sub>2</sub> (1:1) was prepared by physical grinding of commercial TiO<sub>2</sub> and CdS. Figure 6.2.9(a) shows the J-V characteristics of PbS (2), CuS (3), CoS (2) and Pt



versus CdS/TiO<sub>2</sub> (1:1) working electrode, which confirms the better efficiency than CdS. This improved performance may be due to the reduced exciton recombination.

As shown in Table 6.2.2, the efficiencies observed for different counter electrodes were 0.85, 1.3, 0.91 and 0.25 % respectively for PbS(2), CuS(3), CoS(2) and Pt. Among the metal sulfides the best efficiency was observed with copper sulfide counter electrode. The J-V characteristics of copper sulfide counter electrode was compared with that of Cu<sub>2</sub>S electrode on brass which is a commonly used copper sulfide counter electrode in QDSSCs. Figure 6.2.9(b) confirms that the copper sulfide prepared in the present study shows better efficiency. The better efficiency indicated that the metal sulfides may replace Pt counter electrode as well as Cu<sub>2</sub>S on brass in QDSSCs due to smaller charge transfer resistance ( $R_{ct}$ ), which facilitates fast electron transfer from the counter electrode to the electrolyte, favoring the reduction of  $S_n^{2-}$  to  $S^{2-}$ . In order to confirm this point, electrochemical impedance spectral studies were carried out.

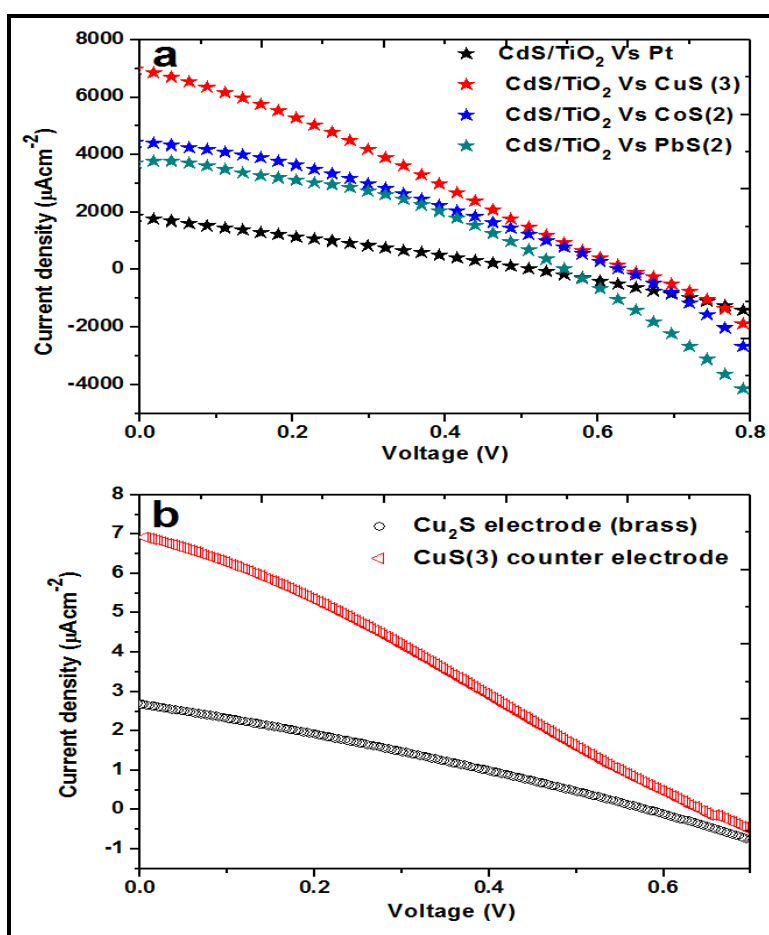


**Figure 6.2.9.** Comparison of J-V characteristics of photoelectrochemical solar cells constructed by using CdS/TiO<sub>2</sub> (1:1) as working electrode versus CuS(3), CoS(2), PbS(2) and Pt as counter electrodes.

**Table 6.2.2. Solar cell parameters for various QDSSC fabricated by using different metal sulfide counter electrodes.**

CdS / TiO <sub>2</sub> (1:1) Vs CE	V <sub>oc</sub> (mV)	J <sub>sc</sub> (μA cm <sup>-2</sup> )	Fill Factor	η (%)
CdS / TiO <sub>2</sub> (1:1) Vs PbS (2)	557	3657	0.34	0.85
CdS / TiO <sub>2</sub> (1:1) Vs CuS (3)	645	6938	0.32	1.3
CdS / TiO <sub>2</sub> (1:1) Vs CoS (2)	630	4422	0.34	0.91
CdS / TiO <sub>2</sub> (1:1) Vs Pt	516	1825	0.27	0.25
CdS / TiO <sub>2</sub> (1:1) Vs Cu <sub>2</sub> S(brass)	580	2672	0.30	0.44

#### 6.2.3.4. Electro chemical impedance spectroscopy

Figure 6.2.10 shows the Nyquist plots obtained from various symmetrical cells of metal sulfides. Charge transfer resistance ( $R_{ct}$ ) was obtained by fitting the curve observed in Nyquist plots to the Randles circuit as shown in figure 6.2.10 (e) and the data on various metal sulfides is shown in Table 6.2.1. Generally, the charge transfer resistance  $R_{ct}$  obtained from Nyquist plots was considered as an indicator to understand the catalytic activity of counter electrode materials [51, 52]. The  $R_{ct}$  values (Fig. 6.2.10 (a)) were found to be 427, 187, 209, 292 and 317  $\Omega \text{ cm}^{-2}$ , respectively for PbS (1), PbS (2), PbS (3), PbS (4) and PbS (10) which is in agreement with the current density values obtained earlier. The higher is the  $R_{ct}$  lesser is the current density. This also suggested that among lead sulfide samples, PbS (2) shows high electrocatalytic activity for the reduction of  $S_n^{2-}$  to  $S^{2-}$ .

In a similar manner, Figure 6.2.10 (b) shows the impedance behavior of copper sulfide samples counter electrodes respectively and the  $R_{ct}$  values were found to be 3.5, 2.9, 0.7, 3.7 and 3.5  $\Omega \text{ cm}^{-2}$  respectively for CuS(1), CuS(2), CuS(3), CuS(4) and CuS(10).

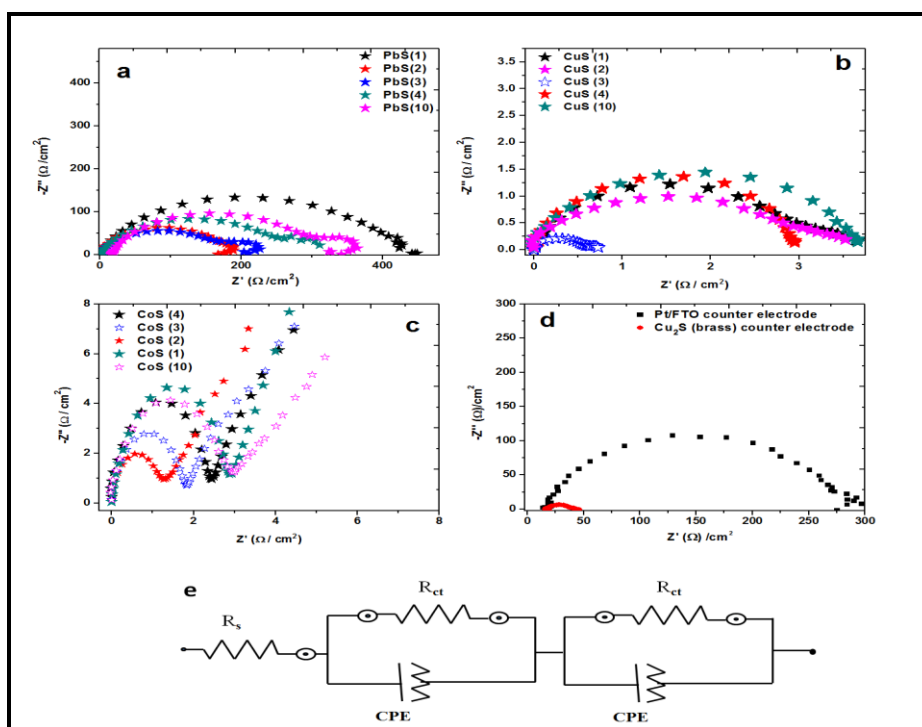


**Figure 6.2.10.** (a) Electro chemical impedance (EIS) spectra of different lead sulfide counter electrodes (b) EIS spectra of different copper sulfide counter electrodes (c) EIS spectra of different cobalt sulfide counter electrodes (d) EIS spectra of Pt counter electrode (e) Equivalent circuit used for fitting the EIS data of the symmetric cells.  $R_s$  is the series resistance, CPE is the constant phase element,  $R_{ct}$  is the charge transfer resistance.

Figure 6.2.10 (c) shows the EIS spectra of cobalt sulfide samples. As shown in Table 6.2.1, the observed  $R_{ct}$  was found to be 5.2, 2.4, 3.8, 4.9 and 5.4 respectively for CoS (1), CoS (2), CoS (3), CoS (4) and CoS (10). This also confirms the better electrocatalytic activity of cobalt sulfide samples than Pt and amongst, CoS (2), showed the best performance probably due to the presence of  $Co_9S_8$  phase found to have lowest  $R_{ct}$ .

Figure 6.2.10(d) shows the impedance behavior of Pt/FTO and  $Cu_2S$  on brass electrodes which upon fitting with equivalent circuit shows  $R_{ct}$  of 272 and 26  $\Omega\text{ cm}^{-2}$  respectively for Pt/FTO and  $Cu_2S$  on brass electrodes. Surprisingly CuS (3) which have the  $Cu_2S$  phase has  $\sim 400$  times lower  $R_{ct}$  than Pt and 37 times lower than  $Cu_2S$  on brass, which is a generally used counter electrode in QDSSCs. This is also in good agreement with the J-V measurements. These studies confirmed that among the metal sulfide tested in the present study, CuS (3) has best electrocatalytic activity.

#### 6.2.4. Conclusions

A facile single pot and stoichiometric synthesis of metal (Pb, Cu, Co) sulfides has been reported.. Oxidant/Fuel ratios have been optimized to in order achieve the best

electrocatalytic properties. A paint approach has been adopted to prepare the counter electrode materials. All metal sulfides studied are found to outperform the conventional Pt counter electrode as well as  $\text{Cu}_2\text{S}$  on brass electrode. Especially,  $\text{Cu}_2\text{S}$  and  $\text{Co}_9\text{S}_8$  exhibited best current density and lowest  $R_{\text{ct}}$ . Therefore this instant synthesis of metal sulfides and facile counter electrode fabrication not only explore a selective method for the synthesis of different stoichiometric compositions of metal sulfides but also provides relatively simpler fabrication of QDSSC.

## References

- [1] Q. Zhang, E. Uchaker, S. L. Candelaria and G. Cao. Nanomaterials for energy conversion and storage. *Chem. Soc. Rev.* 42, (2013) 3127-3171.
- [2] P. V. Kamat. Quantum Dot Solar Cells- Semiconductor Nanocrystals as Light Harvesters. *J. Phys. Chem. C.* 112, (2008) 18737-18753.
- [3] P. V. Kamat, K. Tvrđy, D. R. Baker and J. G. Radich. Beyond Photovoltaics: Semiconductor Nano architectures for Liquid-Junction Solar Cells. *Chem. Rev.* 110, (2010) 6664-6688.
- [4] P. V. Kamat. Capturing hot electrons. *Nature Chemistry.* 2, (2010) 809-810.
- [5] C. Wang, Z. Jiang, L. Wei, Y. Chen, J. Jiao, M. Eastman, H. Liu. Photosensitization of TiO<sub>2</sub> nanorods with CdS quantum dots for photovoltaic applications: A wet-chemical approach. *Nano Energ.* 1, (2012) 440-447.
- [6] A. Kongkanand, K. Tvrđy, K. Takechi, M. Kuno and P. V. Kamat. Quantum Dot Solar Cells. Tuning Photoresponse through Size and Shape Control of CdSe TiO<sub>2</sub> Architecture. *J. Am. Chem. Soc.* 130, (2008) 4007-4015.
- [7] P. V. Kamat. Boosting the Efficiency of Quantum Dot Sensitized Solar Cells through Modulation of Interfacial Charge Transfer. *Acc. Chem. Res.* 45, (2012) 1906-1915.
- [8] R. Vogel, K. Pohl and H. Weller. Sensitization of Highly Porous, Polycrystalline TiO<sub>2</sub> Electrodes by Quantum Sized CdS. *Chem. Phys. Lett.* 174, (1990) 241-246.
- [9] W. Yu, L. H. Qu, W. Z. Guo and X. G. Peng. Experimental Determination of the Extinction Coefficient of CdTe, CdSe, and CdS Nanocrystals. *Chem. Mater.* 15, (2003) 2854-2860.
- [10] R. Vogel, P. Hoyer and H. Weller. Quantum-Sized PdS, CdS, Ag<sub>2</sub>S, Sb<sub>2</sub>S<sub>3</sub> and Bi<sub>2</sub>S<sub>3</sub> Particles as Sensitizers for Various Nanoporous Wide-Bandgap Semiconductors, *J. Phys. Chem. B.* 98, (1994) 3183-3188.
- [11] L. Liu, J. Hensel, R. C. Fitzmorris, Y. Li and J. Z. Zhang. Preparation and Photoelectrochemical Properties of CdSe/TiO<sub>2</sub> Hybrid Mesoporous Structures. *J. Phys. Chem. Lett.* 1, (2010) 155-160.
- [12] D. R. Baker and P. V. Kamat. Photosensitization of TiO<sub>2</sub> Nanostructures with CdS Quantum Dots. Particulate versus Tubular Support Architectures. *Adv. Funct. Mater.* 19, (2009) 805-811.
- [13] N. Remya, B. Narsimha Reddy and M. Deepa. Facile Charge Propagation in CdS Quantum Dot Cells. *J. Phys. Chem. C.* 116, (2012) 7189-7199.

- [14] N. Guijarro, T. Lana-Villarreal, I. Mora-Sero, J. Bisquert and R. Gomez, CdSe Quantum Dot-Sensitized TiO<sub>2</sub> Electrodes: Effect of Quantum Dot Coverage and Mode of Attachment. *J. Phys. Chem. C* 113, (2009) 4208-4214.
- [15] D. Ham, K. K. Mishra and K. Rajeshwar. Anodic Electrosynthesis of Cadmium Selenide Thin Films. *J. Electrochem. Soc.* 138, (1991) 100-108.
- [16] H. J. Lee, M. Wang, P. Chen, D. R. Gamelin, S. M. Zakeeruddin, M. Gratzel and Md. K. Nazeeruddin. Efficient CdSe Quantum Dot-Sensitized Solar Cells Prepared by an Improved Successive Ionic Layer Adsorption and Reaction Process. *Nano Lett.* 9, (2009) 4221-4227.
- [17] Y. Zhang, J. Zhu, X. Yu, J. Wei, L. Hu and S. Dai. The optical and electrochemical properties of CdS/CdSe co-sensitized TiO<sub>2</sub> solar cells prepared by successive ionic layer adsorption and reaction processes. *Solar Energ.* 86, (2012) 964–971.
- [18] P. Brown and P. V. Kamat. Quantum Dot Solar Cells. Electrophoretic Deposition of CdSe C60 Composite Films and Capture of Photogenerated Electrons with nC60 Cluster Shell. *J. Am.Chem. Soc.* 130, (2008) 8890-8891.
- [19] I. Robel, V. Subramanian, M. Kuno and P. V. Kamat. Quantum Dot Solar Cells. Harvesting Light Energy with CdSe Nanocrystals Molecularly Linked to Mesoscopic TiO<sub>2</sub> Films. *J. Am.Chem. Soc.* 128, (2006) 2385-2393.
- [20] T. Yang, M. Lu, X. Mao, W. Liu, L. Wan, S. Miao and J. Xu. Synthesis of CdS quantum dots (QDs) via a hot-bubbling route and co-sensitized solar cells assembly. *Chem. Eng. J.* 225, (2013) 776–783.
- [21] M. P. Genovese, I.V. Lightcap and P.V. Kamat. Sun-Believable Solar Paint. A Transformative One-Step Approach for Designing Nanocrystalline Solar Cells. *ACS Nano*, 6,(2012) 865-872.
- [22] N. Papageorgiou. Counter-electrode function in nanocrystalline photoelectrochemical cell configurations. *Coord. Chem. Rev.* 248, (2004) 1421-1446.
- [23] T. N. Murakami, S. Ito, Q. Wang, M. K. Nazeeruddin, T. Bessho, I. Cesar, P. Liska, R. Humphry-Baker, P. Comte, P. Pechy and M. Gratzel. Highly Efficient Dye-Sensitized Solar Cells Based on Carbon Black Counter Electrodes. *J. Electrochem. Soc.* 153, (2006) A2255-A2261.
- [24] G. Veerappan, K. Bojan, S.-W. Rhee. Amorphous carbon as a flexible counter electrode for low cost and efficient dye sensitized solar cell. *Renew. Energ.* 41, (2012) 383-388.

- [25] P. Li, J. Wu, J. Lin, M. Huang, Y. Huang and Q. Li. High performance and low platinum loading Pt/Carbon black counter electrode for dye-sensitized solar cells. *Solar Energy*. 83, (2009) 845–849.
- [26] N. A.M. Barakat, M. S. Akhtar, A. Yousef, M. El-Newehy, H. Y. Kim. Pd–Co-doped carbon nanofibers with photoactivity as effective counter electrodes for DSSCs, *Chem. Eng. J.* 211–212, (2012) 9–15.
- [27] R. Cruz, D. A. P. Tanaka and A. Mendes. Reduced graphene oxide films as transparent counter-electrodes for dye-sensitized solar cells. *Solar Energ.* 86, (2012) 716–724.
- [28] H.-K. Seo, M. Song, S. Ameen, M. S. Akhtar and H. S. Shin. New counter electrode of hot filament chemical vapor deposited graphene thin film for dye sensitized solar cell. *Chem. Eng. J.* 222, (2013) 464–471.
- [29] W. J. Lee, E. Ramasamy, D. Y. Lee and J. S. Song. Efficient Dye-Sensitized Solar Cells with Catalytic Multiwall Carbon Nanotube Counter Electrodes. *ACS Appl. Mater. Interfaces*. 1, (2009) 1145-1149.
- [30] J. B. Xia, N. Masaki, K. J. Jiang and S. Yanagida. The influence of doping ions on poly (3,4-ethylenedioxythiophene) as a counter electrode of a dye-sensitized solar cell. *J. Mater. Chem.* 17, (2007) 2845-2850.
- [31] H. C. Sun, Y. H. Luo, Y. D. Zhang, D.M. Li, Z. X. Yu, K. X. Li and Q. B. Meng. In Situ Preparation of a Flexible Polyaniline/Carbon Composite Counter Electrode and Its Application in Dye-Sensitized Solar Cells. *J. Phys. Chem. C*, 114, (2010) 11673-11679.
- [32] K. M. Hemant, K. B. Sudip, R. Manohar, R. P. Rajiv, M. Nripan, M. L. Yeng and G. M. Subodh. Solution processed transition metal sulfides: application as counter electrodes in dye sensitized solar cells (DSCs). *Phys. Chem. Chem. Phys.* 13, (2011) 19307-19309.
- [33] A. Ghezelbash, M. B. Sigman and B. A. Korgel. Solventless Synthesis of Nickel Sulfide Nanorods and Triangular Nanoprisms. *Nano Lett.* 4, (2004) 537-542.
- [34] Y. Hu, J. Chen, W. Chen, X. Lin and X. Li. Synthesis of Novel Nickel Sulfide Submicrometer Hollow Spheres, *Adv. Mater.* 15, (2003) 726-729.
- [35] (a) L. Zhang, J. C. Yu, M. Mo, L. Wu, Q. Li and K. W. Kwong. A General Solution-Phase Approach to Oriented Nanostructured Films of Metal Chalcogenides on Metal Foils: The Case of Nickel Sulfide. *J. Am. Chem. Soc.* 126, (2004) 8116-8117. (b) Z. Y. Meng, Y. Y. Peng, W. C. Yu and Y. T. Qian. Solvothermal synthesis and phase control of nickel sulfides with different morphologies. *Mater. Chem. Phys.* 74, (2002) 230-233.
- [36] M. Wu, Xiao. Lin, Yudi. Wang, Liang. Wang, Wei. Guo, Daidi. Qi, Xiaojun. Peng, Anders. Hagfeldt, M. Gratzel and T. Ma. Economical Pt-Free Catalysts for Counter Electrodes of Dye-Sensitized Solar Cells. *J. Am. Chem. Soc.* 134, (2012) 3419-3428.

- [37] M. Thambidurai, N. Muthukumarasamy, S. Agilan, N. Murugan, S. Vasantha, R. Balasundaraprabhu and T. S. Senthil. Strong quantum confinement effect in nanocrystalline CdS. *J. Mater. Sci.* 45, (2010) 3254-3258.
- [38] D. E. Skinner, D. P. Colombo, J. J. Cavaleri and R. M. Bowman. Femtosecond investigation of electron trapping in semiconductor nano clusters. *J. Phys. Chem.* 99, (1995) 7853-7856.
- [39] Y. Lin, J. Zhang, E. H. Sargent and E. Kumacheva. Photonic pseudo-gap-based modification of photoluminescence from CdS nanocrystal satellites around polymer microspheres in a photonic crystal. *Appl. Phys. Lett.* 81, (2002) 3134-3136.
- [40] L. Qi, H. Colfen and M. Antonietti. Synthesis and characterization of CdS nanoparticles stabilized by double-hydrophilic block copolymers. *Nano Lett.* 1, (2001) 61-65.
- [41] J. R. Heath and J. J. Shiang. Covalency in semiconductor quantum dots. *Chem. Soc. Rev.* 27, (1998) 65-71.
- [42] A. N. Buckley and R. J. Woods. Electrochemical and XPS studies of the surface oxidation of synthetic heazlewoodite (Ni<sub>3</sub>S<sub>2</sub>). *Appl. Electrochem.* 21, (1991) 575-582.
- [43] H. W. Nesbitt, D. Legrand and G. M. Bancroft. Interpretation of Ni 2p XPS spectra of Ni conductors and Ni insulators. *Phys. Chem. Miner.* 27, (2000) 357-366.
- [44] L. Sangaletti, F. Parmigiani, T. Thio and J.W. Bennett. Electronic-correlation effects in the X-ray-photoemission spectra of NiS<sub>2</sub>. *Phys. Rev. B.* 55, (1997) 9514-9519.
- [45] J. F. Moulder, W.F. Stickle, P.E. Sobol, K.D. Bomben and J. Chastain, *Handbook of X-ray Photoelectron Spectroscopy*. Perkin Elmer Publication, Eden Prairie MN, 1992.
- [46] N.D. Shinn and K.L. Tsang. Strain-induced surface reactivity: Low temperature Cr/W(110) nitridation. *J. Vac. Sci. Technol. A.* 9, (1991) 1558-1562.
- [47] G.-R. Li, F. Wang, Q.-W. Jiang, X.-P. Gao and P.-W. Shen. Carbon Nanotubes with Titanium Nitride as a Low-Cost Counter-Electrode Material for Dye-Sensitized Solar Cells. *Angew. Chem. Int. Ed.* 49, (2010) 3653-3658.
- [48] X. Wu, H. Ma, S. Chen, Z. Xu and A. Sui. General Equivalent Circuits for Faradaic Electrode Processes under Electrochemical Reaction Control. *J. Electrochem. Soc.* 146, (1999) 1847-1853.
- [49] B. Fang, M. Kim, S.-Q. Fan, J. H. Kim, D. P. Wilkinson, J. Ko and J.-S. Yu. Facile synthesis of open mesoporous carbon nanofibers with tailored nanostructure as a highly efficient counter electrode in CdSe quantum-dot-sensitized solar cells. *J. Mater. Chem.* 21, (2011) 8742-8748.



- [50] K. C. Patil. Advanced ceramics: Combustion synthesis and properties. *Bull. Mater. Sci.* 16, (1993) 533-541.
- [51] S. R. Jain, K. C. Adiga and V. R. P. Verneker. A new approach to thermochemical calculations of condensed fuel-oxidizer mixtures. *Combust. Flame.* 40, (1981) 71-79.
- [52] H. Sun, D. Qin, S. Huang, X. Guo, D. Li, Y. Luo and Q. Meng. Dye-sensitized solar cells with NiS counter electrodes electrodeposited by a potential reversal technique. *Energy Environ. Sci.* 4, (2011) 2630–2637.
- [53] K. Meng, P. K. Surolia, O. Byrne and K. R. Thampi. Efficient CdS quantum dot sensitized solar cells made using novel Cu<sub>2</sub>S counter electrode. *J. Power Sources.* 248, (2014) 218-223.
- [54] G. Hodes, J. Manassen and D. Cahen. Electrocatalytic electrodes for the polysulfide redox system. *J. Electrochem. Soc.* 127, (1980) 544-549.
- [55] S. Gimenez, I. Mora-Sero, L. Macor, N. Guijarro, T. Lana-Villarreal, R. Gomez, L. J. Diguna, Q. Shen, T. Toyoda and J. Bisquert. Improving the performance of colloidal quantum-dot-sensitized solar cells. *Nanotechnology.* 20, (2009) 295204.
- [56] E. Ramasamy, W. J. Lee, D. Y. Lee and J. S. Song. Spray coated multi-wall carbon nanotube counter electrode for tri-iodide (I<sub>3</sub><sup>-</sup>) reduction in dye-sensitized solar cells. *Electrochem. Commun.* 10, (2008) 1087–1089.

# CHAPTER 7

## Summary and Conclusions

---

This thesis mainly focused on the synthesis of materials that can harvest solar energy. Combustion synthesis which is found to be an energy, time and cost effective synthetic method for the synthesis of nanomaterials has been investigated in a detailed manner. Though combustion synthesis is practiced for the synthesis of metal oxides by various researchers, this thesis furnishes important findings such as optimized synthesis of oxidant and optimization of fuel for the synthesis of metal oxide for either C doping or C and N doping. This thesis also reports the applicability of combustion synthesis for the synthesis of various transition, non-transition metal sulfides and composites at ambient atmospheric conditions. The general conclusions that were drawn from the thesis are summarized as follows:

- Titanyl nitrate prepared by slow hydrolysis of Ti(IV) iso-propoxide followed by nitration with excess of nitric acid was found to produce TiO<sub>2</sub> with better properties such as high surface area, low band gap, smaller particle size, more C and N doping as confirmed by various characterization techniques. The as synthesized TiO<sub>2</sub> samples showed best photocatalytic activity for the oxidation of methylene blue (MB) dye under natural sunlight and ambient conditions.
- Effect of fuel on combustion synthesis of C, N doped TiO<sub>2</sub> has been studied in a detailed manner by taking several fuels such as an amino acid (glycine), a tetramine (hexamethylene tetramine) and an amine (triethylamine) as model fuels. In addition to this effect of mixture of fuels on the properties of TiO<sub>2</sub> was also studied. It has been observed that there is a correlation between the number of gases evolved during the combustion and the properties of resulting TiO<sub>2</sub>. It is found that with

increasing number of moles of gases, surface area and C, N doping also increases, on the other hand particle size and band gap decreases. Among the individual fuels studied glycine was found to evolve more number of gases. Moreover it has been observed that compared to the use of mixture of fuels, use of single fuel is more advantageous for obtaining  $\text{TiO}_2$  with suitable properties for photocatalytic applications. This rationale can also be applied to the combustion synthesis of other C, N doped metal oxide nanomaterials. The prepared  $\text{TiO}_2$  nanomaterials have shown excellent visible light activity for the photocatalytic oxidation of MB and reduction of Cr(VI) from aqueous streams.

- Effect of fuel on combustion synthesis of mere C doped  $\text{TiO}_2$  has also been studied by taking selectively citric acid and ascorbic acid as fuels that can facilitate only C doping without any N doping. The prepared C-doped  $\text{TiO}_2$  samples were tested for the individual as well as simultaneous removal of phenol and Cr (VI) by photocatalysis under visible light irradiation. It has been observed that simultaneous removal of pollutants is more favorable than individual pollutants due to the suppression of exciton recombination. This study concludes that C- $\text{TiO}_2$  outperforms C,N- $\text{TiO}_2$  and citric acid is the best fuel for the combustion synthesis of metal oxides.
- Successful syntheses of cadmium sulfide by combustion synthesis without using any inert atmospheric conditions have been achieved. O/F ratio was increased beyond 1 in order to prevent the formation of thermodynamically stable metal oxide phase. Among all the CdS samples, the one prepared at O/F ratio of 2 exhibited best photocatalytic activity towards  $\text{H}_2$  production from water, probably due to the well crystalline nature and suitable band gap energy. as observed from X-ray diffraction and diffuse reflectance UV-Vis spectroscopy respectively.

- Since combustion synthesis is well known for the *in-situ* C, N doping the technique has been extended for the synthesis of ZnS nanomaterials. It has been observed that combustion synthesized ZnS samples have band gap  $< 3.0$  eV and have shown enhanced visible light photocatalytic activity for H<sub>2</sub> production from water containing sacrificial reagents. Different molar ratios (1:2 to 1:6) of zinc and sulfur precursors were used in order to obtain ZnS with better properties. Among all the ZnS samples ZnS(1:5) have shown best activity which was attributed to the optimum C and N doping.
- The versatile combustion synthesis technique has been further extended to the single step synthesis of CdS/TiO<sub>2</sub> hetero nanostructures. Generally synthesis of CdS/TiO<sub>2</sub> involves multiple steps, but the present combustion technique offers the single step synthesis in an energy and time efficient manner without any capping agents and inert atmospheric conditions. The mole ratio of Cd and Ti precursors were varied as 0.5:1, 1:1 and 1:0.5 in order to achieve the optimum sensitization of TiO<sub>2</sub> by CdS. Among the composites CdS/TiO<sub>2</sub>(1:1) have shown more fluorescence quenching, due to facile electron transfer from CdS to TiO<sub>2</sub>. Stoichiometry selective synthesis of cobalt sulfide, nickel sulfide and copper sulfide was achieved at ambient conditions and without any surfactants and capping agents. All these sulfides were found to exhibit less charge transfer resistance than Pt/FTO. It was concluded that the stoichiometry of metal sulfide has an effect on the electrochemical performance. It has been further observed that Co<sub>9</sub>S<sub>8</sub>, Ni<sub>3</sub>S<sub>2</sub> and Cu<sub>2</sub>S are the favorable stoichiometry among the respective metal sulfides to act as counter electrode materials in QDSSCs. Among the various metal sulfides, Cu<sub>2</sub>S was found to have less charge transfer resistance, best electrochemical performance and hence a solar cell efficiency ( $\eta$ ) of 1.3 %.

## LIST OF PUBLICATIONS BASED ON THE RESEARCH WORK

- 1) **A. Daya Mani**, V. Laporte, P. Ghosal and Ch. Subrahmanyam, Combustion synthesized TiO<sub>2</sub> for enhanced photocatalytic activity under the direct sunlight- optimization of titanyl nitrate synthesis, **Materials Research Bulletin**, 47 (2012) 2415–2421.
- 2) **A. Daya Mani**, B. Rama Raju, N. Xanthopoulos, P. Ghosal, B. Sreedhar and Ch. Subrahmanyam, Effect of fuels on combustion synthesis of TiO<sub>2</sub> – Towards efficient photocatalysts for methylene blue oxidation and Cr (VI) reduction under natural sunlight, **Chemical Engineering Journal** 228 (2013) 545–553.
- 3) **A. Daya Mani**, N. Xanthopoulos, Daniele Laub and Ch. Subrahmanyam, Combustion synthesis of cadmium sulfide nanomaterials for efficient visible light driven hydrogen production from water, **Journal of Chemical Sciences** (In press).
- 4) **A. Daya Mani**, P. Ghosal and Ch. Subrahmanyam, Novel synthesis of C, N doped rice grain shaped ZnS Nanomaterials –Towards enhanced visible light Photocatalytic activity for aqueous pollutant removal and H<sub>2</sub> production, **RSC Adv.**, 4 (2014) 23292–23298
- 5) **A. Daya Mani**, Melepurath Deepa, P. Ghosal and Ch. Subrahmanyam, Novel single pot synthesis of metal (Pb, Cu, Co) sulfide nanomaterials -Towards a quest for paintable electrode materials that supersedes Pt electrode, **Electrochim. Acta**. 139 (2014) 365–373
- 6) **A. Daya Mani**, Melepurath Deepa, N. Xanthopoulos and Ch. Subrahmanyam, Novel one pot stoichiometric synthesis of nickel sulfide Nanomaterials as counter electrodes for QDSSCs, **Mater. Chem. Phys.** (Accepted).

7) **A. Daya Mani**, P. M. Reddy, M. Srinivaas and Ch. Subrahmanyam, Highly Efficient TiO<sub>2</sub> Photocatalysts for Simultaneous Removal of Phenol and Cr (VI) under Visible Light, **Mater Res Bull.** (Under Revision).

8) **A. Daya Mani** and Ch. Subrahmanyam, One pot synthesis of CdS/ TiO<sub>2</sub> hetero nanostructures for enhanced H<sub>2</sub> Production from water and removal of pollutants from aqueous streams, **Int. J. Hydrogen Energ.** (Under review).

### **List of International Conferences Attended**

1. **A. Daya Mani**, Md.Unnisa and Ch.Subrahmanyam, C and N doped TiO<sub>2</sub>-Nanophotocatalysts for visible light photocatalysis 2011. “International Conference on Nanoscience and Technology (**Cochin Nano-2011**)” August 14-17, **Cochin, Kerala, India**.
2. **A. Daya Mani** and Ch.Subrahmanyam, Effect of precursors on the properties of solution combustion synthesized TiO<sub>2</sub> for visible light photocatalysis. 2011. “International Conference on Nanomaterials and Nanotechnology” December 18-21, **University of Delhi, Delhi, India**.
3. **A. Daya Mani**, B. Rama Raju and Ch. Subrahmanyam, Facile Single Pot Syntheses of Metal Sulphide Quantum Dots for Solar Cell Applications. **2012**. “4th International Conference on Advanced Nano Materials (**ANM 2012**)”, October 17-19, **IIT Madras, Chennai, India**.
4. **A. Daya Mani** and Ch. Subrahmanyam, CdS/ZnO/NiS ternary hybrid nanostructures for enhanced visible light activity, 2014. “International Conference on Nanotechnology, Nanomaterials & Thin Films for Energy Applications (**NANOENERGY**) 19-21 February, **London, United Kingdom**.”